Institut für Photogrammetrie und Kartographie
der Technischen Universität München
Lehrstuhl für Methodik der Fernerkundung

SAR Interferometry for Volcano Monitoring: 3D-PSI Analysis and Mitigation of Atmospheric Refractivity

Xiaoying Cong

Vollständiger Abdruck
der von der Ingenieurfakultät Bau Geo Umwelt
der Technischen Universität München
zur Erlangung des akademischen Grades eines
Doktor-Ingenieurs (Dr.-Ing.)
genehmigten Dissertation.

Vorsitzender:
Univ.-Prof. Dr.techn. Roland Pail

Prüfer der Dissertation:
1. Hon.-Prof. Dr. rer. nat. Michael Eineder
2. Univ.-Prof. Dr.-Ing. habil. Richard Bamler
3. Univ.-Prof. Dr.-Ing. habil. Stefan Hinz
   Karlsruher Institut für Technologie

Die Dissertation wurde am 13.03.2014 bei der Technischen Universität München eingereicht und durch die Ingenieurfakultät Bau Geo Umwelt am 26.05.2014 angenommen.

Abstract

The monitoring of active volcanoes requires the measurement of surface deformation before, during and after volcanic activities, not only for improving the prediction of eruptions, but also for the better understanding and modeling of the involved geophysical processes. Space-borne synthetic aperture radar (SAR) interferometry (InSAR) provides a powerful tool for surveying the surface changes at a theoretical accuracy in the millimeter-range. In practice, this accuracy is limited due to effects such as phase noise, atmospheric distortions or phase unwrapping errors. Moreover, the application of InSAR techniques to volcanic areas is strongly limited by temporal decorrelation. Therefore, instead of using a single interferogram, the persistent scatterer interferometry (PSI) multi-temporal method, which is commonly used for urban areas is investigated and demonstrated for rocky volcanoes. This method exploits only time coherent pixels known as persistent scatterers (PS). Current meter-resolution SAR missions, such as the TerraSAR-X/TanDEM-X missions, map the Earth's surface with high geometrical resolution and radiometric accuracy and provide highly accurate orbit products. Thanks to the high spatial resolution, stable backscattering from rocks can be detected which indeed behave as persistent scatterers. In the Stromboli test site, the average PS density is about 30.000 PS/km^2 for TerraSAR-X high resolution spotlight (HRSL) images.

In volcanic areas, the atmospheric delay due to vertical stratification, the so-called stratified atmospheric delay, has a great impact on both interferometric and absolute ranging measurements. It causes a time- and height-dependent component in PS deformation estimates. A simple approach such a linear fitting of the final PSI estimation results as a function of height is insufficient in order to eliminate the effect of the stratified delay. In this thesis, an effective method to mitigate the stratified delay based on global 4-dimensional numerical weather prediction (NWP) products is developed: the direct integration method. Two products, ERA-Interim and operational data, provided by European Centre for Medium-Range Weather Forecast (ECMWF) are used for integration of the stratified delay. Two validation approaches are investigated. The first one is based on zenith path delay (ZPD) measurements derived from six permanent global positioning system (GPS) stations located in different meteorological conditions. The second approach is based on slant path delay (SPD) derived from CR-based measurements using 22 TerraSAR-X HRSL images. It is demonstrated that the accuracy of the estimated delay based on these NWP products is in the **centimeter-range** for both the zenith and the slant range directions. Furthermore, the direct integration method has been successfully applied to correct the stratified phase component of the interferometric phase prior to PSI estimation in the Stromboli test site. As a result, the effect of the stratified delay on PSI estimation is effectively mitigated.

Due to the geometrical limitations of SAR, four stacks of TerraSAR-X HRSL images from different geometries have been acquired in order to achieve a complete spatial coverage of the Stromboli volcano. A fusion algorithm for non-urban areas based on the iterative closest point (ICP) algorithm is proposed in order to estimate the elevation offset of each stack. Large range error sources, such as the atmospheric delay and earth tides, are considered in the master geometry in order to ensure an accurate geocoding of the PS points. After geometrical fusion of the multi-track atmospheric-delay-corrected PS clouds, an updated DEM with more than 4.4×10^6 PSs is generated. Due to the available viewing geometries, a deformation inversion limited to the vertical and the east components is presented. Based on both decomposed deformation components, the deformation patterns observed on the most active region of Stromboli, the Sciara del Fuoco (SdF), are interpreted as slope instability phenomena, where the gravitational component produces a constant creep. Moreover, the topographic changes with respect to the SRTM DEM estimated by PSI have a good agreement with the available literature on the recent activity in the Stromboli volcano.

Zusammenfassung

Das Monitoring von aktiven Vulkanen durch Messung der Oberflächendeformation vor, während bzw. nach vulkanischer Aktivität ermöglicht nicht nur die Verbesserung der Vorhersage von Vulkanausbrüchen, sondern auch ein besseres Verständnis für die Modellierung der geophysikalischen Prozesse im Inneren der Vulkane. Satellitenbasierte Synthetik-Apertur-Radar (SAR)-Interferometrie (InSAR) erlaubt die Erfassung und präzise Bestimmung der Oberflächendeformation mit einer theoretischen Genauigkeit im Millimeterbereich. In der Praxis ist diese Genauigkeit aufgrund von verschiedenen Fehlerquellen und Genauigkeitseinflüssen wie z.B. Phasenrauschen, atmosphärischen Störungen oder Fehlern beim Phase-Unwrapping schwer zu erreichen. In vulkanischen Gebieten spielt die temporale Dekorrelation der streuenden Oberfläche eine entscheidende Rolle für InSAR-Anwendungen. Daher wird in dieser Arbeit die multi-temporale Persistent-Scatterer-Methode, die auf der zeitlich kohärenten Streuung einzelner Punkte (sog. Persistent Scatterer, PS) basiert und bereits als robustes Verfahren in urbanen Gebieten bekannt ist, im Hinblick auf ihre Anwendbarkeit für Vulkane untersucht und erfolgreich demonstriert. Die aktuellen hochaufgelösten SAR-Missionen, wie z.B. die TerraSAR-X/TanDEM-X-Missionen, eröffnen die Möglichkeit der Aufzeichnung der Erdoberfläche mit hoher geometrischer Auflösung und hoher radiometrischer Genauigkeit und liefern darüber hinaus präzise Satellitenbahnprodukte. Dank der hohen räumlichen Auflösung der Radardaten, kann das stabile Signal einzelner Punkte wie z.B. Felsen, die sich wie PS verhalten, detektiert werden. Im ausgewählten Testgebiet – dem Stromboli-Vulkan – ergibt sich eine durchschnittliche PS-Punktdichte von ca. 30.000 PS/km^2 unter Anwendung der TerraSAR-X High Resolution SpotLight (HRSL) Szenen.

In vulkanischen Gebieten hat die atmosphärische Laufzeitverzögerung des Radarsignals aufgrund der vertikalen Stratifikation einen großen Einfluss auf interferometrische sowie auch auf absolute Entfernungsmessungen (Absolute Ranging). Sie verursacht zeit- und höhenabhängige Fehlerkomponenten in den PS-Bewegungsschätzungen. Ein Ausgleich der Höhenabhängigkeit mit Hilfe einer einfachen linearen Regression und Korrektur der PSI-Ergebnisse ist unzureichend. In dieser Arbeit wird eine effektive Methode entwickelt, um den Einfluss der stratifizierten Verzögerung zu korrigieren. Diese basiert auf den globalen vierdimensionalen Produkten der Nummerischen Wettervorhersage (NWP) und der direkten Integrationsmethode. Zwei verschiedene Produkte, die ERA-Interim und die sogenannten Operational Data, werden von dem European Centre for Medium-Range Weather Forecast (ECMWF) zur Verfügung gestellt und für die Integration der stratifizierten Verzögerung verwendet. Um die Genauigkeit beider Produkte zu validieren, werden zwei Methoden erprobt. Die erste basiert auf Messungen der Laufzeitverzögerung in Zenitrichung (ZPD) an sechs festen Stationen des Globalen Positionierungssystems (GPS), unter verschiedenen meteorologischen Bedingungen. Die zweite Methode basiert auf Radarreflektor-Messungen der Laufzeitverzögerung in Schrägsicht von 22 TerraSAR-X HRSL Szenen. Die Genauigkeit der atmosphärischen Korrekturen, welche auf NWP-Produkten basiert, liegt im **Zentimeterbereich** sowohl in Zenitrichtung als auch in Schrägsicht. Des Weiteren wird die direkte Integrationsmethode auch erfolgreich auf interferometrische Analysen im Testgebiet Stromboli eingesetzt. Hier wurde die stratifizierte Phasenkomponente der interferometrischen Phase vor der PSI-Schätzung kompensiert. Dadurch wurden die Effekte der stratifizierten Laufzeitverzögerung erheblich reduziert.

Unter Berücksichtigung der Abbildungsgeometrie wurden weiterhin vier Datenstapel von TerraSAR-X HRSL Szenen aus verschiedenen Blickwinkeln aufgenommen, um die komplette Abdeckung des Stromboli Vulkans zu erzielen. Die PS-Punktwolken der verschiedenen Datenstapel wurden dann mit einer neuen Methode basierend auf dem Iterative Closest Point (ICP) Algorithmus fusioniert, indem die Elevationsoffsets in jeder Geometrie gesucht werden. Zuvor werden die Range-Fehler, z. B. durch atmosphärische Laufzeitverzögerungen

und Erdgezeiten, in der Mastergeometrie berücksichtigt, um die Genauigkeit der Geokodierung zu verbessern. Die geometrische Fusion erfolgt mit vier geokodierten PS-Punktwolken (insgesamt mehr als 4.4×10^6 PSs) aus verschiedener Aufnahmegeometrie. Dadurch wird ein neues digitales Geländemodell mit besserer Abdeckung erzeugt. Aufgrund der verfügbaren Beobachtungsgeometrien wurde die Trennung auf die östlichen und vertikalen Bewegungskomponenten limitiert. Die Ergebnisse der Interpretation von zwei Bewegungskomponenten im Testgebiet Stromboli deuten darauf hin, dass Hanginstabilitäten aufgrund der Gravitation im aktivsten Bereich (Sciara del Fuoco, SdF) beobachtet werden. Zusätzlich zu den PSI-Bewegungs-Schätzungen zeigen die topographischen Änderungen im Vergleich zum älteren SRTM DEM eine gute Übereinstimmung mit der verfügbaren Literatur zu den zwei großen bekannten Eruptionen.

Acknowledgement

It was a long journey to finish my PhD thesis. Throughout all these years many people have helped me along this long road. It is a pleasure to express my gratitude to them.

First and foremost, my deepest gratitude goes to my supervisor Prof. Michael Eineder, who always inspires me with his invaluable advices and incisive comments that teach me the importance of the "accuracy". Without his persistent support this thesis would not have been possible.

I am sincerely grateful to Prof. Richard Bamler, firstly for providing me the PhD position in the Chair of Remote Sensing Technology, and more importantly for his insightful comments and suggestions. I would like to offer my special thanks to Prof. Stefan Hinz, who witnesses the first and the last part of my PhD journey. I also thank Prof. Uwe Sörgel who introduced the radar interferometry in my graduate study in Hannover. I would also like to thank Prof. Pail to be part of my defense committee.

Dozens of people have helped and supported me at the DLR IMF. I have received generous support from Dr. Ulrich Balss with his constructive work by providing me experiment data from corner reflector measurements in Wettzell. I want to thank Christian Minet for the installation of corner reflectors in Azores. I would like to show my greatest appreciation to the InSAR team: Nico Adam, Alessandro Parizzi, Ramon Brcic and Fernando Rodriguez Gonzalez, for their long-term support. I also appreciate the valuable discussions with Alessandro and Fernando. I would like to thank Ramon again for providing me the ionospheric delay correction software. I am grateful for the support from Dr. Thomas Fritz during the thesis writing period. I want to thank Bettina Bierkamp-Michalak for the final proof reading. I also thank the colleagues in TUM, particularly Christine Elmauer, Dr. Stefan Auer and Dr. Stefan Gernhardt.

I have greatly benefited from the discussions with Dr. Andreas Dörnbrack from Institute of Atmospheric Physics (DLR), who provided me an extensive introduction in weather forecast and the ECMWF operational data for supporting my experiments.

At every beginning, Marie Lachaise and I have shared our joyful and painful moments together. Several coincidences have brought us together, Wenyu Gong. Thank you all my dear friends in Munich and Hannover for the encouragement and accompaniment.

I owe a lot to my parents, who always provide me unconditional love and support at every stage of my personal and academic life. I would like to dedicate the thesis to my grandfather, who is not with me to share this joy.

Finally, I would like to express the deepest gratitude to Fernando, who plays different roles but equally important in my life at the same time. This thesis would not have been possible to write without his endless patience and support in both private life and at work.

Contents

List of abbreviations

ALOS-PALSAR	Advanced Land Observing Satellite-Phased Array type L-band SAR.
APL	Atmospheric Pressure Loading.
BMBF	German Federal Ministry of Education and Research.
BORJ	Borkum GPS station in EPN in Germany.
CD	Continental Drift.
CDO	Climate Data Operators.
CODE	Center for Orbit Determination in Europe.
CR	Corner Reflector.
CSA	Canadian Space Agency.
DEM	Digital Elevation Model.
DInSAR	Differential SAR Interferometry.
DLR	German Aerospace Center.
DORIS	Doppler Orbitography and Radiopositioning Integrated by Satellite.
DS	Distributed Scatterer.
ECMWF	European Centre for Medium-Range Weather Forecast.
EGM	Earth Gravitational Model.
ENVISAT-ASAR	Environmental Satellite-Advanced Synthetic Aperture Radar.
EPN	EUREF Permanent Network.
ERS1/2	European Remote Sensing Satellites 1 and 2.
ESA	European Space Agency.
ETRF	European Terrestrial Reference Frame.
ETRS	European Terrestrial Reference System.
ETRS89	European Terrestrial Reference System 1989.
EUREF	IAG Reference Frame Sub-Commission for Europe.
GB-InSAR	Ground Based InSAR.
GNSS	Global Navigation Satellite System.
GPS	Global Positioning System.
GSFC	Atmospheric Pressure Loading Service.
h2p	height to phase ambiguity.
HRSL	High Resolution Spotlight.
ICP	Iterative Closest Point.
ID	Ionospheric Delay.
IERS	International Earth Rotation and Reference Systems Service.
IFS	Integrated Forecast System.
IGS	International GNSS Service.
InSAR	Synthetic Aperture Radar (SAR) Interferometry.
ITRF	International Terrestrial Reference Frame.
ITRS	International Terrestrial Reference System.
IWV	Integrated Water Vapor.
IZAN	Guimar GPS station in EPN in Spain.
JMA	Japanese Meteorological Agency.
JPL	Jet Propulsion Laboratory.
KELY	Kangerlussuaq GPS station in EPN in Greenland.
LLR	Lunar Laser Ranging.
LoS	Line of Sight.
LPAL	Roque de los Muchachos GPS station in EPN in Spain.
LSA	Least Square Adjustment.
MAS1	Maspalomas GPS station in ENP in Spain.
MERIS	Medium Resolution Imaging Spectrometer.
MeteoSwiss	Swiss Federal Office of Meteorology and Climatology.

ML	Model Level.
MLE	Maximum Likelihood Estimator.
MM5	5th-generation PSU/NCAR Mesoscale Model.
MODIS	Moderate-resolution Infrared Spectrometer.
MSL	Mean Sea Level.
MWR	Microwave Radiometer.
NCEP	National Centers for Environmental Prediction.
NOTL	Non-Tidal Ocean Loading.
NWP	Numerical Weather Prediction.
OK	Ordinary Kriging.
OMT	Overall Model Test.
OP	ECMWF operational data.
OTL	Ocean Tide Loading.
PDEL	Ponta Delgada GPS station in EPN.
PS	Persistent Scatterer.
PSI	Persistent Scatterer Interferometry.
PSI-GENESIS	PSI module of Generic System for Interferometric SAR of DLR.
PT	Polar Tides.
PW	Precipitable Water.
RAOB	Radiosonde Observation.
RCS	Radar Cross Section.
RMS	Root Mean Square.
rng	range.
RSF	Range Sampling Frequency.
SAR	Synthetic Aperture Radar.
SBAS	Small Baseline Interferometry.
SCR	Signal to Clutter Ratio.
SdF	Sciara del Fuoco.
SET	Solid Earth Tides.
SHD	Hydrostatic Delay in slant range.
SK	Simple Kriging.
SL	Surface Level.
SLR	Satellite Laser Ranging.
SNR	Signal-to-Noise Ratio.
SPD	Slant Range Path Delay.
SRTM	Shuttle Radar Topography Mission.
SWD	Wet Delay in slant range.
TD	Tropospheric Delay.
TEC	Total Electron Content.
UTM	Universal Transverse Mercator.
VFRS	Early Response System.
VHR	Very High Resolution.
VLBI	Very-long-baseline interferometry.
WAP	Wide Area Processor.
WGS84	World Geodetic System 1984.
WMO	World Meteorological Organization.
WRF	Weather Research and Forecast.
WTZR	Wettzell GPS station in EPN in Germany.
ZHD	Zenith Hydrostatic Delay.
ZPD	Zenith Path Delay.
ZTD	Total Zenith Delay.
ZWD	Zenith Wet Delay.

List of Symbols

H	target height referred to geoid, denoted as the orthometric height.
L_{atmo}	atmospheric zenith delay.
L_{iono}	ionospheric slant delay.
L_s	atmospheric slant delay.
N_g	geoid undulation.
N_{atmo}	first three terms of the N.
N_{iono}	ionospheric refractivity.
N	scaled-up atmospheric refractivity.
P_d	partial pressure of dry air in Pascal.
P_{MSL}	mean sea level pressure in Pascal.
P_S	surface pressure in Pascal.
P_{atmo}	the last layer (first level) of the NWP product.
P	total atmospheric pressure in Pascal.
R'	measured slant range distance.
R_d	gas constant for 1 kg of dry air, 287.0 J $K^{-1}kg^{-1}$.
R_w	gas constant for 1 kg of water vapor, 461.51 J $K^{-1}kg^{-1}$.
R_{atmo}	range error caused by atmospheric delay effects.
R_{geod}	range error caused by geodetic effects.
R_{ideal}	gas constant for 1 kg of a gas.
R_{orbit}	range error caused by satellite orbit errors.
R_{sys}	range error caused by systematic errors.
R	slant range distance.
$TECU$	Total Electron Content (TEC) units, with 1 $TECU = 10^{16}m^{-2}$.
T_v	virtual temperature.
T_{MSL}	mean sea level temperature in Kelvin.
T_S	surface temperature in Kelvin.
T_m	weighted mean temperature of the atmosphere in Kelvin.
T	absolute temperature in Kelvin.
$VTEC$	vertical total electron content.
W_{cl}	the cloud water content, unit in g/m^3.
Z_d	compressibility of dry air.
Z_w	compressibility of water vapor.
Z	geopotential height.
$[X, Y, Z]_p$	ground object coordinates.
$[X, Y, Z]_s$	zero-Doppler sensor position.
β	difference between θ and θ_{inc}.
ϵ_0	permittivity of liquid water.
η_0	pixel offset in slant range.
η	range pixel number of an object in the SAR image.
γ	complex coherence, and its absolute value $\|\gamma\|$.
λ	radar wavelength.
$\mathbf{B}_\perp$	effective baseline.
$\mathbf{B}$	baseline vector.
$\mathbf{W}\{\cdot\}$	wrap operator.
$\mathbf{\Phi}_S$	surface geopotential, unit in m^2s^{-2}.
$\mathbf{\Phi}$	geopotential, unit in m^2s^{-2}.
ϕ_{P_0}	flat Earth phase.
ϕ_{noise}	interferometric phase of thermal noise.
ϕ_{orbit}	interferometric phase of orbit uncertainty.

ϕ_{topo}	topographic phase.
ρ_{lw}	density of liquid water.
ρ_w	density of water vapor.
ρ	density of a gas.
τ_{intern}	instrument internal delay.
τ	time interval between transmitted and received signal.
θ'	intersection angle between the radar ray and the ionosphere.
θ_{inc}	incidence angle.
θ_{loc}	local incidence angle.
θ	looking angle.
ε	a constant defined as $R_d/R_w = 0.622$.
$\vec{s}$	elevation direction depends on θ_{loc} and t.
c	speed of light in vacuum.
d_{los}	deformation in line of sight direction.
e_S	surface vapor pressure in Pascal.
e_s	saturation vapor pressure in Pascal.
e	partial pressure of water vapor in Pascal.
f_s	range sampling frequency.
f	radar frequency.
g_0	gravity acceleration constant, where $g_0 = 9.7840$ m/s^2.
g_m	mean gravity acceleration at the mass center of the atmospheric column.
g	gravitational acceleration.
h_s	satellite height referred to the ellipsoid.
h_{atmo}	thickness of the atmosphere.
h	target height referred to the ellipsoid, is referred to the geometric height z in Cartesian coordinate system.
l	elevation offset.
m_d	the mass of dry air.
m_w	the mass of water vapor.
n_e	electron density per cubic meter in the ionosphere.
n	refractive index.
p	logarithm of pressure P ($p = \ln P$).
q	specific humidity, unit in kg $\cdot$ kg^{-1}.
r_S	range coordinates of the integration path which starts at the intersection of the radar ray with the lowest ionosphere.
r_{atmo}	range coordinates of the integration path which ends at the height of the upper limit of the atmosphere z_{atmo}.
r_{eff}	effective troposphere height (z_{eff}) in slant range.
r_{iono}	range coordinates of the integration path which ends at the height of the satellite.
$\vec{r}$	transformation matrix.
t_0	the interval between transmitted and first received radar echo.
t	heading angle (satellite flight direction).
w	the mixing ratio between the mass of water vapor and the mass of dry air, usually expressed in grams of water vapor per kilogram of dry air g $\cdot$ kg^{-1}.
z_S	surface height.
z_{atmo}	upper limit of the atmosphere.
z_{eff}	effective troposphere height.
z_{iono}	height of the ionosphere.
z	geometric height in meter.

1 Introduction

Most of the active volcanoes are located within narrow bands in specific areas and mostly near the oceans. For example, the "Pacific Ring of Fire" is a belt of active volcanoes that surrounds the Pacific Ocean and contains about two-thirds of the world's active volcanoes (Scarth, 1994). Most of them are located in developing countries. Volcanic unrest, producing a variety of geologic and hydrologic hazards that threaten human lives, property and aviation safety, is difficult to predict. Furthermore, volcanic activities are often correlated with other catastrophes such as earthquake and tsunami. Therefore, it is vital to monitor active volcanoes for signs of unrest. One of the important indicators of volcanic unrest is surface deformation which provide the information about the volcanic activities underground and help us to better understand and to improve the geophysical modeling of volcanoes. This kind of surface changes is usually slowly in time and smoothly in space, and therefore, it has to be detected and measured with a millimeter accuracy. Nowadays, precise ground-based geodetic surveying techniques, such as the Global Positioning System (GPS), the electronic distance meter and the tiltmeter, are able to fulfill these requirements. However, the installation of instruments on site might not be feasible during volcanic unrest, and they only provide point-wise deformation measurements. In order to improve the spatial coverage of deformation measurements, the space-borne Synthetic Aperture Radar (SAR) Interferometry (InSAR) technique has been developed based on SAR acquisitions. It is a unique space-based technique that can generate surface deformation maps covering areas from several to a hundred kilometers in size with good accuracy (theoretically in millimeter range). Nevertheless the accuracy and availability of deformation measurements using InSAR techniques is limited due to decorrelation effects, atmospheric disturbances and the SAR side-looking geometry (which causes layover and shadowing). In this thesis, advanced techniques are developed in order to retrieve reliable deformation signal from active volcanoes using high resolution SAR images.

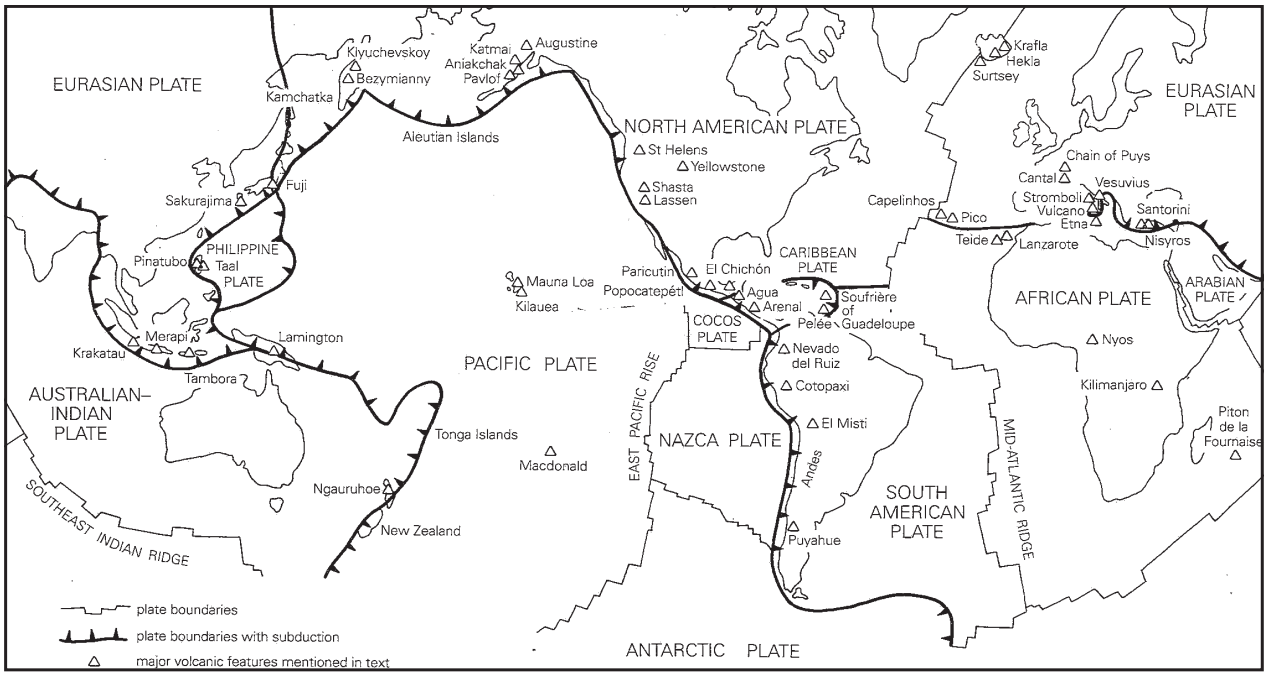

Fig. 1. The world volcano distribution map. The "Pacific Ring of Fire" is marked by the volcanic chains of Japan, Kamchatka, South Alaska and the Aleutian Islands, the Cascade Range of the United States and Canada, Central America, the Andes, New Zealand, Tonga, Vanuatu, Papua-New Guinea, Indonesia, the Philippines, and finally the Mariana, Izu and Bonin Islands. [Source: Scarth (1994)]

1.1 SAR interferometric techniques

- ◇ **The Differential SAR Interferometry (DInSAR)** technique was introduced by Gabriel and Goldstein (1988) at the end of the 1980s for topographic mapping and became popular in the 1990s (Massonnet, 1993; Bamler and Hartl, 1998; Massonnet and Feigl, 1998; Rosen et al., 2000). In 1991 and 1995, the European Space Agency (ESA) launched the European Remote Sensing Satellite 1 and 2 (ERS-1/2), which carried each a C-band SAR sensor on-board. Another C-band SAR satellite (RADARSAT-1) was launched by the Canadian Space Agency (CSA) in 1995. In the 1990s, three SAR sensors in orbit provided the opportunity to observe ground deformation in 100-km scale for applications such as monitoring earthquakes, volcanic eruptions/unrest, landslides and tectonic induced deformations using repeat-pass SAR interferometry (Massonnet et al., 1993, 1994, 1995, 1996; Zebker and Rosen, 1994; Zebker et al., 1999; Peltzer and Rosen, 1995; Peltzer et al., 1999; Meade and Sandwell, 1996; Lanari et al., 1998; Williams and Wadge, 1998; Bawden et al., 2001). SAR interferometry has demonstrated to be a powerful tool for mapping the topography and surveying surface changes. For volcano monitoring, differential SAR interferometry has been mainly applied to the measurement of surface changes which are useful to understand inner processes of volcanoes and to improve volcano geophysical modeling (Zebker et al., 1999; Amelung and Jónsson, 2000; Pritchard and Simons, 2002; Wicks et al., 2006; Sigmundsson et al., 2010; Zhang et al., 2010).
- ◇ **Multi-image InSAR techniques**. Most SAR satellites are located in the upper atmosphere (the ionosphere). The density of the Earth's atmosphere varies at different altitudes, and consequently, affects microwaves propagating through it. The path delay, exerted by the temporal and spatial variation of air composition, has an influence in the interferometric phase (Goldstein, 1995; Tarayre and Massonnet, 1996; Delacourt et al., 1998a; Hanssen, 1999, 2001). Without additional meteorological information or a priori information of the deformation signal, it is difficult to separate the atmospheric signal from the real deformation signal in a single interferogram. In Ferretti et al. (2000, 2001), a method is proposed using Persistent Scatterer (PS), which remains coherent over a series of SAR images, in order to jointly estimate the topographic error and the deformation based on a Maximum Likelihood Estimator (MLE), so-called Persistent Scatterer Interferometry (PSI). A deformation model is chosen in advance (for instance the linear deformation model) in order to eliminate the effect of the atmospheric signal. Kampes (2006), under the assumption that the atmospheric signal correlates in space and decorrelates in time, introduced a filter composed of high pass filter in time and low pass filter in space in order to filter the so-called "atmospheric noise". Due to temporal decorrelation and the lack of PSs in rural areas, the PS-based method is mainly applied in urban areas. The Small Baseline Interferometry (SBAS) method (Berardino et al., 2002; Lanari et al., 2004) has been developed in order to overcome this problem by using the interferograms with small spatial and temporal baselines. The SqueeSAR method proposed by Ferretti et al. (2011) has improved the PS-based method by accounting for Distributed Scatterer (DS) with stable phase history. Multi-image InSAR techniques offer an unique possibility for continuous volcano monitoring with accurate surface deformation measurements (Remy et al., 2003; Colesanti et al., 2003; Berardino et al., 2007; Hooper et al., 2007; Hooper, 2008). Nevertheless, the atmospheric delay has a direct impact on deformation measurements. Moreover, the SAR side-looking geometry limits the application in volcanic areas, due to the layover and shadowing phenomena.
- ◇ **Absolute ranging and absolute phase measurements**. On the other hand, the interferometric phase is sensitive to surface changes with an accuracy of a fraction of the radar wavelength λ. For surface changes larger than $\lambda/4$, the phase ambiguity problem arises. Some well-known phase unwrapping techniques, such as minimum cost

flow, branch-cut, etc., have been developed to solve this problem (Goldstein et al., 1988; Costantini, 1998). Nevertheless, they may fail and even introduce additional errors due to the low coherence and abrupt surface changes. Absolute ranging methods using time-delay measurements between SAR images or a SAR image and ground truth geolocation can derive surface changes absolutely, eliminating thus phase unwrapping errors and simplifying the processing as well. However, compared to phase measurements, the accuracy of absolute methods lies in the decimeter range, which depends on the orbit accuracy, the range bandwidth, the variation of atmospheric delay, Earth's tides and other geodetic effects. Once the effects of the variation of atmospheric delay and solid earth tides in range are precisely accounted for thoroughly, a centimeter-accuracy in line of sight direction can be achieved by means of high-precise orbit determination (Eineder et al., 2011; Schubert et al., 2012; Cong et al., 2012a). In azimuth, orbit and timing errors lead to an accuracy of several centimeters to decimeters. Instead of using full-bandwidth, the split-bandwidth and split-beam interferometry divide the bandwidth in sub-bandwidths for both range and azimuth to derive the absolute interferometric phase by increasing the "wavelength", and thereby avoid the phase unwrapping problem (Bamler and Eineder, 2004, 2005; Jung et al., 2009, 2011; Casu et al., 2011). As a consequence of split-bandwidths, the signal to noise ratio and the spatial resolution decrease. The split-beam interferometry provides additional information in azimuth direction up to a centimeter accuracy.

1.2 Limitations of SAR interferometry in volcanic areas

Volcanoes are often characterized as a conical mountain as presented in *Fig. 2*. Due to the abrupt height change and dense vegetation, the interferometric phase suffers from temporal decorrelation, atmospheric delay effects and SAR geometrical effects (Zebker and Villasenor, 1992; Rosen et al., 1996).

1.2.1 Temporal decorrelation

Unlike in urban areas, there are few man-made structures in rural areas which are stable over a large time span. For short wavelengths like X- and C-band the coherence decreases logarithmic in time (Parizzi et al., 2010). Two X-band differential interferograms over São Miguel Island with time spans of 11 and 308 days respectively are presented in *Fig. 3*. Their coherence images in *Fig. 3(d)* and *Fig. 3(f)* are used to evaluate the phase quality (see section 2.3.2). The Island is covered with dense vegetation (see *Fig. 3(b)*), which leads to temporal decorrelation in X-band data due to scattering changes between two acquisitions. Even after 11 days, the average coherence of rural areas (surrounded by red and blue rectangles in *Fig. 3(b)*) is about 0.17, then it decreases to around 0.14 after 308 days. In contrast, the coherence of urban areas (surrounded by the green rectangle in *Fig. 3*) stays stable over 0.26 for both interferograms in urban areas.

1.2.2 Atmospheric delay distortions

The radar signal travels through the Earth's atmosphere which is different from vacuum. There are two kinds of effects: firstly, the frequency-dependent delay caused by ionosphere; secondly, the frequency-independent delay caused mainly by the lower atmosphere. In this section, we concentrate on the frequency-independent delay, which is divided into two parts: the atmospheric delay due to vertical stratification and due to turbulent mixing. The atmospheric delay due to vertical stratification, define as the stratified atmospheric delay, plays an important role in mountainous regions (Delacourt et al., 1998a; Hanssen, 2001; Doin et al., 2009). In an

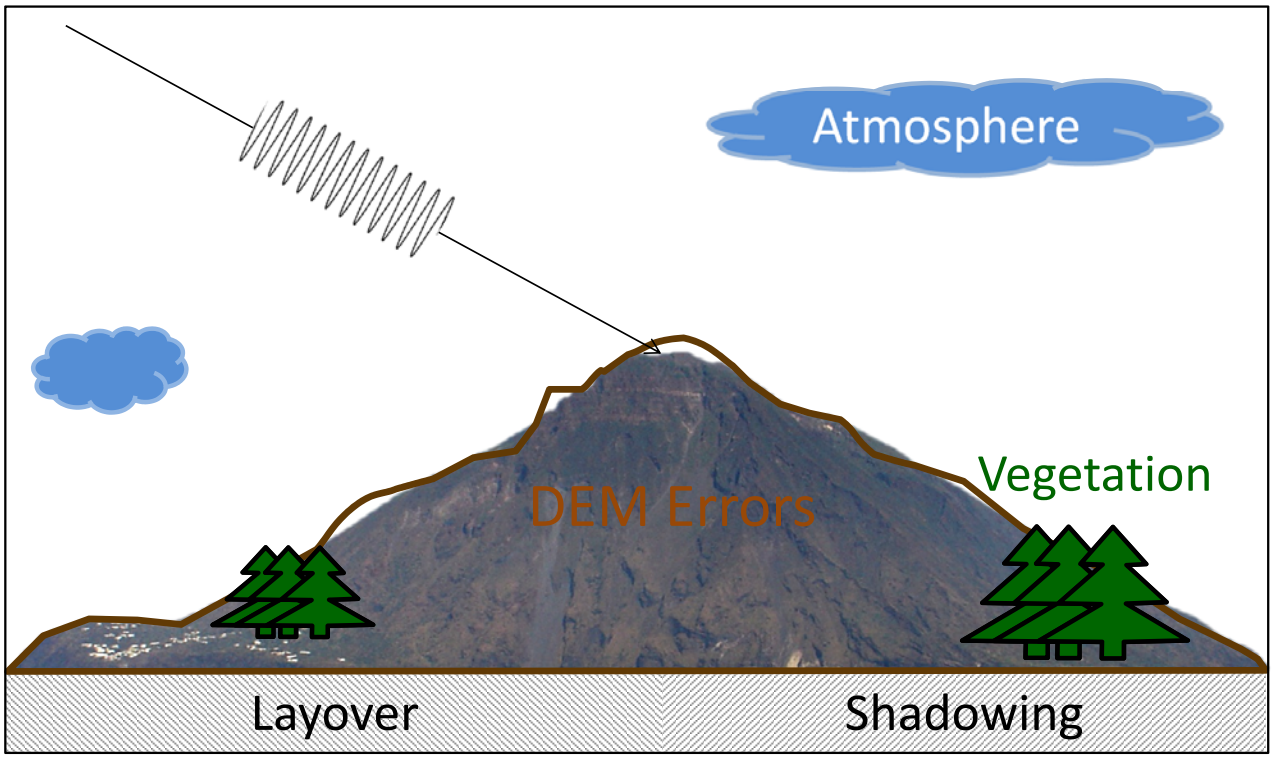

Fig. 2. Potential limitations of SAR interferometry in volcanic areas depicted on the photograph of Stromboli volcano taken from the south coast: temporal decorrelation, atmospheric delay effects, Digital Elevation Model (DEM) errors and SAR geometrical effects. [Source: photographed by Nestor Yague-Martinez in 2008]

interferogram, a height-dependent atmospheric delay difference of 3 mm in 100 m can cause two phase cycles in a 1000-m height mountain for X-band (more details in section 2.2.4) due to different meteorological conditions. The delay effect induced by turbulent atmosphere, described as a spatially correlated and temporally decorrelated effect, is limited in order of centimeter (Hanssen, 2001).

In *Fig. 4*, two differential interferograms over the Hierro Island (Spain) are selected to illustrate these two effects: one dominated by the vertical atmospheric stratification, and the other by turbulent mixing. In *Fig. 4(c)*, the differential phase after compensating the topographic component exhibits a significant correlation with height. From the sea level to the top of the mountain, there are about five fringe cycles, which are caused by the stratified atmospheric delay. The differential interferogram shown in *Fig. 4(d)* is affected mainly by the turbulent atmosphere. This delay effect is considered as a random effect in time and correlated in space which is difficult to model. As shown in *Fig. 4(d)*, there is no significant correlation between the phase and the height, whereas the phase pattern is highly correlated in space. More examples and discussions are presented in Chapter 3.

1.2.3 SAR Side-looking Geometry

Shadowing and layover areas are inevitable in mountainous areas due to the side-looking geometry of SAR systems. In order to visualize these problems, SAR images of Stromboli volcano (Italy) acquired by the TerraSAR-X satellite with four different acquisition geometries are presented in *Fig. 5*. Problematic regions, such as layover and shadowing areas, are illustrated in yellow and blue, respectively. As shown in *Fig. 5(a)*, at least two complementary geometries are required in order to obtain a full-coverage. However, scattering characteristics are different from different acquisition geometries and different acquisition times in volcanic areas. Therefore, it is difficult to find identical points (or PSs) from two geometries. At this point the challenge of fusing multi-geometrical interferograms arises.

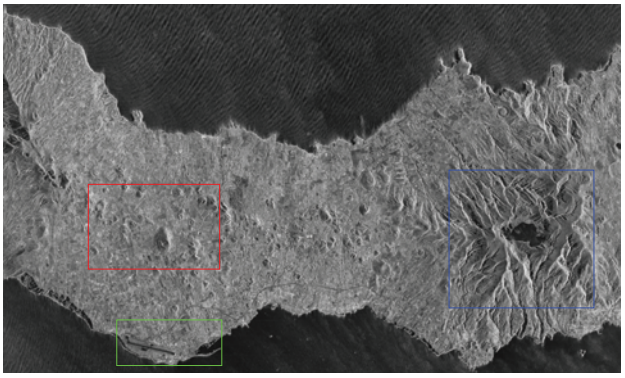

(a) SAR image of São Miguel Island

(b) The southeastern coast of São Miguel Island with the landscape of the Povoaşão caldera

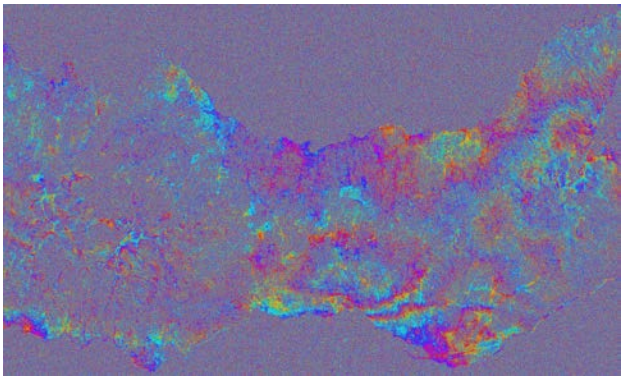

(c) Differential interferogram (11 days interval)

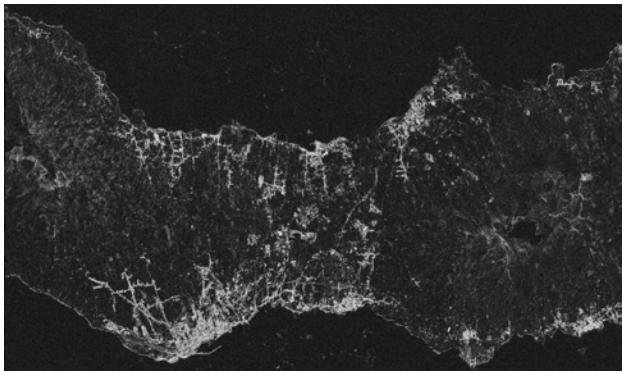

(d) Coherence image (11 days interval)

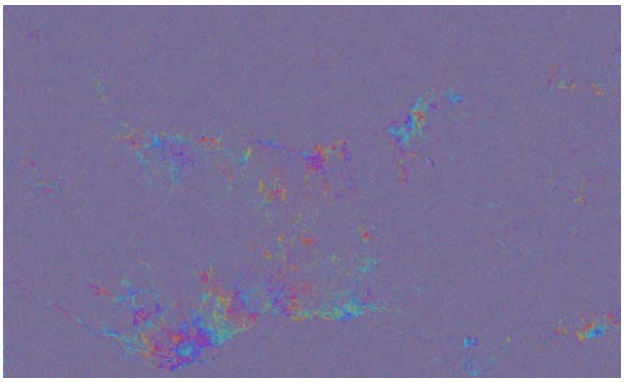

(e) Differential interferogram (308 days interval)

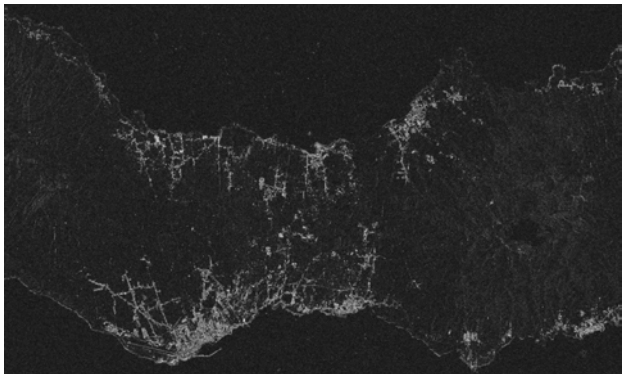

(f) Coherence image (308 days interval)

Fig. 3. Temporal decorrelation effect on SAR interferometry: an example in São Miguel Island using TerraSAR-X repeat-pass differential interferograms and their coherence images. (a) The amplitude image acquired on 13 January 2008 from TerraSAR-X satellite with selected regions: the volcano lake - Lagoa do Fogo (blue), Ponta Delgada airport (green) and the selected vegetated area near southeastern coast (red). (b) A photo of São Miguel Island was taken in April 2009. (c) The differential interferogram is generated using the master acquired on 13 January 2008 and the slave on 24 January 2008, and its effective baseline is about −101 m. (d) The coherence image of (c). (e) The differential interferogram is generated using the master acquired on 13 January 2008 and the slave on 16 November 2008, and its effective baseline is about −152 m. (f) The coherence image of (e).

1.3 Goal of this thesis - advanced techniques of SAR interferometry

In this thesis, the goal is to accurately and reliably derive and estimate surface deformation in volcanic areas using SAR interferometry. Several advanced SAR interferometry techniques

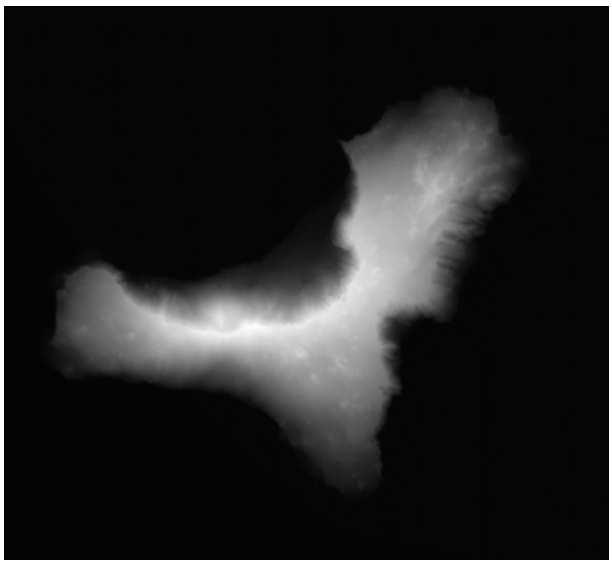

(a) DEM of Hierro Island

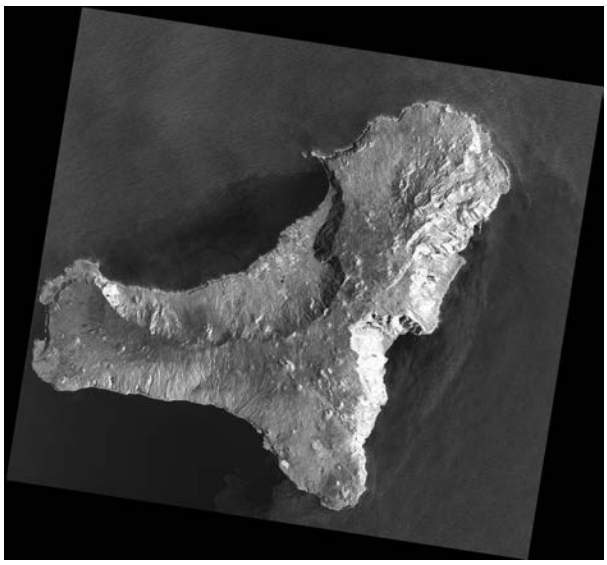

(b) SAR amplitude image

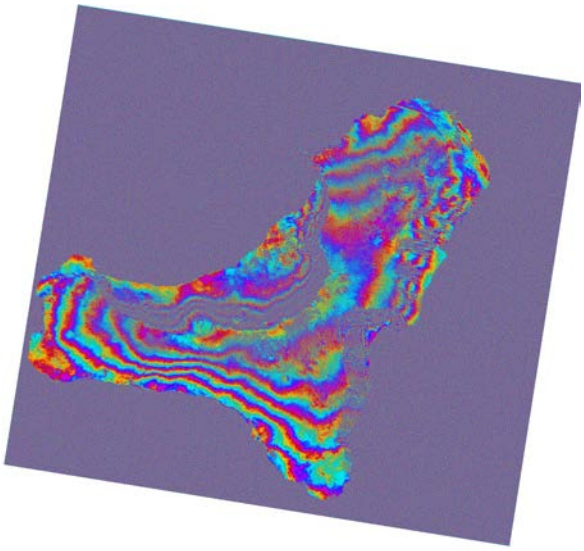

(c) Effects of vertical atmospheric stratification

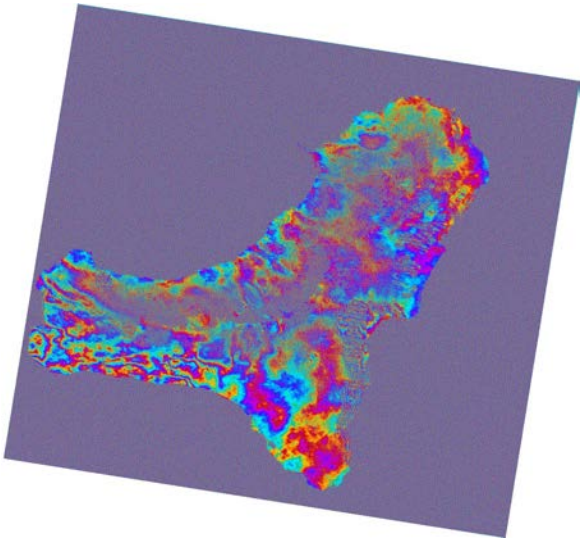

(d) Effects of turbulent mixing

Fig. 4. Propagation delay effects on SAR interferometry due to vertical stratification and turbulent mixing: an example in Hierro Island (Spain) using TerraSAR-X StripMap images. (a) The digital elevation model of Hierro Island, and the elevation varies from the sea level 0 m (black) to about 1542 m (white). (b) The SAR intensity image acquired on 10 October 2011. (c) The differential interferogram is generated using the master image acquired on 10 October 2011 and the slave image on 21 October 2011, and the effective baseline is about 58 m, where the differential phase is mainly contributed by atmospheric delay due to vertical stratification. (d) The differential interferogram is generated using the master image acquired on 4 December 2011 and the slave image on 15 December 2011, and the effective baseline is about 80 m, where the differential phase is mainly contributed by atmospheric delay due to turbulent mixing.

have been developed in order to overcome the limitations of SAR interferometry in volcanic areas discussed in section 1.2.

1.3.1 PSI processing using Very High Resolution SAR images

Current Very High Resolution (VHR) SAR missions, such as the TerraSAR-X/TanDEM-X missions, the Cosmos-SkyMed and the Radarsat-2, achieve sub-meter spatial resolution. Stable backscattering from rocks is able to be observed in SAR images and it can be detected as PSs in rocky volcanoes. Previous missions such as European Remote Sensing Satellites 1 and 2

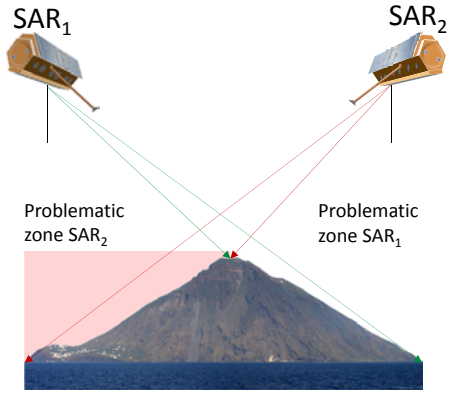

(a) Problematic zone by SAR side-looking geometry in volcanic areas

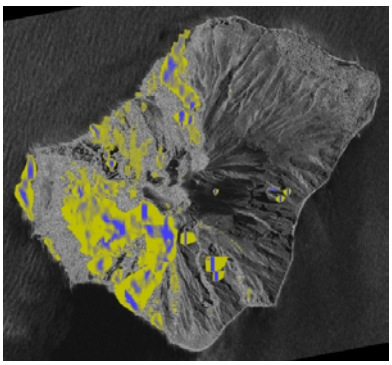

(b) Ascending acquisition (incidence angle: 32 °)

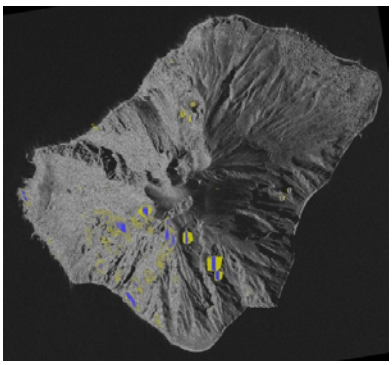

(c) Ascending acquisition (incidence angle: 46 °)

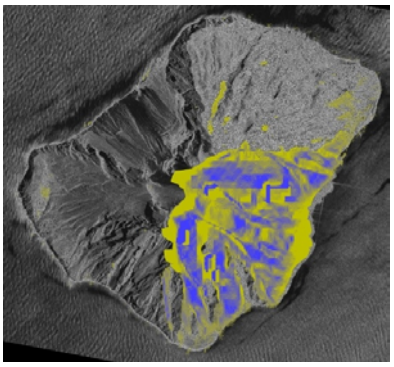

(e) Descending acquisition (incidence angle: 28 °)

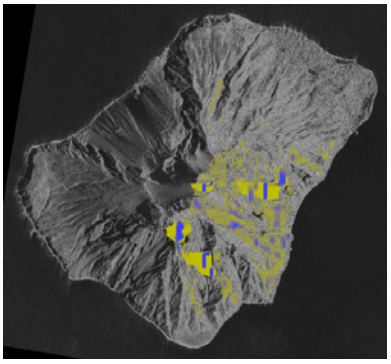

(f) Descending acquisition (incidence angle: 43 °)

Fig. 5. Geometrical problems of SAR side-looking geometry in Stromboli (Italy) with TerraSAR-X High Resolution Spotlight (HRSL) acquisitions in four geometries: two ascending geometries with incidence angles of 32 ° in (b) and 46 ° in (c); two descending geometries with incidence angles of 28 ° in (e) and 43 ° in (f). Layover areas are depicted in yellow and shadowing areas in blue.

(ERS1/2) and ENVISAT-ASAR have been designed to map large surface areas (about 100 km x 100 km) with a coarser spatial resolution of about 30 meter in which stable natural scatterers are difficult to be observed. In *Fig. 6*, two SAR intensity images from ENVISAT-ASAR and TerraSAR-X over the Stromboli volcano are presented. In *Fig. 6(b)*, explicit textures, such as craters and ridges, are clearly represented in the TerraSAR-X image acquired in the High Resolution Spotlight (HRSL) mode, whereas only coarse shapes are observable in the ENVISAT-ASAR image in *Fig. 6(a)*. In order to exploit stable natural scatterers in volcanic areas for interferometric approaches, the phase stability should be firstly verified. Two experiments have been carried out on selected volcanoes using corner reflectors and stable natural scatterers, which are discussed in section 2.4.3.

1.3.2 Compensation of atmospheric delay distortions on interferometric phase observations

The atmosphere affects the radar rays along the propagation path followed by the radar echoes from the satellite to the Earth and back. The atmosphere is divided into two regimes: the ionosphere and the rest of the atmosphere (including mesosphere, stratosphere and troposphere). Atmospheric gases, rain precipitation, clouds, fog and free electrons in the ionosphere are the main sources that induce delays, attenuation, noise, scintillations and depolarization in SAR images (see section 2.2.4.2). From these effects, the delay effects occurred

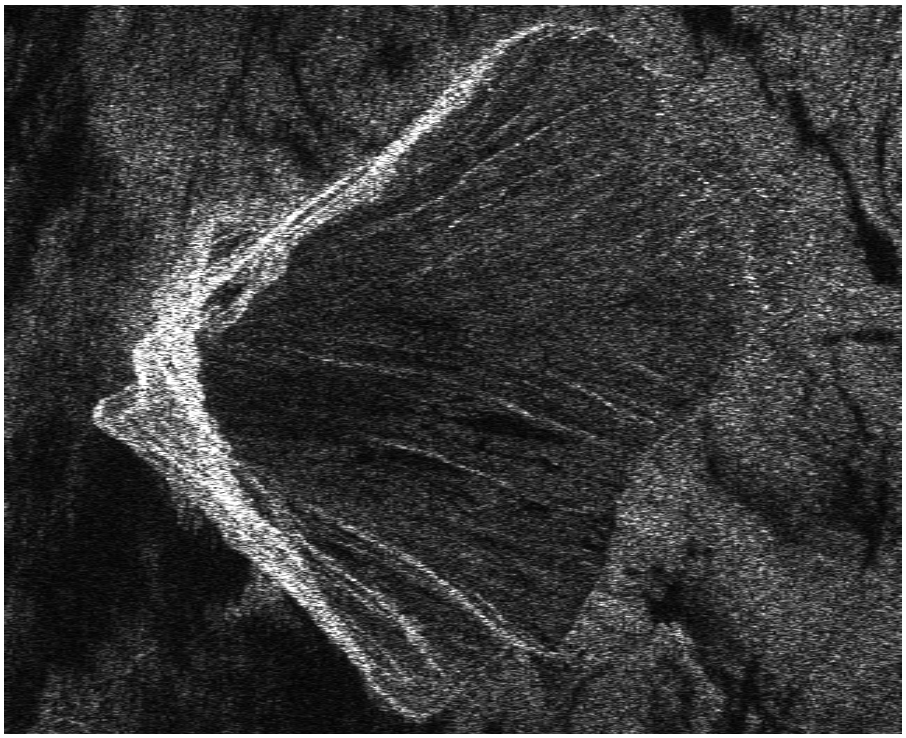

(a)

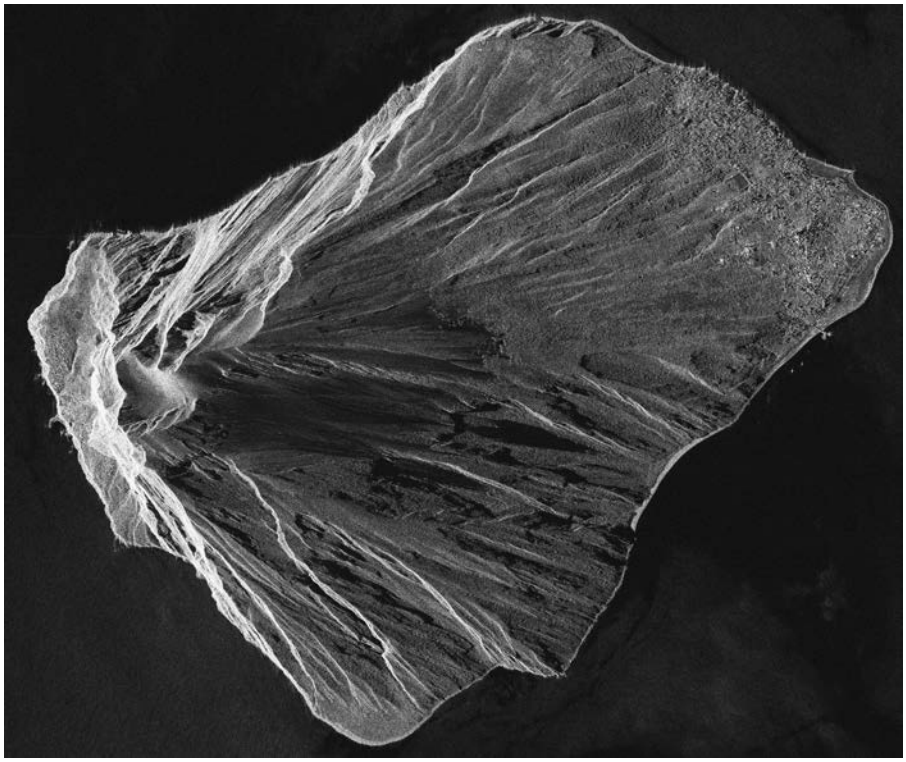

(b)

Fig. 6. SAR images of the Stromboli volcano, Italy: (a) image acquired from ENVISAT-ASAR sensor on 6 July 2007 in ascending orbit with 22.8 ° incidence angle; (b) image acquired from TerrSAR-X High Resolution Spotlight image mode on 2 May 2008 in ascending orbit with 32.0 ° incidence angle.

in both regimes will be considered. The ionospheric effects are frequency-dependent. They have a larger impact with higher electron densities and lower frequencies. Since the ionosphere changes homogeneously in time and in space, the ionospheric delay can be reduced and efficiently compensated by using TEC maps generated by GPS measurements around the acquisition time,

at least for high frequency X- and C-band SAR, even with coarse spatial resolution (e.g. 1 ° grid).

The troposphere contains almost 80% of the total atmosphere's mass. Due to the complex convection processes in the lower troposphere, it is important to obtain a better understanding of the tropospheric delay. Its delay effect can be decomposed into two components: the dry delay and the wet delay. The dry delay is a function of the surface temperature and the surface pressure, which can be well modeled and compensated for by surface measurements and models. The wet delay is produced by atmospheric water vapor, which is essential for terrestrial atmospheric processes. The duration of convection processes in the boundary layer (in the lower troposphere) takes from several minutes to days in mesoscale, defined in the range from 200 m to 200 km (see Wallace and Hobbs, 2006, P376). However, the turbulence flow in microscale (up to 200 m) is chaotic, which constitutes a major difficulty for weather modeling. State-of-the-art numerical weather models assimilate millions of observations (into the weather model) to improve the weather forecast reliability and its spatial resolution as well. The meteorological parameters (e.g. pressure, temperature and water vapor content) derived from weather models can be used to estimate the tropospheric delay in SAR images. A centimeter-level standard deviation agreement has been reported in Cong et al. (2012a) using ERA-Interim reanalysis data provided by European Centre for Medium-Range Weather Forecast (ECMWF) with comparison against the GPS Zenith Path Delay (ZPD). In this thesis, ERA-Interim data are used for the estimation and compensation of the tropospheric delay in single interferograms. Detailed description and results are reported in Chapter 3.

1.3.3 Fusion of multi-geometrical PSI clouds

Due to the geometrical limitations of the SAR side-looking geometry (layover and shadowing), multiple SAR stacks with different geometries have been proposed to achieve a full coverage. Each stack has been processed independently using the PSI technique. The independent results must be fused together afterwards. In urban areas, identical point scatterers and features like a roof of a building, a street or a railway trace can be found and extracted from different geometries, which can then be used to fuse different stacks. However, it is almost impossible to find identical points from different geometries in volcanic areas. In this thesis, an iterative method based on the total distance between point clouds is applied in Chapter 4.

1.3.4 Contributions

The main innovations of this dissertation are discussed in following sections:

(1) The possibility and the potential of using VHR SAR interferometry and PSI techniques are explored and analyzed for deformation monitoring of rocky volcanoes. Several applications have been published in Cong et al. (2008, 2010a,b,c).

(2) A new method reported in Cong et al. (2012a) is developed that applies the global weather model data to integrate and to compensate the atmospheric delay in absolute range measurements as well as in interferometric phases. Then, the influence of the atmospheric delay due to vertical stratification in the PSI processing is discussed. This method has been successfully demonstrated in various test sites in Cong et al. (2011, 2012b); Cong and Eineder (2012); Balss et al. (2012); Yague-Martinez et al. (2012).

(3) A new fusion method presented in Gernhardt et al. (2012) is developed to merge PS clouds from different geometries in volcanic areas to accomplish a full coverage. Two applications have been reported in Cong et al. (2010a); Cong and Eineder (2011).

2 SAR and InSAR techniques for volcanic areas - theory and experiments

SAR interferometry was originally introduced for applications in volcanic areas in the 1980s. First interest was to generate a Digital Elevation Model (DEM) using single-pass or repeat-pass interferograms (Mackenzie and Ringrose, 1986; Gabriel and Goldstein, 1988; Moreira et al., 1995; Fornaro et al., 1996). In volcanic areas, the complexity of the topography and the surface change due to the vegetation lead to problems, such as atmospheric delay, decorrelation, phase unwrapping errors etc. (Zebker and Villasenor, 1992; Massonnet, 1993; Goldstein, 1995; Tarayre and Massonnet, 1996; Rosen et al., 1996; Delacourt et al., 1998b). As an introduction, *Fig. 7* shows the SAR images, an interferogram and an differential interferogram acquired from ALOS-PALSAR of a volcano island in Italy, called "Vulcano", which is the origin of the name "volcano". This small volcano has an area of about 22 km^2 and rises a mere 500 m above sea level. In *Fig. 7*, the interferogram has a height to phase ambiguity (h2p) of 337 m per cycle, and it is about one and a half fringe cycle from the coast to the peak of the mountain. No significant change has been shown in the differential interferogram of 45 days interval.

In section 2.1, the principles of SAR imaging geometry and its limitations in volcanic areas are explained. The reader, who is familiar with SAR imaging geometry and the geometrical limitations in volcanic areas, may skip this section. In section 2.2, a summary of error sources for absolute SAR geometric accuracy is given. More details on the atmospheric propagation delay effects are discussed in section 2.2.4, as well as geodetic effects in section 2.2.5. A short introduction to repeat-pass interferometry is given in section 2.3. Techniques based on time series measurements are discussed in section 2.4.

2.1 SAR imaging geometry and its geometrical limitations in volcanic areas

The two-dimensional SAR imaging coordinate system is defined by the azimuth and slant range coordinates. In a Cartesian coordinate system, the azimuth direction is parallel to the sensor velocity vector. The radar pulse is sent from the SAR sensor to the ground object $[X, Y, Z]_p$ and reflected back with looking angle θ, then focused at the so-called zero-Doppler sensor position $[X, Y, Z]_s$, which is the closest range from the satellite S to the target P (see *Fig. 8(a)*). The slant range distance R between the satellite and the object is given by:

$$R = \sqrt{(X_s - X_p)^2 + (Y_s - Y_p)^2 + (Z_s - Z_p)^2}. \tag{1}$$

Due to the curvature of the Earth, the incidence angle θ_{inc}, defined as the local perpendicular to the ellipsoid, is different from the looking angle θ, the difference being the angle β. The local incidence angle θ_{loc} is defined as the intersection angle between the radar line of sight and the vector perpendicular to the local terrain. In the case of a flat terrain, the incidence angle θ_{inc} and the local incidence angle θ_{loc} are identical. In the case of non-flat topographic relief, the two angles are different, as shown in *Fig. 8(b)*. The satellite and the target heights referring to the ellipsoid are defined as h_s and h, respectively. The target height is often referred to the geoid (denoted as the orthometric height H), which has a height difference N_g to the reference ellipsoid due to the so-called geoid undulation. The relationship between the geoid height H and the ellipsoidal height h can be defined thus as:

$$h = H + N_g. \tag{2}$$

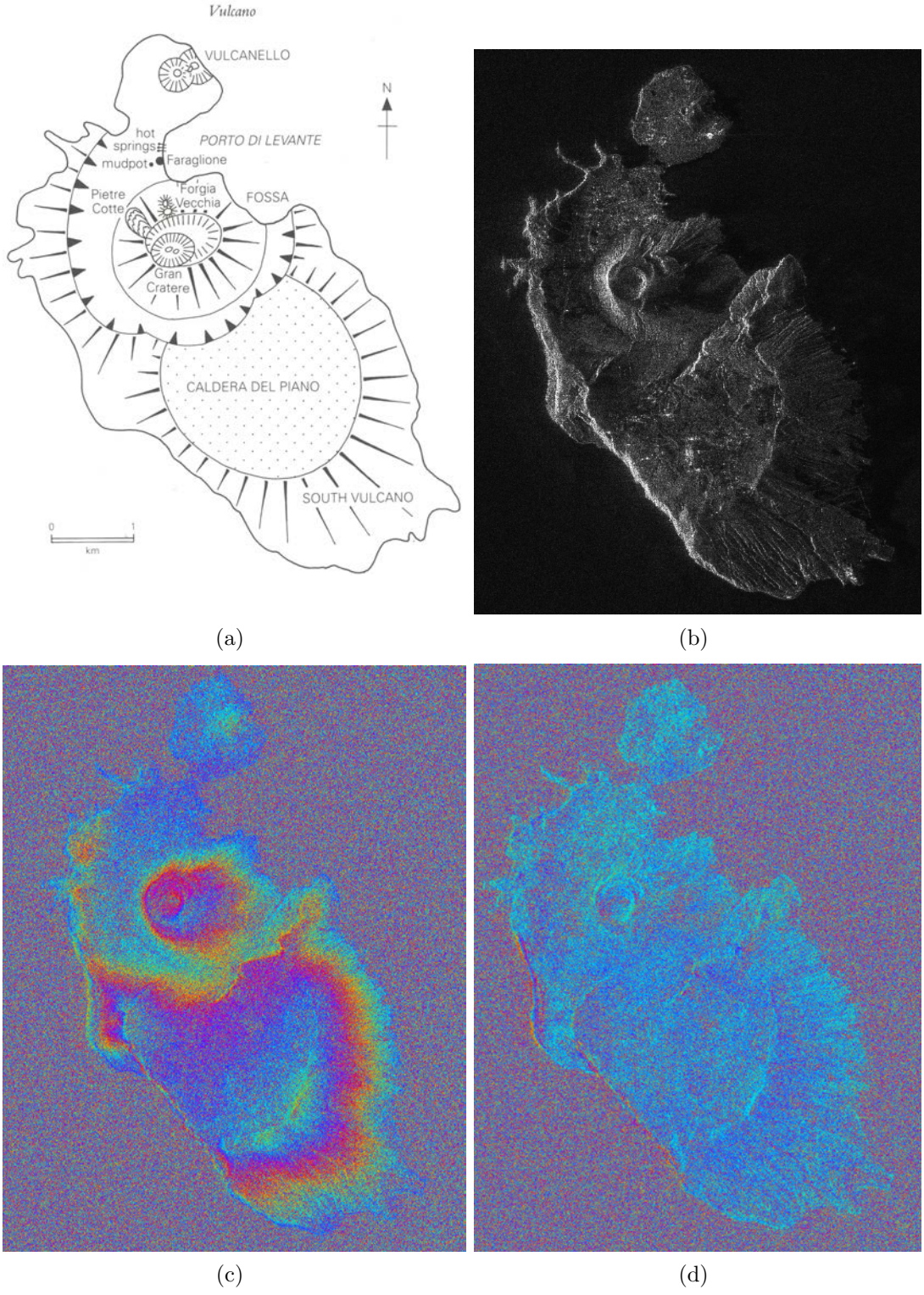

Fig. 7. An example of the interferogram and the differential interferogram on Vulcano, Italy: (a) Geographical map of volcano island - Vulcano; (b) the SAR image of Vulcano acquired from the ALOS-PALSAR sensor on 16 March 2008; (c) the interferogram with the master on 31 January 2008 and the slave on 16 March 2008; (d) the differential interferogram.

Latter in section 2.2.4 and Chapter 3, the geometric height z which is connected with the geopotential height Z is used instead of the ellipsoidal height h for describing the atmospheric delays. The conversion between z and Z is discussed in Appendix F.

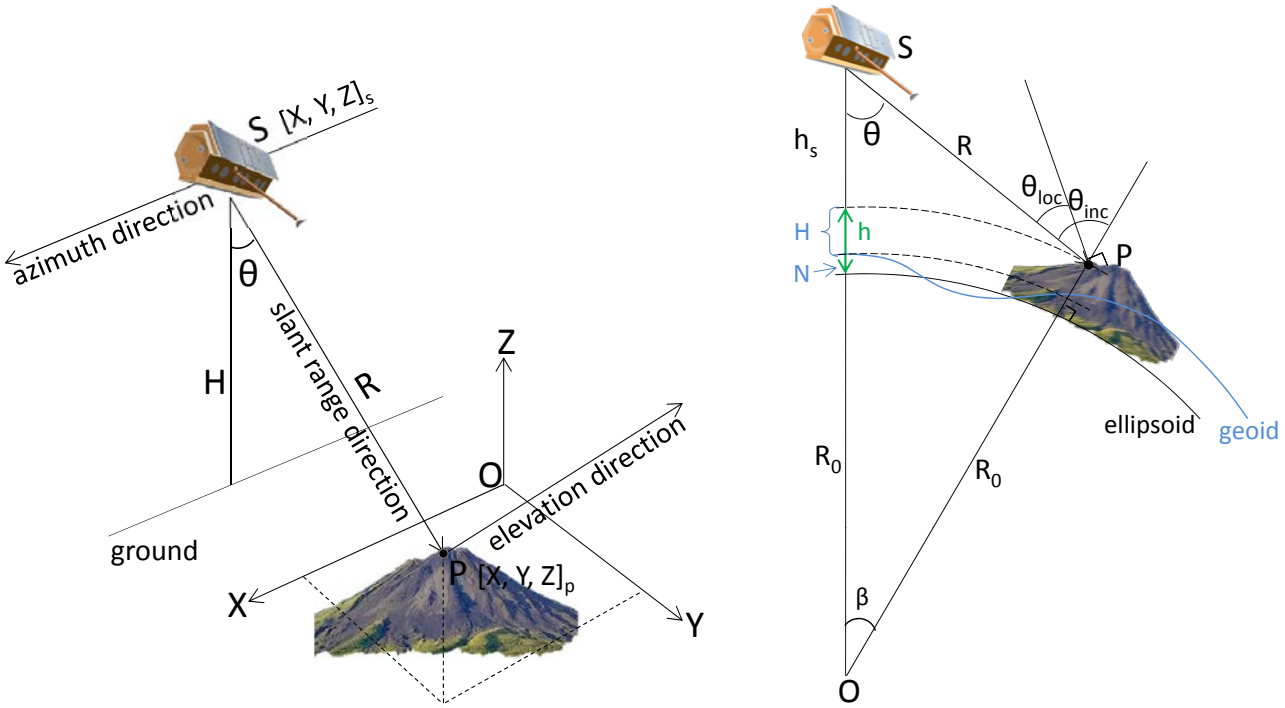

Fig. 8. SAR imaging geometry in a Cartesian coordinate system. (a) SAR imaging coordinates and its Cartesian coordinate system. The azimuth direction is the direction aligned with the sensor velocity vector (flight direction). The radar echo is sent from the sensor with a looking angle θ. The distance from zero-Doppler position $[X, Y, Z]_s$ to target $[X, Y, Z]_p$ is called slant range. In the context of SAR processing, a SAR image is produced in azimuth and slant range coordinates. The third direction is called elevation direction, which is the complementary direction to azimuth-slant range plane. (b) Illustration of the SAR cross-track coordinates on a reference ellipsoid with the incidence angle θ_{inc} and the local incidence angle θ_{loc}; illustration of different height systems with the ellipsoidal height of the object h, the orthometric height H from the object to the geoid and the geoid undulation N_g.

One of the major limitations in the use of SAR interferometry in volcanic areas is geometrical distortions due to the SAR side-looking geometry. An example of the SAR side-looking geometry in a mountainous area is illustrated in *Fig. 9*. The slant range represents the propagation direction of the radar ray, so-called the Line of Sight (LoS) direction, and the ground range is the projection of the slant range on the reference plane. Radar pulses are represented in a series of parallel dashed lines which are perpendicular to the LoS direction (see *Fig. 9*). As illustrated in *Fig. 9*, ground ranges are shortened, overlaid and shaded in the slant range due to the variation of the topography.

These problematic areas are depicted in different colors on the rectangle parallel to the slant range: foreshortening (green), layover (red) and shadowing (blue). The problem of foreshortening arises, while the ground range is shortened in the slant range. In more extreme situation, two or more ground points are overlaid in one pixel, because the range distances from the satellite to these ground points are identical. A simple mathematical formula is given to describe layover and shadowing areas according to the local incidence angle θ_{loc}: where $\theta_{loc} < 0$ indicates the layover and $\theta_{loc} > 90\,^\circ$ the shadowing.

Nevertheless the shadowing is unavoidable in the presence of steep topography. With respect to simulation results reported in Eineder (2003), it is possible to increase or even complete the visibility by combining SAR images from different viewing geometries. Therefore, complementary geometries are needed in order to obtain the objects in problematic areas.

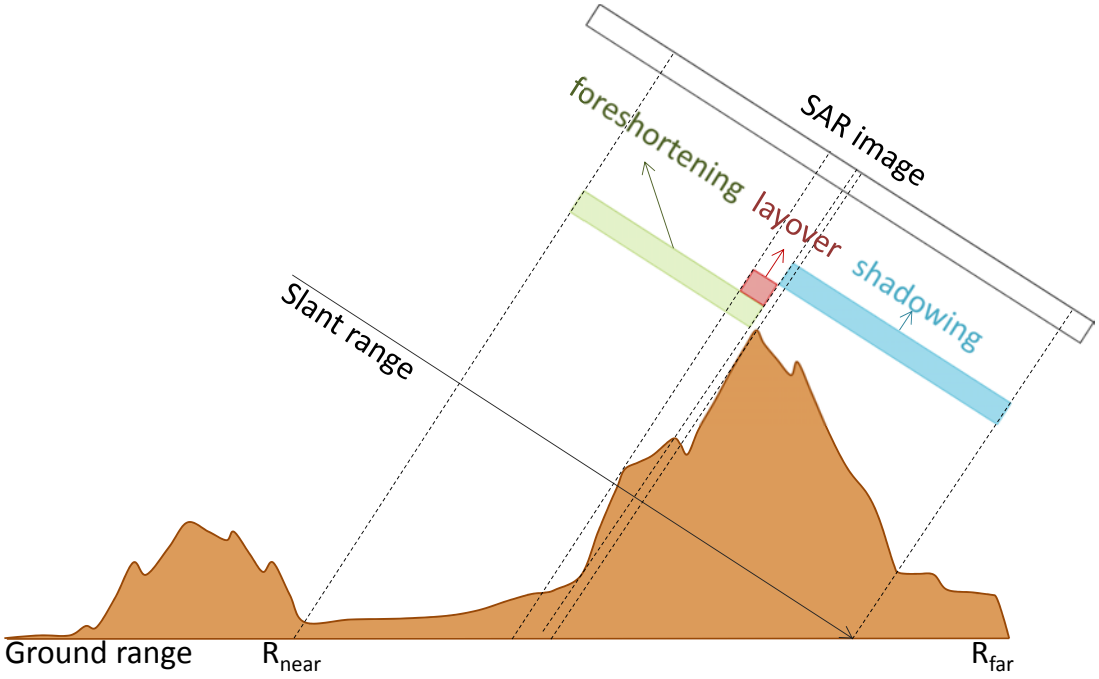

Fig. 9. SAR side-looking geometry in a mountainous area. The SAR ground range is the projection of the slant range on the reference plane. Depending on the traveling time of radar pulses, the slant range is divided from the near range to the far range. Problematic areas are depicted on the rectangle parallel to the slant range: the green area indicates the foreshortening area, the red area indicates the layover area and the blue area the shadowing area.

2.2 SAR Range geometric accuracy

The SAR geometric accuracy can be divided into two aspects: the range accuracy and the azimuth accuracy. The azimuth geometric accuracy is mainly dependent on azimuth timing, geodynamic effects, ionospheric gradients and focusing techniques (Breit et al., 2010; Balss et al., 2012; Meyer, 2011), which are out of the range of this thesis. Therefore, the azimuth geometric accuracy will not be discussed in detail. Regarding the range accuracy, the discussion of different error sources is divided into five sections: an introduction of the possible range sources is given in section 2.2.1; in section 2.2.2, the systematic errors of the range sampling frequency and the pixel localization are discussed; a short revision of satellite orbit errors for current satellite missions is given in section 2.2.3; the delay effect through the ionosphere and the troposphere is explained in section 2.2.4; finally, the geodetic effects of Earth tides and continental drifts are introduced in section 2.2.5.

2.2.1 Range components

The SAR range accuracy is affected mainly by four factors: systematic errors, satellite orbit errors, atmospheric propagation delay and geodetic effects (more details: solid Earth tides, ocean loading and atmospheric loading) (Mohr and Madsen, 2001; Shimada et al., 2009; Breit et al., 2010; Eineder et al., 2011). These error sources are visualized in *Fig. 10*, where the atmosphere has been decomposed in its main layers. In principle, the range distance R *eq. (1)* can be measured as $c \cdot \tau/2$, where τ is the time interval between transmitted and received signal and c is the speed of light in vacuum. Considering the influence of the error sources on range, the measured range R' is different from the expected range R, and may be written as:

$$R' = R + R_{sys} + R_{orbit} + R_{atmo} + R_{geod}, \tag{3}$$

where R_{sys}, R_{orbit}, R_{atmo}, R_{geod} are the range error caused by systematic errors, satellite orbit error, atmospheric delay and geodetic effects, respectively. The following sections will analyze each of these components.

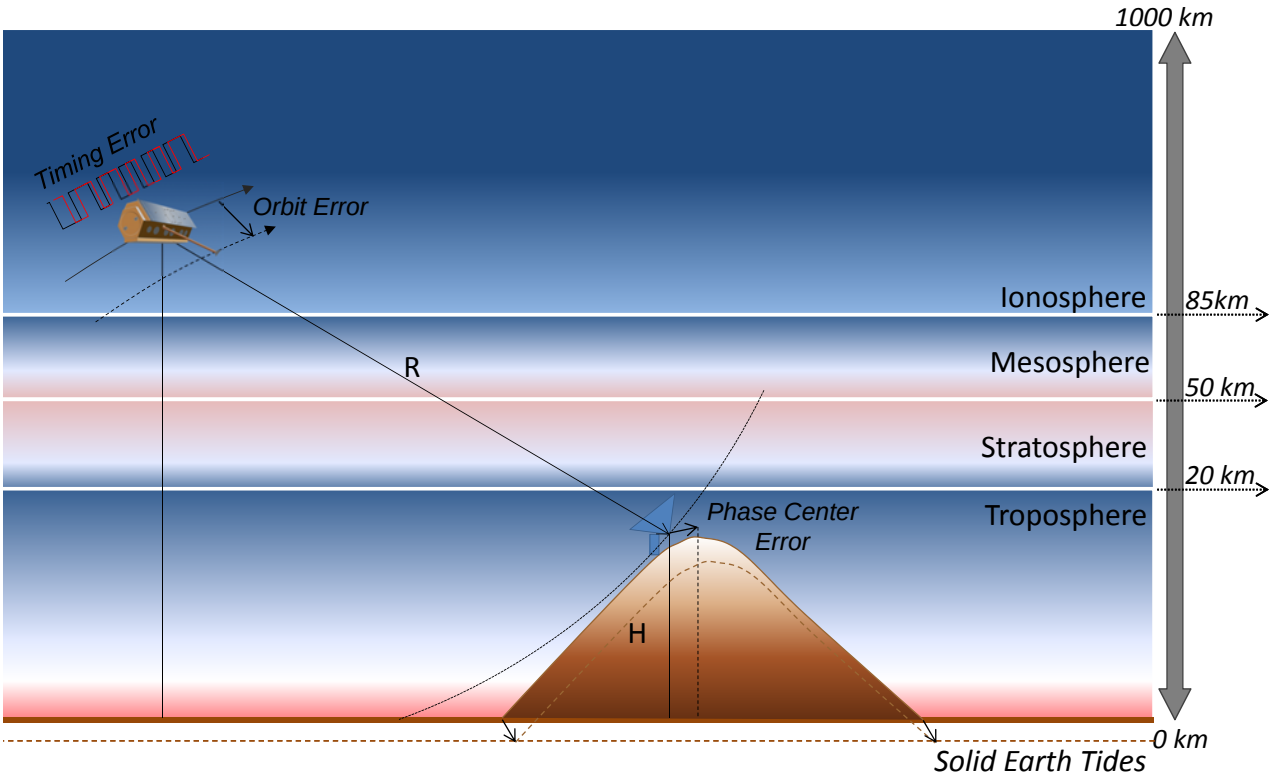

Fig. 10. A summary of error sources in range for the absolute range measurement from the object to the satellite, illustrated in the figure, are the systematic timing error, satellite orbit errors, effects due to the atmospheric propagation delay and geodetic effects, respectively. The atmosphere is depicted as the composition of four layers: the troposphere, the stratosphere, the mesosphere and the ionosphere. More details of atmospheric stratification can be found in section 2.2.4.3.

2.2.2 Systematic errors

The systematic errors in range are due to timing errors, which are mainly caused by the inaccuracy of the instrument internal delay τ_{intern} and the inaccuracy of the sampling frequency f_s (Breit et al., 2010; Eineder et al., 2011). For a given Range Sampling Frequency (RSF) f_s, the real range distance R' in vacuum can be calculated by using the measured range pixel coordinate:

$$R' = \left(\frac{(\eta + \eta_0)}{f_s} + \tau_{intern}\right)\frac{c}{2}. \tag{4}$$

where η is the range pixel number of an object in the SAR image and η_0 is a pixel offset in slant range, which represents the interval t_0 between transmitted and first received radar echo: $t_0 = \eta_0/f_s$. The internal delay is composed of different time delays, which can be considered as a constant value that can be well determined and calibrated for different beams (Mohr and Madsen, 2001; Shimada et al., 2009; Breit et al., 2010; Schwerdt et al., 2010). However, the accuracy of f_s has an influence on the range accuracy, which can be expressed by using the derivative of *eq. (4)*:

$$\frac{\partial R'}{\partial f_s} = -\frac{(\eta + \eta_0)}{f_s^2}\frac{c}{2}. \tag{5}$$

Using parameters from current satellite missions and assuming some reference looking angles θ, the range inaccuracy due to the error in the RSF has been calculated and presented in *Fig.*

11. For instance, for a TerraSAR-X acquisition with high resolution image model in 300 MHz and with looking angle θ of 40 °, in order to achieve 1 cm of range accuracy, the RSF should be stable to 4.47 Hz. In contrast, for ALOS-PALSAR dual-polarization model with 16 MHz and θ of 40 °, the frequency accuracy needs to be stable and accurate to 0.2 Hz.

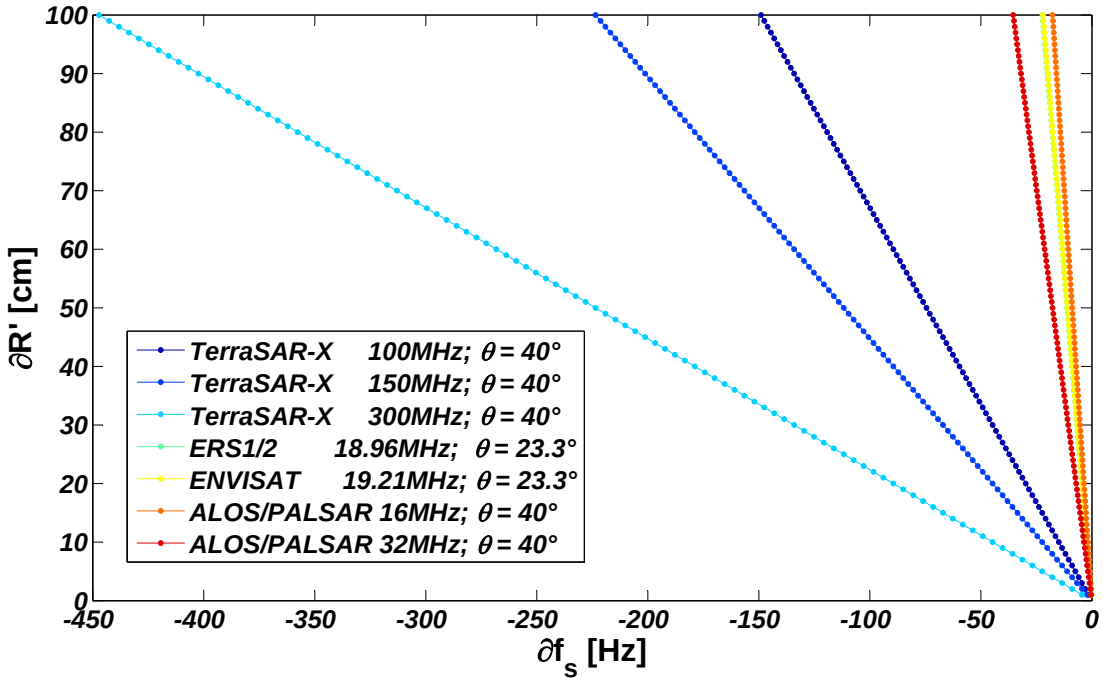

Fig. 11. Slant range error due to RSF error for different satellite missions. Horizontal axis represents the relative error of RSF ∂f_s in Hz and vertical axis represents the range error in centimeter. RSF errors of three TerraSAR-X acquisition modes with different range sampling frequencies and the same looking angle θ of 40 ° are depicted: 100 MHz in dark blue, 150 MHz in blue and 300 MHz in light blue, respectively. RSF errors of ERS1/2 with 18.96 MHz and θ of 23.3 ° are plotted in green. RSF errors of ENVISAT-ASAR with 19.21 MHz and θ of 23.3 ° are plotted in yellow. RSF errors of two ALOS-PALSAR acquisition modes and θ of 40 ° are depicted: 16 MHz in orange and 32 MHz in red.

2.2.3 Satellite orbit error

The accuracy of the satellite orbit affects directly the accuracy of slant range measurements. By applying geodetic survey techniques, such as Satellite Laser Ranging (SLR), GPS, Doppler Orbitography and Radiopositioning Integrated by Satellite (DORIS) etc., the orbit accuracy of current SAR satellite missions reaches from several centimeters to less than one meter (Scharroo and Visser, 1998; Doornbos et al., 2002; Yoon et al., 2009). In Scharroo and Visser (1998), using a more precise gravity model, it is possible to achieve a radial root-mean-square orbit accuracy of 5 cm for the ERS-1 satellite. As well, in Yoon et al. (2009) and Eineder et al. (2011), the orbit accuracy of TerraSAR-X has been proven to be around centimeter-level accuracy and stable in time.

2.2.4 Atmospheric propagation delay

The Earth's atmosphere is composed of a mixture of gases with a total mass of about 5×10^{18} kg. It stretches from the Earth's surface to the outer space (more than 1000 km). According to the temperature changes in the vertical direction, the atmosphere can be divided into five main layers - from the Earth's surface to the top of the atmosphere: troposphere, stratosphere, mesosphere, thermosphere and exosphere. Another important layer called ionosphere is generated primarily by the ionization of neutral atmospheric constituents

by solar radiation and it stretches from 50 to 1000 km. Radar satellites commonly have an orbit with the height lower than 1000 km, and are thus located between the thermosphere and the exosphere and within the ionosphere, as depicted in *Fig. 10*.

The microwaves transmitted by the satellite travel through the atmosphere and are thus affected by it. Firstly, due to air refractivity the velocity of the radar echo (the speed of light) is slower than in vacuum. Moreover, the propagation direction changes along the traveling path within the atmosphere effect, which is defined as the geometric excess. In this thesis, I concentrate on the atmospheric path delay. The variation of the geometric excess path due to bending is negligible, since the bending angle is under 0.02 ° for incidence angles from 20 ° to 40 ° which has a total effect less than 1 mm (Hobiger et al., 2008).

The general equation of air refractivity is given in section 2.2.4.1. The path delay effects are discussed separately for the ionosphere in section 2.2.4.2 and, more detailed, for the troposphere in 2.2.4.3.

2.2.4.1 Air refractivity and atmospheric propagation delay

The refractive index n varies along the radar echo propagation path. $(n-1)$ indicates the variation due to the atmosphere. However, $(n-1)$ is not directly used in atmospheric applications, since n is very close to 1. Therefore, a scaled-up refractivity $N = (n-1) \times 10^6$ is introduced. Neglecting non-ideal gas effects, N can be written as (Smith and Weintraubt, 1953; Hanssen, 2001; Hobiger, 2006; Healy, 2011):

$$N = (n-1) \times 10^6 = \underbrace{k_1 \frac{P_d}{T}}_{dry\ air} + \underbrace{k_2 \frac{e}{T} + k_3 \frac{e}{T^2}}_{wet\ air} + \underbrace{1.45 \cdot W_{cl}}_{liquid\ water} + \underbrace{K \cdot 10^6 \frac{n_e}{f^2}}_{ionosphere}, \tag{6}$$

where P_d is the partial pressure of dry air in Pascal, e is the partial pressure of water vapor in Pascal (Pa), T is the absolute temperature in Kelvin (K), W_{cl} is the cloud water content in g/m^3, n_e is the electron density per cubic meter in the ionosphere and f is the radar frequency (e.g. TerraSAR-X 9.65 GHz). The refraction effect caused by dry air is given by the first term, and the wet air effect by the second and third terms. The fourth term is due to the liquid water within the clouds (Hanssen, 2001). Finally, the dispersive effect of the ionosphere is the fifth term. The constants summarized by Hanssen (2001) are derived from laboratory measurements: $k_1 = 0.776$ K Pa^{-1}, $k_2 = 0.716$ K Pa^{-1}, $k_3 = 3.75 \times 10^3$ K^2 Pa^{-1} and the constant $K = 40.28$ m^3/s^2. However, (Healy, 2011) provided more precise values for coefficients $k_1 = 0.77643$ K Pa^{-1} and $k_3 = 3.75463 \times 10^3$ K^2 Pa^{-1}. In section 3.3.1, the atmospheric delay, integrated based on two sets of coefficients, is compared with the Zenith Path Delay (ZPD) derived from a selected GPS station in the EUREF Permanent Network (EPN) and in the International GNSS Service (IGS). Moreover, Different sets of coefficients are summarized in section 3.1.2.4. In section 2.2.4.3.2, a more general expression for the air refractivity (without terms from the ionosphere and the liquid water) is introduced by including non-ideal gas effects.

2.2.4.2 Ionospheric signal group delay

The ionospheric refractivity N_{iono} is used instead of the electron density n_e in the fifth term in *eq. (6)* to express the dispersive effect of the ionosphere. The relationship is expressed in the following equation (Hobiger, 2006; Meyer et al., 2006):

$$N_{iono} = K \cdot 10^6 \frac{n_e}{f^2}. \tag{7}$$

The ionospheric delay L_{iono} can be formulated by integrating the ionospheric refractivity N_{iono} along the ray path (Meyer, 2011; Eineder et al., 2011). Since the vertical variation of the ionospheric refractivity from the surface z_S to the height of the ionosphere z_{iono} is difficult to measure, the Total Electron Content (TEC) is used to estimate the propagation delay caused by a constant ionosphere:

$$L_{iono} = \frac{1}{10^6} \int_{r_S}^{r_{iono}} N_{iono} \mathrm{d}r \approx -\frac{K}{f^2} \cdot \frac{VTEC}{\sin\theta'}, \quad \text{with} \quad VTEC = \int_{z_S}^{z_{iono}} N_{iono} \mathrm{d}z, \tag{8}$$

where r_S and r_{iono} represent the start and end range coordinates of the integration path which starts at the intersection of the radar ray with the lowest ionosphere and ends at the height of the satellite, $VTEC$ indicates the vertical total electron content. TEC units, with 1 $TECU = 10^{16}$ m^{-2}, are used for the delay calculation for convenience. For example, one $TECU$ can induce ca. 0.4 cm and 1.4 cm of group delay in zenith for range measurements from X- and C-band. For lower frequency L-band, the delay effect is about 1 m for 4 $TECUs$. In order to obtain the slant range delay, the vertical delay has been projected via the intersection angle θ' between the radar ray and the ionosphere. This angle is not the same as the local incidence angle θ_{loc}. For instance, θ' is about 1.24 ° smaller than θ for an average ionospheric height of 250 km and an incidence angle of 30 ° (more details given in Appendix A).

In practice, the ionosphere induced delay can be determined by recording multifrequencies transmitted by GPS satellites (Brunner and Gu, 1991). Moreover, based on a global network of GPS stations, a global $VTEC$ map is available. Global ionospheric models are provided by the Center for Orbit Determination in Europe (CODE) (CODE, 2012) and by the German Aerospace Center (DLR) (SWACI, 2012). The global TEC map is derived mostly from ground-based Global Navigation Satellite System (GNSS) networks and space-based radio-occultation measurements. Since the TerraSAR-X satellite flies in the ionosphere at a height of 514 km, an empirical scaling factor of 75% of the total ionospheric delay is applied (Balss et al., 2012). In Gisinger (2012), an improved method was introduced to estimate the ionospheric delay between the TerraSAR-X satellite and a target by separating the ionosphere above and below the satellite using both ground- and space-based GPS observations and the global ionospheric model of CODE. Furthermore, Bamler and Eineder (2004) have introduced an alternative method for estimating and compensating the relative ionospheric delay in SAR interferogram using split-spectrum method which has been realized by Brcic et al. (2011).

2.2.4.3 Atmospheric path delay in the neutral atmosphere

In contrast to the ionosphere, the neutral atmosphere is composed of electrically neutral gases. It is located below the ionosphere. The path delay is in the meter-range both in zenith and in slant range. In this thesis, two types of atmospheric delays can be distinguished according to their physical origins: one is dominated by vertical stratification, while the other one by turbulent mixing (Hanssen, 2001). On a global scale, the atmosphere is in hydrostatic equilibrium. Under this condition, the vertical structure of the atmosphere tends to be stratified under the arrangement of gravity, where the higher densities are found below the lower densities. Furthermore, the density is a function of temperature and pressure, which are highly correlated with height. Therefore, the height-dependent path delay, which is caused by vertical atmospheric stratification, is defined as *stratified atmospheric delay*. On the other hand, the *atmospheric delay induced by turbulent mixing*, which is dominated by nonhydrostatic processes, has poor or no correlation with topography. In section 2.4 and 3.4, the stratified delay is estimated by the atmospheric delay integrated based on products from a hydrostatic Numerical Weather Prediction (NWP) model and the residual delay is considered as atmospheric delay induced by turbulent mixing.

In this section, the hydrostatic equation and the vertical structure of atmosphere are firstly presented in section 2.2.4.3.1. Then, the basic equations regarding air refractivity and integrated atmospheric delay in zenith and slant range are explained in section 2.2.4.3.2. The moisture parameter, specific humidity, is introduced in 2.2.4.3.3. After that, a short revision of definitions and abbreviations of atmospheric delays is given in section 2.2.4.3.4. Finally, a review of different correction methods for atmospheric delay in absolute and relative SAR range measurements is discussed in section 2.2.4.3.5.

2.2.4.3.1 Hydrostatic equilibrium and atmospheric stratification

In the lower atmosphere (< 80 km), gravitational attraction and air pressure regulate the vertical atmospheric motion in a hydrostatic equilibrium. The relationship between height, air pressure and temperature can be expressed by combining the hydrostatic equation *(9)* and the ideal gas equation *(10)* (Wallace and Hobbs, 2006):

$$-\frac{\partial P}{\partial z} = -g\rho, \tag{9}$$

$$P = \rho R_{ideal} T = \rho R_d T_v \quad \text{with } T_v = T \Big/ \Big(1 - \frac{e}{P}(1-\varepsilon)\Big), \tag{10}$$

where P, z, T and ρ are pressure (in Pascal), geometric height (in meter), temperature (in Kelvin) and density of the gas, respectively; g is the gravitational acceleration; R_{ideal} is a constant for 1 kg of a gas, e.g. $R_d = 287.0$ J K^{-1}kg^{-1} is the gas constant for 1 kg of dry air and $R_w = 461.51$ J K^{-1}kg^{-1} the gas constant for 1 kg of water vapor, and the constant ε is defined as $R_d/R_w = 0.622$. The virtual temperature T_v is used to derive the temperature lapse rate of moist air (see Appendix C).

Since the density of the gas ρ is generally not known or measured, *eq. (10)* is used to eliminate ρ in *eq. (9)*:

$$\frac{\partial P}{\partial z} = -\frac{Pg}{R_{ideal} T} = -\frac{Pg}{R_d T_v}. \tag{11}$$

According to the temperature dependency with height and pressure, the atmosphere is divided into four layers: troposphere, stratosphere, mesosphere and thermosphere. Within the troposphere, temperature decreases linearly with height up to the tropopause. Then, temperature stays stable with respect to increasing height in the lower stratosphere. And then it increases continually linearly up to the stratopause. In the mesosphere, temperature decreases with height up to the mesopause (Wallace and Hobbs, 2006). Without consideration of small-scale effects and turbulence, the atmosphere can be considered in hydrostatic balance. Under this assumption, air pressure observed in *Fig. 12(c)* decreases exponentially with height above the surface. Therefore, the atmosphere appears stratified. Normally, these vertical variations in pressure/height and temperature/density are much higher in magnitude than the corresponding horizontal variations. During different acquisition time, different vertical distributions are observed by temperature and pressure (see *Fig. 12*).

2.2.4.3.2 Integrated atmospheric delay in zenith and in slant range

Ignoring the effects of the ionosphere and clouds, air refractivity N_{atmo} is expressed as a function of temperature, pressure and specific humidity in *eq. (6)*. From Dalton's law of partial pressures, the total atmospheric pressure P can be constituted as $P = P_d + e$. Under the assumption of an ideal gas, the first three terms of the *eq. (6)* can be written in an alternative form:

$$N_{atmo} = k_1 \frac{P}{T} + \Big(k_2 - k_1\Big)\frac{e}{T} + k_3 \frac{e}{T^2}, \tag{12}$$

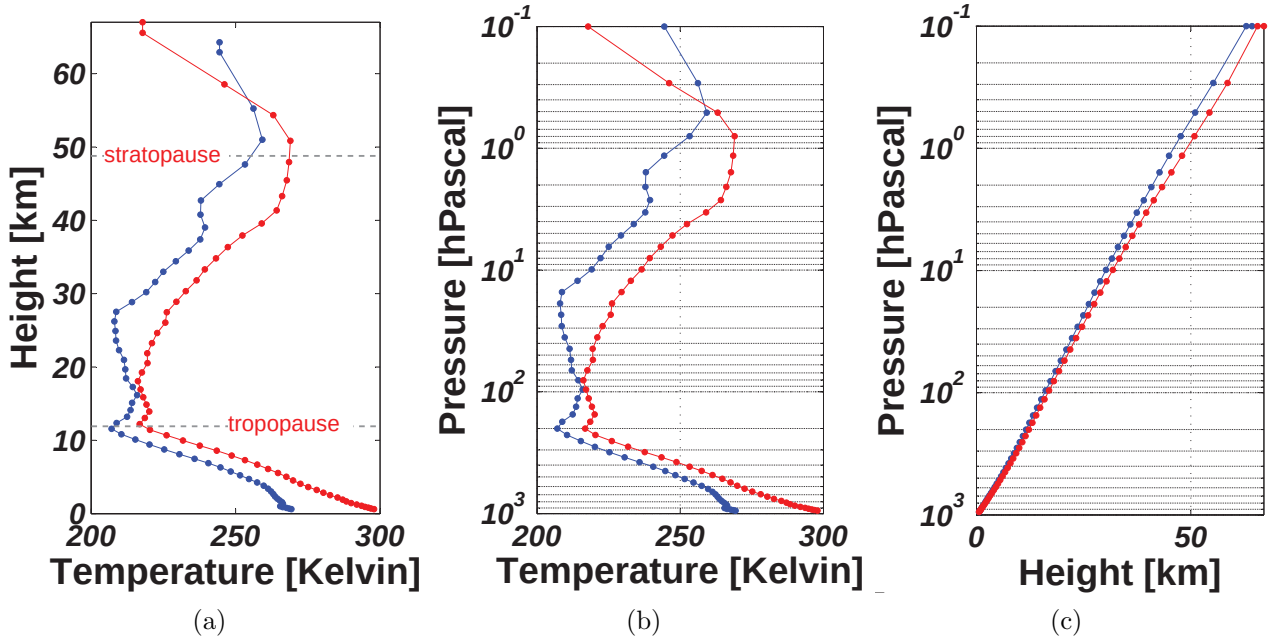

(a) (b) (c)

Fig. 12. Atmospheric parameters in winter in blue (on 26 January 2012 0 h) and in summer in red (on 26 July 2012 0 h) of the Wettzell GPS station (Germany) extracted from ERA-Interim data: (a) the vertical temperature profile in Kelvin (x-axis) and height in kilometer (y-axis); (b) the vertical temperature profile in Kelvin (x-axis) pressure in hPascal (y-axis) ; (c) the vertical pressure profile in hPascal (y-axis) and height in km (x-axis).

For precise geodetic applications, Thayer (1974) introduced a general equation for air refractivity by including non-ideal gas effects, so that the *eq. (12)* can be rewritten as:

$$N_{atmo} = \frac{k_1 P_d}{Z_d T} + \frac{k_2 e}{Z_w T} + \frac{k_3 e}{Z_w T^2}, \tag{13}$$

where Z_d and Z_w are the compressibility of dry air and water vapor, respectively. As well as the density of dry air and water vapor in *eq. (10)* can be written as:

$$P_d = \rho_d R_d T Z_d, \quad e = \rho_w R_w T Z_w. \tag{14}$$

The empirical equations for Z_w and Z_d derived from Owens (1967) are given by:

$$Z_d^{-1} = 1 + P_d\Big[57.97 \cdot 10^{-10}\Big(1 + \frac{0.52}{T} - 9.4611 \cdot 10^{-6}\frac{t^2}{T}\Big)\Big], \tag{15a}$$

$$Z_w^{-1} = 1 + 16.50 \cdot \frac{e}{T^3}\Big[1 - 0.01317t + 1.75 \cdot 10^{-5}t^2 + 1.44 \cdot 10^{-6}t^3\Big], \tag{15b}$$

where t is the temperature in degree. The effect of the compressibilities over the integration result is discussed in section 3.1.2.4.2.

Combining *eq. (13)*, *(14)* and *(11)*, the refractivity equation can be expressed as:

$$N_{atmo} = k_1\rho_d R_d + \frac{k_2 e}{Z_w T} + \frac{k_3 e}{Z_w T^2} \tag{16a}$$

$$= k_1\rho R_d - k_1\rho_w R_d + \frac{k_2 e}{Z_w T} + \frac{k_3 e}{Z_w T^2} \tag{16b}$$

$$= k_1\frac{P}{T_v} + \Big(k_2 - \frac{R_d}{R_v}k_1\Big)\frac{e}{Z_w T} + \frac{k_3 e}{Z_w T^2} \tag{16c}$$

$$= k_1\frac{P}{T_v} + \Big(k_2 - \varepsilon k_1\Big)\frac{e}{Z_w T} + \frac{k_3 e}{Z_w T^2}. \tag{16d}$$

It is known that the moist air is less dense than dry air (Wallace and Hobbs, 2006). Therefore, T_v is larger than T in order to keep at the same P for mixed atmosphere. Nevertheless, since $e \ll P$, we assume that $T_v \approx T$, which leads to an increase of the air refractivity, where the atmosphere is moist. Furthermore, in Owens (1967), Z_w is about 1.00049 with $e = 6.014$ hPa and $T = 273$ K. Therefore, we assume that Z_w and approximately equal to 1, so the refractivity function can be simplified as:

$$N_{atmo} = k_1 \frac{P}{T} + \left(k_2 - \varepsilon k_1\right) \frac{e}{T} + k_3 \frac{e}{T^2}, \quad \text{with} \quad \varepsilon = \frac{R_d}{R_w}. \tag{17}$$

The atmospheric delay L_{atmo} in the zenith direction is the integral of the air refractivity from Earth's surface z_S to the upper limit of the atmosphere z_{atmo}. The integration step in elevation is defined as dz. Therefore L_{atmo} can be written as:

$$L_{atmo} = 10^{-6} \int_{z_S}^{z_{atmo}} \left(k_1 \frac{P}{T} + k_2' \frac{e}{T} + k_3 \frac{e}{T^2}\right) \mathrm{d}z, \quad \text{with} \quad k_2' = (k_2 - \varepsilon k_1) = 0.233 \text{ KPa}^{-1} \tag{18}$$

As shown in *Fig. 13*, the atmospheric delay depends mainly on the pressure and temperature vertical distributions. Furthermore pressure decreases exponentially with height, from about 1.003×10^5 Pa at sea level to 1 Pa at 80 km (Wallace and Hobbs, 2006). In order to derive accurately the atmospheric delay, accurate pressure estimates along the integration path are essential, especially close to the surface.

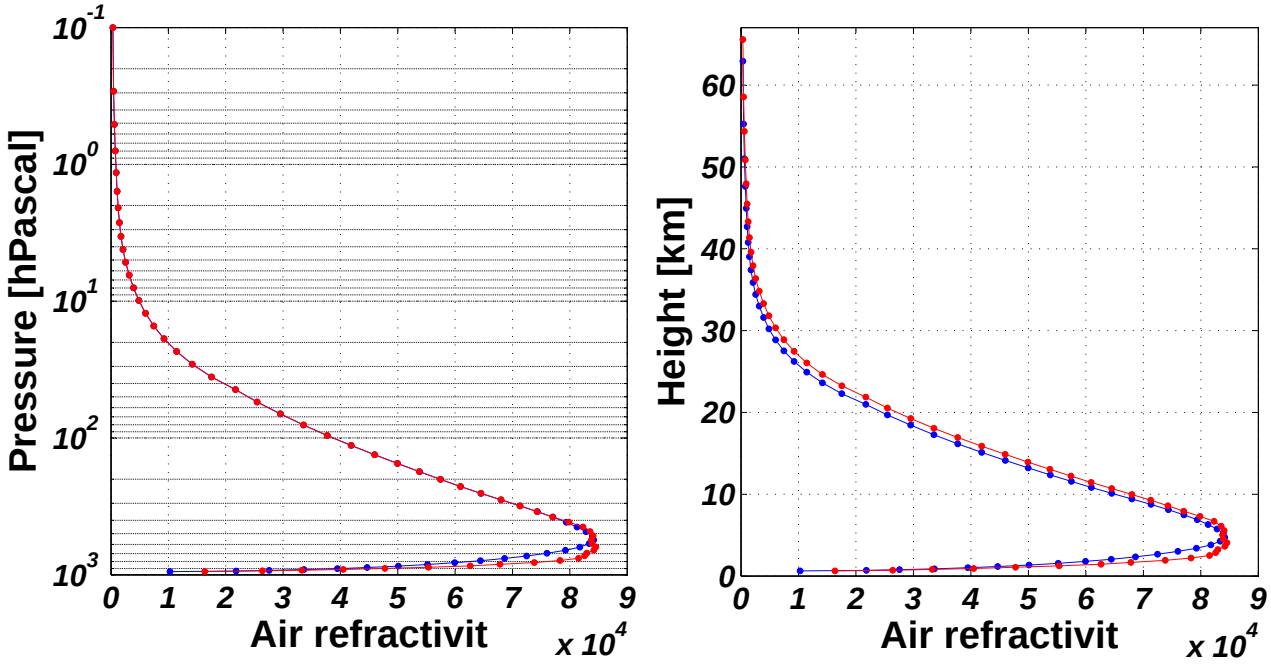

(a) (b)

Fig. 13. Vertical air refractivity profile in winter on 26 January 2012 0 h (blue) and in summer on 26 July 2012 0 h (red) of the Wettzell GPS station (Germany) calculated using ERA-Interim data; (a) with pressure in hPascal as y-axis; (b) with height in kilometer as y-axis.

Since radar pulses travel in the slant range direction from the satellite to the ground, the slant range atmospheric delay should be integrated along the observation direction. The normalized vector of slant range $\vec{r}$ can be determined using the incidence angle θ_{inc} and the heading angle t (satellite flight direction). It must be pointed out that by convention only the one-way distance is used in radar terminology. Starting from the initial point on the surface $\vec{p_0} = [x_0, y_0, z_0]$, the

next intersection point $\vec{p_1} = [x_1, y_1, z_1]$ is determined by the vector $\vec{r}$ and the integration step $\mathrm{d}z$:

$$\vec{p_1} = \vec{p_0} + \vec{r} \cdot \mathrm{d}z, \quad \text{with } \vec{r} = [\cos t \sin \theta_{inc}, -\sin t \sin \theta_{inc}, \cos \theta_{inc}]^T . \tag{19}$$

The one-way delay in slant range (SPD, slant range path delay) L_s is defined using start point $\vec{r}_S$ on the Earth's surface and the intersection of the radar signal's path (from this point to the satellite) with the upper part of the atmosphere $\vec{r}_{atmo}$:

$$L_s = 10^{-6} \int_{\vec{r}_S}^{\vec{r}_{atmo}} \left(k_1 \frac{P}{T} + k_2' \frac{e}{T} + k_3 \frac{e}{T^2} \right) \mathrm{d}r. \tag{20}$$

2.2.4.3.3 Moisture parameter - specific humidity

In practice, the amount of water vapor in *eq. (20)* in the atmosphere is often determined as a ratio between the mass of water vapor m_w and the mass of dry air m_d, such as *mixing ratio* $w = m_v/m_d$. In this thesis, the specific humidity q is used to measure the amount of water vapor in the air, which is defined as the mass of water vapor m_w in a unit mass of air ($m_w + m_d$) (Wallace and Hobbs, 2006):

$$q \equiv \frac{m_v}{m_v + m_d} = \frac{w}{1 + w}. \tag{21}$$

The formula to convert the specific humidity q to the partial pressure of water vapor e is given by:

$$e = \frac{w}{w + \varepsilon} P = \frac{q}{q(1 - \varepsilon) + \varepsilon} P. \tag{22}$$

Assuming that $q(1 - \varepsilon) \to 0$, then:

$$e \approx \frac{q}{\varepsilon} P. \tag{23}$$

2.2.4.3.4 Different definitions and abbreviations of atmospheric delay

The troposphere contains approximately 80% of the total atmosphere's mass and nearly 99% of its water vapor. The refractivity decreases nearly linearly from its maximum value ca. $8.5 \cdot 10^4$ (around the height of 5 km) to $3 \cdot 10^4$ at the top of the troposphere (about 17 km). Then it decreases exponentially near to zero at the height of 70 km, as presented in *Fig. 13*. According to the vertical distribution of the refractivity, it can be concluded that the atmospheric delay is mainly generated in the troposphere. Furthermore, significant exchanges of atmospheric mass (convection) occur mainly in the planetary boundary layer in the lower part of the atmosphere. On the contrary, it is relatively stable in the stratosphere and in the mesosphere. Therefore, for relative measurements like SAR interferometry and for absolute ranging in the decimeter accuracy, the **atmospheric delay** (except ionospheric delay) is thus often referred as **tropospheric delay** in the literature. Under the assumption of hydrostatic balance in the lower atmosphere (troposphere), the **dry** delay, also known as **hydrostatic delay**, can be expressed using surface pressure (Saastamoinen, 1972; Davis et al., 1985; Bevis et al., 1992, 1994), in contrast with **wet delay**, which is characterized by the water vapor pressure profile, the so-called **wet delay**. Depending the integration direction, two sets of abbreviation are mostly used. In zenith, Zenith Hydrostatic Delay is abbreviated as **ZHD**, Zenith Wet Delay as **ZWD**, and Total Zenith Delay as **ZTD**, more discussions about the ZHD and the ZWD are presented in section 3.1.2.4. In slant range, hydrostatic delay is abbreviated as **SHD**, wet delay as **SWD** and total path delay as **SPD**, respectively.

2.2.4.3.5 Compensating SPD in absolute range measurements

As introduced in section 2.2.4.3.2, SPD can be expressed as the integral of air refractivity along the propagation path. This method is defined as the direct integration method. It requires three dimensional weather data at the acquisition time as input. Depending on the availability and the accuracy of weather data, the accuracy of range measurements can be improved up to centimeter level (Balss et al., 2011; Cong et al., 2012a). An explicit description of the direct integration method is presented in section 3.1. In this section, a short overview of the state-of-the-art atmospheric delay estimation methods is given.

According to the required input data, the methods can be classified into the five following categories:

(1) **Simplified height-dependent model**. A height-dependent exponential model has been applied using a constant mean ZPD value at sea level for generating SAR geocoded products for the TerraSAR-X satellite (Breit et al., 2010) and for SAR geometrical calibration of TerraSAR-X (Schwerdt et al., 2010). This model-based method is sufficient for a range accuracy of around 30 cm. However, it can be simply improved by replacing the empirical ZPD value by actual GPS ZPD measurements, which can be derived from global/regional permanent GPS network as in Danklmayer et al. (2009); Eineder et al. (2011); Balss et al. (2012) or directly estimated using GPS ephemeris data from a local GPS receiver (Tuttas, 2011). Depending on the distance between the GPS antenna and the SAR acquisition center and the GPS data availability, the range accuracy varies from several decimeters to around 1 cm, assuming that solid Earth tides and ionospheric delay have been accurately accounted for.

(2) **Height-dependent model based on surface meteorological measurements**. Based on the hydrostatic equation, ZHD can be expressed as a function of surface pressure with a given temperature lapse rate. Under the assumption that temperature decreases nearly constantly with height, the wet component is expressed as a function of surface meteorological measurements, namely surface temperature and partial pressure of water vapor on surface. This method has been applied in Askne and Nordius (1987); Delacourt et al. (1998b); Jehle et al. (2008).

(3) **Ray-tracing method using three dimensional weather model data**. In Jehle et al. (2008), the nonhydrostatic local area model COSMOS-2 operated by the Swiss Federal Office of Meteorology and Climatology (MeteoSwiss) was used as source of numerical weather model data. The integration path was determined by using satellite orbit and position of an object. A comparison between a height-dependent model (2) and a ray-tracing method (3) was carried out. In Hobiger et al. (2010), both electromagnetic delay and geometric excess have been taken into account in a ray-tracing model. The atmospheric parameters have been extracted from the mesoscale weather model from the Japanese Meteorological Agency (JMA). The author has compared quantitatively the differences of SPD between the projection using the mean incidence angle and the actual incidence angle, as well as the ray-tracing method. In Doin et al. (2009); Cong et al. (2012a), a global weather model from the ECMWF Interim reanalysis project has been used instead of mesoscale data. Doin et al. (2009) combined the ZHD modeled by surface pressure and the ZWD integrated using water vapor pressure and temperature profiles. This paper focused on the compensation of the relative delay between two SAR acquisitions (SAR interferometry). In Cong et al. (2012a), ERA-Interim reanalysis data have been validated using GPS ZPD from the EPN with a standard deviation of approximately 1.0 cm. As well as in Balss et al. (2011), the absolute range accuracy of corner reflector measurements from the TerraSAR-X calibration campaign has been improved from decimeter to centimeter range by using the direct integration method in Cong et al. (2012a) instead of the simple model based method in Breit et al. (2010).

(4) **Mesoscale weather model simulation with higher spatial and temporal resolution**. Gong et al. (2010); Nico et al. (2011); Catalão et al. (2011); Cimini et al. (2012) have focused on water vapor spatial variations for SAR interferometric applications. In Gong et al. (2010); Nico et al. (2011); Catalão et al. (2011), a weather situation at each acquisition time has been assimilated using the Weather Research and Forecast (WRF) model in order to retrieve the relative atmospheric delay between two acquisitions. In Cimini et al. (2012), water vapor measurements from different methods (simulation, ground-based and space-borne measurements) have been evaluated, validated and compared. The 5th-generation PSU/NCAR Mesoscale Model (MM5) associated with ECMWF products has been used to simulate the water vapor content in SAR interferograms. Random errors of 11.3 mm in MM5 and of 10.2 mm in ECMWF products have been determined by validation using RAdiosonde OBservations (RAOB) as reference.

(5) **Ground-based and space-borne water-vapor measurements**. Besides GPS ZPD measurements, Microwave Radiometers (MWR) and RAOB can also be used to retrieve the water vapor content with millimeter accuracy, as shown by Sahoo et al. (2011); Cimini et al. (2012). These water vapor measurements are often regarded as reference data. Cimini et al. (2012) reported that the ground-based measurements from MWR and RAOB demonstrated an excellent accuracy under 6 mm. The spatial distribution of water vapor can be observed by passive satellite measurements from instruments/sensors, such as the Medium Resolution Imaging Spectrometer (MERIS) and the Moderate-resolution Infrared Spectrometer (MODIS) (Li et al., 2007; Lindenbergh et al., 2008; Li et al., 2009; Cimini et al., 2012; Li et al., 2012). In Li et al. (2007), the accuracy of MERIS water vapor maps varies from 5 mm in winter to 8 mm in summer in comparison with GPS integrated water vapor. A cross-validation between space-borne measurements and GPS ZWD has been carried out in Cimini et al. (2012). The accuracy of MERIS water vapor maps was about 6 mm and that of MODIS was from 13 to 19 mm.

2.2.4.3.6 Impact of precipitating clouds and volcanic ash clouds

Apart from the delay effects in clear atmosphere, a fraction of the atmospheric delay is caused by the liquid water content in clouds and in volcanic ash clouds. The non-dispersive delay can be derived from the permittivity of cloud droplets and aerosol particles smaller than 1 mm in diameter.

The refractivity of cloud droplets is approximated by using the Clausins-Mossotti equation (Solheim et al., 1999),

$$N_{cl} = \frac{3}{2}\frac{W_{cl}}{\rho_{lw}}\left[\frac{\epsilon_0 - 1}{\epsilon_0 + 2}\right] = 1.45 W_{cl}, \tag{24}$$

where W_{cl} is the liquid water content in g/m^3, ρ_{lw} is the density of liquid water (about 1 g/cm^3 at 273 K) and ϵ_0 is the permittivity of liquid water. The integrated delay is scaled to the depth of cloud layer in kilometers. For example, a cumulus cloud with liquid water content of 1 g/cm^3 induces an integrated delay of 1.45 mm over a distance of 1 km, which is negligible in comparison with the atmospheric delay (Solheim et al., 1999; Hanssen et al., 1998; Hanssen, 2001).

During periods of volcanic activity and eruptions, volcanic ash might be released into the atmosphere. It normally consists of a mixture of solid materials and gases. In Solheim et al. (1999), the typical density of volcanic ash is about 2.6 g/cm^3, and its total amount varies between 2×10^2 to 4×10^4 g/cm^3. According to the Clausins-Mossotti equation, the integrated path delay due to volcanic ash particle is smaller than 0.016 cm. Therefore, the perturbation induced by volcanic particles is ignored for SAR range delay. However, under circumstance of

significant water vapor release, its influence on range measurements cannot be ignored. This effect can be observed and compensated by using satellite data (Adams et al., 1996).

2.2.5 Geodetic effects

Internal and external forces act on the Earth, generating a series of deformation effects on its surface, known as geodetic effects. The variation of Earth's surface due to tidal effects, non-tidal effects and tectonic motion affects directly range measurements, as defined in the last terms of *eq. (3)*. Nowadays, these displacements exerted by geodetic effects can be detected, measured and modeled with millimeter accuracy. An overview of Earth tides and their effects are given in section 2.2.5.1. The continental drift effect is shortly discussed in section 2.2.5.2.

2.2.5.1 Effect of Earth tides

Earth tides are defined by Zschau (1989) as *"the response of the solid Earth and its liquid outer core to the combined luni-solar gravitational attraction"*. The Earth system can be considered as a simplified model with a **solid inner core** and its **liquid outer core**, the **atmosphere** and **oceans**. Obviously, the Earth system is considered as a non-rigid system. Inner and outer forces act on the deformable Earth system and induce tidal effects, which have exerted considerable influence for precise geodetic measurements (such as Very-long-baseline interferometry (VLBI), Lunar Laser Ranging (LLR), SLR and GPS). The International Earth Rotation and Reference Systems Service (IERS) has released three reports in 1996, 2003 and 2010, in which tidal effects included on the elastic Earth system have been defined and modeled, and formulas for accurate tidal corrections have been determined by Mccarthy (1996, 2003); Petit and Luzum (2010). The amplitude of these tidal distortions reaches from several millimeters to decimeters. The perturbations caused by tidal effects need to be accurately compensated in order to perform high-precision absolute SAR geolocation (Eineder et al., 2011; Schubert et al., 2012; Balss et al., 2012). Further discussions on the effects of Earth tides on absolute and relative range measurements in SAR images can be found in section 2.4.

In geodesy, an Earth-fixed Cartesian coordinate system is commonly used to describe the location of a certain point in space. The origin is often defined as Earth's physical center and the z-axis as the direction pointing towards the North Pole, which does not coincide exactly with the actual rotation axis. Furthermore, the origin and the rotation axis vary in space periodically and in long-term due to the redistribution of Earth's mass. The so-called **Polar Tides (PT)** are caused by this mismatch of axes, so that the Earth tries to make its surface an equipotential surface in the gravity field of an Earth rotating around the actual axis (Beutler, 2005). The PT effects were estimated in radial component and horizontal components (north and east) by using the mean pole path approximated by a linear model in Mccarthy (2003) and improved in Petit and Luzum (2010) by combination of a cubic model valid over the period 1976-2010 and a linear model for extrapolation after 2010. The estimated polar tides displacement reaches a maximum in radial direction of approximately 25 mm and in horizontal of about 7 mm.

The deformation of the elastic Earth due to the gravitational forces of both the Sun and the Moon is known as **Solid Earth Tides (SET)**. It is an essential distortion that has to be considered for the determination of precise coordinates of reference points in geodetic networks. Its radial component can reach more than 40 cm, which accounts for 85% of the total tidal effects (Scherneck, 1991). Nowadays, the SET displacements are well modeled and compensated with an accuracy of 1 mm (Scherneck, 1991; Mccarthy, 2003; King et al., 2010). In *Fig. 14*, a time-series of SET displacements from the Reference Frame Sub-Commission for Europe (EUREF) GPS station Wettzell (WTZR) is estimated by using the 'solid' software provided by Milbert (2012). The SET displacements are presented in three directions (vertical, north and east) and are plotted for three time spans: *Fig. 14(a)* for a whole year in 2012, *Fig. 14(b)* for a selected month in November 2012 and *Fig. 14(c)* for a selected date on 13 November 2012.

Semidiurnal, diurnal and long-term periods are observed in the tidal deformations in *Fig. 14*. A variation of nearly 40 cm in vertical component from peak to peak occurs in 7 hours see *Fig. 14(c)*. The vertical component of SET dominates the SET displacement, whereas the north component is about one third of the vertical component, and the east component only half of the north component.

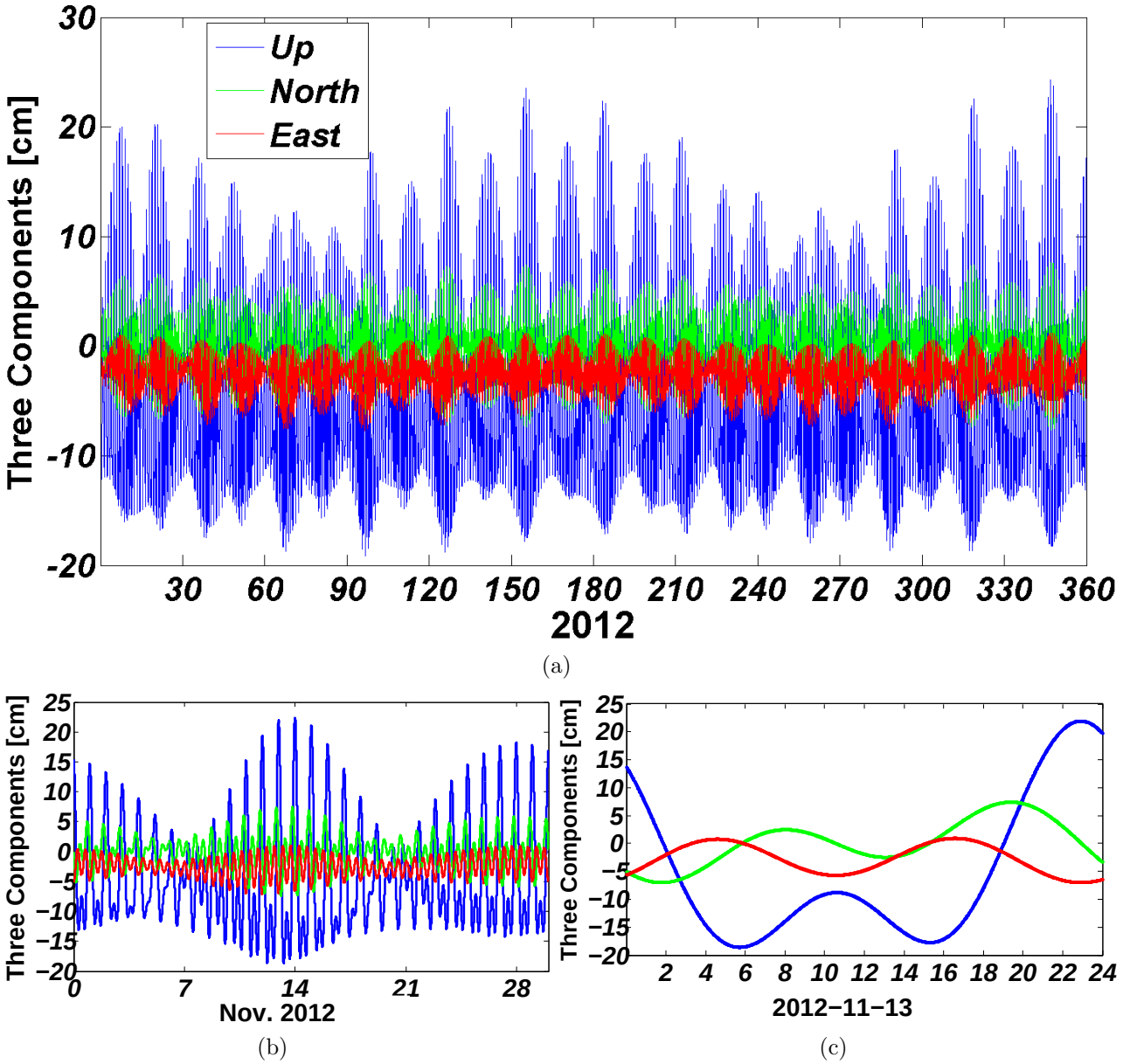

Fig. 14. SET effects on the EUREF GPS station WTZR. The up-component is depicted in blue, the north component in green and the east component in red: (a) shows SET displacements for 2012; (b) presents SET displacements on November 2012; (c) shows SET displacements on 13 November 2012. [source: (Milbert, 2012)]

Due to the gravitational attraction of the Moon and the Sun, the ocean mass distribution varies temporally. This variation produces time-varying and spatially-dependent deformations of the Earth caused by the associated load on the crust, called **Ocean Tide Loading (OTL)**. Its effect at the WTZR GPS station is shown in *Fig. 15(a)*. Unlike the SET, the OTL is strongly dependent on local and regional conditions that affect fluid flow, and can reach up to 100 mm. The ocean tide can be measured from remote sensing satellites (e.g. altimetry) and tide gauges. The OTL displacements can be extracted from space geodetic measurements (Mccarthy, 2003; Petit and Luzum, 2010), and can be estimated using different OTL models based on Green's function proposed by King (2005). In order to improve the OTL accuracy to 1 mm,

Scherneck (1991) proposed a parameterized tide observation model for compensating the SET and OTL effects in VLBI measurements. An online service "Ocean Tide Loading Provider" for daily OTL effects based on Scherneck (1991) is available[1]. Some open-source softwares for computing the OTL effects are available: OLFG/OLMPP by Scherneck (1991), SPOTL by Agnew (1997, 2005), GOTIC2 by Matsumoto et al. (2001) and CARGA by Bos and Baker (2005), respectively. DiCaprio and Simons (2008) has revisited the above-mentioned open-source softwares for calculating the OTL displacements and reported that the OTL influences caused about 26 mm displacement in LoS with a time interval of 35 days in Iceland for ENVISAT-ASAR interferograms. The OTL effects on the WTZR GPS station from 2012 have been estimated with the SPOTL software and then visualized in *Fig. 15*, for yearly *Fig. 15(a)*, monthly *Fig. 15(b)* and daily *Fig. 15(c)* variation. The maximum displacement in the vertical direction is about 20 mm from peak-to-peak in the whole year. The displacements in the horizontal directions are about 5 mm in north and about 2 mm in east.

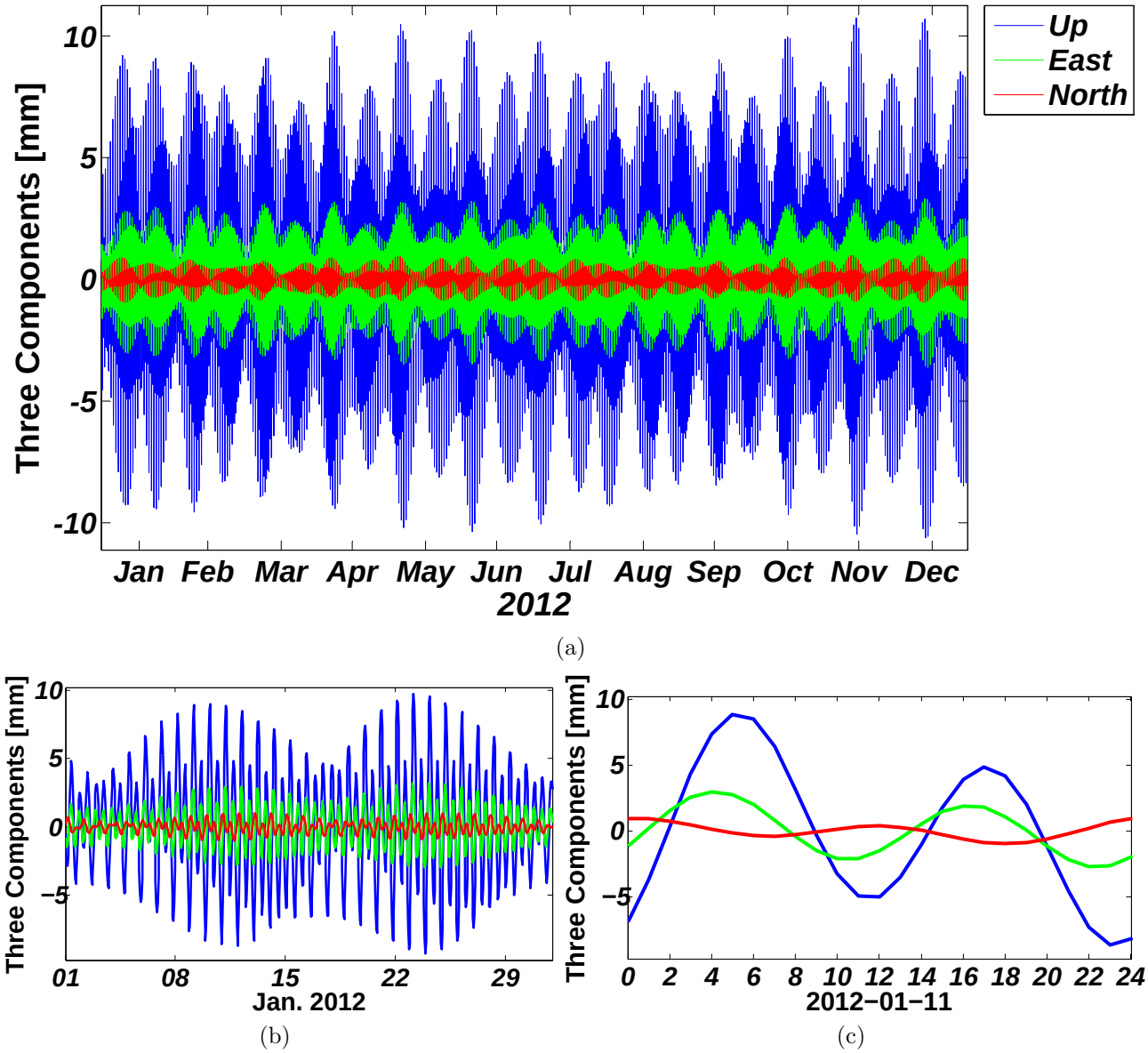

Fig. 15. OTL effects on the EUREF GPS station WTZR. The up-component is depicted in blue, the east component in green and the north component in red: (a) shows OTL effects in 2012; (b) presents OTL effects on January 2012; (c) shows SET effects on 1 January 2012. [source: (Matsumoto et al., 2001)]

[1] http://froste.oso.chalmers.se/loading/

Variations of the **atmospheric pressure** act as a **loading** (Atmospheric Pressure Loading (APL)) which deforms Earth's surface. The APL induced displacements can be observed in very highly accurate geodetic measurements from VLBI and GPS reported by Dam et al. (1994); Dam and Herring (1994); Petrov (2004). APL causes crustal displacements which can reach up to mm for the vertical component and 3 mm for the horizontal component (Mccarthy, 2003; Petrov, 2004). APL displacements should be taken into account for highly precise geodetic measurements in the order of 1 mm accuracy. In geodesy, global surface pressure time series from a meteorological service (e.g. ECMWF) have been used to estimate and compensate APL displacements. In Petrov (2004), an average Root Mean Square (RMS) of 0.4 mm for the vertical component and 0.1 mm for the horizontal component has been obtained based on a VLBI data set using pressure data from the National Centers for Environmental Prediction (NCEP) Reanalysis project. In *Fig. 16*, the deformation signal exerted by APL is provided by the "Atmospheric Pressure Loading Service" [2] from the GSFC VLBI Group has been visualized in vertical and horizontal (north and east) components for the WTZR station during the period from June 2007 to October 2012 with a 6 hour resolution. APL displacements vary from −1.6 to 2.0 cm peak-to-peak in vertical and −3.0 mm to 3.0 mm peak-to-peak in horizontal. More discussions over the APL estimation software have been presented in Dam (2005). Some errors could arise under extreme pressure variations, which are not included in the sparse pressure measurement data set used for APL calculation. Therefore, pressure measurements with a better temporal and spatial resolutions are necessary in order to improve the accuracy of APL corrections which is demonstrated by Boehm et al. (2009).

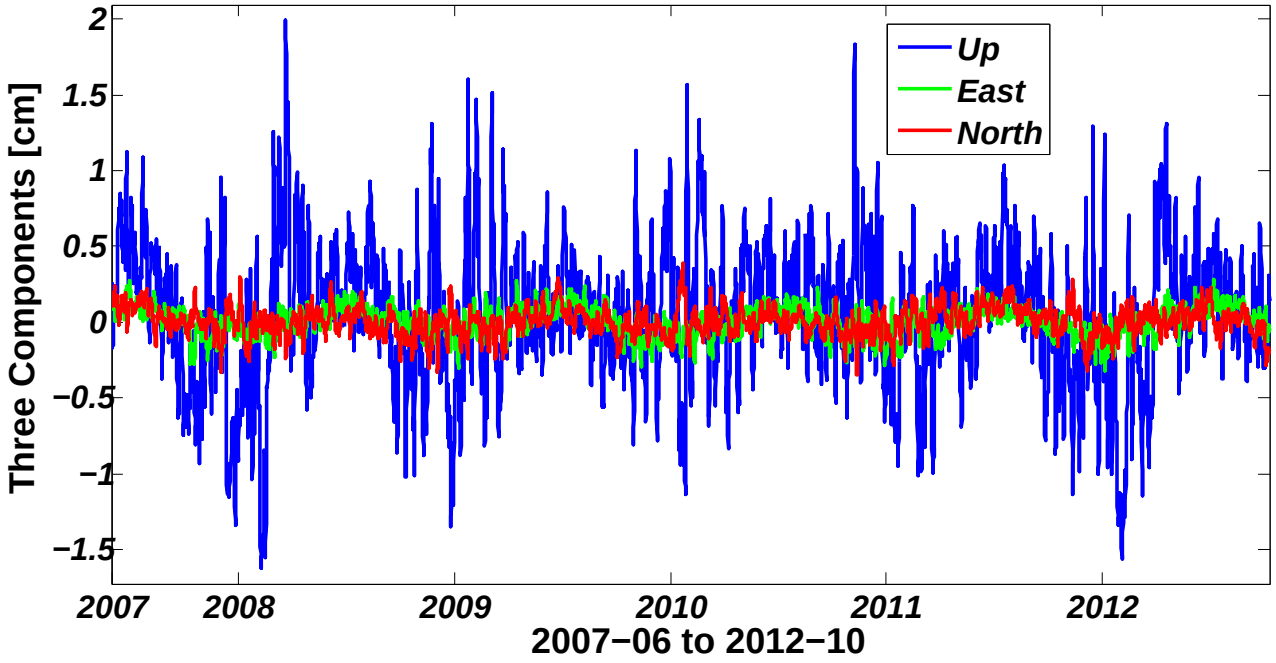

Fig. 16. Displacements due to APL on the EUREF GPS station WTZR from June 2007 to October 2012. The up component is depicted in blue, the east component in green and the north component in red. [source: http://gemini.gsfc.nasa.gov/aplo/]

Another mass loading effect called **Non-Tidal Ocean Loading (NOTL)** is important for areas near the coast, where the variation of ocean bottom pressure caused by changes in water mass, atmospheric pressure or ice mass is large. This effect has been observed in GPS time series (Dong et al., 2002; Williams and Penna, 2011; Dam et al., 2012). It must be compensated for accurate positioning techniques, such as VLBI. Three dimensional displacements caused

[2] http://gemini.gsfc.nasa.gov/aplo/

by NOTL are provided by "Non-tidal Ocean Loading Service" [3] in 12-hour time series from 1993 until the last epoch of new ocean bottom pressure data released by the Jet Propulsion Laboratory (JPL) team. The NOTL displacements for WTZR VLBI station from January 1993 to October 2012 are visualized in *Fig. 17*. The NOTL variation exerts displacements in the millimeter-level: maximum values are in vertical component and about 1.8 mm in absolute value.

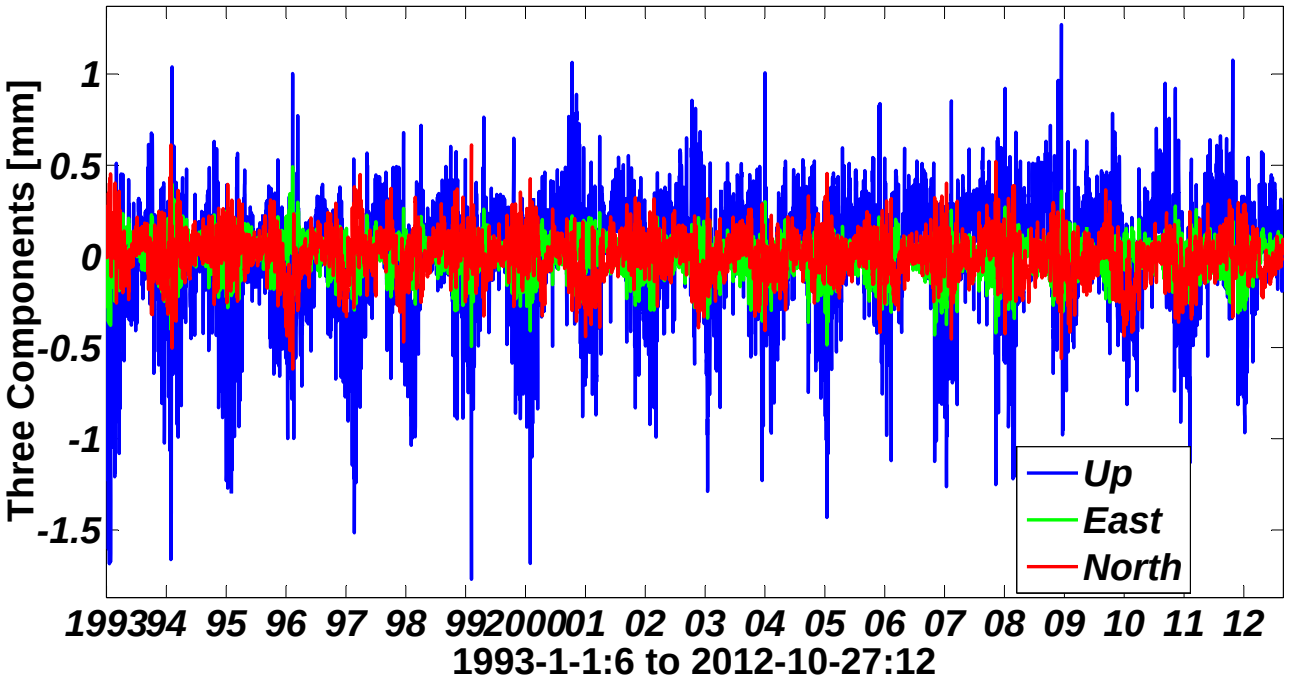

Fig. 17. NOTL effects on the EUREF GPS station WTZR from January 1993 to October 2012. The up component is shown in blue, the east component in green and the north component in red. [source: http://lacerta.gsfc.nasa.gov/oclo/]

2.2.5.2 Continental Drift (CD)

The CD is a concept derived from motion of continents. Its theory was firstly scientifically formulated by Taylor and Wegener in the 1910s (Romm, 1994). The modern theory of plate tectonics was introduced during the last decade of the 20th century in order to describe the motion of Earth's lithosphere on a global scale. Nowadays, the velocity of plate motion can be determined with an accuracy under 1 mm/year (Altamimi et al., 2012). For convenience, regional/continental frames have been defined in addition to the global frame in order to avoid the effect of the CD in geodetic measurements. For instance, the European Terrestrial Reference Frame (ETRF) is used in Europe. Coordinate time series of the EUREF GPS station WTZR for both International Terrestrial Reference System (ITRS) and European Terrestrial Reference System 1989 (ETRS89) are shown in *Fig. 18* (Bruyninx, 2004). The pink dashed vertical lines separate the time series into different realizations of ITRS: ITRF94, ITRF96, ITRF97, ITRF2000, ITRF2005 and ITRF2008; and of European Terrestrial Reference System (ETRS): ETRF94, ETRF96, ETRF97 and ETRF2000. Obviously, the horizontal trends shown in the International Terrestrial Reference Frame (ITRF) observations (ca. 17 mm/year in north component and 19 mm/year in east component) have been flattened in ETRS89 since ETRS "moves" with the European plate. However, SAR orbits are usually defined in global frames (e.g. TerraSAR-X orbit products are defined in ITRF2005 until 17 April 2011, afterwards in ITRF2008). A discrepancy arises when a ground reference point is measured in a

[3] http://lacerta.gsfc.nasa.gov/oclo/

regional/continental frame. In this thesis, the definition of CD is used to describe the coordinate differences between ITRF and ETRF for a defined location.

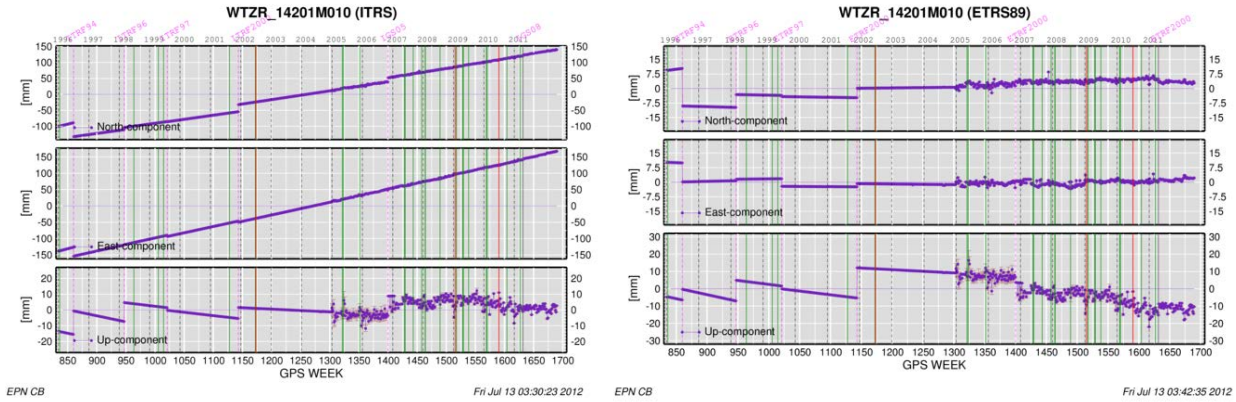

(a) (b)

Fig. 18. Coordinate time series of the EUREF GPS station WTZR from 1996 to 2012 depicted in north, east and up components for different coordinate frames: (a) in ITRS; (b) in ETRS89. The station clearly drifts horizontally within the ITRF global frames, whereas it remains stable in the ETRF frames, the regional frame where the station is located. [Source: (Bruyninx, 2004)]

2.2.6 Corner Reflector experiment in Wettzell, Bad Kötzting, Germany

Previously different sources of distortions for SAR ranging measurements have been introduced. In this section, a corner reflector experiment is presented in order to practically explain and visualize the effect of each of the distortions in SAR absolute range measurements as reported in Balss et al. (2012). For this experiment, a trihedral Corner Reflector (CR) with 1.5 meters edge was installed at the WTZR geodetic observatory in Bad Kötzting, Germany (see *Fig. 19(a)*). From 12 June 2011 to 7 November 2012, 27 TerraSAR-X High Resolution Spotlight (HRSL) images have been acquired over the WTZR test site. An intensity image of a TerraSAR-X acquisition with the CR is shown in *Fig. 19(b)*. A summary of range distortions from different sources is firstly discussed in section 2.2.6.1. In section 2.2.6.2, range distortions are compensated, component by component. Finally, the correlation between absolute localization residuals and distortions are discussed also in section 2.2.6.2.

2.2.6.1 Summary of distortions in range

The CR was installed in June 2011 in the WTZR test site, which is located about 240 m away from the EUREF permanent GPS station WTZR. More details about EUREF can be found in Bruyninx (2004). Therefore the Tropospheric Delay (TD) on the CR has been directly estimated by mapping the WTZR ZPD in slant range using the local incidence angle θ_{loc} (see section 2.2.4.3.5). The Ionospheric Delay (ID) has been estimated by Gisinger (2012) using an improved method mentioned in section 2.2.4.2. For each geodetic effect, such as Solid Earth Tides (SET), Ocean Tide Loading (OTL), Atmospheric Pressure Loading (APL) and Continental Drift (CD), 3-D displacements have been determined according to the methods presented in section 2.2.5 and then projected in the SAR slant range direction.

In order to obtain an overview of the different range distortions, range corrections for atmospheric delays and geodetic effects have been determined at each acquisition time and are depicted in *Fig. 20*. Each of them has been centered around its mean value. The mean value is shown in *Fig. 21(a)*. It is obvious that TDs with a mean value of about 2.713 m and

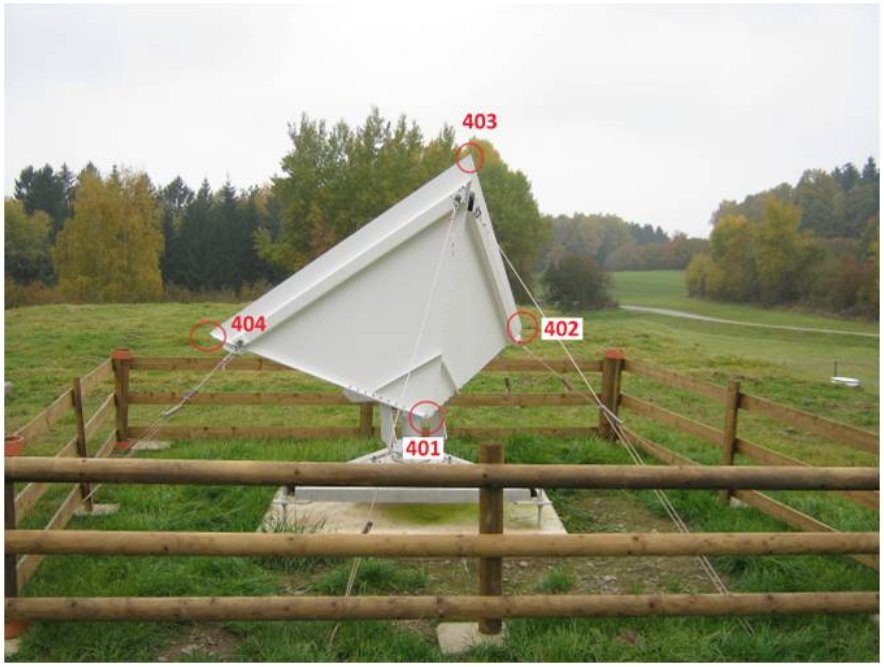

(a)

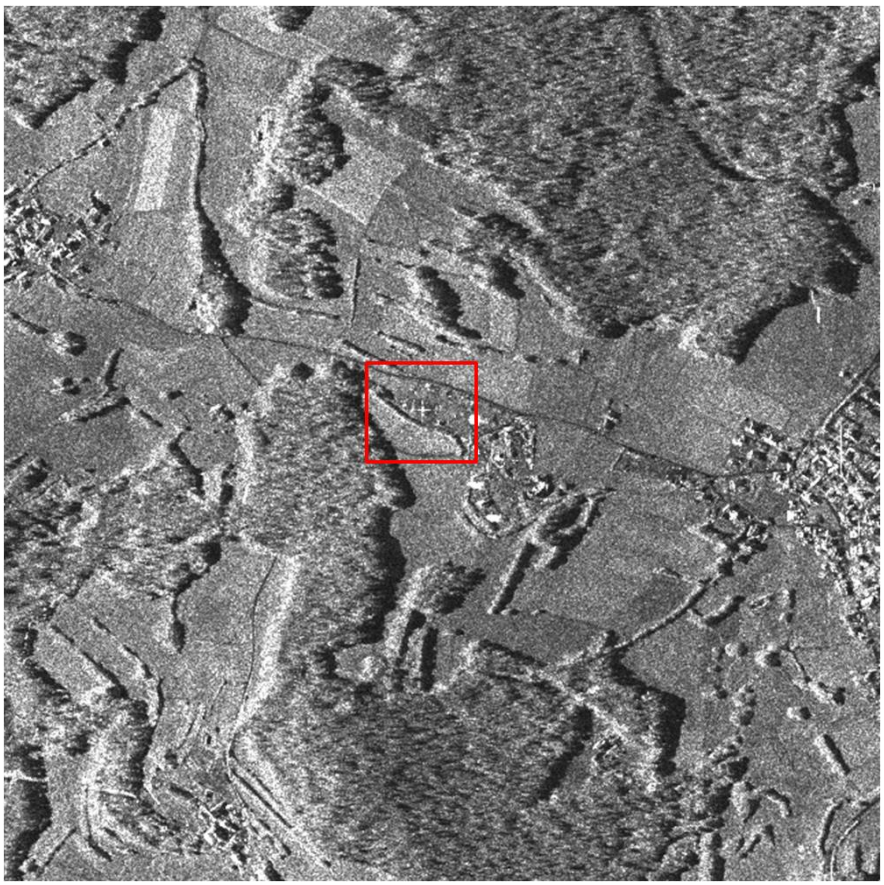

(b)

Fig. 19. The CR experiment at the WTZR geodetic observatory in Bad Kötzting, Germany. (a) The trihedral CR with 1.5 meters edge was installed in the WTZR test site. (b) TerraSAR-X acquisition over the test site with the backscatter of the reflector in the middle of the image (in the red rectangle).

a standard deviation of 6.1 cm are dominant in range. Time series of TDs reveal an annual period with maximum delay during summer acquisitions and minimum delay during winter acquisitions. The second largest component is the SET delay. Its time series mean value is

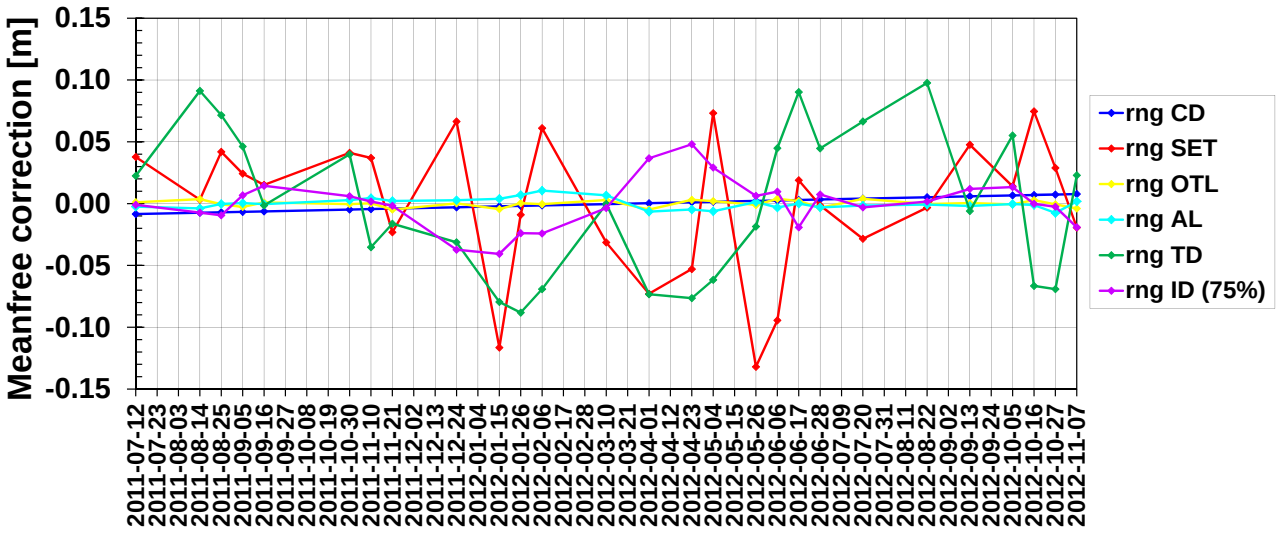

Fig. 20. Time series (for 27 TerraSAR-X acquisitions) of range distortions. The time series mean value has been independently compensated for each component (see *Fig. 21(a)*). The components in Range (rng) are Continental Drift (CD) in blue, Solid Earth Tides (SET) in red, Ocean Tide Loading (OTL) in yellow, Atmospheric Pressure Loading (APL) or (AL) in cyan, Tropospheric Delay (TD) in green and Ionospheric Delay (ID) in magenta.

about 7.2 cm, whereas its standard deviation reaches up to approximately 5.7 cm, which is only 4 mm smaller than that of TDs. The mean value of ID time series is about 6.6 cm and its standard deviation is about 2.0 cm. The other three geodetic effects (CD, OTL and APL) have relatively small effects on the absolute range measurements, with an average magnitude under 1 cm. The standard deviation of OTL delay is about 2.7 mm. Furthermore, the mean value of APL delay is around zero, whereas its standard deviation is over 4 mm. Due to the continually drift caused by CD, range delays increase almost linearly in time, which has a mean value of about 8.7 mm.

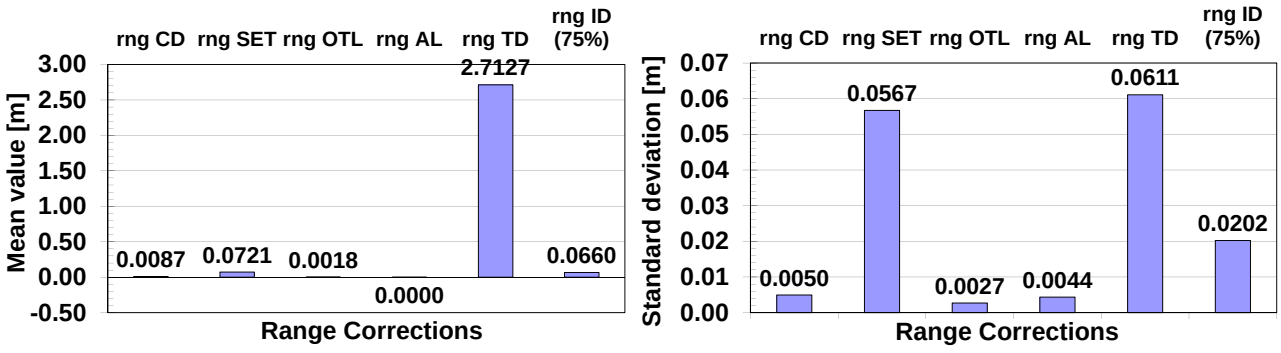

Fig. 21. The mean value and the standard deviation of range distortions (see *Fig. 20*) are depicted in (a) and (b) respectively. The components in range (rng) are CD, SET, OTL, APL or AL, TD and ID.

2.2.6.2 Absolute CR localization measurements with range corrections

The range distortions discussed in section 2.2 have been visualized for each acquisition time in section 2.2.6.1 for the WTZR test site. Due to these distortions, a discrepancy exists in range between the measured CD position and the expected position in SAR images which can be estimated using the in-situ measured CD position and the satellite orbit product. Based on the method 'Imaging Geodesy' proposed in Eineder et al. (2011), different range corrections have been applied to the range discrepancies (also known as range delays) derived from the CD

experiment in Wettzell. Detailed information on the measurement method has been reported in Balss et al. (2012). Range errors and measurements from 27 TerraSAR-X acquisitions are summarized in Table B.1 in Appendix B.

In *Fig. 22* the correction process is progressively illustrated in four steps. The original SAR range delay measurements (SAR Rng) have been plotted in grey in *Fig. 22* after compensating their mean values. The standard deviation is 8.1 cm. The following progressive corrections steps have been visualized in *Fig. 22*:

(1) TD delays have been applied as the first correction on SAR Rng (green dashed line): the standard deviation is improved from 8.1 cm to approximately 5.4 cm.

(2) SET delays have been then corrected on the residuals (orange dashed line): the standard deviation decreases from 5.4 cm to about 2.2 cm.

(3) ID delays have been also compensated on the residuals (blue dashed line): a further improvement of about 1.1 cm is achieved.

(4) The small geodetic effects from OTL, APL and CD have been considered at last (black line): a slight improvement of ca. 1 mm is yielded.

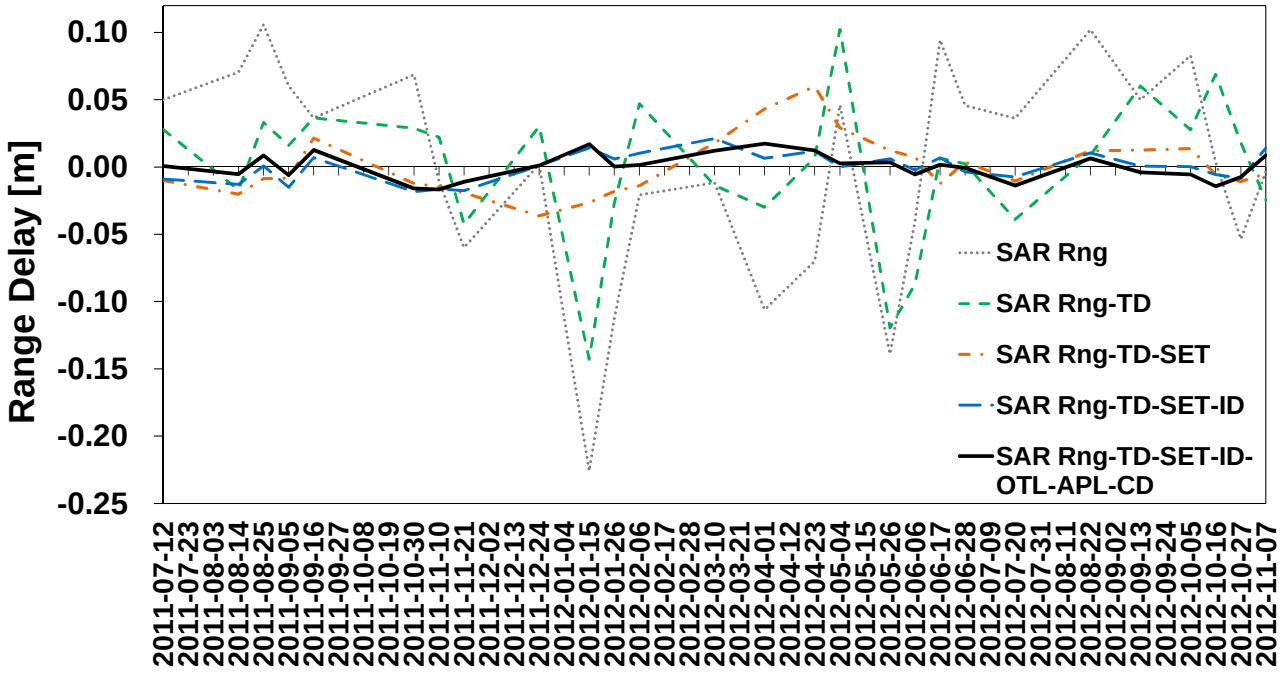

Fig. 22. Absolute CR range measurements in (grey) with recursive range corrections from TD (green), TD+SET (orange), TD+SET+ID (blue) and with all corrections TD+SET+ID+OTL+APL+CD in (black). After each correction, the mean value of the remaining time series has been compensated (centering around zero).

The analysis of the corrections and the residuals has been performed using the range distortions discussed in section 2.2.6.1 and the range residuals derived from the range delay values after compensation of certain distortions. For example, a clear correlation is presented in *Fig. 23(a)* between the range delays measured by GPS (GPS TD) and the range residuals (SAR TD), which are derived from the range delay after correction of SET, ID, OTL, APL and CD. In *Fig. 23(b)*, a strong correlation is also observed between the modeled SETs and the range residuals (SAR SET), which are derived from the range delay after correction of TD, ID, OTL, APL and CD. Their correlation coefficients are 98.6% and 98.5% respectively. Moreover, these two effects, in total, account for over 70% of the total delay effects. In X-band, less than 30% is contributed by the ID delay and small geodetic effects. According to two fitted functions in *Fig. 23*, a range offset of 35.97 cm is observed between GPS TD and SAR TD, and 39.21 cm between modeled SET and SAR SET. This systematic effect is caused by the operational

sensor calibration without consideration of atmospheric delays and geodetic effects. Depending on different calibration versions, the offsets might be different (Eineder et al., 2011; Balss et al., 2011, 2012; Schubert et al., 2012; Cong et al., 2012a).

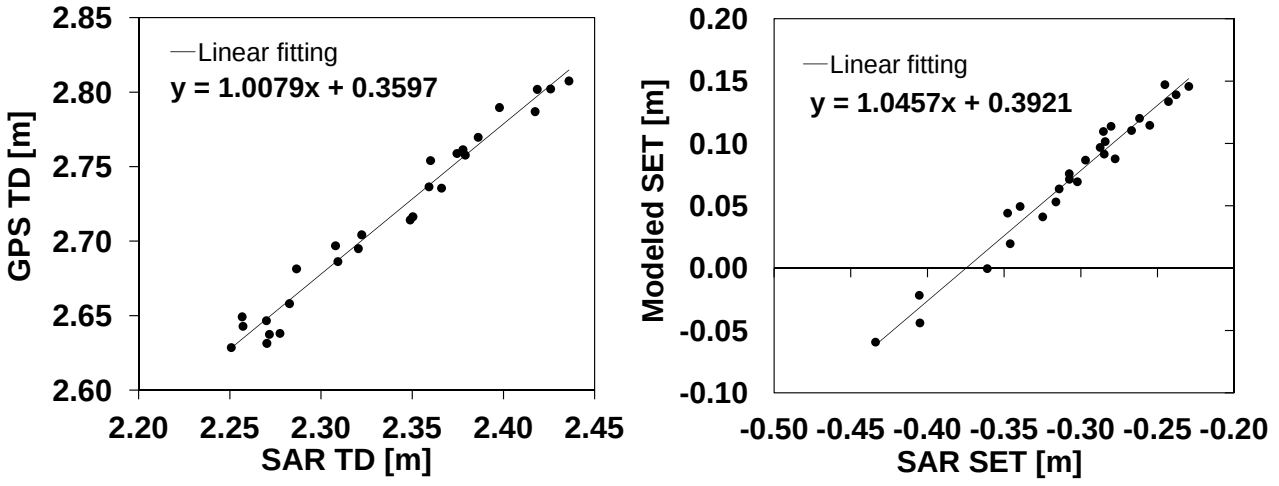

(a) (b)

Fig. 23. Correlation analysis of absolute localization residuals: (a) correlation between the range delays measured by GPS (GPS TD) and the range residuals (SAR TD), which are derived from the range delay after correction of SET, ID, OTL, APL and CD; (b) correlation between the modeled SETs and the range residuals (SAR SET), which are derived from the range delay after correction of TD, ID, OTL, APL and CD. A linear fitting has been carried out for each correlation plot and the fitted function is visualized.

2.3 Repeat-pass SAR interferometry for deformation monitoring

A short review of space-borne Synthetic Aperture Radar (SAR) Interferometry (InSAR) for volcanic deformation monitoring has been presented in section 1.1. In this section, the basic principles of repeat-pass InSAR and Differential SAR Interferometry (DInSAR) are briefly described (section 2.3.1). Furthermore, the decorrelation phenomenon, its cause and its dependency on the wavelength are introduced (section 2.3.2).

2.3.1 The interferometric phase and its components

Given two complex SAR images (s_1 and s_2) acquired from slightly different geometries, their interferogram is defined as $i = s_1 \cdot s_2^*$. For each point, its phase contains accurate information (in the order of millimeter) about the difference of the distances from the point to each of the sensors. Let $\mathbf{SAR_1}$ and $\mathbf{SAR_2}$ be the positions of the SAR satellite at two acquisition times. Given a point $\mathbf{P_0}$ on the Earth's surface, the interferometric phase at that point ϕ_{P_0} is given by:

$$\phi_{P_0} = -\frac{4\pi}{\lambda}(R_2 - R_1) = -\frac{4\pi}{\lambda}\Delta R, \tag{25}$$

where R_1 and R_2 are the distances from $\mathbf{P_0}$ to $\mathbf{SAR_1}$ and $\mathbf{SAR_2}$, respectively. This geometry is illustrated in *Fig. 24*, where a section in the range/cross-range plane is shown. The spatial difference between the two satellite positions $\mathbf{SAR_1}$ and $\mathbf{SAR_2}$ is defined as the *baseline vector* $\mathbf{B}$. For space-borne acquisitions it may well be assumed that $B = \|\mathbf{B}\| \ll R_1, R_2$. Under this

hypothesis, ϕ_{P_0} can be approximated as:

$$\phi_{P_0} \approx -\frac{4\pi}{\lambda} B \sin(\theta_1 - \alpha), \tag{26}$$

where θ_1 is the look angle and α an auxiliary angle (Rosen et al., 1996; Bamler and Hartl, 1998; Hanssen, 2001).

Let $\mathbf{P}$ be a point located at the same distance from $\mathbf{SAR_1}$ like $\mathbf{P_0}$ but a height H according to a reference plane. The inclination angle β is defined between the reference plane and $\overrightarrow{P_0P}$. The distance to $\mathbf{SAR_2}$ and the incidence angle are different from those of $\mathbf{P_0}$. Its look angle is given by $\theta_1 + \delta\theta$. Its phase difference with respect to ϕ_0 can be approximated as:

$$\phi_P - \phi_{P_0} = -\frac{4\pi}{\lambda} B \sin(\theta_1 + \delta\theta - \alpha) - \phi_{P_0} \approx -\frac{4\pi}{\lambda} \underbrace{B \cos(\theta_1 - \alpha)}_{B_\perp} \frac{H}{R_1 \sin\theta_1}, \tag{27}$$

where $\mathbf{B}_\perp$ is the so-called *effective baseline*, that is, the baseline component perpendicular to the look direction. The phase difference between the two points is due to the height h and is thus called *topographic phase* $\phi_{topo} = \phi_P - \phi_{P_0}$. Thus the effective baseline represents the sensitivity of the interferogram with respect to topography. Conversely, ϕ_{P_0} is known as the *flat Earth phase*.

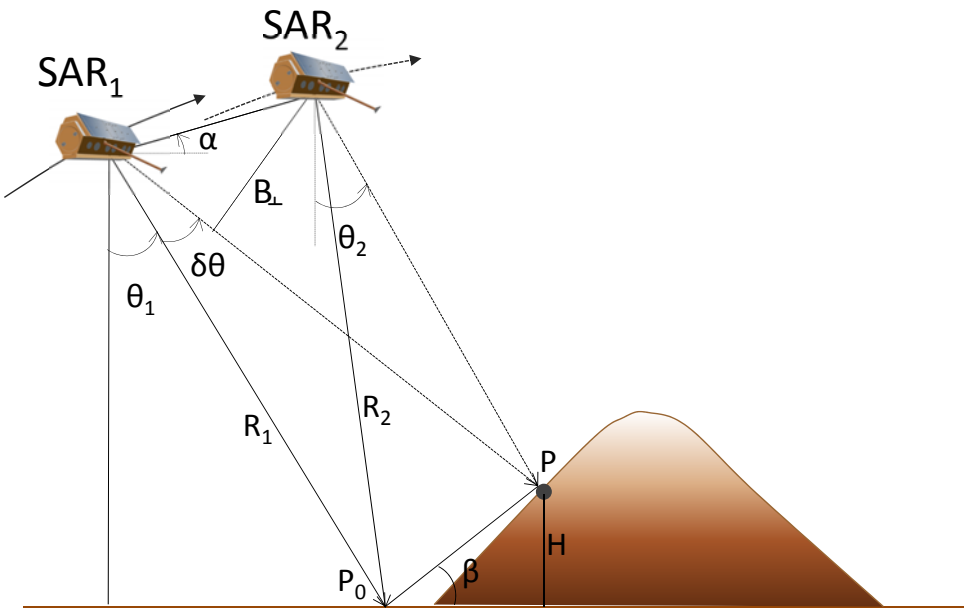

Fig. 24. Repeat-pass SAR interferometric geometry. $\mathbf{SAR_1}$ and $\mathbf{SAR_2}$ represent satellite positions at an acquisition time for master and slave acquisition respectively. R_1 and R_2 are the slant ranges of point P_0. θ_1 and θ_2 are the looking angles of master and slave acquisition respectively. $\delta\theta$ is the look angle increment from $\mathbf{P_0}$ and $\mathbf{P}$. $\mathbf{B}_\perp$ is the perpendicular baseline. α is an auxiliary angle defined by the baseline vector and a reference horizontal plane. h represents the ground elevation of point P_0.

Equation (25) accounts only for the slant range difference due to the different observation geometries, an effect which is known as *parallax*. In other words, it assumes that the position of the point has not changed between both acquisitions. A surface deformation between two acquisitions induces a further slant range difference ΔR_{defo}. Moreover, as introduced in section 2.2.4.3, different atmospheric propagation delays produce also a slant range change ΔR_{atmo}. Both phenomena have thus an associated phase component, given by:

$$\phi_{defo} = -\frac{4\pi}{\lambda} \Delta R_{defo} \qquad \text{and} \qquad \phi_{atmo} = -\frac{4\pi}{\lambda} \Delta R_{atmo}. \tag{28}$$

Further components included in the interferometric phase are orbit uncertainties ϕ_{orbit} and thermal noise ϕ_{noise}. The tidal effects presented in section 2.2.5.1 can be considered as a spatially homogeneous effect over the entire interferogram, with the exception of OTL displacements near the coast (DiCaprio and Simons, 2008), which exhibit higher spatial variations.

Assuming that the phase contributions, due to atmospheric delay, thermal noise and orbit errors, are negligible, the deformation occurred between the two acquisitions can be derived by compensating the topographic phase ϕ_{topo} corresponding to a reference Digital Elevation Model (DEM). This method is known as Differential SAR Interferometry (DInSAR). Unfortunately, in mountainous areas these assumptions do not always apply. On one hand, the differential atmospheric delay may be considerably high. On the other hand, height errors in the reference DEM introduce additional errors due to wrong topographic phase compensation. Furthermore, decorrelation noises may also introduce additional errors due to wrong phase unwrapping. Therefore these phenomena cannot be ignored in mountainous areas. One example is presented in section 2.4.3 in order to visualize different phase components.

2.3.2 Coherence and decorrelation sources

In SAR interferometry, the *complex coherence* γ is defined as the complex correlation coefficient of two complex SAR images s_1 and s_2:

$$\gamma = \frac{E[s_1 \cdot s_2^*]}{\sqrt{E[|s_1|^2]E[|s_2|^2]}}. \tag{29}$$

Its absolute value $|\gamma|$ reflects the quality of the interferometric phase and is named *coherence*. It varies from 0.0 (s_1 and s_2 fully decorrelated) to 1.0 (s_1 and s_2 fully correlated). In repeat-pass interferometry, several phenomena lead to a coherence reduction. The main decorrelation sources are: temporal decorrelation, spatial decorrelation and thermal noise.

In rural areas, temporal decorrelation is the dominant source of decorrelation due to rapid changes of the Earth's surface (e.g. by vegetation), especially for short wavelengths. According to a simplified coherence model demonstrated in Parizzi et al. (2010), coherence decreases exponentially with time for short wavelengths since they are highly sensitive to surface changes. The decorrelation time constant and the long-term residual coherence are different for each wavelength. In order to illustrate this phenomenon, X- and L-band interferograms of the same test site with similar acquisition parameters are shown in *Fig. 25*. After only 11 days between the two X-band acquisitions, large areas around the volcano are highly decorrelated (*left column*). In contrast, the L-band interferogram is still coherent in this area even after 46 days (*right column*). Hence, L-band is the wavelength of choice for the interferometric monitoring of slow natural processes in non-urban areas. Nevertheless, the L-band sensor ALOS-PALSAR is less suitable due to few acquisitions of repeat geometry.

More information on thermal and geometrical decorrelation can be found in Zebker and Villasenor (1992); Massonnet (1993); Bamler and Hartl (1998); Rosen et al. (2000); Hanssen (2001). All these decorrelation phenomena reduce the accuracy of the deformation estimation in DInSAR.

2.4 Time series methods using multi-temporal SAR data

The accuracy of deformation estimation using a single interferogram is limited by the accuracy of the reference DEM, the differential atmospheric delay, decorrelation noises and phase unwrapping errors. Several methods based on multi-temporal interferograms have been

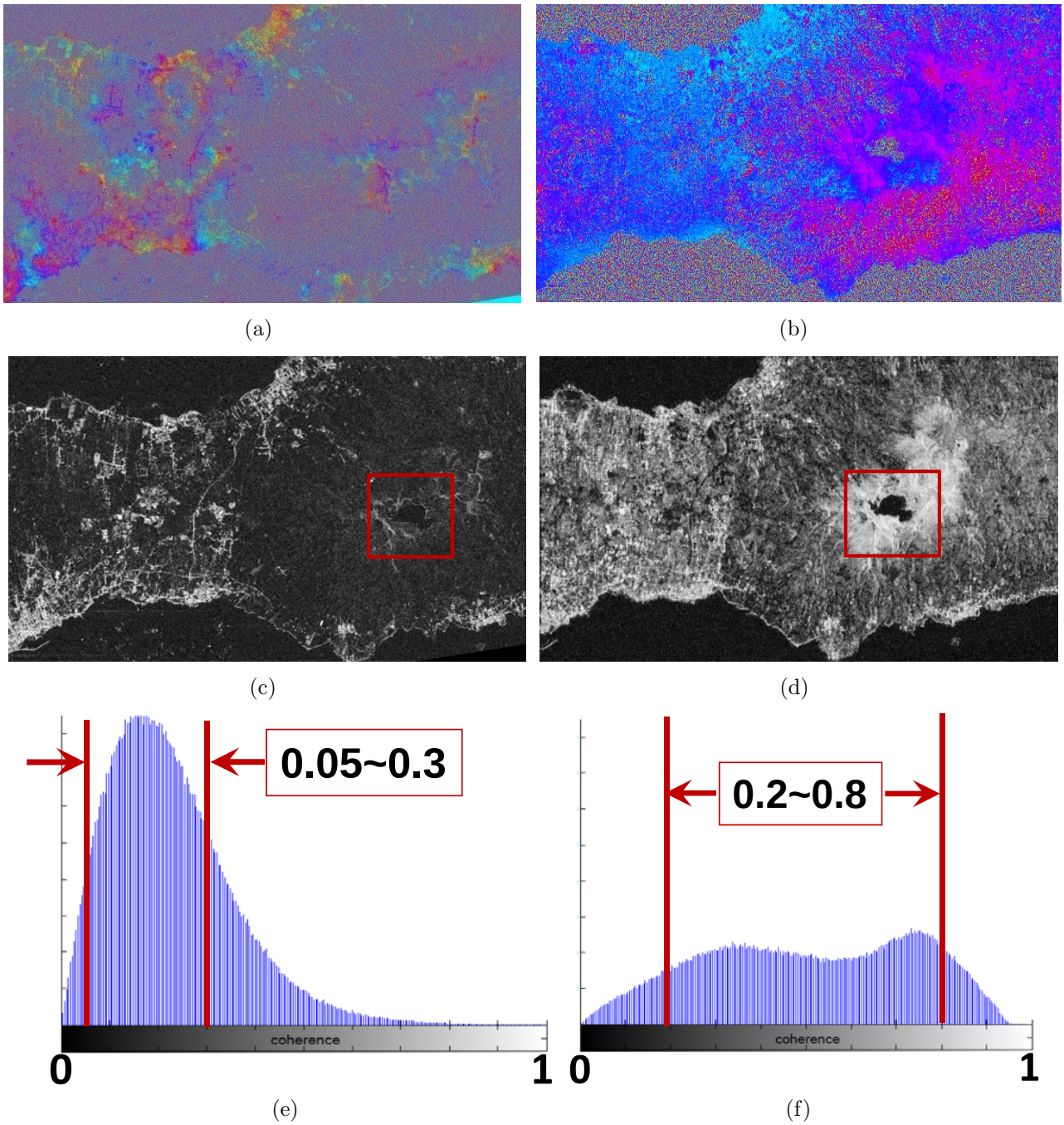

Fig. 25. (Left) X- and (right) L-band interferograms over Fogo Volcano (Azores) in Portugal. On the left column: (a) the interferogram is generated by TerraSAR-X acquisitions with master image on 30 April 2009 and slave image on 11 May 2009. Its effective baseline is about 12.5 m and its height to phase ambiguity (h2p) −640.6 m/cycle; (c) coherence image; (e) coherence histogram. On the right column: (b) the interferogram is generated by ALOS-PALSAR acquisitions with master image on 24 June 2007 and slave image on 9 August 2007. Its effective baseline is about 9.4 m and its h2p 19834.59 m/cycle; (d) coherence image; (f) coherence histogram.

developed in order to achieve a millimeter accuracy in deformation estimation. In section 2.4.1, a brief introduction to the Persistent Scatterer Interferometry (PSI) method is given. Alternative methods using directly range measurements are described in section 2.4.2.

2.4.1 Persistent scatterer interferometry

The concept of persistent scatterer interferometry was first proposed by Ferretti et al. (2001). Instead of using the whole interferogram, the PSI technique exploits only coherent pixels,

which are stable over long time intervals. These pixels are the so-called *Persistent Scatterers (PSs)*. Moreover, the estimation assumes a given deformation model. A functional model of the wrapped phase observations was proposed in Kampes (2006). For the application to volcanic areas, it is necessary to extend it in order to account for the different atmospheric phase components and for the Ocean Tide Loading component, as previously mentioned in section 2.3.1. The updated model for a point x is thus the following:

$$\phi_x^k = \mathbf{W}\Big\{\phi_{topo,x}^k + \phi_{defo,x}^k + \phi_{(atmo,s),x}^k + \phi_{(atmo,t),x}^k + \phi_{otl,x}^k + \phi_{noise,x}^k\Big\}, \text{ with } k = 1, \cdots, n, \quad (30)$$

where $\mathbf{W}\{\cdot\}$ is the wrap operator, k is the interferogram index, n is the number of interferograms in the time series, $\phi_{topo,x}^k$ is the phase component caused by inaccuracy of the reference height information, $\phi_{defo,x}^k$ is the phase component induced by surface displacement, $\phi_{(atmo,s),x}^k$ is the phase component caused by the atmospheric vertical stratification, $\phi_{(atmo,t),x}^k$ is the phase component due to the turbulent atmosphere, $\phi_{otl,x}^k$ is the phase component due to Ocean Tide Loading (which is important for test sites near the coast) and $\phi_{noise,x}^k$ is the phase component due to the decorrelation. The phase component generated by orbit errors $\phi_{orbit,x}^k$ and that of the object scattering $\phi_{obj,x}^k$ are not discussed in this thesis.

PSI estimation is based on a redundant network of relative estimations between close PSs in order to mitigate the impact of the turbulent atmosphere. Given two PSs x and y linked by an arc within the estimation network, the relative phase between them in the interferogram k is decomposed into

$$\Delta\phi_{x,y}^k = \mathbf{W}\Big\{\Delta\phi_{topo}^k + \Delta\phi_{defo}^k + \Delta\phi_{atmo,s}^k + \Delta\phi_{atmo,t}^k + \Delta\phi_{otl}^k + \Delta\phi_{noise}^k\Big\}, \text{ with } k = 1, \cdots, n, \quad (31)$$

where $\Delta\phi_{topo}^k = \phi_{topo,y}^k - \phi_{topo,x}^k$, $\Delta\phi_{defo}^k = \phi_{defo,y}^k - \phi_{defo,x}^k$, $\Delta\phi_{atmo,s}^k = \phi_{(atmo,s),y}^k - \phi_{(atmo,s),x}^k$, $\Delta\phi_{atmo,t}^k = \phi_{(atmo,t),y}^k - \phi_{(atmo,t),x}^k$ and $\Delta\phi_{otl}^k = \phi_{otl,y}^k - \phi_{otl,x}^k$ respectively. In Kampes (2006, Chapter 3), the random variable that jointly models the atmospheric, orbit and noise phase differences should have zero expectation. Over the flat areas, the influence of stratified atmospheric delay can be cancelled out in arc measurements. In volcanic areas, the gradient of vertical refractivity profiles changes considerably according to the local weather. For instance, a 1.3 cm relative delay change in 1 km vertically at incidence angle of 30 ° causes about one cycle phase change in X-band and about a half cycle in C-band and a quarter cycle in L-band.

The number of unknowns in the system of equations *eq. (31)* can be reduced by using an a priori deformation model based on a linear combination of base functions (Kampes, 2006). Due to the difficulty in modelling and prediction of volcanic deformation patterns, a linear deformation model has been applied in this thesis in order to estimate the main deformation trend, and its phase component is written as $\Delta\phi_{defo,l}$. The topographic residual ΔH is jointly estimated with the deformation by solving the equation system. The phase component due to vertical stratification $\Delta\phi_{atmo,s}$ can be previously compensated by means of the direct integration method with weather model data. Once the estimation network has been inverted, it is possible to compensate the deformation and topography components and then unwrap the remaining residual phase. Afterwards the phase component corresponding to the turbulent atmosphere $\Delta\phi_{atmo,t}$ is compensated by performing a combination of a temporal high-pass and a spatial low-pass filtering (Ferretti et al., 2000). Finally, the non-linear deformation can be estimated after eliminating the noise component.

The PSI-GENESIS software and its upgraded version Wide Area Processor (WAP) PSI Processor from the DLR have been used for PSI processing in this thesis (Kampes, 2006; Adam et al., 2011). The GENESIS software has been developed based on the STUN algorithm (Kampes, 2006). An explicit description of the PSI processing workflow using the current version of PSI-GENESIS software has been given in Gernhardt (2011, Chapter 2). In order to deal with

large scenes (e.g. 100×100 km^2), numerous modifications have been performed concerning processing efficiency and robustness. The main contributions to the WAP PSI Processor have been published in Liebhart et al. (2010); Rodriguez Gonzalez et al. (2011); Liebhart et al. (2012).

2.4.2 Alternative methods

Thanks to the high orbit determination accuracy and the high image resolution in recent space-borne SAR missions, it is possible to detect large deformations directly with ranging techniques once atmospheric and geodetic corrections have been performed. This concept was first proposed in Bamler and Eineder (2004). Eineder et al. (2011) have improved the absolute ranging method with the introduction of accurate atmospheric delay and solid Earth tides corrections, establishing thus the concept of *Imaging Geodesy*. The error sources in range determination have been summarized in section 2.2.

Different experiments have been conceived and performed in order to validate this technique. In the CR experiment at the Fogo Volcano, once the distortions described in *eq. (3)* have been compensated, a ranging standard deviation of 2.6 cm has been reached. A further description about this experiment can be found in section 2.4.3.1. In the experiment based on the correlation method in Venice city a higher standard deviation of 3.8 cm has been obtained. This is due to the larger distance (114 km) to the GPS station which was used for atmospheric delay compensation. An improvement from 3.8 to 3.2 cm has been reported in Cong et al. (2012a) based on the direct integration method using numerical weather model data from ERA-Interim reanalysis (see section 3.3). A first application of Imaging Geodesy has been successfully demonstrated for the detection of coseismic displacement of the 2011 Tohoku-Oki Earthquake, as reported in Yague-Martinez et al. (2012).

Imaging Geodesy is a useful technique for deriving large deformations (in the decimeter range or higher). It does not require a high amount of acquisitions as for the PSI technique. Moreover, since the measurements are directly absolute, there is no need of phase unwrapping. Nonetheless, the atmospheric delay uncertainty is still in the centimeter-level and unmodelled tidal components affect the accuracy by millimeters. A detailed explanation of the atmospheric delay and its limitations is presented in section 3.4.

2.4.3 Time series experiments in volcanic areas

Two experiments are presented in this section to illustrate the time-series analysis over two types of volcanoes: in section 2.4.3.1 the vegetated volcano by means of Corner Reflectors (CRs) and in section 2.4.3.2 the rocky volcano with natural scatterers. In section 2.4.3.1, the backscattering of CRs has been analyzed, as well as the phase stability has been presented. In section 2.4.3.2, multi-geometrical stacks are selected in order to obtain the full coverage of the test site. The basic stack information is also presented, such as the baseline distribution and the PS density. At the end, PS deformation map of each geometry is obtained using standard PSI processing described in Gernhardt (2011, Chapter 2).

2.4.3.1 Corner reflector experiment in São Miguel Island, Azores, Portugal

In the Exupéry project, São Miguel Island (Azores) was selected as the main test site due to the seismic swarms which took place from 2002 to 2010 (Silva et al., 2012). The Exupéry project is a German project that is funded by German Federal Ministry of Education and Research (BMBF). Its aim is to set up an Early Response System (VFRS) for volcanic activity, exploiting different data sources from: seismicity, ground deformation and remote sensing tools (Hort, 2009). A campaign for testing instruments and methods took place in 2009 around the Fogo volcano.

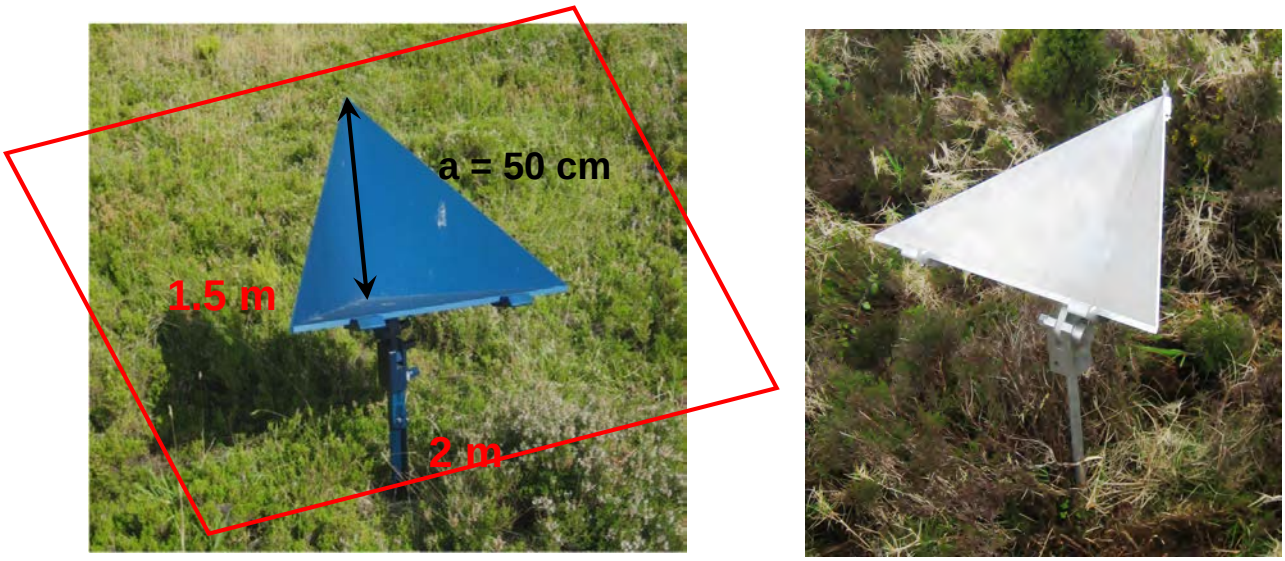

(a) (b)

Fig. 26. Two trihedral CRs installed in Lagoa do Fogo (Azores) during the campaign from April to August 2009: (a) installed near the volcano lake on the bottom of the Fogo caldera and (b) on the top of the Fogo caldera. In (a), the red parallelogram represents the pixel size of the acquired TerraSAR-X StripMap images. The ridge length of both CRs a is 50 cm.

As presented in section 2.3.2, X-band data suffer from temporal decorrelation due to the dense vegetation on the island. In order to extract more information using time-series data, two trihedral CRs were installed in Lagoa do Fogo (Azores) during the campaign from April to August 2009 (Cong et al., 2010a,b), which are shown in *Fig. 26*. The CRs are designed for the TerraSAR-X satellite. They are made of aluminium and have a weight of about 15 kg. During the campaign 11 TerraSAR-X StripMap scenes were acquired over the test site. An average intensity map was generated using all of them, which is shown in *Fig. 27*. The two CRs can be distinguished from the background clutter due to their high intensity values.

The initially measured backscatter powers are in agreement with the theoretical **Radar Cross Section (RCS)** values. RCS is defined as the energy ratio that is scattered back to the source of the wave (called backscattering) in Doerry and Brock (2009). An approximated function for the theoretical value is used to evaluate the stability of both CRs:

$$RCS = \frac{4 \cdot \pi a^4}{3 \cdot \lambda^2}, \tag{32}$$

where a is the ridge length of a corner reflector and λ is the radar wavelength. Theoretical RCSs are calculated in $\mathrm{dB/m^2}$ in order to evaluate the stability of the installed CRs and are depicted as reference in *Fig. 28* by a green line. Red and blue lines show the backscatterer from each acquisition and for each CR. The location of each CR was determined with sub-pixel accuracy using oversampling of a small selected area around it. The measured values from the corner located at bottom have a good agreement with the theoretical value. The measured RCSs of CR installed on the top does not agree with the model, except for the first acquisition. This is due to two reasons: firstly, the CR has no water drainage system so that the water accumulates into it when it rains; secondly, heavy storms slightly rotated it permanently and tilted its baseplate. Thus, the RCS changed. The theoretical RCS is 24.34 $\mathrm{dB/m^2}$; the mean RCS of both CRs are 24.49 $\mathrm{dB/m^2}$ and 21.13 $\mathrm{dB/m^2}$, respectively.

Phase history between two corner reflectors. In *Fig. 29*, the phase history of the arc linking the two CRs is illustrated in order to perform time-series analysis with the master acquisition set on 8 April 2009. Assuming that geodetic effects are homogeneous on both CRs,

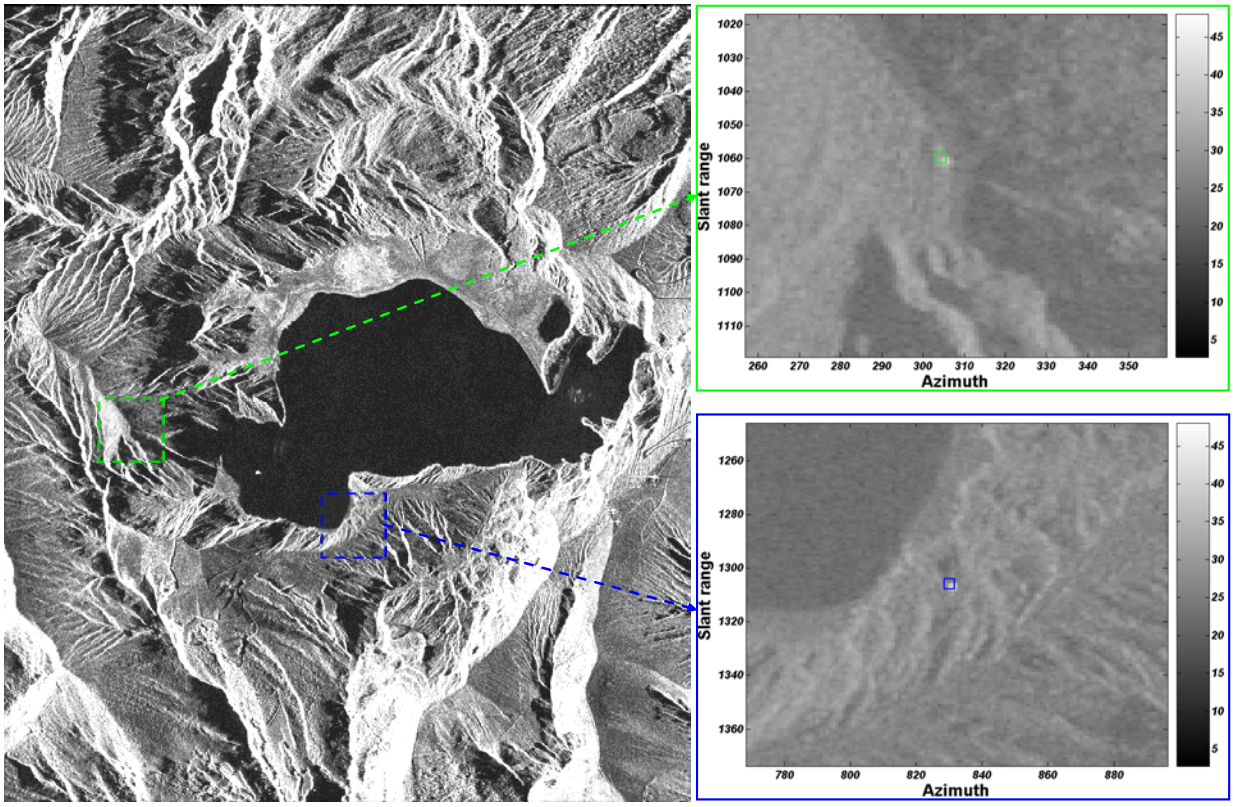

Fig. 27. Average intensity map of 11 TerraSAR-X StripMap images acquired from April to August 2009 over Lagoa do Fogo. Two zoom images are selected around the two CRs of the experiment: the CR installed on the top (green) and that on the bottom (blue).

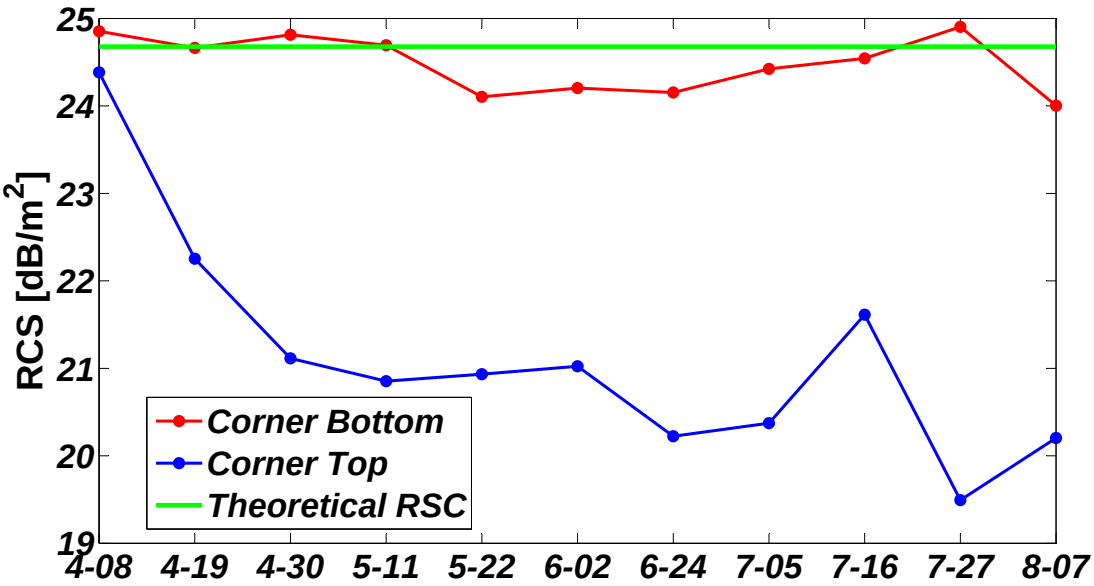

Fig. 28. Theoretical RCSs vs. measured backscatter energy of the two CRs installed at the Lagoa do Fogo (Azores) test site based on *eq. (32)*. During April and August 2009, 11 TerraSAR-X StripMap images were acquired. The RCSs of both CRs are measured on each acquisition. The measured RCSs for the CR installed on the bottom (Corner Bottom) are depicted in red, and the measured RCSs for the CR installed on the top (Corner Top) in blue.

they are cancelled out in the arc. The elevation of both CRs was measured using a Leica GPS receiver, which after post-processing achieves an accuracy in the millimeter range. Consequently, topographic phases have been calculated with these height measurements and then compensated in the arc phase history. After correcting the topographic phase, the standard deviation of the

phase history decreases from 1.88 rad to 1.41 rad. Since there is a nearly 200 m height difference between the two corner reflectors, the influence of stratified atmospheric delay is not negligible. In order to estimate the relative atmospheric phase, the ZPD from the Ponta Delgada GPS station (PDEL) in EPN has been used to derive the SPD at each acquisition time (Bruyninx, 2004). After compensating the topographic and the atmospheric phases on the arc, the standard deviation has been improved down to 1.08 rad.

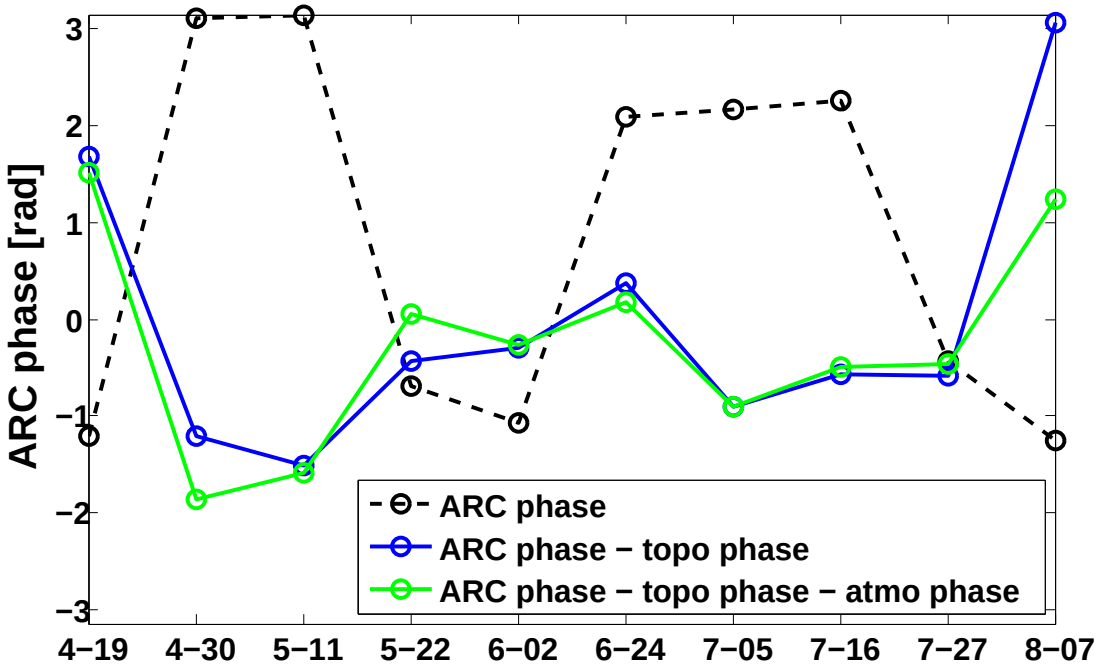

Fig. 29. The phase history of the ARC between the two CRs installed at the test site with the master acquisition on 8 April 2009: (black) original ARC phases; (blue) ARC phases are compensated with topographic phases; (green) ARC phases are compensated with topographic and atmospheric phases compensated.

2.4.3.2 Natural persistent scatters on the rocky Stromboli volcano, Italy

Stromboli is an active volcano with an area of about 12.6 km^2. It is well known due to its so-called *Strombolian* type of eruption, which is characterized by short-lived eruptions accompanied with ejection of basalts and sometimes andesites in form of cinder cones and lava-flows (Scarth, 1994). Detailed information about the geophysical characterization and the deformation pattern of Stromboli is presented in Chapter 5.

Data selection and coverage. This test site is relatively small compared to the Azores test site. Therefore, SAR acquisitions with a coarser spatial resolution are inappropriate for this application, e.g. ENVISAT-ASAR in C-band and ALOS-PALSAR in L-band. In order to obtain a better spatial resolution, TerraSAR-X HRSL data with 1 meter spatial resolution and 11 days revisit time have been selected for this experiment. Four stacks from ascending and descending orbits with different incidence angles have been acquired in order to increase the temporal resolution and the spatial coverage, which is limited by the side-looking geometry (shadow and layover). The acquisition footprints are illustrated in *Fig. 30*. During January to October 2008, 68 SAR images have been acquired, which constitutes about 1 acquisition every 3.6 days. The main parameters of each stack are summarized in Table 1. More than 25 thousands points have been detected as PSs.

SAR interferometry in Stromboli. An example of a differential interferogram is presented in *Fig. 31*. The *Sciara del Fuoco (SdF)*, a big horseshoe-shaped depression delimited with white dashed line in *Fig. 31(a)*, has good coherence and shows a significant spatial phase variation. The northern part of the island is decorrelated due to vegetation and the east part is less

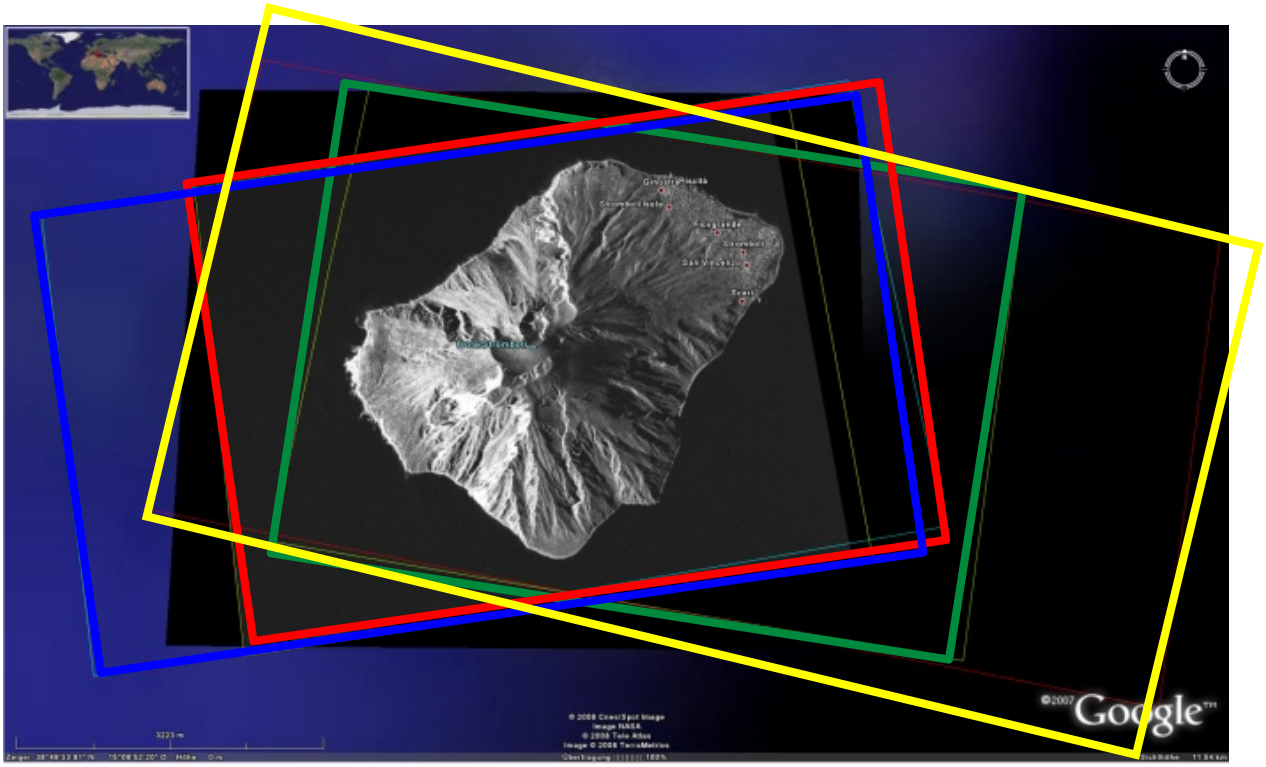

Fig. 30. Footprints of the four TerraSAR-X HRSL acquisition geometries in ascending and descending orbits: (blue) beam 033, (green) beam 061, (red) beam 069 and (yellow) beam 024, respectively. Layover image generated in Google Earth^{TM}.

Table 1. Summary of main parameters of the acquisition geometries over the Stromboli test site.

Beam Number	**Number of Acquisitions**	**Incidence Angle [°]**	**Cross Direction**	**Orbit Number**	**Detected PSs**	**PSs OMT < 1.0**
beam 033	18	32	Ascending	55	258177	89937
beam 061	17	43	Descending	108	332129	146651
beam 069	16	46	Ascending	131	570801	212283
beam 024	17	28	Descending	17	283150	115273

coherent because of the observation geometry. The SRTM DEM, acquired in 2000, has been used for compensating the topographic phase. During the eruptions in 2002 several landslides have been triggered in *SdF* (Baldi et al., 2008). The deformation signal is overlaid with the topographic signal in the differential phases. It is impossible to separate them from a single interferogram. Therefore, the PSI method has been applied.

PSI processing in Stromboli. The PSI method has been briefly introduced in section 2.4.1. In practice, a *master* image need to be selected based on the temporal and spatial distribution. *Fig. 32* depicts the temporal and spatial distribution of the four stacks. According to the distribution, the master image has been selected to optimize the stack coherence.

Thanks to the VHR SAR image, stable rocks behave and are detected as PS in rocky volcanoes like Stromboli. In descending geometries, around 3×10^5 PSs were detected with a Signal to Clutter Ratio (SCR) larger than 3.0 (see Table 1) (Gernhardt, 2011). Since there is a high PS density, a plausible estimation can be carried out on the PS-network inversion stage except for layover areas due to the steep looking angle, as it can be observed in *Fig. 33(d)*. By the last steps of PSI processing, an Overall Model Test (OMT) is carried out with a defined threshold. This procedure is introduced by Kampes (2006) as alternative hypotheses to guarantee the correctness of PSI estimation. The number of the estimated PSs varies depending on the

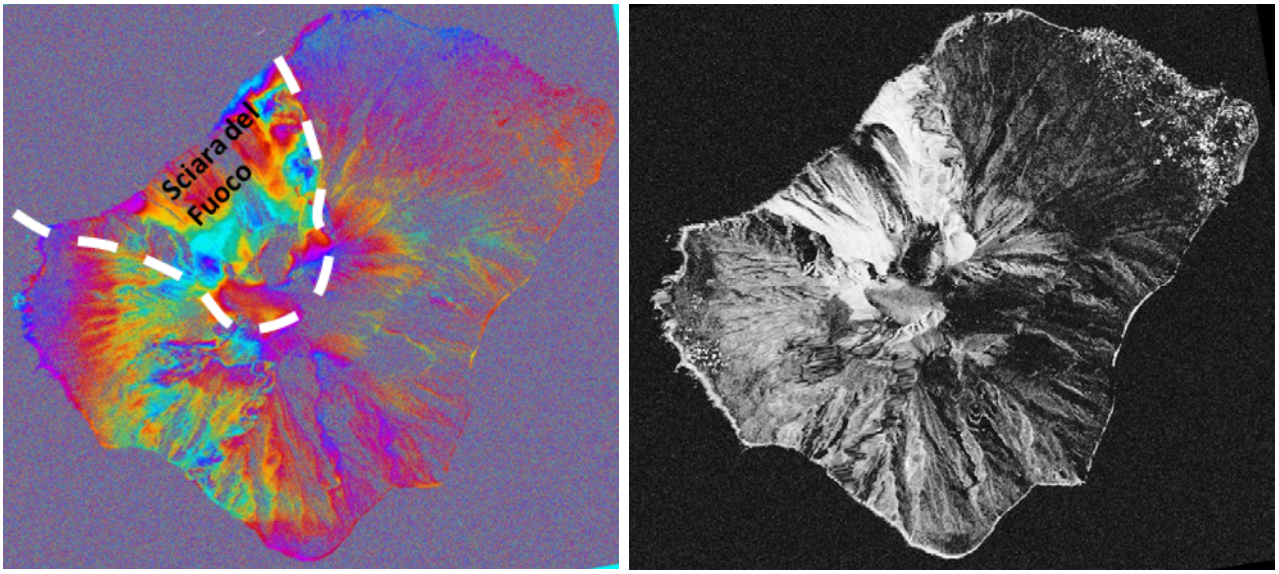

(a) (b)

Fig. 31. 11-day repeat-pass TerraSAR-X HRSL differential interferogram of the Stromboli test site: (a) wrapped differential interferogram (color red-green-blue indicates the range $-\pi$ to π); (b) coherence image (gray scale black-white indicates the range 0 to 1). The SAR images have been acquired on 29 January 2008 and 9 February 2008 in ascending orbit with an incidence angle of 46 °. The perpendicular baseline is −37.5 m. The shape of the *SdF* is depicted with a white dashed line.

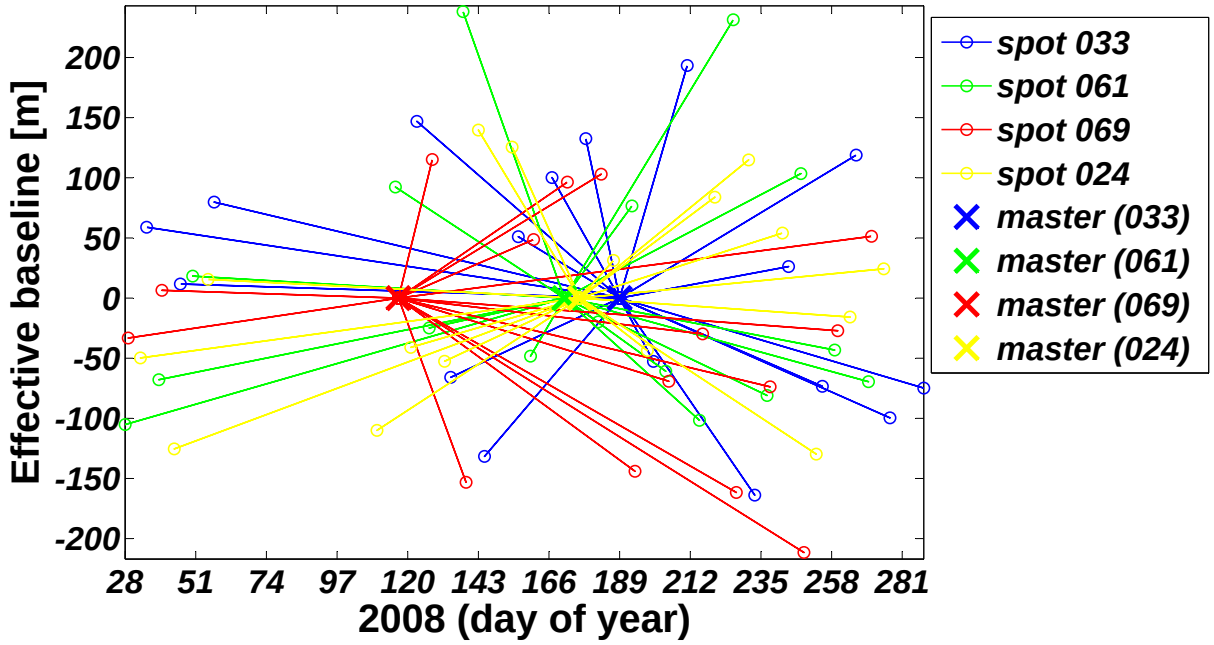

Fig. 32. Baseline distribution plots versus temporal baseline for each of the four stacks acquired. The master image has been selected based on the stack coherence. The color matches that of *Fig. 30*.

threshold of the OMT value. In this case, an OMT threshold of 1.0 is performed. As final PSI results, there are around 1×10^5 PSs with OMT smaller than 1.0 as shown in Table 1 which are presented in *Fig. 33*. On the contrary, only 700 PSs were detected from a stack of 30 ENVISAT-ASAR acquisitions in descending orbit (Ferretti et al., 2008). Nevertheless, a clear correlation between deformation estimates and height values is observed in scatter plots (see *Fig. 33*). This effect is induced by the variation of vertical atmospheric stratification over the acquisition period. In Chapter 3, an effective method to estimate and compensate the atmospheric delay effect using 4-D numerical weather model data is introduced.

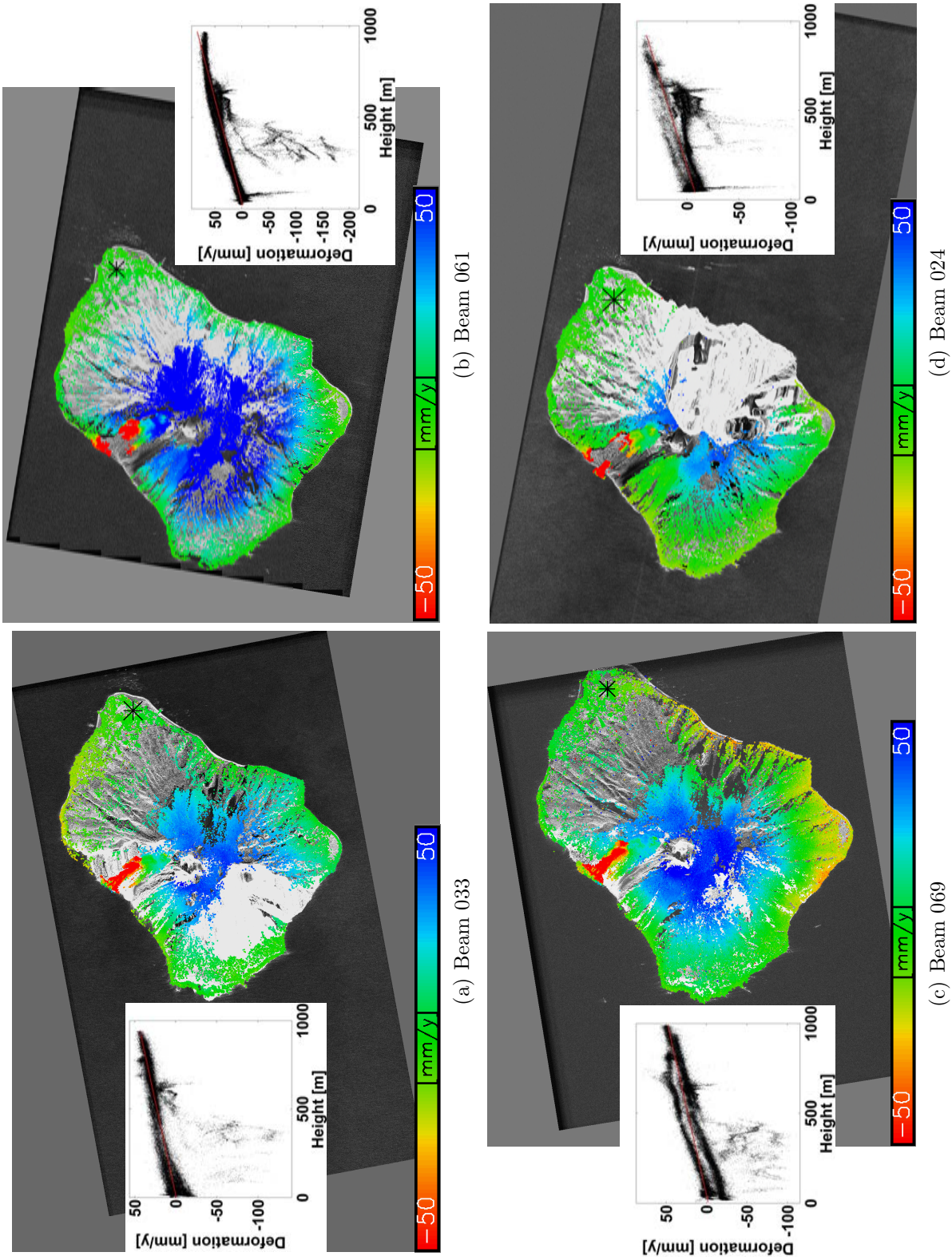

Fig. 33. PS deformation map of four stacks with the geocoded average amplitude image as background. On each deformation map, a scatter plot of deformation versus height is illustrated. A linear fit is presented in a red line on each scatter plot. Based on the trend lines, a clear correlation between the deformation estimates and the height values is observed. This effect is induced mainly by the stratified atmospheric delay variation.

3 Mitigation of atmospheric delay effects in SAR interferometry in volcanic areas

The purpose of this section is to introduce an effective method to mitigate atmospheric delay effects in SAR interferometry. This method is based on the 4-dimensional data derived from Numerical Weather Prediction (NWP) model products. The input parameters, which are necessary for the integration method and the method itself are presented in section 3.1.

In this thesis, two products from ECMWF have been selected: the ERA-Interim reanalysis (section 3.2.1) and the ECMWF operational data (OP) (section 3.2.2). In order to validate the accuracy and the reliability of the NWP products and of the integration method, different validation approaches have been carried out: for both products with respect to GPS ZPD (section 3.3.1), and for ERA-Interim products with respect to the tropospheric delay derived from CR range measurements (section 3.3.2).

In section 3.4, the integration method based on the NWP products will be applied for mitigating the atmospheric delay in SAR interferometry in volcanic areas. Firstly, the formation of the atmospheric delay in volcanic areas is discussed in section 3.4.1 for the atmospheric signal due to vertical stratification and in section 3.4.2 for the atmospheric signal due to turbulent mixing. Afterwards, two application cases based on ERA-Interim products are described: firstly in section 3.5 for PSI processing and secondly in section 3.5 for SAR cross-correlation measurements.

The integration method and the validation approaches are based on two publications: Cong et al. (2012a); Cong and Eineder (2012). Nevertheless, the integration method is explicitly explained and discussed in further detail in this section. Moreover, validation tests with both ERA-Interim and OP data have been performed, as well as atmospheric phase compensation in SAR interferometry.

3.1 Integration of tropospheric delay using 4-dimensional NWP products

Air refractivity N at a certain location can be expressed as a function of the parameters (T, P and e) as described in section 2.2.4.3.2. The total atmospheric delay L_{atmo} is calculated by integrating N along the propagation path, from the Earth's surface z_S to the upper limit of the atmosphere z_{atmo}. Therefore, the values of these parameters (T, P and e) along the propagation path are necessary in order to calculate L_{atmo}.

The parameters derived from the products of the NWP models are listed and described in section 3.1.1. The description of the integration method based on these parameters is structured into three parts within section 3.1.2. Firstly, the preprocessing of the NWP products is presented (section 3.1.2.1). Secondly, the vertical interpolation/extrapolation approach on the real topography is described (section 3.1.2.2). Thirdly, two effective parameters for direct integration are discussed in section 3.1.2.3. Finally, different integration equations and their coefficient constants are summarized in section 3.1.2.4.

3.1.1 Input parameters

According to the atmospheric refractivity equation (*eq. (17)*), the parameters, temperature T, pressure P and partial pressure of water vapor e, are required in four dimensions. These parameters can be retrieved both from meteorological measurements (such as radiosonde)

and from NWP models. Although the parameters derived directly from meteorological measurements are commonly more accurate and are actually used as observation for the data assimilation of NWP models, these measurements are unfortunately available only sparsely in space and in time. Products derived from NWP models have a regional/global coverage depending on different scales of the models, and provide a much higher density of parameter estimates. In practice, the meteorological measurements are often used as quality control for the validation of the NWP modeling results (Persson and Grazzini, 2007).

Depending on the different NWP models, the products are provided in different structures. According to the horizontal representation, they can be divided mainly into two types: the discrete grid point models and the spectral models, which use continuous wave functions. According to the vertical structure, there are several types of representations, such as sigma (σ) coordinates, eta (η) coordinates and hybrid coordinates (Povic, 2006). Since the ECMWF products have been selected in this thesis, the structure based on an η-hybrid coordinate is described in detail (Trenberth et al., 1993; Persson and Grazzini, 2007).

In general, the parameters required for the integration method are classified in two categories: three-dimensional parameter field (section 3.1.1.1) and surface parameter field (section 3.1.1.2). An example of a hybrid model is shown in *Fig. 34*. The surface parameter field or Surface Level (SL) is depicted with a thick black line. The parameters estimated in this field are surface geopotential $\mathbf{\Phi}_S$, surface temperature T_S and surface pressure P_S. Moreover, the three-dimensional parameter field is structured in vertical into the so-called half and full Model Levels (MLs), which are depicted in solid and dashed thin black lines. In ECMWF products, parameters such as temperature T and specific humidity q (see section 2.2.4.3.3) are specified for the full Model Level (ML) (T_k, q_k); whereas pressure P and geopotential $\mathbf{\Phi}$ which can be derived according to the model coefficients (see Appendix D) with respect to surface parameters for the half ML ($P_{k-1/2}$, $\mathbf{\Phi}_{k-1/2}$) are usually used to define vertical coordinates.

3.1.1.1 Three-dimensional parameter field

Depending on the different NWP models, the parameters are described in different vertical coordinates, such as pressure P or/and geopotential $\mathbf{\Phi}$. Therefore, conversions among $\mathbf{\Phi}$, P and conventional geometrical height h are required in order to perform the air refractivity integration into a Cartesian coordinate system. These conversions are explained in detail in Appendix F.

In the case of pressure level representation, the parameters are estimated on defined pressure values in vertical, e.g. on 1000 hPa. The pressure values at MLs are determined with predefined model coefficients. The MLs are divided into two types: the half MLs and the full MLs (see *Fig. 34*). The parameters T and q are specified within the product for the full ML. The parameters P and $\mathbf{\Phi}$ can be calculated for the half ML according to the procedure described in Appendix C, which is based on the predefined model coefficients (see Appendix D).

In order to describe the integration method, we assume that the vertical coordinates of the three-dimensional parameter field are presented with pressure levels P, with the corresponding geometrical heights z.

3.1.1.2 Surface parameters field

The surface model orography, known as $\mathbf{\Phi}_S$, is often different from the real topography, especially in mountainous areas. However, the parameters derived from the NWP models are assimilated based on this orography. As a consequence, a discrepancy exists near the surface. In order to perform an appropriate interpolation close to the model orography or extrapolation under it (see section 3.1.2.2.2), several surface parameters like P_S and mean sea level pressure P_{MSL} are needed.

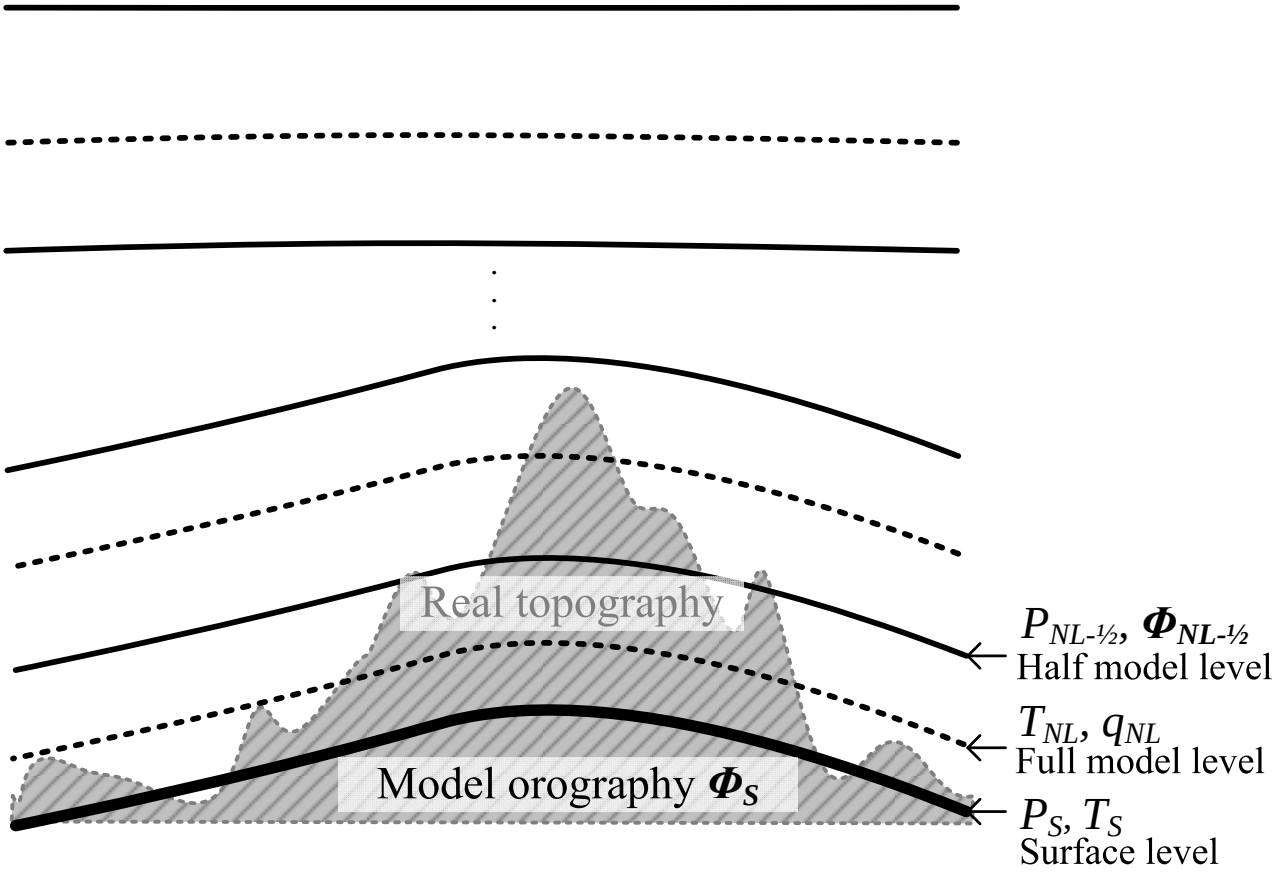

Fig. 34. Introduction of ECMWF hybrid vertical model in three components: firstly, SL is defined on the model orography and depicted with a thick black line. The parameters provided in this field are surface geopotential $\mathbf{\Phi}_S$, surface temperature T_S and surface pressure P_S; secondly, full MLs are depicted in dashed thin black lines, parameters e.g. temperature T_{NL} and specific humidity q_{NL} are presented on the NLth full ML; thirdly, half Model Levels (MLs) are illustrated in solid grey lines, parameters pressure $P_{NL-1/2}$ and geopotential $\mathbf{\Phi}_{NL-1/2}$ are presented on the $(NL-1/2)$th half ML. Model orography presents a filtered elevation in the weather model resolution, which is differed from the real topography.

The parameters related to the temperature, such as T_S and mean sea level temperature T_{MSL}, are not directly given in NWP products. They can be computed by using the parameters in the vertical levels and based on the temperature lapse rate. More information about this procedure can be found in Appendix E.

3.1.2 Integration method based on 4-dimensional NWP products

In this section, the air refractivity integration procedure using 4-dimensional NWP products is described. Firstly, the NWP products are prepared in a proper horizontal resolution (section 3.1.2.1). Then, vertical interpolation and/or extrapolation of the products is performed in order to retrieve the parameters on the real surface topography and along the integration path (section 3.1.2.2). Thirdly, the effects of the integration step and the effective tropospheric height over the total integrated delay are discussed (section 3.1.2.3). Finally, a short discussion over air refractivity equations and different coefficient settings are carried out (section 3.1.2.4).

3.1.2.1 Data preprocessing

Some of the parameters, such as P_S, $\mathbf{\Phi}_S$ and T, are represented in the ECMWF products in spectral coordinates, which are described by harmonic coefficients. Other parameters are

represented in the so-called reduced Gaussian grid, which is irregular in latitude (Hortal and Simmons, 1991). As illustrated in the flow-chart (*Fig. 35*), two transformation steps are necessary in order to convert the spectral coordinates to the normal Gaussian grid. These transformations are performed using the Climate Data Operators (CDO) provided by Max Planck Institute for Meteorology (Schulzweida et al., 2009). After transformations, the products are presented in a regular lat-lon grid.

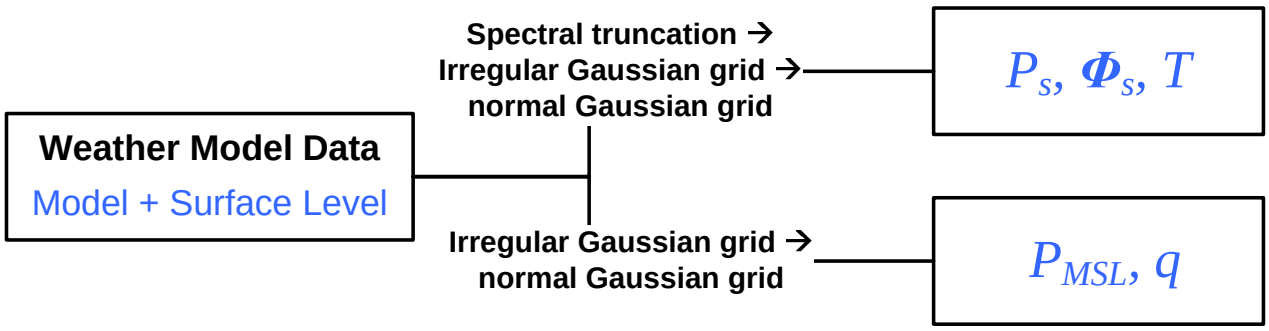

Fig. 35. Transformations from the spectral coordinates and the reduced Gaussian grid to the normal Gaussian grid. Parameters, such as P_S, $\mathbf{\Phi}_S$ and T, are given in spectral coordinates, which are converted by a two-step transformation to the normal Gaussian grid. Other parameters, such as P_{MSL} and q, are converted from the irregular to the regular Gaussian grid.

The global-scale NWP products provide horizontal resolution in the kilometer-range (around ten to hundred kilometers). Although some mesoscale models can provide better horizontal resolutions (down to the meter-range) by means of very time-consuming weather simulations, the accuracy of simulation results is strongly dependent on initialization of the simulation parameter, which are thus crucial. Therefore, global-scale NWP products have been selected for this thesis. Due to the coarse horizontal resolution, a spatial interpolation approach using the kriging interpolation method is proposed, as depicted in *Fig. 36*. The coarse grid is interpolated into a finer one based on the SRTM DEM grid resolution (ca. 90 m). More details over the horizontal interpolation using the kriging method are described in Appendix G.

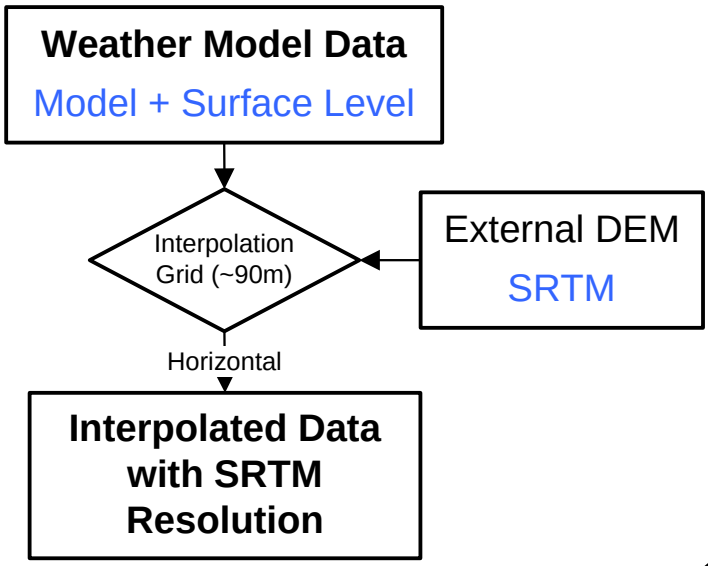

Fig. 36. Flow-chart of the horizontal interpolation of the NWP product. The coarse grid is interpolated into a finer interpolation based on the SRTM DEM grid resolution (ca. 90 m).

3.1.2.2 Vertical interpolation and extrapolation for the NWP products

The three-dimensional parameter fields have usually a higher resolution in vertical than in horizontal, since the parameters like P and T vary exponentially or linearly with the height, as shown in *Fig. 12*. In order to accurately calculate the value of the air refractivity, it is essential to interpolate/extrapolate the parameters P, T and q along the integration path. A general approach for the interpolation at a given height between two pressure levels is described in section 3.1.2.2.1. The determination of the parameters close to and at the real topography is essential and more complicated. The approaches for the different possible cases are summarized in section 3.1.2.2.2.

3.1.2.2.1 Vertical interpolation with a given height between two model levels

The vertical interpolation between two MLs is based on the hydrostatic equation (see *eq. (9)* and *(11)*). An integrated form between two pressure levels P_{n+1} and P_n can be thus derived:

$$g\Delta z = g \int_{z}^{z+\Delta z} dz = -R_{ideal} \int_{p}^{p+\Delta p} T dp = -R_d \int_{p}^{p+\Delta p} T_v dp, \tag{33}$$

where p is the logarithm of P ($p = \ln P$) and Δp is the logarithmical difference of two pressures. In the model vertical coordinates, the level number starts with the maximum number, then decreases gradually to 1, which is the top (highest) level of the model. Therefore, $\Delta p = p_n - p_{n+1}$ and similarly, $\Delta z = z_n - z_{n+1}$ (see *Fig. 37*).

In comparison with the pressure levels, the vertical coordinates represented with geometrical height z are more intuitive and convenient for integration in a Cartesian coordinate system. The problem of the vertical interpolation between two pressure levels P_{n+1} and P_n, corresponding to the geometric heights z_{n+1} and z_n, with a known height z is illustrated in *Fig. 37*.

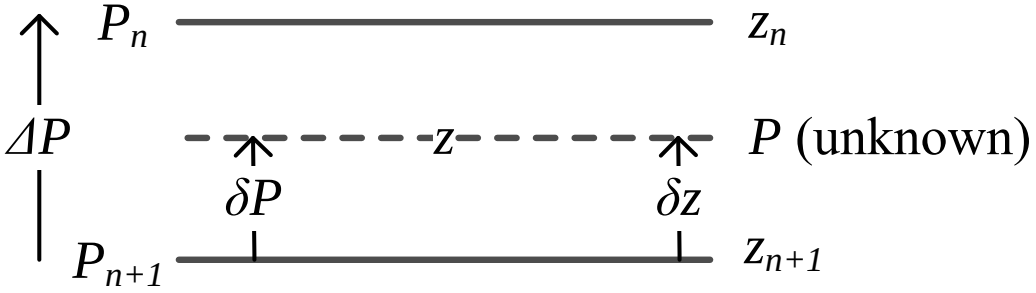

Fig. 37. Illustration of the data arrangement for solving an unknown pressure at a given height between two MLs, where P_{n+1} and P_n are the pressure at the layer $n+1$ and n, respectively; ΔP is the pressure difference between P_{n+1} and P_n; P is the unknown pressure at the height z, which is between z_{n+1} and z_n, the height values corresponding to the two pressure levels. δz and δp are the increments of z and the unknown P relative to the level $n+1$.

We assume that the temperature T changes linearly with p, in other words $T \sim p$. Therefore, the temperature variation over the pressure range between layer $n+1$ and n is given by:

$$T = \bar{T}_v + \Gamma(p - \bar{p}), \tag{34}$$

where the mean logarithm pressure is expressed as $\bar{p} = (p_{n+1} + p_n)/2$, and the temperature lapse rate $\Gamma = (T_n - T_{n+1})/(p_n - p_{n+1}) = \Delta T/\Delta p$. The virtual temperature T_v is defined in *eq. (10)* and can be approximated by *eq. (C.5)*. Since the q is a small value (close to zero), in the next step we assume that $T_v \approx T$ in *eq. (33)* in order to simplify the integration. The total effect on the total zenith delay caused by this approximation should be smaller than 0.1 mm based on practical experiences.

Substituting the *eq. (34)* in the integration form of the hydrostatic equation (*eq. (33)*) yields:

$$\Delta z = -\frac{R_d}{g}\int_{p}^{p+\Delta p}\Big(\bar{T}_v + \Gamma(p-\bar{p})\Big)\partial p = -\frac{R_d}{g}\Big((\bar{T}_v - \Gamma\bar{p}) - \Gamma(p+\Delta p/2)\Big)\Delta p. \tag{35}$$

Therefore, the mean virtual temperature $\bar{T}_v$ between two layers can be solved:

$$\bar{T}_v = \Gamma\bar{p} - \Gamma(p+\Delta p/2) - \frac{g}{R_d}\frac{\Delta z}{\Delta p}. \tag{36}$$

Assuming that $\bar{p} = (p+\Delta p/2)$, then $\bar{T}_v$ can be thus simplified by:

$$\bar{T}_v = -\frac{g}{R_d}\frac{\Delta z}{\Delta p}. \tag{37}$$

To interpolate the pressure P or p at a given height z between two MLs $n+1$ and n with given relative height increment $\delta z = z - z_{n+1}$ with respect to the lower layer $n+1$, the integrated form of hydrostatic equation *eq. (35)* can be rewritten (William, G. C., 1983):

$$\delta z = -\frac{R_d}{g}\left(\bar{T}_v + \Gamma(\delta p + \Delta p)\right)\Delta p, \tag{38}$$

where $\bar{T}_v$ between the two MLs is calculated by $\Big(-g(z_n - z_{n+1})\Big)/\Big(R_d(p_n - p_{n+1})\Big)$ and δp is the increment of the logarithm pressure p, in other words $\delta p = p - p_{n+1}$.

The solution of p can be derived straightforwardly as:

$$p = \frac{2\cdot\delta z}{-B + \sqrt{B^2 - 2R_d\Gamma\delta z/g}} + p_{n+1}, \tag{39}$$

where

$$B = -R(\bar{T}_v + \Gamma(p_{n+1} - p_n)/2)/g.$$

Afterwards, at a given P (or p), the temperature T at height z is calculated with *eq. (34)* and *eq. (36)*. Since the partial pressure of water vapor e does not comply with the hydrostatic equilibrium, the q at given p is accomplished with linear interpolation by:

$$q = \alpha\cdot q_n + (1-\alpha)\cdot q_{n+1}, \quad \text{with} \quad \alpha = \frac{p - p_{n+1}}{p_{n+1} - p_n}. \tag{40}$$

3.1.2.2.2 Vertical interpolation/extrapolation near the surface level field

In the surface orography, the mountains and the valleys have been smoothed in order to obtain a homogeneous surface. Therefore, discrepancies exist in volcanic areas between the model surface and the real topography. In *Fig. 38*, an illustration of the model surface $z_{S,model}$ (thick black line) has a smooth variation in height, whereas the real topography $z_{S,real}$ (dashed grey line) varies abruptly. The lowest half level $NL+1/2$ is overlaid with the SL, where NL is the number of levels. It means that $P_{NL+1/2} = P_S$. Moreover, an extra layer is introduced as the lowest layer: the Mean Sea Level (MSL). The height of the MSL is identical with the geoid, more

discussion about the height conversions see Appendix F. P_{MSL} and T_{MSL} are also available on MSL.

In order to obtain the exact surface parameter on the real topography, the vertical interpolation between two levels or extrapolation under the surface level is required near the SL field. In comparison with the real surface height $z_{S,real}$ in vertical levels, there are three possibilities (see *Fig. 38*):

(1) $z_{S,real} > z_{NL}$, the point is above the lowest full ML;

(2) $z_{S,model} < z_{S,real} < z_{NL}$, the point is between the full ML and the SL;

(3) $z_{S,real} < z_{S,model}$, the point lies below the *sl*.

Therefore, the pressure levels between two MLs defined as $n+1$ (lower) and n (upper) can be determined:

in case (1), there are NL and $NL-1/2$;

in case (2), the $n+1$ layer is replaced with the SL, and n with NL;

in case (3), the MSL and the SL are used for $n+1$ and n layer.

Finally, the normal interpolation procedure according to section 3.1.2.2.1 is carried out for T and P.

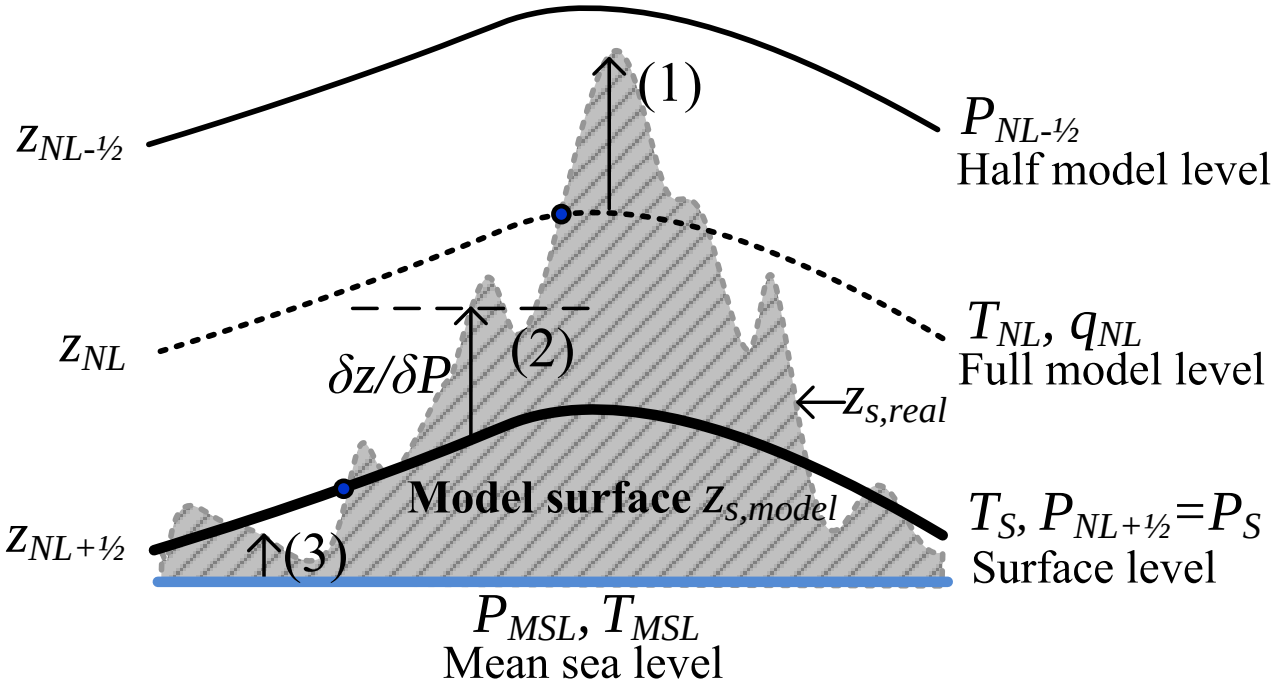

Fig. 38. Vertical interpolation and extrapolation near the surface topography. Three Model Levels (MLs) are illustrated: lowest half model level $NL+1/2$ (thick black line), lowest full model level NL (dashed thin black line) and the half ML $NL-1/2$ (solid thin black line). The $NL+1/2$ is identical to the SL, which means that $P_{NL+1/2} = P_S$ and $\mathbf{\Phi}_{NL+1/2} = \mathbf{\Phi}_S$. The geometric heights z correspondent to each level are marked in the left side. The MSL with the parameters P_{MSL} and T_{MSL}, depicted in bold blue line, is added as the lowest level. The real topography is illustrated in background with abrupt variations (dashed light grey line). Three possible point locations relative to these models are presented in the figure: (1) between the half and the full model level; (2) between the SL and the lowest full ML; (3) below the SL.

The parameter q is not available on the MSL and the SL. In case (1), the q is linearly interpolated given p (derived from given height z) between p_{NL} and $p_{NL-1/2}$ according to *eq. (39)*. In case (2) and (3), the extrapolation approach is deployed with a spline interpolation method using at least 6 closest levels.

3.1.2.3 Direct integration - effective troposphere height and integration interval

Instead of using a continuous integration formula, the discrete formula derived for numerical computation based on Riemann sum method for *eq. (18)* is first given in zenith by:

$$L_{atmo} = \begin{cases} 10^{-6} \sum\limits_{n=0}^{I_1} \left(k_1 \frac{P_n}{T_n} + k_2' \frac{e_n}{T_n} + k_3 \frac{e_n}{T_n^2} \right) \Delta z_1 & \text{for } z_S \leq z_n \leq z_{eff}, n = 0, \cdots, I_1, \\ 10^{-6} \sum\limits_{n=I_1}^{I_2} \left(k_1 \frac{P_n}{T_n} + k_2' \frac{e_n}{T_n} + k_3 \frac{e_n}{T_n^2} \right) \Delta z_2 & \text{for } z_{eff} < z_n \leq z_{atmo}, n = I_1, \cdots, I_2, \end{cases} \tag{41}$$

where Δz is the integration interval which is selected according to the height of the integration step (z_n) in the atmosphere. In this thesis, the atmosphere is divided into two parts: the lower part starts from the the surface z_S to z_{eff} where the atmosphere varies fast in vertical, thus a smaller interval Δz_1 is used to trace the detailed variation of the atmosphere; the upper part is from z_{eff} to the top of the atmosphere z_{atmo} where the variation of the atmosphere is slower. Therefore, a larger interval Δz_2 is applied. P_n, T_n and e_n are the parameters at the height z_n:

$$z_n = \begin{cases} \frac{\Delta z_1}{2} + \sum\limits_{n=0}^{I_1} \Delta z_1 (n-1) & \text{for } z_S \leq z_n \leq z_{eff}, \\ z_{I_1} + \frac{\Delta z_2}{2} + \sum\limits_{n=I_1}^{I_2} \Delta z_2 (n-1) & \text{for } z_{eff} < z_n \leq z_{atmo}. \end{cases} \tag{42}$$

The total number of integration steps n is equal to $I_1 + I_2$, where $I_1 = [z_{eff}/\Delta z_1]$ is the number of the steps within the lower part of the atmosphere ($z_S \leq z_n \leq z_{eff}$) and $I_2 = [(z_{atmo} - z_{eff})/\Delta z_2]$ is the number of the steps between z_{eff} and the height of the product z_{atmo} ($z_{eff} < z_n \leq z_{atmo}$).

Similarly, *eq. (20)* for integration in slant range can be written in discrete form as:

$$L_s = \begin{cases} 10^{-6} \sum\limits_{n=0}^{I_1} \left(k_1 \frac{P_n}{T_n} + k_2' \frac{e_n}{T_n} + k_3 \frac{e_n}{T_n^2} \right) \Delta r_1 & \text{for } z_S \leq r_n \leq r_{eff}, n = 0, \cdots, I_1 \\ 10^{-6} \sum\limits_{n=I_1}^{I_2} \left(k_1 \frac{P_n}{T_n} + k_2' \frac{e_n}{T_n} + k_3 \frac{e_n}{T_n^2} \right) \Delta r_2 & \text{for } r_{eff} < r_n \leq r_{atmo}, n = I_1, \cdots, I_2. \end{cases} \tag{43}$$

where Δr is the integration increment along the slant range $\vec{r}$, which is simplified as the shortest line between the satellite coordinates $[X, Y, Z]_s$ and the object coordinates $[X, Y, Z]_p$ (see section 2.2.4). Similar to the integration interval in zenith Δz, two integration increments are defined: Δr_1 in the lower and Δr_2 in the upper part of the atmosphere. In *eq. (43)*, z_{eff} and z_{atmo} are replaced by r_{eff} and r_{atmo} which can be converted by using the local incidence angle $\cos\theta'_{inc}$ at a defined height as (see Appendix A):

$$\begin{aligned} r_{eff} &= z_{eff} / \cos\theta'_{inc,z_{eff}}, \\ r_{atmo} &= z_{atmo} / \cos\theta'_{inc,z_{atmo}}. \end{aligned} \tag{44}$$

The direct integration approach is illustrated in *Fig. 39*, as well as the processing flow-chart. The integration starts from a given point (a GPS receiver or and a PS point); then meteorological parameters at each integration step are interpolated or extrapolated along the integration path in zenith or in slant range direction (see *Fig. 39(a)*). Two integration intervals are defined for the lower and the upper part of the atmosphere which are divided by the effective tropospheric height z_{eff} (see *eq. (42)*).

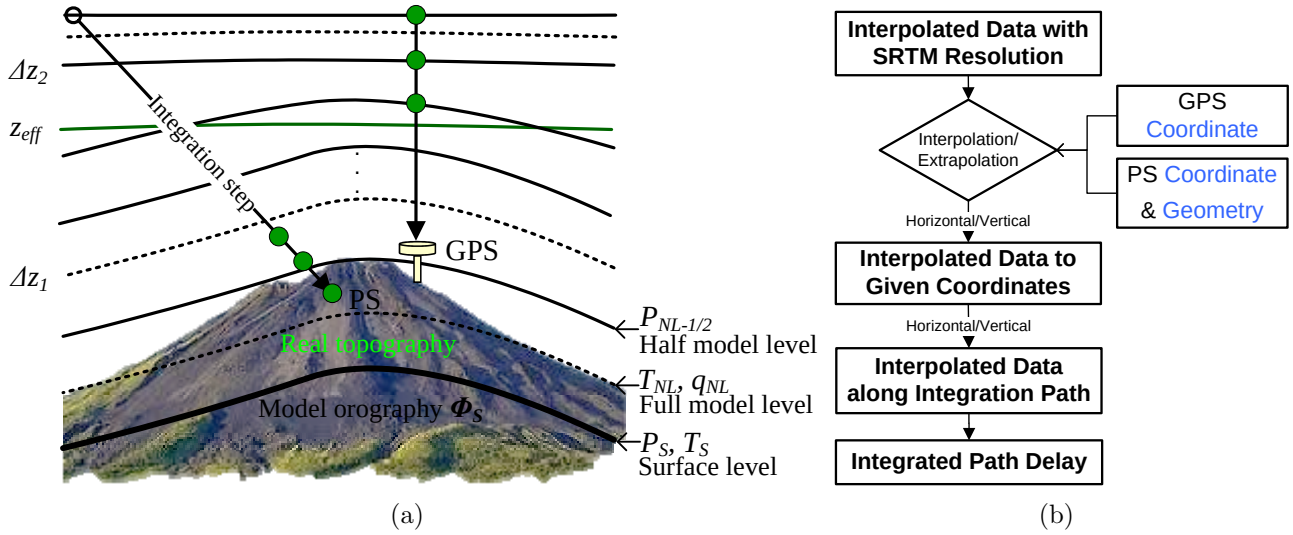

Fig. 39. Direct integration methods using NWP products: (a) direct integration in zenith from a GPS receiver and in slant range direction from a PS point. Two integration intervals are defined for lower and upper part of the atmosphere which are divided by the effective tropospheric height z_{eff} (green bold line); (b) the flow-chart of direct integration approach.

For numerical computation, the integration steps (Δz and Δr) and the effective tropospheric height z_{eff} influence the integration result.

- ◇ **Effective height** often correlates with the tropopause, which is known as the boundary layer of the troposphere, where the parameters have a fast variation against the height. Depending on the temperature variation in height, the tropopause can be clearly observed since the temperature lapse rate becomes positive. For example, the tropopause locates at the height of $\sim$ 12 km in *Fig. 12*. The empirical values are given in Wallace and Hobbs (2006): the mean tropopause is $\sim$ 17 km in tropical areas and $\sim$ 11 km in extratropical areas. For global application, the height of 17 km is applied for the z_{eff}.

- ◇ **Integration interval** In order to determine an appropriate integration interval, a simulation is carried out by integrating ZPD at the WTZR GPS station with a set of predefined integration increments. The interval Δz_1 is defined from 0.1 to 1000 m with irregular samples (see Fig. 40), and the Δz_2 is fixed with a constant value which is equal to 100 m. For integration, the ERA-Interim data set on 19 January 2010 at 18h is selected. The integrated ZPDs are presented in *Fig. 40* with respect to the Δz_1 intervals. The total variation of integrated ZPDs is about 4.3 mm. The ZPD decreases firstly from 2.222 to 2.214 m with increasing integration increments from 0.1 to 1 m. Afterwards, the variation of ZPDs is relative stable within 1 mm with the intervals from 1 to 100 m, where the minimum ZPD reaches at the interval 8 m with 2.213 m. Then the ZPD increases steadily from the minimum with increasing value of the interval. Moreover, the ZPDs with integration intervals from 4 to 20 m have a difference of 0.1 mm with the minimum value. Therefore, the integration step can be selected from 4 to 20 m depending on the computational intensity. In this thesis, the interval 10 m increment is chosen for integrating the atmospheric delay on a single point, such as for GPS ZPD and CR SPD.

3.1.2.4 Summary of integration equations and coefficient constants

For precise geodetic applications such as VLBI and GPS, the atmospheric delay has to be compensated accurately in order to achieve a millimeter ranging accuracy. Normally, vertical measurements of the atmospheric parameters are not available. Therefore, a series of equations have been derived which are based on surface measurements (Davis et al., 1985; Askne and

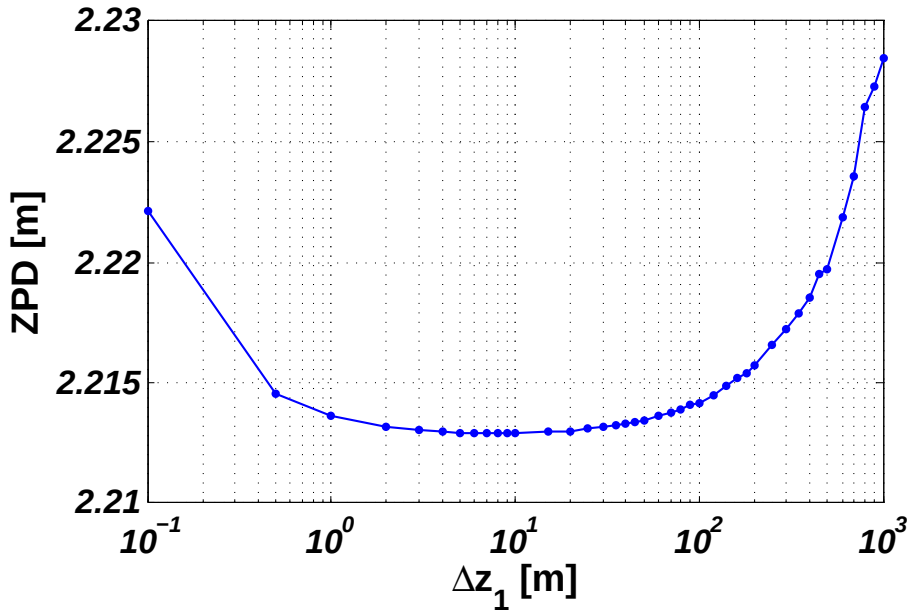

Fig. 40. The simulation test for determining an appropriate integration interval with a varied integration increments of Δz_1 from 0.1 to 1000 m and a constant interval of $\Delta z_2 = 100$ m. Moreover, the effective tropospheric height z_{eff} is defined on 17 km. The ERA-Interim data set on 19 January 2010 at 18 h is used for simulation.

Nordius, 1987; Bevis et al., 1992; Böhm, 2004). For those applications, the delay effect is usually divided into two parts: (1) the Zenith Hydrostatic Delay (ZHD), which is described in section 3.1.2.4.1; (2) the Zenith Wet Delay (ZWD), which is presented in section 3.1.2.4.2. Nevertheless, the coefficient constants in *eq. (16)* are not consistent due to different experiments, assumptions and approximations. A summary of the constants extracted from selected papers is presented in section 3.1.2.4.3.

3.1.2.4.1 Hydrostatic delay

Two expressions of ZHD are derived based on the hydrostatic equation (*eq. (9)*) and the air refractivity for an ideal (*eq. (12)*) and non-ideal gas (*eq. (17)*). For an ideal gas, the ZHD $L_{h,ideal}$ can be expressed as a function of the surface pressure P_S:

$$L_{h,ideal} = 10^{-6} \int_{P_{atmo}}^{P_S} \frac{k_1 R_d}{g} \mathrm{d}P = 10^{-6} \frac{k_1 R_d P_S}{g_m}. \tag{45}$$

where P_{atmo} is the last layer (first level) of the NWP product; g_m is the mean gravity acceleration at the mass center of the atmospheric column (Böhm, 2004):

$$g_m = \frac{\int_{z_S}^{z_{atmo}} \rho(z) g(z) \mathrm{d}z}{\int_{z_S}^{z_{atmo}} \rho(z) \mathrm{d}z}. \tag{46}$$

Saastamoinen (1972) provides an approximate form according to the latitude λ and the geometric height z:

$$g_m \approx g_0(1 - 0.00266 cos(2\lambda) - 0.28 \cdot 10^{-6} z), \tag{47}$$

where the constant g_0 is equal 9.7840 m/s^2.

Theoretically, the first term of *eq. (13)* or *eq. (16)* should be used as the ZHD $L_{h,nonideal}$ for non-ideal gas:

$$L_{h,nonideal} = 10^{-6} \int_{z_S}^{z_{atmo}} k_1 \frac{P(z)}{T_v(z)} \mathrm{d}z. \tag{48}$$

According to *eq. (17)*, an approximate hydrostatic equation can be derived as:

$$L_{h,approx} = 10^{-6} \int_{z_S}^{z_{atmo}} k_1 \frac{P(z)}{T(z)} \mathrm{d}z. \tag{49}$$

For comparison, the NWP products, interpolated on the WTZR GPS station coordinate, during August 2011 are used. The ZHDs are determined according to *eq. (45)*, *eq. (48)* and *eq. (49)*, and then depicted in *Fig. 41*. The ZHDs $L_{h,ideal}$ and $L_{h,nonideal}$ have a good agreement with a mean offset of about 0.2 mm and the standard deviation of < 0.1 mm. In comparison, a mean offset about 3.4 mm is observed between $L_{h,approx}$ and $L_{h,ideal}$, and the standard deviation increases to 0.8 mm. It is caused by approximation of the virtual temperature T_v by the temperature T which leads to an increase of the ZHD due to the water vapor. In spite of the greater offset and standard deviation $L_{h,approx}$ is applied in our applications, since Smith and Weintraubt (1953) use the ideal gas equation *eq. (12)* to derive k_1, which is 0.036 smaller than the k_1 based on the non-ideal gas equation in Healy (2011) (see section 3.1.2.4.3).

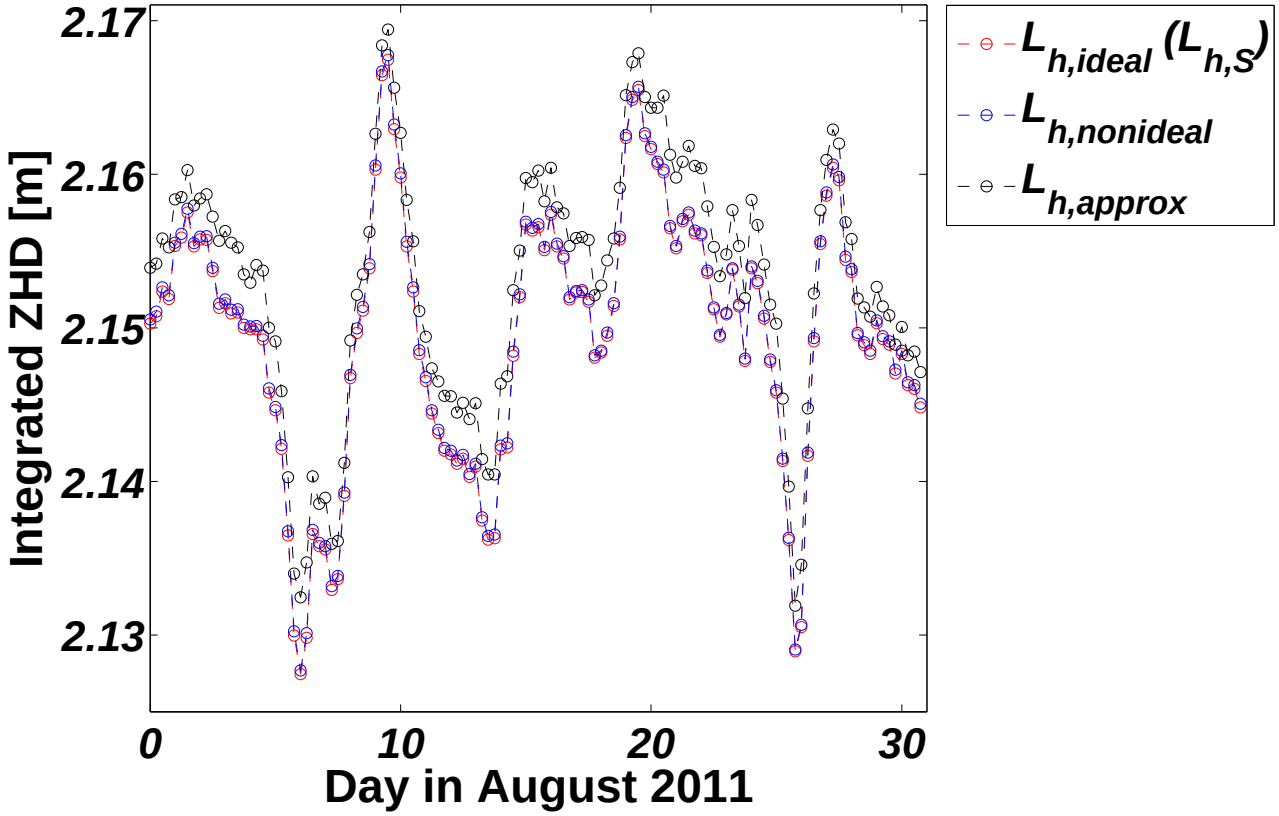

Fig. 41. Comparison of ZHDs calculated according to $L_{h,ideal}$ based on surface pressure P_S in black (*eq. (45)*), $L_{h,nonideal}$ in red (*eq. (48)*) and $L_{h,approx}$ in blue (*eq. (49)*). The NWP products during August 2011, interpolated on the WTZR GPS station coordinate, are used.

3.1.2.4.2 Wet delay

Similarly, the ZWD for a non-ideal gas $L_{w,nonideal}$ can be expressed with the second and third terms of *eq. (16)*:

$$L_{w,nonideal} = 10^{-6} \int_{z_S}^{z_{atmo}} k_2' \frac{e(z)}{Z_w T(z)} + \frac{k_3 e(z)}{Z_w T(z)^2} \mathrm{d}z. \tag{50}$$

Under the assumption that Z_w is approximately equal to 1, the approximated form of $L_{w,nonideal}$ can be expressed regarding to *eq. (17)* as:

$$L_{w,approx} = 10^{-6} \int_{z_S}^{z_{atmo}} k_2' \frac{e(z)}{T(z)} + k_3 \frac{e(z)}{T(z)^2} \mathrm{d}z. \tag{51}$$

Furthermore, for an ideal gas, the ZWD $L_{w,ideal}$ is written with the last two terms of *eq. (12)* by:

$$L_{w,ideal} = 10^{-6} \int_{z_S}^{z_{atmo}} \Big(k_2 - k_1\Big) \frac{e(z)}{T(z)} + k_3 \frac{e(z)}{T(z)^2} \mathrm{d}z. \tag{52}$$

An approximation of the ZWD based on the surface humidity measurements e_S is derived by Böhm (2004):

$$L_{w,S} \approx 7.48 \cdot \frac{e_S}{T_S^2}. \tag{53}$$

Using the provided NWP products, the ZWDs are calculated according to *eq. (50)*, *eq. (52)*, *eq. (51)* and *eq. (53)*, and then depicted in *Fig. 42*. The ZWDs: $L_{w,nonideal}$, $L_{w,ideal}$ and $L_{w,approx}$ are nearly identical with mean differences of < 0.3 mm and standard deviations of < 0.1 mm. Obviously, the ZWD $L_{w,S}$ has a great discrepancy with other three ZWDs. The mean offsets are around 18.5 mm, as well as large standard deviations around 20.7 mm are observed. For our applications, the $L_{w,approx}$ is selected.

For meteorological purposes, the measure of the water vapor content is often replaced by Integrated Water Vapor (IWV), which is expressed as the integration of the water vapor density along a vertical profile (Bevis et al., 1992):

$$IWV = \int \rho_w \mathrm{d}z \approx 10^6 \frac{L_w}{\Big(\frac{k_3}{T_m} + k_2'\Big) R_w}, \tag{54}$$

where ρ_w is the density of water vapor in $\mathrm{kg} \cdot \mathrm{m}^{-3}$ and T_m is the weighted *mean temperature* of the atmosphere:

$$T_m = \frac{\int (\rho_w / T) \mathrm{d}z}{\int (\rho_w / T^2) \mathrm{d}z}. \tag{55}$$

An approximation is suggested by Bevis et al. (1992) for the T_m in lower troposphere (< 1.6 km):

$$T_m \approx 70.2 + 0.72 T_s. \tag{56}$$

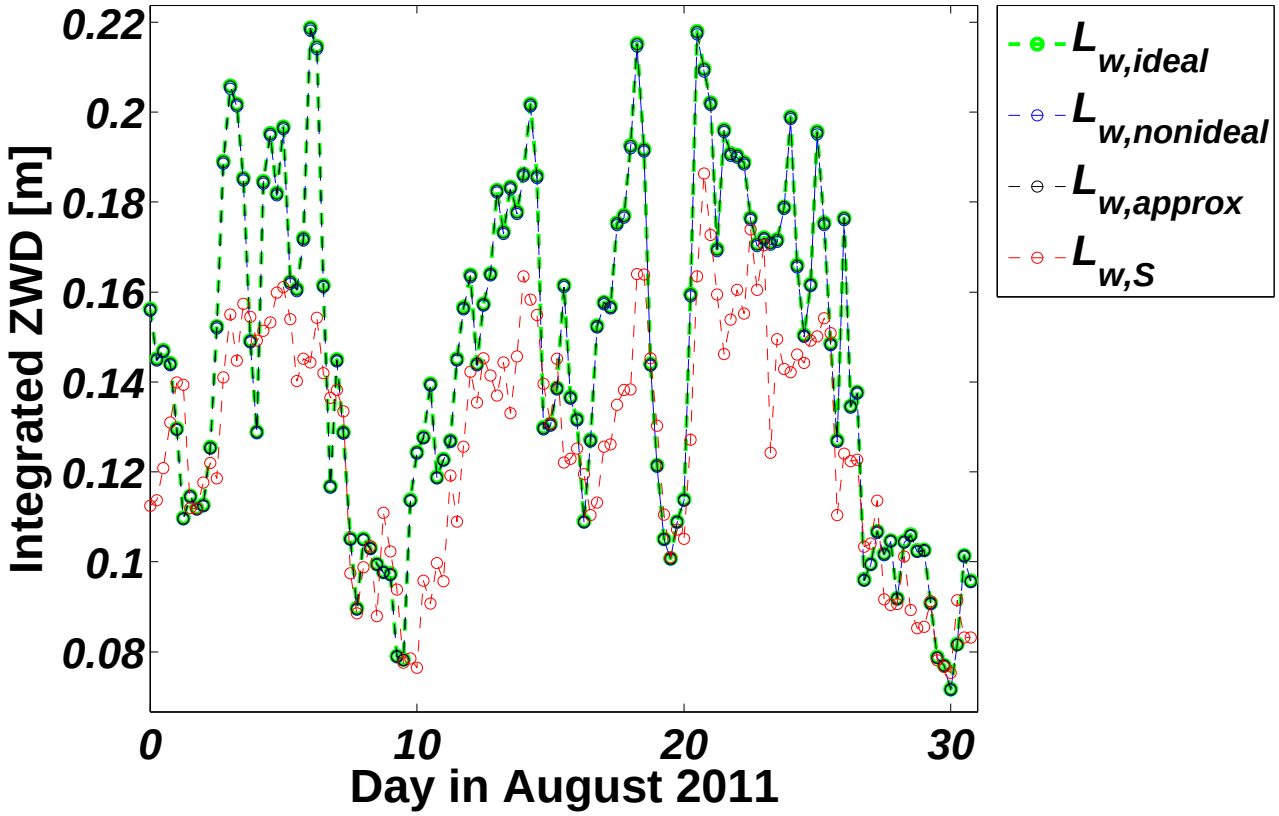

Fig. 42. Comparison of ZWDs calculated according to *eq. (53)* based on surface parameters e_S and T_S (red), *eq. (52)* (green), *eq. (50)* (blue) and *eq. (51)* (black). The NWP products during August 2011 are selected and interpolated on the WTZR GPS station coordinate.

Frequently, IWV is converted to the depth of an equivalent column of liquid water (Precipitable Water (PW)) by means of a useful rule of thumb (Bevis et al., 1992):

$$PW = \frac{IWV}{\rho_{lw}} \approx \frac{ZWD}{\Pi}, \quad \text{with} \quad \Pi \approx 6.4, \tag{57}$$

where ρ_{lw} is the density of liquid water.

3.1.2.4.3 Coefficient constants

The coefficient constants k_1, k_2 and k_3 are empirical values which can be retrieved from laboratorial experiments, such as Smith and Weintraubt (1953); Thayer (1974). For geodetic applications, different sets of coefficient constants are proposed by Saastamoinen (1972); Davis et al. (1985); Bevis et al. (1994). Recently, Rüeger (2002); Healy (2011) suggest more accurate coefficient constants for precise geodetic applications and GPS radio occultation.

In order to evaluate the influences of the different sets of coefficient constants in the total delay, we summarize them in Table 2. Regarding different assumptions, they are divided into three groups: (1) ideal gases based on *eq. (12)*; (2) non-ideal gases based on *eq. (16)*; (3) non-ideal gases based on an approximated equation *eq. (17)*. Their integration forms can be written as a combination of ZHD and ZWD:

(1) $L_{atmo,ideal} = L_{h,ideal} + L_{w,ideal}$;

(2) $L_{atmo,nonideal} = L_{h,nonideal} + L_{w,nonideal}$;

(3) $L_{atmo,approx} = L_{h,approx} + L_{w,approx}$.

For comparison, the reference ZPD is integrated according to the approximated equation *eq. (17)* and the coefficient constants from Smith and Weintraubt (1953), which is rounded to 0.1. Differences relative to the reference ZPD are calculated by using the NWP products during August 2013. Their mean value and the standard deviation are specified in Table 2.

Table 2. Summary of the coefficient constants k_1, k_2 and k_3 from Smith and Weintraubt (1953); Saastamoinen (1972); Thayer (1974); Davis et al. (1985); Bevis et al. (1994); Rüeger (2002); Healy (2011). They are divided into three groups: (1) ideal gases based on *eq. (12)*; (2) non-ideal gases based on *eq. (16)*; (3) non-ideal gases based on an approximated equation *eq. (17)*. Differences relative to the reference ZPD ($L_{atmo,approx}$ with rounded Smith and Weintraubt (1953) coefficient constant) are calculated by using the NWP products during August 2013. The mean value and the standard deviation of differences are presented.

Authors (Year)	$\mathbf{k_1}$ [K/hPa]	$\mathbf{k_2}$ [K/hPa]	$\mathbf{k_3 \times 10^{-5}}$ [$\mathbf{K^2}$/hPa]	**ZPD Diff. [mm]** Mean	Std
Ideal Gas (*eq. (12)*)					
Smith and Weintraubt (1953)	77.607 ± 0.01	71.600 ± 8.5	3.747 ± 0.031	-0.2	0.1
Saastamoinen (1972)	77.624	64.70 ± 0.08	3.719	-0.9	0.4
Rüeger (2002) (best available)	77.695	71.970	3.75406	2.4	< 0.1
Rüeger (2002) (best average)	77.6890	71.2952	3.75463	2.3	< 0.1
Healy (2011) [4]	77.643	71.2952	3.75463	1.1	< 0.1
Non-ideal Gas (*eq. (16)*)					
Thayer (1974)	77.60 ± 0.014	64.80 ± 0.08	3.776 ± 0.004	-2.2	0.6
Davis et al. (1985) [5]	77.604 ± 0.008	65.27 ± 10	3.776 ± 0.03	-2.1	0.6
Healy (2011)	77.643	71.2952	3.75463	-1.7	0.8
Non-ideal Gases - Approximated Equation (*eq. (17)*)					
Bevis et al. (1994)	77.60 ± 0.05	70.40 ± 2.2	3.739 ± 0.012	-3.6	1.0

Regarding the statistical analysis of ZPD differences presented in Table 2, the mean value varies from -3.6 to 2.4 mm, and the standard deviation from < 0.1 mm to 1.0 mm. In general, the reference ZPD is close to the ZPD under the assumption of an ideal gas, since their standard deviations are all < 0.5 mm. The reference constants are derived from Smith and Weintraubt (1953), the minimum offset of -0.2 mm is observed, which is mainly caused by the different integration equations. Whereas the maximum standard deviation (1.0 mm) and the mean value (-3.6 mm) are yielded by the approximated formula. The next closest constants are provided by Healy (2011) under the assumption of an ideal gas, where the standard deviation is less than 0.1 mm and the offset is about 1.1 mm. In summary, for an ideal gas, the discrepancies by mean values are mainly caused by the difference in k_1; for non-ideal gas, the differences are primarily induced by different formulae of ZHD.

It is clear that there is no perfect coefficient constant for the real air refractivity. The approximated air refractivity equation (*eq. (17)*) and the rounded Smith and Weintraubt (1953) coefficient constants have been selected for our application. Therefore, by replacing these constants, the air refractivity (*eq. (17)*) can be thus written as:

$$N_{atmo} = 0.776 \cdot \frac{P}{T} + 0.2333 \cdot \frac{e}{T} + 3.75 \times 10^3 \frac{e}{T^2}. \tag{58}$$

[4] Rüeger (2002) (best average): k_1 is adjusted for GPS radio occultation, k_2 and k_3 remain unchanged.
[5] Thayer (1974) coefficients are chosen with experimental uncertainties.

3.2 ECMWF products

In the last decades, the Numerical Weather Prediction (NWP) has gained immense improvements in prediction accuracy and reliability with increased computational power, increased observation coverage and development of atmospheric physical theories. Nowadays, the NWP process can simulate a variety of atmospheric parameters in global dimension with horizontal resolution of < 100 km and often better vertical resolution. It provides an unique possibility to derive the 4-dimensional atmospheric parameters (P, T and q), which are necessary inputs for the direct integration method defined in section 3.1.

Two kinds of NWP products from the European Centre for Medium-Range Weather Forecast (ECMWF), which are generated by ECMWF Integrated Forecast System (IFS), can be used for direct integration. They are ERA-Interim and ECMWF operational data (OP), respectively (see Table 3). ERA-Interim is the latest ECMWF global atmospheric reanalysis, which covers the period from 1 January 1979 to present with approximately 3-months delay (Dee et al., 2011). Unlike the OP, reanalysis is produced with a fixed data assimilation version and a fixed resolution for the whole period. This product is more suitable for studying long-term variability in climate. Major improvements of ERA-Interim according to the previous reanalysis project ERA-40 can be summarized in following points (Uppala et al., 2005; Dee et al., 2011):

- ◇ better assimilation methods: using 4D-Var instead of 3D-Var;
- ◇ better models: improvements on the forecast model by replacing IFS release *Cycle 23r4* with *Cycle 31r2*;
- ◇ better input data: using best available observations with enhanced quality control and data selection, including bending angles measured by GPS radio occultation since 2001 and performing sophisticated bias corrections, etc.

Atmospheric daily data sets of ERA-Interim are freely available from the ECMWF Data Server [6] for research usage. The basic product specifications, such as horizontal and vertical resolution and IFS release cycle, are presented in Table 3. Although, the operational forecast based on the up-to-date IFS version enables a near real-time analysis with a wider range of atmospheric parameters and a better horizontal/vertical resolution. Unfortunately, these data sets are not free of charge. Therefore, the ERA-Interim is mainly used in this thesis, and the OP is only applied for a short time period around the Hierro test site, Canary Islands (Spain), which is provided by the Institute of Atmospheric Physics, DLR.

Table 3. Summary of ERA-Interim, ERA-40 and OP specifications: horizontal resolution in spectral truncation and in geographical latitude/longitude; vertical resolution in Model Level (ML) with pressure as unit; IFS release cycles (Uppala et al., 2005; Dee et al., 2011).

ECMWF Products	**Horizontal Resolution** [7]		**Vertical Resolution** [7]	**IFS Release** [8]
	Spectral Truncation	**Lat/Lon [deg]**		
Operational	T1279 (N640)	0.125	91-Level (up to 1 Pa)	*Cycle 38r1*
ERA-Interim	T255 (N125)	0.75	60-Level (up to 10 Pa)	*Cycle 31r2*
ERA-40	T159 (N80)	1.125	60-Level (up to 10 Pa)	*Cycle 23r4*

In this section, the NWP products, which are used in section 3.3 and section 3.4, are summarized in section 3.2.1 for ERA-Interim and section 3.2.2 for OP.

[6] http://data-portal.ecmwf.int/data/d/interim_moda
[7] http://www.ecmwf.int/products/data/archive/data_faq.html
[8] http://www.ecmwf.int/products/data/technical/model_id/index.html

3.2.1 ERA-Interim (ECMWF Interim reanalysis)

The ERA-Interim analysis is weather model data provided four times per day with 6 hours interval, namely at 0, 6, 12 and 18 h. In order to analyze the accuracy and the stability of ERA-Interim over a long period (see section 3.3.1), we collected a four-year data set from the ECMWF Data Server. The period starts on 1 January 2008 and ends on 31 December 2011. There are 5844 data entries in total. Because of the global coverage, this data set can be employed for the applications in section 3.5, as well.

In practice, the set of input parameters required for direct integration (section 3.1.1) are listed in Table 4, with the correspondent field code, horizontal format and unit defined in ECMWF.

Table 4. Summary of required atmospheric parameter fields with field codes: 129, 130, 133, 151 and 152. Their correspondent field name, unit, horizontal format and description are presented.

Field Code	**Field Name**	**Horizontal Format**	**Unit**	**Description**
129	Geopotential $\mathbf{\Phi}_S$	T255	m^2s^{-2}	SL data
130	Temperature T	T255	Kelvin (K)	ML data
133	Specific humidity q	N128	kg/kg	ML data
151	Mean sea level pressure P_{MSL}	N128	Pascal (Pa)	SL data
152	Log surface pressure $\log P_S$	T255	–	SL data
172	Land sea mask	T255	–	SL data

In order to provide a visual example of ERA-Interim products, a set of atmospheric parameters (such as $\mathbf{\Phi}_S$, $\log P_S$, T and q), selected on 31 July 2011 at 18:00, is presented in *Fig. 43*[9] . A clear correlation between the $\mathbf{\Phi}_S$ (*Fig. 43(a)*) and the $\log P_S$ (*Fig. 43(b)*) is observed, since the pressure decreases exponentially with increasing height (see section 2.2.4.3.1). According to the global temperature distribution (*Fig. 43(c)*) and the average temperature over latitude (*Fig. 43(e)*), the northern hemisphere is warmer than the southern hemisphere on the selected date. The coldest average temperature lies near the stratopause between latitude $-90\,^\circ$ and $-75\,^\circ$. *Fig. 43(d)* reveals the distribution of the water vapor that is mostly concentrated near tropical areas. On the average specific humidity over latitude (*Fig. 43(f)*), there is a very low water vapor level near the Antarctic due to the extreme low temperature, and also in vertical above 8 km.

3.2.2 ECMWF operational data

The operational analysis data, similar to ERA-Interim data, can provide the required parameters with 6 hours interval. A three-months data set has been collected from 1 September 2011 to 29 February 2012 around the Canary Islands (Spain), which spans from $25\,^\circ$ to $30\,^\circ$ in latitude and $-20\,^\circ$ to $-10\,^\circ$ in longitude. Altogether 732 data entries have been prepared for the GPS validation in section 3.3.1.3.

For comparison, four atmospheric parameters ($\mathbf{\Phi}_S$, P_S, T and q) are presented in *Fig. 44*. Obviously, OP with horizontal resolution of about 12.5 km presents more details compared to ERA-Interim (see *Fig. 44(a)-(d)*). A strong correlation can also be observed between the $\mathbf{\Phi}_S$ and the P_S (see *Fig. 44(a)* and *(b)*). In the presence of the topography, the T decreases with increasing height due to the vertical atmospheric stratification (see section 2.2.4.3.1). Nevertheless, the variation of T can be effected by various factors, e.g. location, sun position, etc. This elevation-dependence is less significant by q in mountainous areas (see *Fig. 44(b)*). Moreover, the vertical resolution is improved due to 21 additional vertical levels in OP, especially in troposphere.

[9] The visualization of parameter fields is performed by using an open software *Panoply* provided by NASA. The latest version 3.1.7 was released on 31 December 2012 at website: http://www.giss.nasa.gov/tools/panoply/.

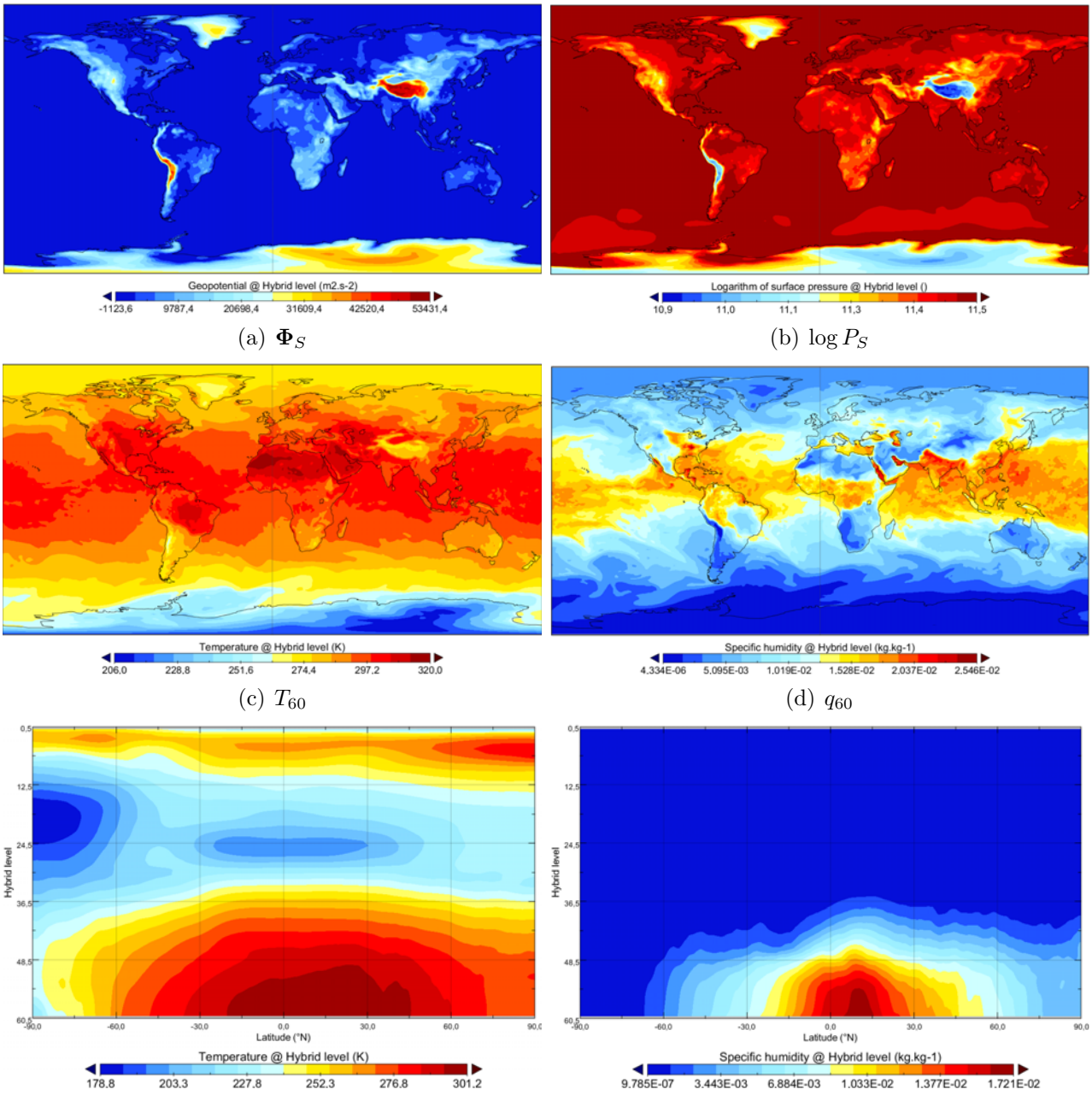

(a) $\mathbf{\Phi}_S$ (b) $\log P_S$

(c) T_{60} (d) q_{60}

(e) average T over latitude (f) average q over latitude

Fig. 43. Visualization of selected parameter fields from ERA-Interim data using *Panoply* on 31 July 2011 at 18:00. (a) surface geopotential $\mathbf{\Phi}_S$; (b) logarithm of surface pressure $\log P_S$; the lowest layer of temperature T_{60} in (c) and specific humidity q_{60} in (d); the average value of T in (e) and q in (f) over latitude. The y-axis is the model level number, and x-axis is the latitude in degree.

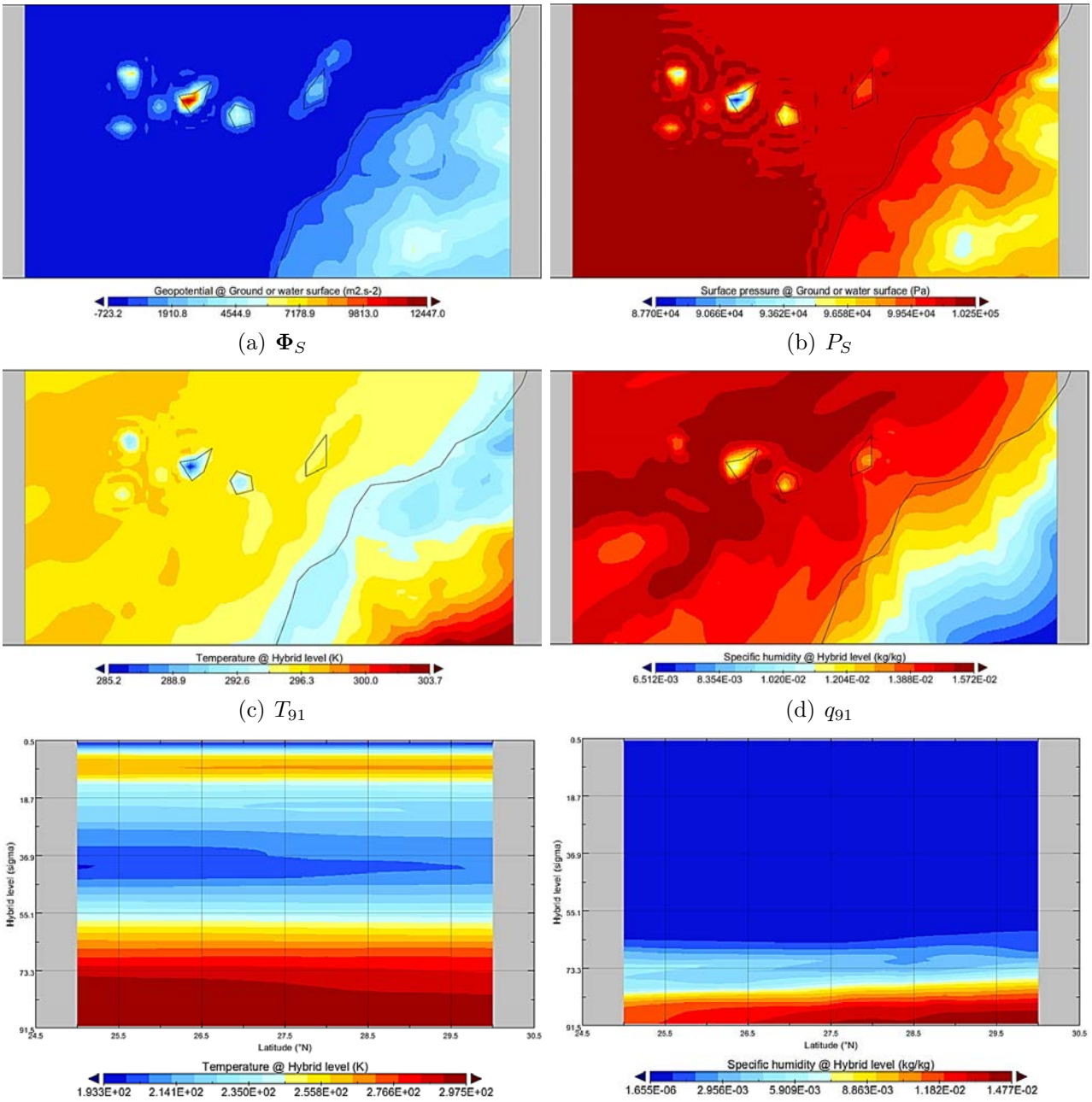

(a) $\mathbf{\Phi}_S$ (b) P_S

(c) T_{91} (d) q_{91}

(e) average T over latitude (f) average q over latitude

Fig. 44. Visualization of selected parameter fields from OP around the Canary Islands (Spain) using *Panoply* on 1 September 2011 at 00:00. (a) surface geopotential $\mathbf{\Phi}_S$; (b) surface pressure P_S; the lowest layer of temperature T_{91} in (c) and specific humidity q_{91} in (d); the average value of T in (e) and q in (f) over latitude.The y-axis is the model level number, and x-axis is the latitude in degree.

3.3 Validation of integrated atmospheric delays based on ECMWF products

The ECMWF IFS performs each data assimilation with millions of observations from an extensive range of inputs, which are not error-free. The quality of the input data varies depending on the different observation techniques, instrument calibration, processing techniques etc. Even performing a thorough data control and bias correction (Dee and Uppala, 2009; Healy, 2011), the accuracy of the products is perturbed by some uncorrected effects, e.g. warm bias in some aircraft reports. A forecast model is utilized to predict the meteorological parameters on the locations where the observation parameter does not exist. Due to model imperfections, additional/systematic errors can be introduced in the simulation results. Therefore, it is important to determine the accuracy and the reliability of ECMWF products for the calculation/determination of the integrated atmospheric delay. According to the air refractivity equation (*eq. (58)*), the accuracy of the delay depends on the accuracy of P, T and e (or q see section 2.2.4.3.3). A recent publication from Dee et al. (2011) provides an overview of the general assessment of ERA-Interim products in comparison with different reanalysis data, ECMWF operational data and different observations. Compared to the accuracy of P and T (Mooney et al., 2011; Dee et al., 2011), the accuracy of water vapor (related to q) is limited due to the complexity of the modeling and the accuracy of the input data (Bock et al., 2005; Flentje et al., 2007; Schäfler et al., 2010, 2011).

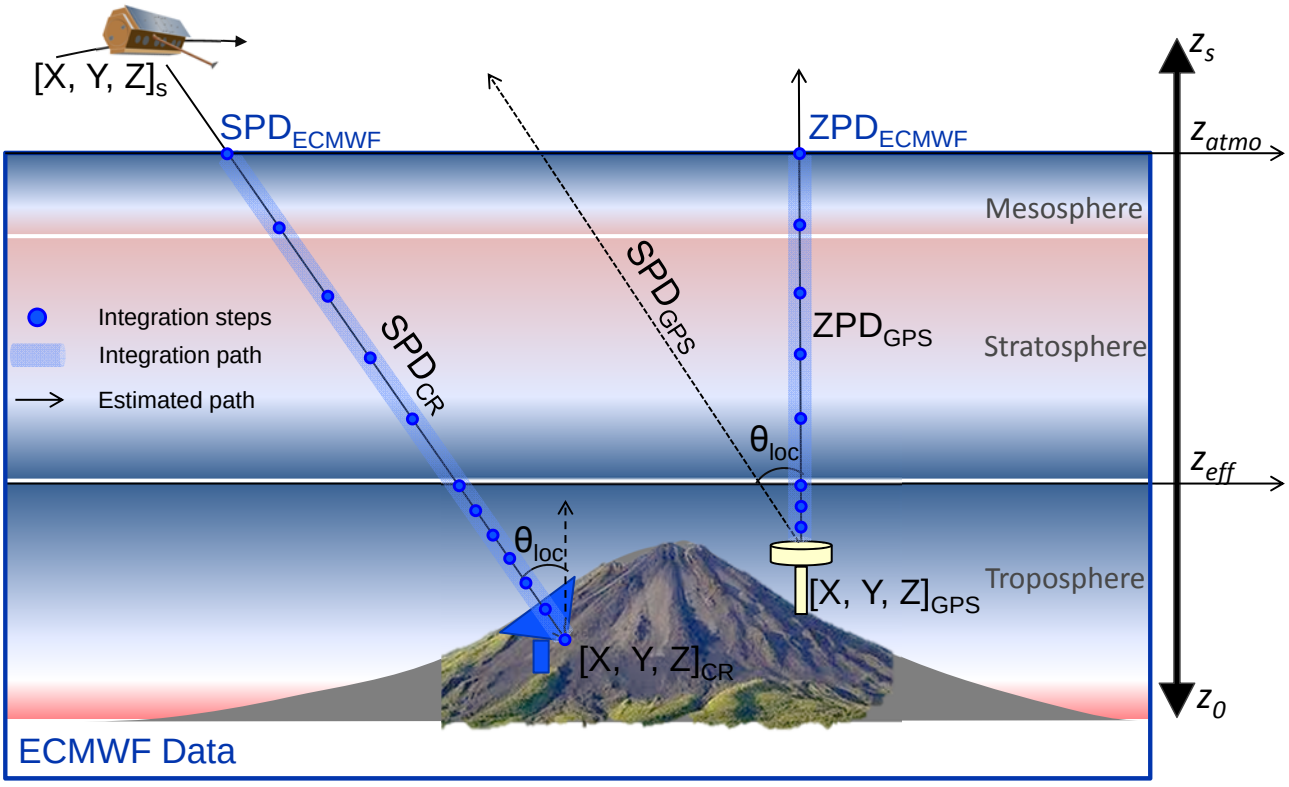

Fig. 45. Sketch of validation methods. Three methods are illustrated in the figure: (1) from GPS measurements estimated zenith path delay ZPD_{GPS} on the GPS coordinates $[X, Y, Z]_{GPS}$, the slant path delay SPD_{GPS} is projected with the local incidence angle θ_{loc}; (2) from CR measurements estimated slant path delay SPD_{CR} in slant range R from the CR coordinates $[X, Y, Z]_{CR}$ to the satellite orbit coordinates $[X, Y, Z]_s$; (3) integrated zenith path delay ZPD_{ECMWF} on $[X, Y, Z]_{GPS}$ and integrated slant path delay SPD_{ECMWF} for slant range R using ECMWF products, which covers the height range from z_S to z_{atmo}. z_{eff} is the effective height defined for separating two integration steps (see section 3.1.2.3).

In this section, we propose an approach to evaluate the ECMWF integrated atmospheric delay using GPS and CR observations. A sketch of the validation concept is depicted in *Fig. 45*. The reference atmospheric delays are Zenith Path Delay (ZPD) derived from GPS measurements (ZPD_{GPS}) and Slant range Path Delay (SPD) estimated from CR observations (SPD_{CR}) based on *Imaging Geodesy* described in section 2.4.2. For comparison, these delays are integrated both in zenith (ZPD_{ECMWF}) and in slant range (SPD_{ECMWF}) direction using ECMWF products. In section 3.3.1, ZPD_{ECMWF} from both ERA-Interim and operational data are compared to ZPD_{GPS} from IGS and Reference Frame Sub-Commission for Europe (EUREF). In section 3.3.2, the comparison of ERA-Interim in slant range SPD_{ECMWF} is performed with SPD_{CR} from the Wettzell experiment (section 2.2.6).

3.3.1 Validation with GPS ZPD

For precise positioning purposes, the atmospheric propagation delay is the noise which needs to be compensated a priori on the range measurements (Saastamoinen, 1972; Davis et al., 1985). On the other hand, GPS can provide us the integrated atmospheric delay independent from ECMWF assimilations (Bevis et al., 1992; Duan et al., 1995). Therefore, the Zenith Path Delay (ZPD) has been widely used for comparison of the integrated total delay and/or integrated delay of water vapor (ZWD) derived from radiosonde, microwave radiometer and NWP products (Tregoning et al., 1998; Vedel, 2000; Niell, 2000; Pacione et al., 2001; Bock et al., 2005; Steigenberger et al., 2007). The accuracy of GPS ZPD measurements is proven of about 5 mm, in which the uncertainty in GPS ZHD is less than 1 mm and in GPS ZWD is around 4 mm. GPS ZPD estimates from IGS and EUREF are selected as reference data (Bruyninx, 2004; Kruczyk, 2008; Dow et al., 2009). The information about selected stations and time periods is summarized in section 3.3.1.1. The validation approach for ERA-Interim is presented in section 3.3.1.2 and for operational data in section 3.3.1.3.

3.3.1.1 GPS reference data information: selected stations and periods

The selection of GPS stations is based on the distribution of EUREF network. Altogether, six permanent stations have been chosen. They are: Wettzell (WTZR) and Borkum (BORJ) in Germany, Kangerlussuaq (KELY) in Greenland, Maspalomas (MAS1), Roque de los Muchachos (LPAL) and Guimar (IZAN) in Spain, respectively. For long-term stability analysis, four years of ZPD data from WTZR station are collected from IGS and EUREF. A two-years analysis is carried out for KELY, MAS1 and BORJ. A short-term analysis prepared for both ECMWF products is performed for MAS1, LPAL and IZAN. The information of GPS data is summarized in Table 5. All GPS stations are available in the EPN network, whereas only three of them are in the IGS network (WTZR, KELY and MAS1). For these stations, IGS provides ZPD in 5 minutes interval. However, a hourly interval is allowed in EUREF for a accurate ZPD estimate.

Table 5. GPS reference data information about selected stations, station location, comparison period, GPS ZPD data and available ECMWF products.

Site	Location (Land)	Comparison Period	GPS Data	ECMWF Products
WTZR	Wettzell (DE)	Jan. 2008 - Dec. 2011	IGS & EUREF	ERA-Interim
KELY	Kangerlussuaq (GL)	Jan. 2008 - Dec. 2009	IGS & EUREF	ERA-Interim
BORJ	Borkum (DE)	Jan. 2008 - Dec. 2009	EUREF	ERA-Interim
MAS1	Maspalomas (ES)	Jan. 2008 - Dec. 2009	IGS & EUREF	ERA-Interim
MAS1	Maspalomas (ES)	Sep. 2011 - Feb. 2012	IGS & EUREF	ERA-Interim & Operational
LPAL	Roque de los Muchachos (ES)	Sep. 2011 - Feb. 2012	EUREF	ERA-Interim & Operational
IZAN	Guimar (ES)	Sep. 2011 - Feb. 2012	EUREF	ERA-Interim & Operational

3.3.1.2 Comparison with long-term GPS ZPD using ERA-Interim

The integration starts from coordinates of selected GPS stations until the top of the ERA-Interim data based on the direct integration method presented in section 3.1.2. Firstly, detailed information is given in section 3.3.1.2.1 for the comparison on WTZR station. Then, the statistical information of all long-term comparison is summarized in section 3.3.1.2.5.

3.3.1.2.1 Test site WTZR GPS station - ECMWF ZPD summary

A four-year time series of ECMWF ZPD is generated using 5844 ERA-Interim data fields on WTZR station from the beginning of 2008 until the end of 2011. In *Fig. 46*, the time series are depicted in 3 parts: the hydrostatic delay ZHD in *Fig. 46(a)*, the wet delay ZWD in *Fig. 46(b)* and the total delay ZPD in *Fig. 46(c)*. The spectrum analysis of ZPD time series is performed using fast Fourier transformation (Cong and Eineder, 2012). Two dominant frequencies explaining the yearly and daily variation are observed, as well as in ZWD time series. On the contrary, there is no comparable dominant frequency in ZHD time series.

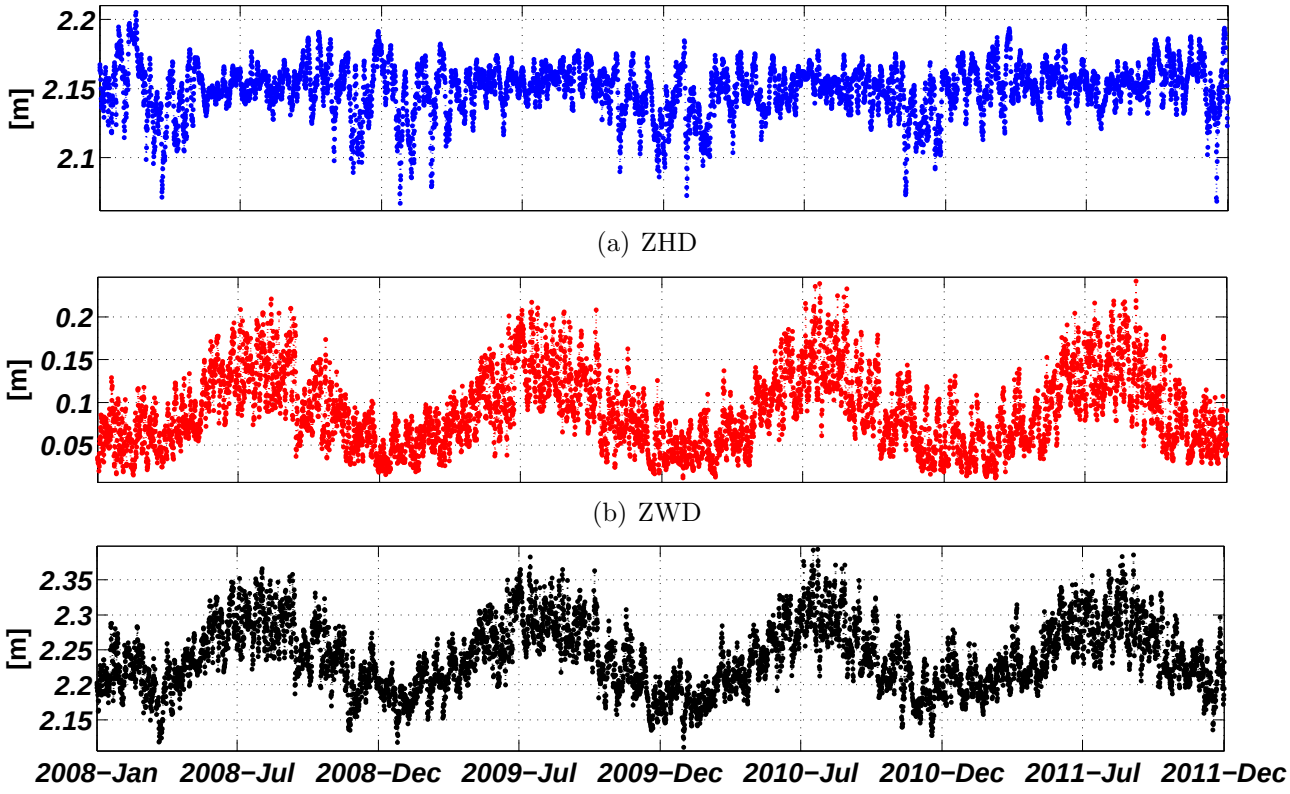

(a) ZHD

(b) ZWD

(c) ZPD

Fig. 46. Four-year time series of integrated atmospheric delays on WTZR station using ERA-Interim data from 1 January 2008 to 31 December 2011: (a) hydrostatic delay ZHD; (b) wet delay ZWD; (c) total delay ZPD.

ZPD mean value over four years is about 2238.8 mm, where ZHD contributes about 96% to the total delay and ZWD only 4%. ZPD standard deviation is about 48.2 mm. Main contribution is made by ZWD with a standard deviation of 44.1 mm. The variation of ZHD is less significant with a standard deviation of 18.3 mm. The maximum and minimum value of ZPDs are measured in 2010: they are 2393.4 mm on 23 July at 0 h and 2110.6 mm on 30 January at 6 h.

ERA-Interim analysis data are available at 0, 6, 12 and 18 h. Their mean and standard deviation values at each analysis time are listed in Table 6. ZHD remains stable (< 1 mm) at the different analysis times for both mean and standard deviation, where surface pressure P_S has a small variation during a day. Therefore, the variation observed in ZPD is mainly due to ZWD. For ZPD, the maximum of mean and standard deviation is observed at 0 h with 2240.7 mm and

49.2 mm, and the minimum is at 6 h with 2236.1 mm and 47.2 mm. Similarly, ZWD maximum is observed at 0 h, and its minimum at 6 h.

The diurnal variation of water vapor is induced by many processes (Dai et al., 2002), such as surface evapotranspiration (maximum around noon), atmospheric large-scale vertical motion, vertical mixing in the planetary boundary, atmospheric low-level moisture convergence and precipitation, etc. During a day, the variation of air temperature is highly correlated with the incoming solar radiation. As temperature increases after sunrises (around 6 h) so does the process of evaporation. Mean ZWD increases from 86.9 mm at 6 h to 90.7 mm at 18 h. A small difference of 0.4 mm is observed between mean ZWD at 0 h and at 18 h, which might be caused by diurnal cycle of the large-scale vertical motion. In addition, changes in the wind direction can induce changes in water vapor as well. The standard deviation of ZWD represents the yearly variation of ZWD at a given processing time. During summer, due to the diurnal cycle of large scale vertical motion, surface moisture convergence and precipitation occur more frequently from late evening to early morning (Dai et al., 1999). The maximum is observed at 0 h with 45.4 mm and the second maximum is at 12 h with 44.2 mm.

Table 6. Summary of hourly statistical analysis at 0, 6, 12 and 18 h over the four-year time series on WTZR station.

ERA-Interim	**ZPD [mm]**		**ZHD [mm]**		**ZWD [mm]**	
Analysis [h]	**M** [10]	**SD** [11]	**M**	**SD**	**M**	**SD**
0	2240.7	49.2	2149.6	18.3	91.1	45.4
6	2236.1	47.2	2149.2	18.5	86.9	42.8
12	2238.6	48.5	2149.6	18.4	89.0	44.2
18	2239.6	47.8	2149.0	18.1	90.7	43.8

In order to better understand of the influence of T on ZWD and its relation with e, surface vapor pressure (e_S) at each analysis time is separately depicted against surface temperature (T_S) in *Fig. 47*. The saturation vapor pressure (e_s), which is the amount of water vapor to make the air saturated at a given T, is plotted as upper boundary reference line (Wallace and Hobbs, 2006). Obviously, there is less water vapor in cold air (see *Fig. 47(b)*) than in warm air (see *Fig. 47(c)*). It is due to the fact that warm air has the potential to hold more water vapor. In the early morning (6 h), the air tends to be saturated, where e_S is close to e_s, whereas the air tends to be unsaturated at the midday (12 h). The vapor pressure increases rapidly after the sunrises (12 h) due to evaporation, after the sunsets decreasing slowly in the afternoon and midnight (18 h), and then decreasing rapidly until the early morning (6 h), whereas T decreases slowly from 18 h to 0 h. As a result, e_S tends to be saturated (see *Fig. 47(a)* and *47(d)*). The diurnal variation of T and e can explain the increase of both mean and standard deviation values of ZWD increases from 6 h to 12 h in Table 6.

Monthly and yearly analysis of the zenith delay time series are depicted in *Fig. 48*. Monthly mean values are presented in *Fig. 48(a)*. ZPD remains relatively stable from January to March, then it increases from April to July, afterwards decreases slowly until September, and finally drops dramatically to a minimum in December. Regarding the monthly standard deviation values of ZHD, ZWD and ZPD in *Fig. 48(b)*, a negative correlation between the ZHD and ZWD can be observed. In winter, water vapor pressure decreases with decreasing temperature (see *Fig. 47*). Pressure increases in winter, and then decreases again in summer. Therefore, from January to March, ZPD standard deviation is mainly caused by ZHD. From April to October, the ZPD standard deviation is mainly affected by water vapor variations (ZWD). As presented in *Fig. 47*, both the absolute water vapor pressure and its variance increase. The maximum variations occur in June and October, whereas January, February and March are relative stable

[10] The abbreviation **M** stands for mean value.
[11] The abbreviation **SD** stands for standard deviation.

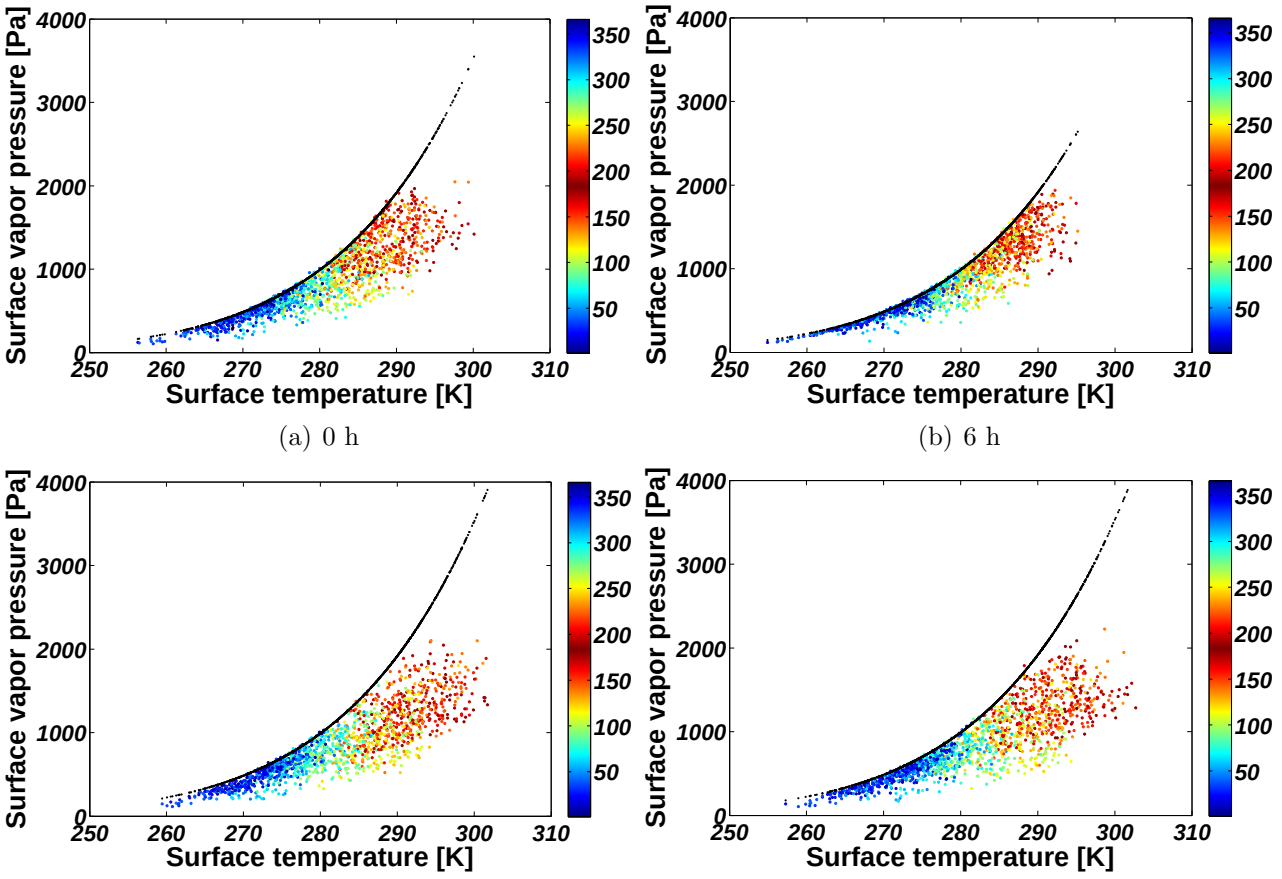

(a) 0 h (b) 6 h

(c) 12 h (d) 18 h

Fig. 47. The relationship between surface vapor pressure (e_S) and surface temperature (T_S) is illustrated for each analysis time and color-coded with the day of year. Black points present saturation vapor pressure (e_s) at the given T_S.

months. According to mean values by ZPD yearly analysis (see *Fig. 48(b)*), the difference between the minimum in 2010 and the maximum 2011 is about 12.1 mm. Furthermore, the maximum variation is observed in 2010.

3.3.1.2.2 Test site WTZR GPS station - Effect of height error in atmospheric delays

The atmospheric delay has a strong correlation in vertical with the height. The height inaccuracy effects thus directly the accurateness of atmospheric delay. In order to quantify this effect, two months of ERA-Interim data on WTZR are selected from the four-year time series: firstly for a winter month with minimum water vapor content and variation; then a summer month with maximum water vapor content and variation. Therefore, the monthly mean and standard deviation of ZWD are used as indicators of the water vapor content. Height errors varying from -130 to 2000 m are added additionally on the *real* height provided by the WTZR station. Then *pseudo* delays are integrated for each pseudo height, and residuals are computed according to the *real* delays in section 3.3.1.2.1. At the end, monthly mean residual are calculated.

January 2009 with a mean ZWD of 39.9 mm and standard deviation of 16.3 mm is selected for the winter month; and August 2011 with a mean ZWD of 145.3 mm and standard deviation of 37.9 mm is selected for the summer month. Residuals between the *pseudo* delays and the *real* delays are evaluated individually for ZHD, ZWD and ZPD and depicted in *Fig. 49*. In general, ZPD residuals in summer are larger than in winter. Assuming a linear relation between height errors and the residuals, the ZPD residual in summer is about 0.27 mm/m in average, in winter 0.25 mm/m. In winter, the impact of ZWD reduced to about 0.01 mm/m, thus the rest delay of 0.24 mm/m is dominated by ZHD. In summer, the influence of ZWD is four times

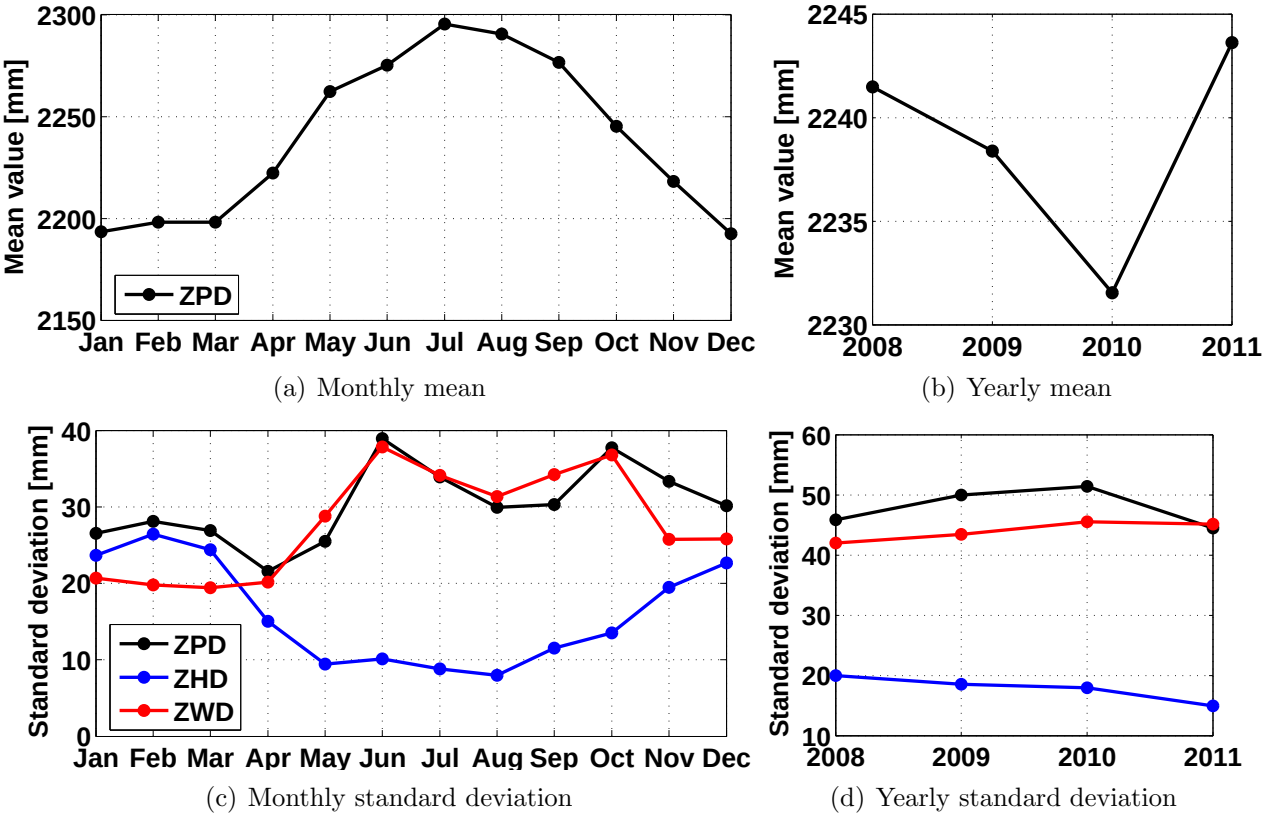

(a) Monthly mean (b) Yearly mean

(c) Monthly standard deviation (d) Yearly standard deviation

Fig. 48. Statistic analysis of integrated atmospheric delays (ZPD, ZHD and ZWD) on WTZR station. (a) ZPD monthly mean value; (b) ZPD yearly mean value; (c) monthly standard deviation; (d) yearly standard deviation.

larger than in winter, which is about 0.04 mm/m in average; and the ZHD decreases slightly to 0.23 mm/m. The maximum ZPD residual in summer reaches 0.29 mm/m due to the increasing water vapor content, and 0.26 mm/m in winter.

3.3.1.2.3 Test site WTZR GPS station - Fitting with exponential function

The linear relation between height and delay is only valid within 100 m height difference (see *Fig. 49(c)*). Therefore, an empirical exponential function widely used is applied instead (see section 2.2.4.3.5), which can be written as:

$$ZPD(z) = ZPD(z_S)\exp\left(-\frac{(z - z_S)}{h_{atmo}}\right), \tag{59}$$

where ZPD(z) is the ZPD at a given height z; ZPD(z_S) is the ZPD at the surface height z_S; h_{atmo} is the thickness of the atmosphere. The thickness parameter for a given time is unknown. As a consequence an empirical value of 6000 m is used (Fritz et al., 2008; Breit et al., 2010). Assuming this value and given a known ZPD at a GPS station whose height is known, the ZPD at a required height near the GPS station can be approximated according to *eq. (59)*.

Unfortunately, the thickness of the atmosphere h_{atmo} changes with location and time. This parameter has a major impact in the accuracy of the exponential model estimation. In order to understand the effect of $h_{atmo}$the following analysis has been performed. Firstly, the monthly mean of *pseudo* ZPDs integrated at height values $z_{WTZR} + \Delta z$, where z_{WTZR} is the elevation of the WTZR station and $\Delta z \in [-130, 2000]$ m, has been calculated (see section 3.3.1.2.2). Secondly, given the delay at the WTZR station, the height-dependent delay curve has been fitted according to *eq. (59)*, obtaining thus an optimal atmospheric thickness. The accuracy of the estimation based on the exponential model for the empirical and the optimal atmospheric thickness has been evaluated. The results are depicted in *Fig. 50*.

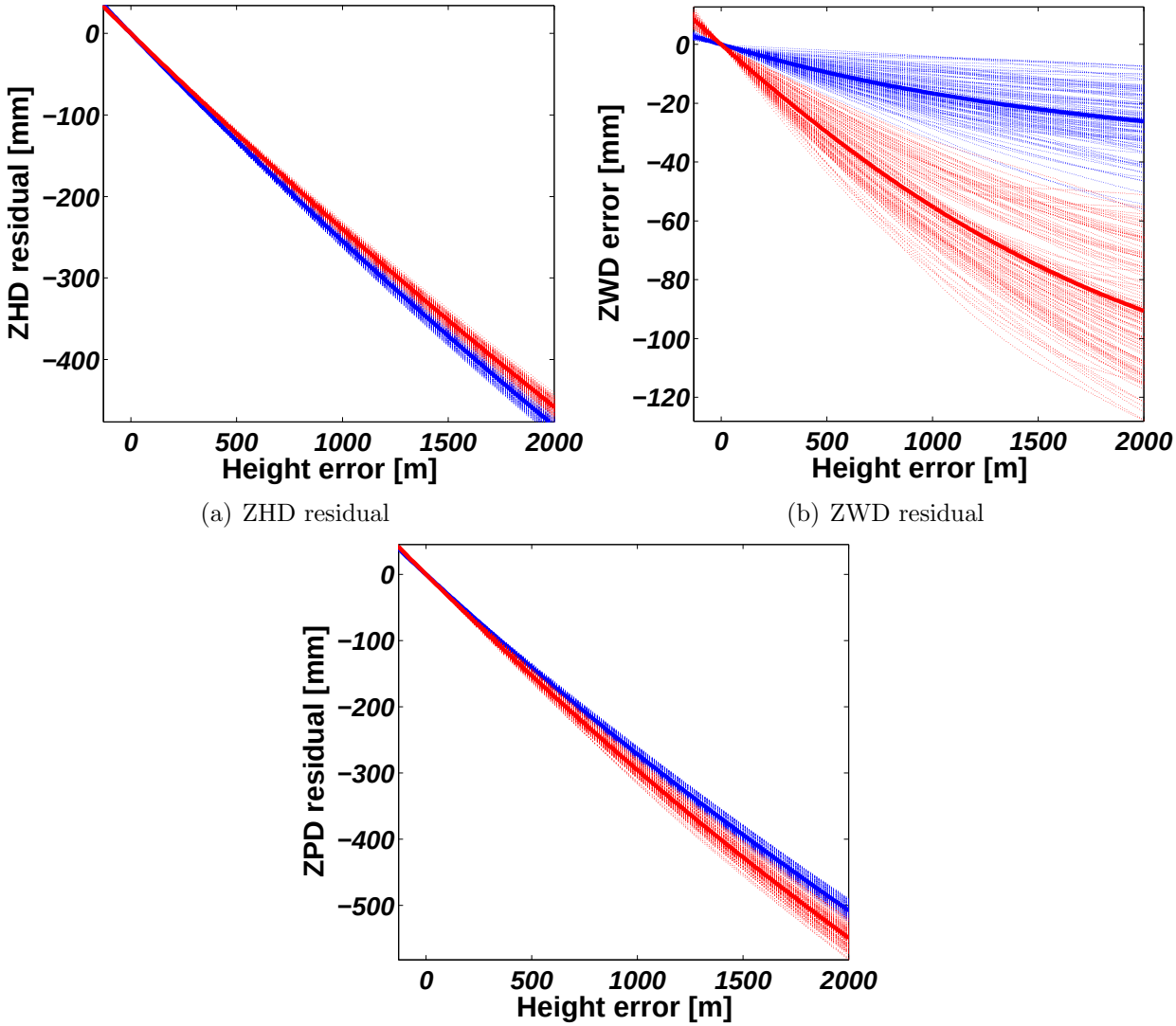

(a) ZHD residual

(b) ZWD residual

(c) ZPD residual

Fig. 49. Simulation-based atmospheric delay residuals induced by a height error evaluated on two months on WTZR station: January-2009 in blue color and August-2011 in red color, which has the minimum and the maximum mean and standard deviation of ZWD. The height error is presented in x-axis from −130 to 2000 m. The residuals according to the *real* delays are depicted in: (a) for ZHD residual; (b) for ZWD residual; (c) for ZPD residual. Their monthly-mean residuals at each height error are plotted with bold lines.

For monthly mean ZPD in January 2009 in *Fig. 50(a)*, the best-fitted atmospheric thickness h_{atmo} is 7560 m with the standard deviation of the fitting error of 0.5 mm and the maximum residual of 1 mm. In general, the ZPD residual increases with increasing height difference to the GPS station. The maximum absolute ZPD residual reaches 112 mm at $\Delta z = 2000$ m and the standard deviation is about 35 mm. For monthly mean ZPD in August 2011 in *Fig. 50(b)*, the optimal h_{atmo} decreases by 260 to 7300 m. The standard deviation of ZPD residuals increases slightly to 0.8 mm, and the maximum residual increases to 2.2 mm as well. However, the maximum contrast ZPD residual with empirical h_{atmo} decreases about 9 to 103 mm at $\Delta z = 2000$ m that is about 0.5 mm/m. Moreover, the standard deviation reduces about 3 to 32 mm. In conclusion, the atmospheric thickness h_{atmo} is an important factor for this usage. The accuracy varies from the optimal h_{atmo} of less than 1 mm to decimeter range by using the empirical thickness (6000 m). Therefore, it is essential to determine an optimal h_{atmo}, which depends on location and time.

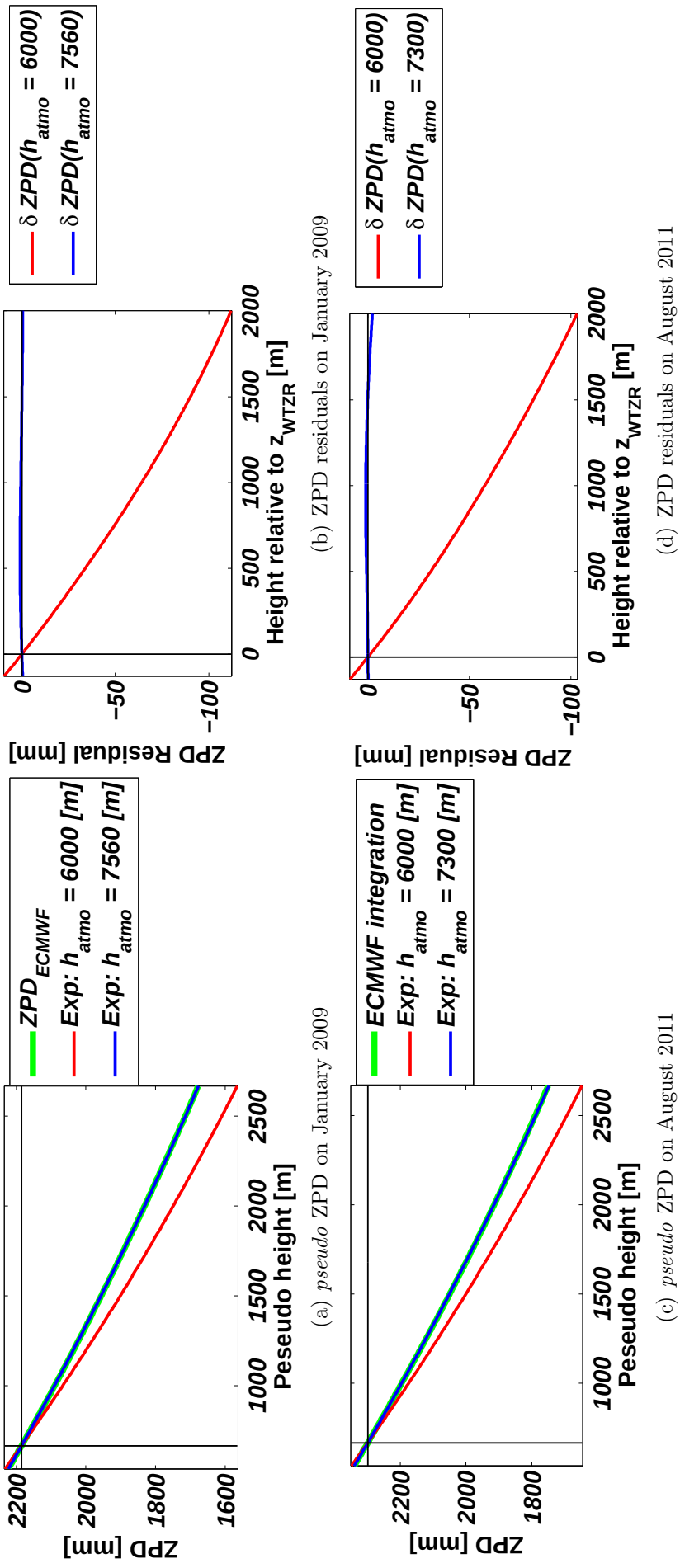

(a) *pseudo* ZPD on January 2009

(b) ZPD residuals on January 2009

(c) *pseudo* ZPD on August 2011

(d) ZPD residuals on August 2011

Fig. 50. Fitting the monthly mean of *pseudo* ZPDs with the empirical and the optimal thickness of the atmosphere (h_{atmo}) on WTZR station for: (a) January 2009 and (c) August 2011. The station height z_{WTZR} is about 666 m above the ellipsoid. Their ZPD residuals (δZPD) are presented in (b) and (d), respectively. The monthly mean ZPD is depicted in a bold green line. ZPD with empirical h_{atmo} = 6000 m is illustrated in red line, and ZPD with optimal h_{atmo} is illustrated in blue line. The thin black lines are reference lines for the real WTZR ZPD station.

3.3.1.2.4 Test site WTZR GPS station - Validation using GPS ZPD

For validation, two GPS ZPD time series are retrieved from IGS and EUREF in the same period at each ECMWF analysis time. IGS ZPD at WTZR is available almost daily from 00:00 with a 5 min interval to 23:45 from 1 January 2008 to 16 April 2011, where 66 ZPDs are not available. From 17 April 2011, a large gap of 260 days until 31 December 2011 exists. In order to estimate the GPS ZPD during the gap, an additional GPS station WTZA close to WTZR is used in this period instead. The geometric distance between two station is about 3 meters, and the height difference is less than 0.1 m that can induce a delay error of less than 0.1 mm (see section 3.3.1.2.2). Therefore, we assume that the ZPD on WTZR station can be replaced by the ZPD estimates on WTZA station. According to the given standard deviation of GPS ZPD estimates, a threshold of 5 mm is defined (Bock et al., 2005). Consequently, there are 78 estimates not available in total. The hourly EUREF data start at 00:30. Thus the nearest GPS ZPD is determined as the reference ZPD. During the whole period, there are 55 entries without comparable ZPD estimates. The ECMWF ZPD time series have been presented and analyzed in section 3.3.1.2.1.

From the WTZR GPS station three time series are depicted in *Fig. 51*. ZPD_{ECMWF} integrations are illustrated with black circles and connected with black dashed lines in *Fig. 51(a)*. ZPD_{GPS} time series derived from EUREF (ZPD_{EUREF}) are depicted with blue circles, and ZPD_{GPS} time series from IGS (ZPD_{IGS}) are plotted with cyan circles and on WTZA with light blue squares. The differences between ZPD_{ECMWF} time series and two ZPD_{GPS} time series, considered as residuals, are presented in *Fig. 51(b)*, and their histograms are generated accordingly in *Fig. 51(c)* with correspondent colors. X-axis represents the comparison time period, which starts from 1 January 2008 and ends on 31 December 2011.

With regard to *Fig. 51(a)*, it is obvious that the ZPD_{ECMWF} time series has a very good agreement with both ZPD_{GPS} time series. The overall correlation of 98% is observed among them. In order to evaluate the accuracy of ZPD_{ECMWF}, we compute the residuals according to the ZPD_{EUREF} and ZPD_{IGS} time series, which will be denoted as $\delta\mathrm{ZPD}_{ECMWF,EUREF}$ and $\delta\mathrm{ZPD}_{ECMWF,IGS}$, respectively. The mean offsets of ZPD_{ECMWF} over the entire time series are 0.6 mm referring to ZPD_{EUREF} and 2.4 mm according to ZPD_{IGS} (see Table 7). Furthermore, their standard deviations are about 1 cm, 9.9 mm for $\delta\mathrm{ZPD}_{ECMWF,EUREF}$ and 10.1 mm for $\delta\mathrm{ZPD}_{ECMWF,IGS}$. In other words, the typical ECMWF data accuracy in temperate and cool region with frequent rainfall is about 1 cm. More accuracy analyses of ECMWF data are performed in section 3.3.1.2.5.

Furthermore, the hourly, monthly and yearly statistical analyses of the two residuals have been performed and summarized in Table 7 and in *Fig. 52*, similar to section 3.3.1.2.1. In Table 7, hourly mean and standard deviation are calculated at each ECMWF analysis time. The standard deviation of $\delta\mathrm{ZPD}_{ECMWF,EUREF}$ varies from minimum 9.7 mm at 6 h to maximum 10.2 at 0 h. Similarly, the maximum standard deviation of $\delta\mathrm{ZPD}_{ECMWF,IGS}$ is also observed at 0 h with 10.4 mm. However the minimum locates at 12 h and 18 h with 9.9 mm. The large discrepancy appears at 0 h for both GPS ZPD time series which may be induced by the increasing ZWD variation presented in Table 6.

Table 7. Summary of statistical analysis on WTZR station over entire residual time series and hourly statistical analysis at 0, 6, 12 and 18 h.

GPS	Total Diff. [mm]		Hourly Analysis[mm]							
			00		06		12		18	
Service	M [10]	SD [11]	M	SD	M	SD	M	SD	M	SD
EUREF	0.6	9.9	1.9	10.2	−0.5	9.7	−0.1	9.8	1.0	9.9
IGS	2.4	10.1	3.7	10.4	1.3	10.1	1.6	9.9	3.0	9.9

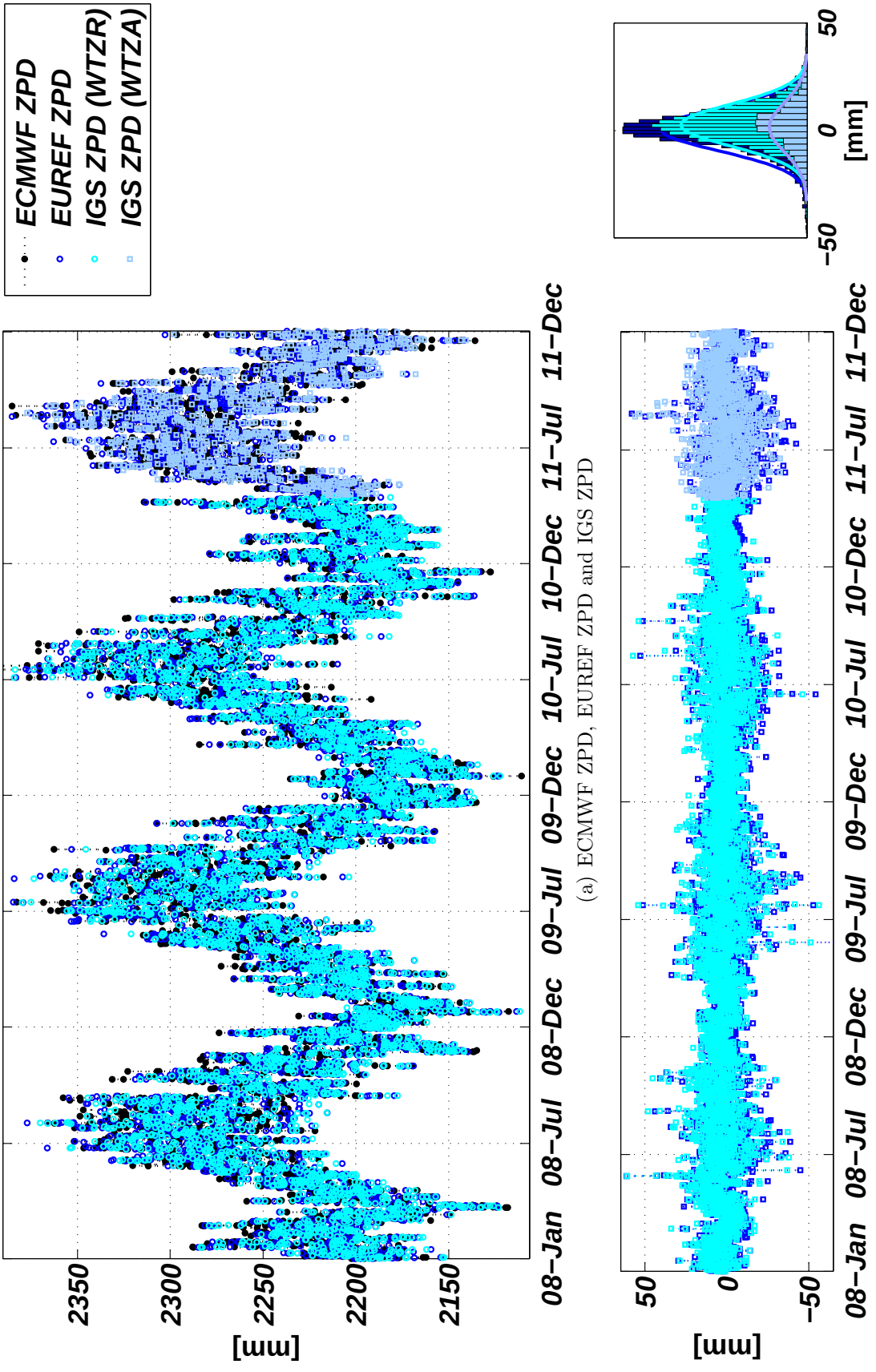

(a) ECMWF ZPD, EUREF ZPD and IGS ZPD

(b) ZPD differences

(c) Histogram

Fig. 51. Validation of ECMWF ZPD with GPS ZPD derived from EUREF and IGS services on the WTZR station. In total, 5844 ECMWF entries from 1 January 2008 to 31 December 2011 are used for validation. In (a), three time series are depicted: ZPD_{ECMWF} integrations illustrated with black circles and connected with black dashed lines; ZPD_{GPS} time series derived from EUREF (ZPD_{EUREF}) depicted with blue circles; ZPD_{GPS} time series from IGS (ZPD_{IGS}) plotted with cyan circles on WTZR station and with light blue squares on WTZA station. The differences between ZPD_{ECMWF} and ZPD_{EUREF}, ZPD_{ECMWF} and ZPD_{IGS} are presented in (b). Their histograms are generated accordingly in (c).

The results of monthly and yearly analysis are depicted in *Fig. 52*. In *Fig. 52(a)*, the monthly mean reaches 4.7 mm for $\delta\text{ZPD}_{ECMWF,EUREF}$ and 6.2 mm for $\delta\text{ZPD}_{ECMWF,IGS}$ both on April, where the minimum monthly mean is observed on August for $\delta\text{ZPD}_{ECMWF,EUREF}$ and on March for $\delta\text{ZPD}_{ECMWF,IGS}$. The monthly standard deviation can be interpreted as an indicator the ECMWF quality on a certain month. Generally, the standard deviation is lower in winter than in summer, which is correlated with ZPD presented in *Fig. 48(a)* mainly due to the variation of ZWD. According to *Fig. 52(c)*, four months (January, February, March and December) have lower standard deviations, which are less equal 7 mm; April and October are between 8 to 10 mm; the rest is above 10 mm. The peaks arrive above 13 mm in July and August.

In *Fig. 52(b)*, the yearly mean of both time series decrease linearly from 2008 to 2010. Afterwards the mean value of $\delta\text{ZPD}_{ECMWF,EUREF}$ has a further decrease in 2011, whereas the mean value of $\delta\text{ZPD}_{ECMWF,EUREF}$ has a slightly increase in 2011. The yearly standard deviation, presented in *Fig. 52(d)*, is correlated with yearly mean ZPD shown in *Fig. 48(d)*. The minimum standard deviation of about 9.2 mm is derived from 2010.

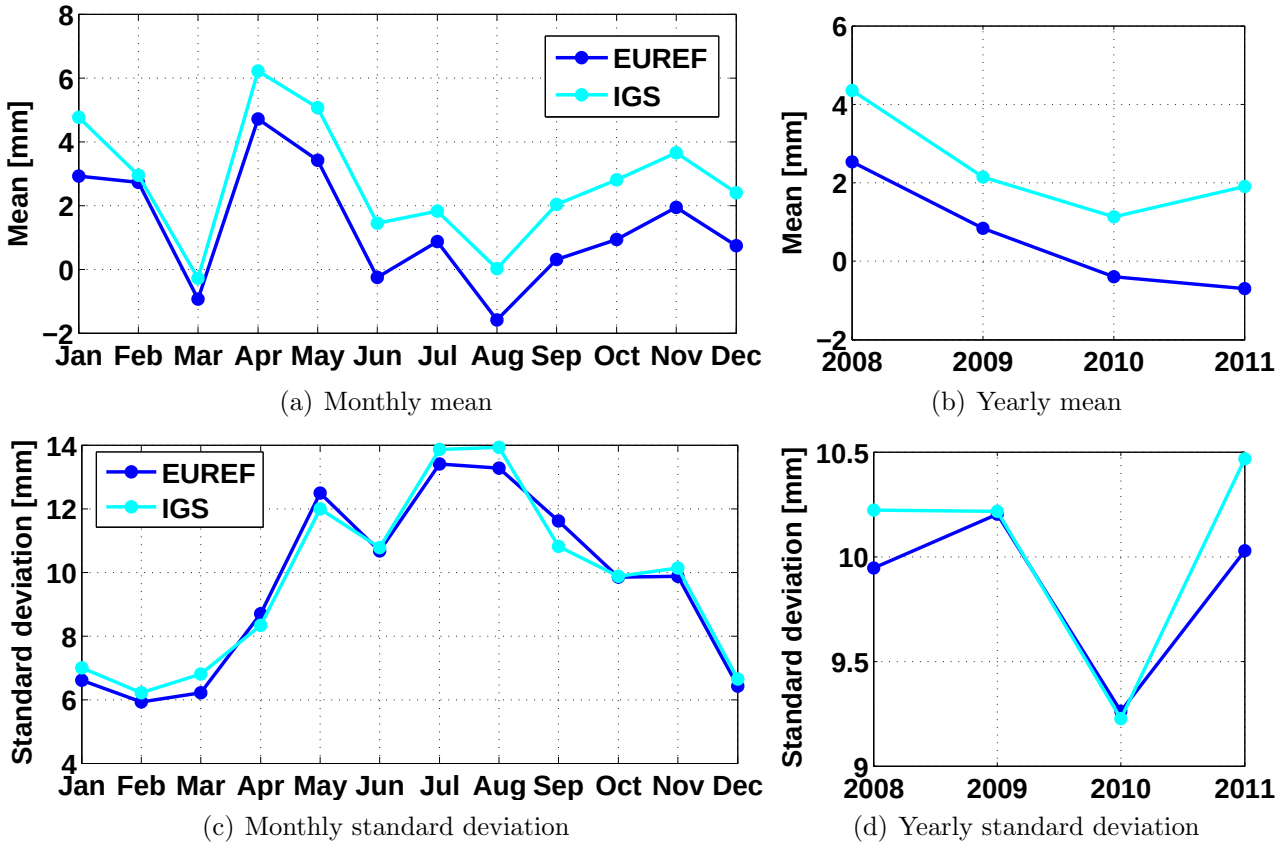

(a) Monthly mean

(b) Yearly mean

(c) Monthly standard deviation

(d) Yearly standard deviation

Fig. 52. Monthly and yearly statistical analysis based on the two series of residuals on WTZR station: (a) monthly mean value; (b) yearly mean value; (c) monthly standard deviation; (d) yearly standard deviation.

3.3.1.2.5 Summary of validation tests using three GPS stations with 2-years time series

Apart from the GPS station in Wettzell, the validation is carried out for another three GPS stations which are selected in different meteorological conditions (see Table 5): first, the KELY station locates in western Greenland (Kangerlussuaq); second, the BORJ station is installed on the Borkum Island in North sea; last, the MAS1 station locates in Maspalomas, Canary Islands. They are characterized by subarctic, oceanic and subtropical climate, respectively.

The period is defined from 1 January 2008 0 h to 31 December 2009 18 h. In total, 2924 ECMWF Interim data entries have been collected. Based on the processing steps described in section 3.1, three ZPD time series (ZPD_{ECMWF}) have been prepared for three GPS stations. For validation,

the correspondent GPS ZPD time series have been gathered from EUREF (ZPD_{EUREF}) and IGS (ZPD_{IGS}) according to Table 5. Unfortunately, GPS ZPDs are not always available during this period. The number of unavailable data sets are listed in Table 8 in days. The validation procedure, described in section 3.3.1.2.4, has been carried out for each GPS station. Similar to *Fig. 51*, the comparison plots of entire time series are presented separately for each GPS station in Appendix H. Obviously, all ZPD time series have a clear annual period which is highly correlated with the annual temperature variation (Wikipedia, 2013a,b,c).

The total and the hourly statistics are summarized in Table 8. Analyzing the total statistic, the smallest standard deviation is observed on KELY station. They are 7.4 mm for $\delta ZPD_{ECMWF,EUREF}$ and 6.8 mm for $\delta ZPD_{ECMWF,IGS}$. In contrary, the largest standard deviation is observed on the MAS1 station. They are 13.4 mm for $\delta ZPD_{ECMWF,EUREF}$ and 13.2 mm for $\delta ZPD_{ECMWF,IGS}$ which is almost twice of the KELY station. Since the average temperature of the KELY station, which is dominated by subarctic climate, is below zero (Wikipedia, 2013b), the atmosphere is dry and contains less water vapor. The MAS1 station is dominated by subtropical climate, and the average temperature is above 20 ° C. Therefore, the standard deviation of ZPD_{ECMWF} is about 37 mm compared to the KELY station 43 mm and the BORJ station 50 mm. The MAS1 station is installed the south coast, which might be effected by evaporation of sea water.

On the KELY station, more than 50% of ZPD_{IGS} and more than 40% of ZPD_{EUREF} are not available. Therefore, the statistical analysis based on these data sets is not completed. Further discussion is concentrated on the BORJ and MAS1 stations. Based on the hourly statistical analysis of $\delta ZPD_{ECMWF,EUREF}$ in Table 8, the maximum standard deviation is observed at 0 h on the BORJ station, and the minimum at 06 h; on the MAS1 station the maximum is observed at 18 h, and the minimum at 12 h. Moreover, the analysis based on ZPD_{IGS} on the MAS1 station is slightly different: the maximum standard deviation is at 18 h, but the minimum observed at 6 h with 11.9 mm is 0.1 mm smaller than the standard deviation at 12 h.

Table 8. Statistical analysis of residuals in time series started from 1 January 2008 0 h to 31 December 2009 18 h on three GPS stations, namely, KELY, MAS1 and BORJ. Two GPS services are available, namely, EUREF and IGS. The GPS data availability is listed. The mean value and the standard deviation are summarized for total time series as well as the hourly analysis at 0, 6, 12 and 18 h.

GPS			**Total**		**Hourly Analysis[mm]**							
Name	**Service**	**Gap**	**Diff. [mm]**		**00**		**06**		**12**		**18**	
		[day]	**M**	**SD**	**M**	**SD**	**M**	**SD**	**M**	**SD**	**M**	**SD**
KELY	EUREF	306.5	2.8	7.4	2.7	9.5	2.1	6.4	3.5	6.2	2.9	7.2
	IGS	433.75	2.7	6.8	2.9	6.9	1.6	6.6	2.7	6.8	3.5	6.9
MAS1	EUREF	12	11.7	13.4	13.2	12.9	17.3	12.3	9.6	12.1	6.8	14.0
	IGS	19	11.6	13.2	12.1	13.1	16.4	11.9	11.0	12.0	6.9	13.8
BORJ	EUREF	12.75	10.0	8.6	10.9	9.2	9.4	8.2	9.7	8.5	9.9	8.6
	IGS	-	-	-	-	-	-	-	-	-	-	-

3.3.1.3 Validation of OP data using 7-months time series

ECMWF operational data (OP) described in section 3.2.2 provides a better horizontal and vertical resolution compared to ERA-Interim (see Table 3). In order to evaluate the accuracy of OP data, a 7-months time series is provided by the Institute of Atmospheric Physics (DLR) which starts on 1 September 2011 and ends on 29 February 2012. The spatial coverage spans over the region of Canary Islands in Spain (see *Fig. 44*). Three permanent GPS stations from EUREF have been selected (see Table 5). They are installed in three Islands at different heights: firstly, the MAS1 station on Gran Canaria with the ellipsoidal height of about 193 m; secondly, the LPAL station on La Palma with the ellipsoidal height of about 2207 m; thirdly, the IZAN station on Tenerife with the ellipsoidal height of about 2417 m.

Altogether, 728 entries from OP and ERA-Interim have been collected. six ZPD time series (ZPD_{OP} and $ZPD_{Interim}$) have been prepared for three GPS stations according to the processing steps described in section 3.1. For comparison, the GPS ZPD products during the period have been collected from EUREF and IGS (see Table 5). Similar to section 3.3.1.2.5, the statistical analysis has been carried out based on the residual ZPD time series ($\delta ZPD_{ECMWF,EUREF}$ and $\delta ZPD_{ECMWF,IGS}$) and summarized in Table 9.

Table 9. Statistic analysis of residual in time series started from 1 September 2011 at 0 h to 29 February 2012 at 18 h on three GPS stations, namely, MAS1,LPAL and IZAN. Two ECMWF data sets are available during this period: ERA-Interim (Interim) and operation data (OP). Two GPS services are available for MAS1, namely, EUREF and IGS. The mean value and the standard deviation are summarized for total time series as well as the hourly analysis at 0, 6, 12 and 18 h.

GPS		**ECMWF**	**Total**		**Hourly Analysis[mm]**							
Name	**Service**		**Diff. [mm]**		**00**		**06**		**12**		**18**	
		data	**M**	**SD**	**M**	**SD**	**M**	**SD**	**M**	**SD**	**M**	**SD**
MAS1	EUREF	Interim	16.0	12.5	16.5	11.7	21.6	11.3	14.9	11.8	10.8	12.9
		OP	4.1	11.1	4.0	11.9	5.5	10.4	4.5	10.1	2.5	11.8
	IGS	Interim	16.7	13.1	17.6	12.7	19.8	12.6	18.1	12.3	11.3	13.3
		OP	4.8	11.5	5.1	12.3	3.7	10.8	7.7	10.5	2.9	11.8
LPAL	EUREF	Interim	−1.3	7.7	−1.6	8.0	−0.4	7.7	−2.2	7.7	−1.0	7.4
		OP	−1.0	6.1	−1.2	6.9	−0.8	5.9	−1.0	5.4	−1.2	6.1
IZAN	EUREF	Interim	6.2	5.5	6.1	5.7	6.4	6.2	6.2	4.9	6.2	4.9
		OP	2.3	5.7	2.4	6.1	3.6	5.1	1.3	5.6	1.9	5.9

Due to different altitudes, the mean values of ZPD_{OP} and $ZPD_{Interim}$ time series on three stations vary from 1789.4 mm on the IZAN station by using OP to 2407.0 mm on the MAS1 station by using ERA-Interim. Moreover, the standard deviations are effected by different altitudes as well, since the minimum standard deviation is observed on the IZAN station by using OP with about 25.1 mm and the maximum on the MAS1 station by using ERA-Interim with about 38.2 mm. Nevertheless, the mean value on the LPAL station are 1839.2 mm by using ERA-Interim and 1837.6 mm by using OP, and the standard deviation are 28.3 mm and 25.6 mm, respectively. They are similar with the values on the IZAN station, since the height difference is smaller.

According to the statistical analysis using the entire time series in Table 9, the standard deviations from both OP and ERA-Interim on three GPS stations are similar with the maximum discrepancy of 1.6 mm on the MAS1 station with $\delta ZPD_{ECMWF,IGS}$. With the exception of the IZAN station, the ZPDs integrated using OP data have a better agreement with GPS ZPDs in comparison with the ZPDs integrated using ERA-Interim data. Due to the higher altitudes on the LPAL and IZAN stations, the lower part of troposphere is not integrated into ZPD, where the turbulent mixing mostly occurs. Therefore, the standard deviations of $\delta ZPD_{OP,EUREF}$ are around 6 mm which is about 5 mm smaller than on MAS1.

Hourly statistical analysis has been carried out at each analysis time defined in ECMWF at 0, 6, 12 and 18 h. Unlike to the hourly analysis summarized in section 3.3.1.2.4 and 3.3.1.2.5, the hourly analysis differs from station to station. However, the standard deviations at 6 and 12 h are usually more stable in comparison with the standard deviations at 0 and 18 h .

Large mean offsets have been observed by using ERA-Interim data on the MAS1 and IZAN stations. They are about 16 mm and 6 mm, respectively. In contrary, the offsets are smaller by using OP data, where they are about 4 mm on MAS1 and 2 mm IZAN. It means that the ERA-Interim data have the tendency to overestimate the ZPD. One assumption is that the humidity is overestimated in ECMWF model as reported in Schäfler et al. (2011).

3.3.1.4 Summary and conclusion

The validation with GPS ZPDs presented in section 3.3.1.2.4, 3.3.1.2.5 and 3.3.1.3 indicates that the accuracy of the ERA-Interim data is in the millimeter to centimeter range. This accuracy is dependent on factors such as location, altitude, weather condition and observation time, which varies from 6 mm (subarctic climate) to 13 mm (subtropical climate). A long-term stability has been proven in section 3.3.1.2.4 and 3.3.1.2.5 with a four-years time series and three two-years time series. The comparison of OP data with ERA-Interim performs an improvement of approximately 1.5 mm on the MAS1 and LPAL stations.

3.3.2 Validation with CR SPD in Wettzell

The atmospheric delay in slant range (SPD) has an effect in the meter-range. In order to achieve the centimeter-level geolocalization accuracy in range, it should be effectively compensated by means of external atmospheric delay measurements, such as GPS ZPD (see section 2.2.6). Unfortunately, the GPS ZPD is available only sparsely in space with limited number of GPS stations which are managed and provided by GPS services, for instance EUREF and IGS. Furthermore, GPS ZPD is projected into slant range (Rng TD) by using the local incidence angle under the assumption of an isotropic atmosphere. In contrary, NWP products are globally available which can be used to integrate SPD directly along the propagation ray from the CR to the satellite (see section 3.1.2.3). In this case, the ERA-Interim reanalysis data are used for integration (see section 3.2.1).

In this section, the validation of ERA-Interim data is carried out with respect of CR SPDs in the WTZR test site (see section 2.2.6). Sophisticated geodynamic and ionospheric corrections on range measurements are listed in Table B.1 in Appendix B.

3.3.2.1 Comparison with CR SPD using ERA-Interim

For validation, 27 ERA-Interim data entries have been collected close to the acquisition time, prepared at the CR coordinates and have been integrated directly along the slant range (see section 3.1.2). Instead of GPS TD, ECMWF SPDs have been applied to compensate TD (see Table I.1 in Appendix I). By comparing the standard deviation in Table B.1, a decline of 7.7 mm in accuracy has been observed where the standard deviation increases from 9.8 to 17.5 mm. Additionally, small difference of 2.9 mm is observed by mean value.

Similar to *Fig. 23*, in *Fig. 53* the ECMWF SPD has been used to replace the GPS TD. In *Fig. 53(a)*, ECMWF SPD and SAR TD show a clear correlation with a correlation coefficient of 95.4%. As well as in *Fig. 53(b)*, a correlation coefficient of 95.0% is observed between modeled SET and the range residuals (SAR SET using ECMWF SPD). However, two outliers have been detected in both figures on 22 August and 16 October 2012 according to the residuals presented in Table I. They are caused by the large discrepancy between ECMWF SPD and GPS TD: -38.9 mm on 22 August and 30.6 mm on 16 October 2012. The average standard deviation σ on the WTZR station in zenith is about 14.0 mm in August and 10.0 mm in October (see *Fig. 52(c)*) which is about 16.9 mm and 12.1 mm in slant direction. Obviously, the two outliers still fall into the $3 \cdot \sigma$ region. Excluding these two outliers, both correlation coefficients can be improved to 97.4%. As well as, the standard deviation can be improved from 17.5 to 12.6 mm.

3.3.2.2 Summary and conclusion

ERA-Interim data are validated with respect to SAR range measurements. A good overall agreement has been observed with a correlation of over 95.0%. The standard deviation of the range residuals increases about from 9.8 to 17.5 mm by replacing the Rng TD with ECMWF SPD. Since ERA-Interim data are available only four times per day, there is up

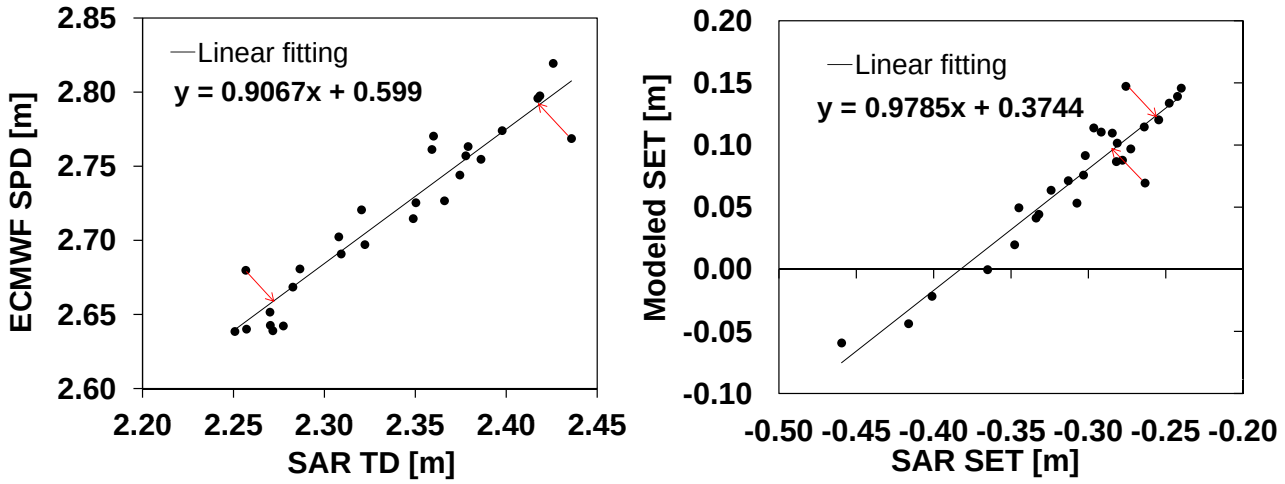

(a) (b)

Fig. 53. Correlation analysis of absolute localization residuals: (a) correlation between the range delays estimated by using ERA-Interim data (ECMWF SPD) and the range residuals (SAR TD) which are derived from the range delay values measured after corrections of SET, ID, OTL, APL and CD; (b) correlation between the range delays modeled SET and the range residuals (SAR SET) which are derived from the range delay values measured after corrections of ECMWF SPD, ID, OTL, APL and CD. A linear fitting has been carried out for each correlation plot and the fitted function is visualized. Two outliers have been detected according to the distance (depicted with red line) from the point to the fitted line.

to 3 hours difference between the acquisition and the analysis time. In case of stormy weather, the atmospheric delay could be biased, such as the outliers on 22 August and 16 October 2012. Nevertheless the two outliers still fall into the the $3 \cdot \sigma$ range. On the other hand, ERA-Interim provides global spatial coverage and temporal coverage from 1979 to near current (with 3 months delay) in case no GPS station is available.

3.4 Atmospheric delay effect on SAR interferometry - its formation and effect in volcanic areas

The absolute accuracy of ECMWF data has been validated against GPS and CR measurements in the last section 3.3. Before applying this atmospheric delay correction to SAR interferometry, it is important to understand, identify and quantify the effect of the atmospheric delay in the interferometric phase.

Basically, the differential atmospheric phase screen on one interferogram ϕ_{atmo} is induced by the differential atmospheric delay in range (ΔR_{atmo}) due to the different meteorological conditions between two acquisitions (see *eq. (28)*). Furthermore, phase measurements in InSAR are always relative, which means that we are actually interested in the relative differential atmospheric delay in range between two pixels. In this case, the atmospheric phase on the reference point acts as a constant phase offset, and will be cancelled out by arc measurements. Therefore, the atmospheric phase between two points x and y in an arc measurement is hence expressed as:

$$\phi_{atmo,(x,y)} = -\frac{4\pi}{\lambda}\Delta R_{atmo,(x,y)}, \quad \text{where} \quad \Delta R_{atmo,(x,y)} = \Delta R_{atmo,y} - \Delta R_{atmo,x}. \tag{60}$$

As discussed in section 2.2.4.3, two types of atmospheric signal can be observed in interferograms: one strongly height-dependent and one not. Firstly, the height-dependent atmospheric delay is dominated by vertical atmospheric stratification and known as stratified atmospheric delay. It is mainly contributed by the hydrostatic delay and a part of the wet

delay, where the movement of the atmosphere occurs mainly in vertical due to gravity and external heat. This delay can be modeled with good accuracy by means of direct integration using ECMWF data (see section 3.1.2.3). Based on the simulated results for the Stromboli test site, the causes and the effect of the stratified atmospheric delay are explained and discussed in section 3.4.1. Secondly, the atmospheric delay dominated by turbulent mixing has no significant height-dependence and is decorrelated in time. Since the atmospheric turbulence is characterized by its chaotic nature and is governed by highly nonlinear processes, it is difficult to accurately simulate and to derive the absolute delay caused by turbulence effects. A short discussion is given in section 3.4.2.

3.4.1 Atmospheric delay dominated by the vertical stratification

In volcanic areas, due to the high variation of terrain topography, the variation of the stratified atmospheric delay dominates that of the total atmospheric delay, which thus exhibits a clear height dependency, as shown in *Fig. 13*. In order to demonstrate the stratified atmospheric delay, two SAR images acquired at Stromboli from beam 061 on 28 January 2008 (in winter) and on 2 August 2008 (in summer) have been selected (see section 2.4.3.2). Differential interferometric phases on selected PSs of the PSI reference network (more than 2.0×10^5 points) are presented in *Fig. 54*. The effective baseline is about -5.6 m, which means that the height to phase ambiguity (h2p) factor is about 2085 m/cycle. Therefore, a DEM error of 50 m induces a phase error about 0.05 rad (8.6 °), which can be neglected. Nevertheless, about three phase cycles, about 4.7 cm converted to delay, can be observed in *Fig. 54* following the topography also outside of the highly active deformation area (SdF) (see *Fig. 31*).

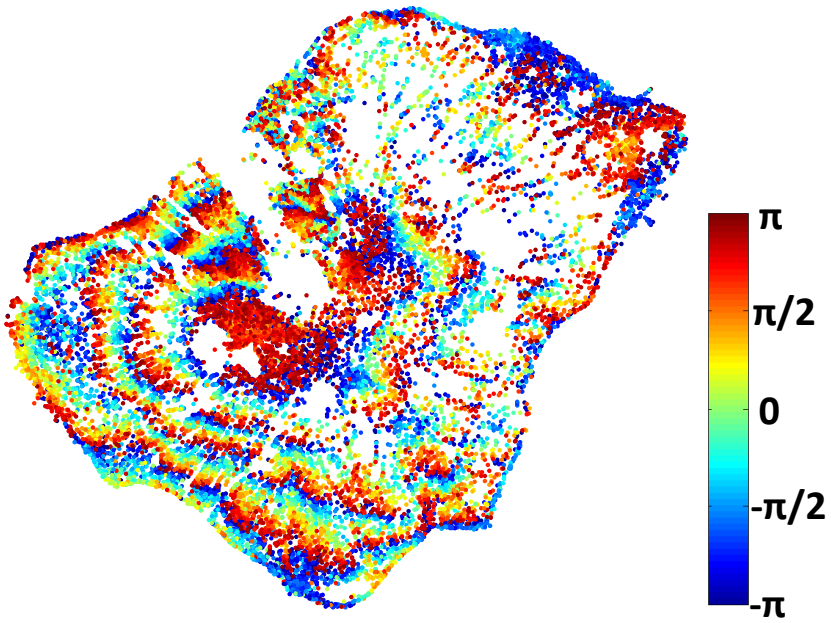

Fig. 54. Differential interferometric phases on selected PSs of the PSI reference network (more than 2.0×10^5) in Stromboli acquired from beam 061 (a full color cycle indicates the range $-\pi$ to π). The master image was acquired on 28 January 2008 (winter), and the slave image on 2 August 2008 (summer). The effective baseline is about -5.6 m, and the h2p is about 2085 m/cycle, around three topography correlated fringes can be observed also outside of the highly active deformation area (SdF) (see *Fig. 31*).

3.4.1.1 Hydrostatic and wet atmospheric delay components

In order to distinguish the atmospheric signal from the deformation signal, the stratified atmospheric delay is simulated on the selected PSs using ERA-Interim data (see section 3.1.2.3). This delay has two components: the SHD ($L_{h,approx}$ in *eq. (49)*) which is mainly dependent on

the surface pressure and the SWD ($L_{w,approx}$ in *eq. (51)*). For each PS the stratified atmospheric delay (SPD) has been integrated along the propagation path for each acquisition date, as well as the SHD and the SWD. The integrated delays are depicted as a function of height in *Fig. 55*, the winter acquisition in blue and the summer acquisition in red. As expected, the total one-way delay in summer is larger than in winter (see *Fig. 55(c)*). The SPD in summer varies from 3.086 to 3.507 m from the sea level to the top of the mountain and the SPD in winter is from 2.930 to 3.305 m. The SHD in winter is larger than in summer, which is satisfied with the interpretation in section 3.3.1.2.4. Due to the lower temperature and higher pressure in winter, the difference varies from about 1.7 cm to about 0.1 cm from the bottom to the top of the mountain (see *Fig. 55(a)*). It is mainly caused by the temperature difference between summer and winter (see *eq. (17)*). Unlike SHD, the variation of the SWD with elevation is not linear (see *Fig. 55(b)*). However, the SWD contributes only less than 10% in the total delay. The absolute ZWD delay difference between summer and winter acquisition reaches 20 cm due to the increasing water vapor content.

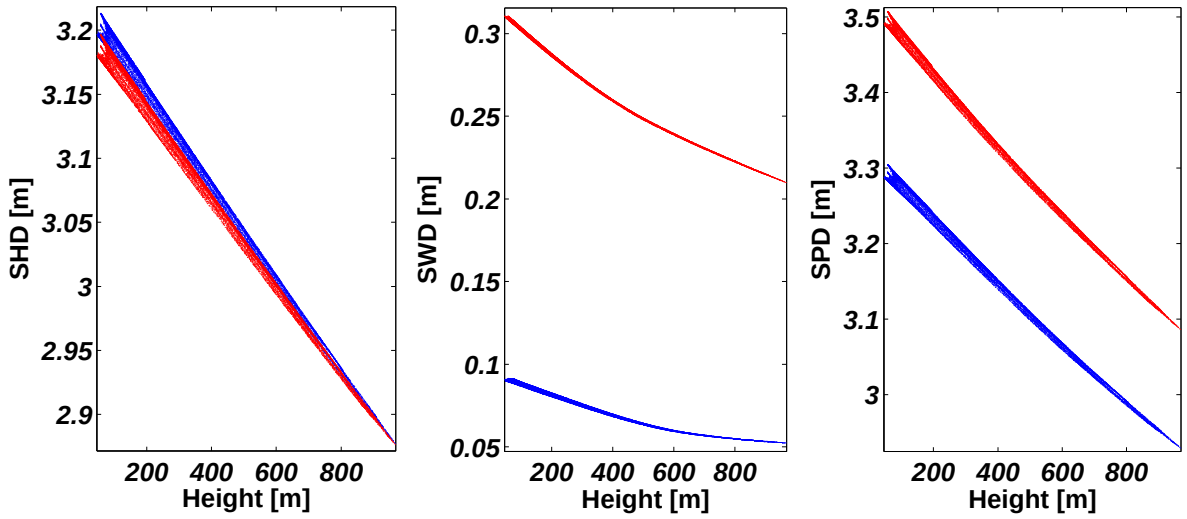

(a) SHD (b) SWD (c) SPD

Fig. 55. Stratified atmospheric delays are simulated for two acquisitions on 28 January 2008 in winter (blue) and on 2 August 2008 in summer (red). They are depicted against the height in: (a) SHD; (b) SWD; (c) SPD = SHD + SWD.

The atmospheric phase observed in an interferogram is induced by the atmospheric delay difference between two points (see *eq. (60)*), where the atmospheric delay on reference point is considered as an offset. The phase component caused by the stratified atmospheric delay is thus due to the relative atmospheric delay variation between two points at different heights. The differential atmospheric delay has been calculated for SHD, SWD and SPD with winter acquisition as master (see *Fig. 56*). The ΔSPD varies from about -20.4 cm to -15.7 cm and is dominated by the ΔSWD, where the variation is from -22.0 to -15.8 cm. The ΔSHD varies from 0.1 to 1.7 cm.

The atmospheric phases induced by SHD and SWD respectively are presented in *Fig. 57(a)* and *57(b)*. It is obvious that the offset in the differential delay has effect ϕ_0, but not for phase difference $\phi_{x,y}$ at the same height. Nevertheless, the relative changes of the differential atmospheric delay between two elevations induce the stratified atmospheric delay. For instance, in *Fig. 57(c)* around three cycles following the topography can be observed. The difference of ΔSPD from bottom to top of the volcano is about 4.7 cm, which has a good agreement with the observation described in section 3.4.1. The relative difference of ΔSWD accounts for 6.2 cm, which induces about one cycle more than the relative difference of ΔSPD. Nevertheless, the relative difference of ΔSHD is about -1.6 cm , that is in the opposite direction, mitigating thus the effect from ΔSWD.

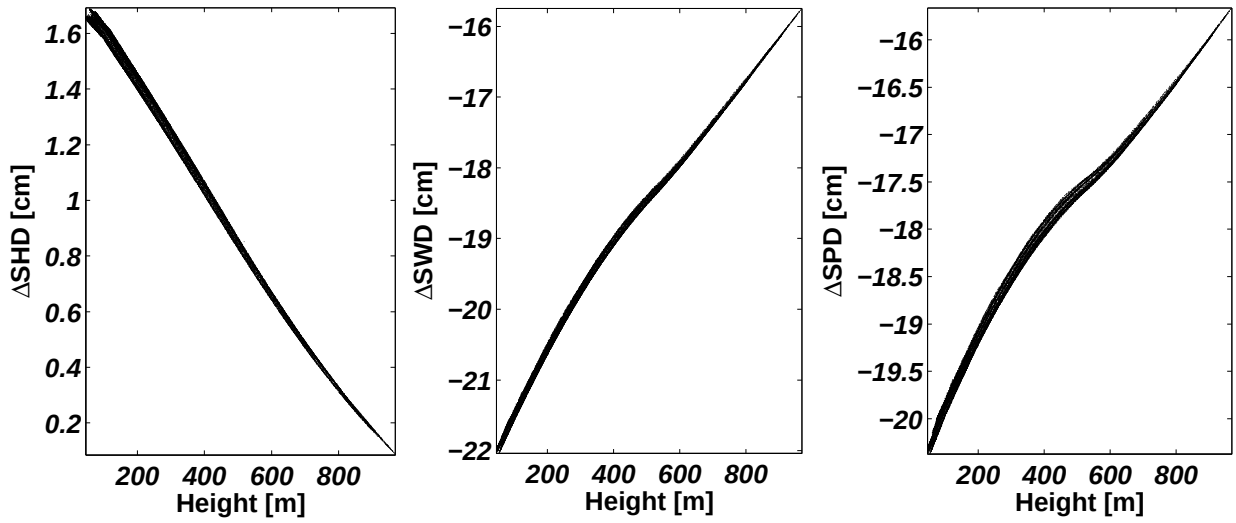

(a) ΔSHD (b) ΔSWD (c) ΔSPD

Fig. 56. Difference of stratified atmospheric delays between the two acquisitions as a function of height: (a) ΔSHD; (b) ΔSWD; (c) ΔSPD.

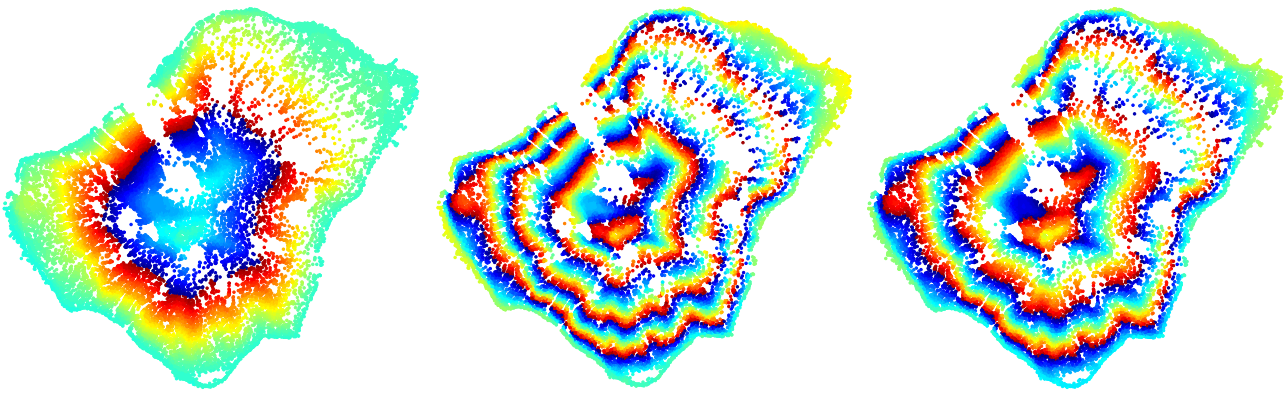

(a) Hydrostatic phase (ΔSHD) (b) Wet phase (ΔSWD) (c) Stratified phase (ΔSPD)

Fig. 57. Simulated stratified atmospheric phase induced by SHD, SWD and SPD according to the differential atmospheric delay displayed in *Fig. 56*. The hydrostatic phase is presented in (a), the wet atmospheric phase in (b) and the stratified atmospheric phase in (c). A full color cycle indicates the range $-\pi$ to π.

3.4.1.2 Mitigating the stratified atmospheric delay in the interferometric phase

The stratified atmospheric phase for a PS x is calculated by:

$$\phi^k_{(atmo,s),x} = -\frac{4\pi}{\lambda} \cdot \Delta SPD^k_x, \quad \text{with } k = 1, \cdots, n, \tag{61}$$

where $\Delta SPD^k_x = SPD^m_x - SPD^k_x$ and m indicates the master scene.

The simulated phase can be directly used to mitigate stratified atmospheric phases. The updated PS phase observation is thus formulated as:

$$\phi^k_x = \mathbf{W}\left\{\phi^k_{topo,x} + \phi^k_{defo,x} + \phi^k_{(res,s),x} + \phi^k_{(atmo,t),x} + \phi^k_{otl,x} + \phi^k_{noise,x}\right\}, \quad \text{with } k = 1, \cdots, n, \tag{62}$$

where $\phi^k_{(res,s),x}$ is the residual phase induced by unmodeled or/and inaccurate stratified delay.

An example is presented in *Fig. 58*, where the original phase (*Fig. 54*) is directly compensated by using the stratified atmospheric phase (*Fig. 57(c)*). Evidently, the stratified atmospheric phase component has been significantly mitigated. After this compensation the deformation signal pattern around the active area SdF, as well as the effect induced by turbulent mixing, can be observed.

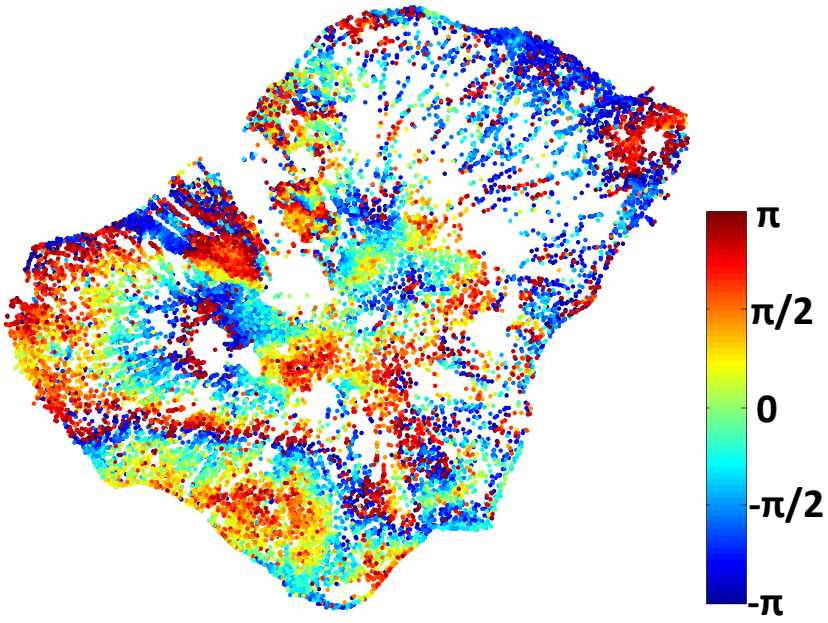

Fig. 58. The differential phase in *Fig. 54* after applying the stratified atmospheric delay compensation which is simulated in *Fig. 57(c)*.

3.4.2 Atmospheric delay induced by turbulent mixing in volcanic areas

Atmospheric turbulence is defined as small scale air flow influenced by winds, solar radiation, planetary boundary layer (known as boundary layer of turbulence) etc. Turbulent processes, especially water vapor fluctuations, are characterized by random processes and chaotic motions, which pose difficulties in deterministic mathematical formulation. Therefore, statistical methods are applied in order to analyze the structure of turbulence and their properties (Kolmogorov (1941)). One of them is the structure function which is introduced in section 3.4.2.1. An experiment for the Stromboli test site is carried out in section 3.4.2.2.

3.4.2.1 Statistic model of atmospheric turbulence

Atmospheric turbulence, which is characterized by its chaotic and irregular motion varying from small to large scales, poses difficulties and challenges for PSI estimation. The mathematical description of turbulent convection processes is complicated and highly non-linear. Therefore, a spatial statistical analysis, such as the structure function, is usually applied to describe turbulence fluctuations. In this section, the spatial variation of the refractivity N between two nearby locations is analyzed. The statistical characterization can be formulated by means of following structure function (Treuhaft and Lanyi, 1987; Williams et al., 1998; Hanssen, 2001):

$$D_N(\vec{R},\vec{r}) = E\Big[\Big(N(\vec{R}+\vec{r}) - N(\vec{R})\Big)^2\Big], \tag{63}$$

where $\vec{r}$ is a displacement vector between the two locations $\vec{R}$ and $\vec{R}+\vec{r}$. Under the hypothesis of isotropic turbulence, the structure function $D_N(\vec{R},\vec{r})$ is a function of the distance $r = |\vec{r}|$

between two points. This distance serves also as the scale of the turbulent flow. Due to the wind shear and solar heating, the energy in the eddy exceeds a critical Reynold's number, then the eddy becomes instable, where the energy is transferred to smaller eddies. In the small scale, viscous effects in atmosphere cannot be ignored and the energy of small eddies is thus dissipated. According to the different scales, statistical properties of turbulence fluctuations can be presented in form of a power-law:

$$D_N(r) = C^2 r^{\alpha} \quad \text{with} \begin{cases} \alpha = 2/3, & \text{for} \quad r \gg h_{eff} \\ \alpha = 5/3, & \text{for} \quad r \ll h_{eff}, \end{cases} \tag{64}$$

where C is the structure constant which characterizes the roughness or the energy of the turbulence, and the power index α indicates the decorrelation velocity, which depends on the distance r and the effective height h_{eff} of the wet troposphere. The first power-law exponent applies the famous Kolmogorov's "two-third" law at large scale where $r \gg h_{eff}$. The second exponent 5/3 is valid for small scale ($r \ll h_{eff}$) and was derived based on the VLBI measurements proposed by Treuhaft and Lanyi (1987).

Hanssen (2001) proposed similar exponents based on power spectrum measurements in the frequency domain on ERS1/2 Tandem interferograms:

$$P_{\phi}(f) = P_0 \left(\frac{f}{f_0} \right)^{-\beta}, \tag{65}$$

where f is the spatial or temporal frequency, β is the spectral index such that $\alpha = \beta - 1$ (Williams et al., 1998), and P_0 and f_0 are normalizing constants. Analogous to the power-law exponent of the structure function in *eq. (64)*, β equals 5/3 at large scale r and 8/3 at small r. Moreover, an additional exponent $\beta = 2/3$ is introduced for $50 \leq r < 500$ m.

3.4.2.2 Observations in time-series

Structure functions are calculated in order to derive the statistical properties of turbulence induced phase screen in X-band interferograms. These structure functions are derived from unwrapped residual phases (ϕ_{res}), where linear deformation and DEM error components have been estimated and compensated:

$$\phi_{res} = \phi_{(atmo,s),res} + \phi_{atmo,t} + \phi_{defo,res} + \phi_{topo,res} + \phi_{noise}, \tag{66}$$

where $\phi_{atmo,s}$ is the vertical stratification induced phase delay and $\phi_{(atmo,s),res}$ is uncorrected stratified phase (see *eq. (62)*), $\phi_{atmo,t}$ is the turbulence mixing induced phase delay, $\phi_{defo,res}$ is residual phase due to nonlinear deformation, $\phi_{topo,res}$ is the residual phase induced by incorrect topography estimates. Two sets of unwrapped residual phases have been evaluated: case I, without mitigation of stratified atmospheric delay; case II, after the compensation of stratified atmospheric delay using ECMWF ERA-Interim data. In case I, $\phi_{(atmo,s),res,I}$ is the unprojected part of stratified atmospheric delay, whereas $\phi_{(atmo,s),res,II}$ is caused by inaccuracy of the stratified atmospheric delay compensation. Based on different temporal-baseline distribution, the stratified atmospheric delay may be projected into deformation and DEM error estimates (see section 3.5).

The structure functions of 16 interferograms in the Stromboli test site acquired from beam 061 (see Table 1). It has been assumed that the effective height (h_{eff}) of the wet troposphere varies from less than 1 km to 2 km in the lower troposphere. The structure function is derived by using unwrapped phases from an estimation interval of 5 m up to a maximum distance of 3 km. The results are presented in log-log scale in *Fig. 59*. Power-law functions with exponents of 2/3 and 5/3 are plotted with dotted lines as reference. The estimates at each bin are depicted with black bold lines for each interferogram.

A fitting based on the power-law function has been carried out in the three different regions according to the effective height h_{eff}: regime (1) large scale with $r \in (1000, 2000]$ m; regime (2) intermediate scale, which is defined in the region smaller than h_{eff}, with $r \in (50, 1000]$ m; regime (3), small scale at the resolution level, with $r \in [5, 50]$ m. The fitted power-law functions are depicted by red bold lines for each region in *Fig. 59*. In this case, the definition of these scales is slightly different as is the one given in Hanssen (2001). It is due to the fact that the pixel resolution, the spatial coverage and the incidence angle of TerraSAR-X images are different from those of ERS1/2 images. In mountainous areas, such as Stromboli, the thickness of the atmosphere varies is adapted from 2 to 1 km due to the topography.

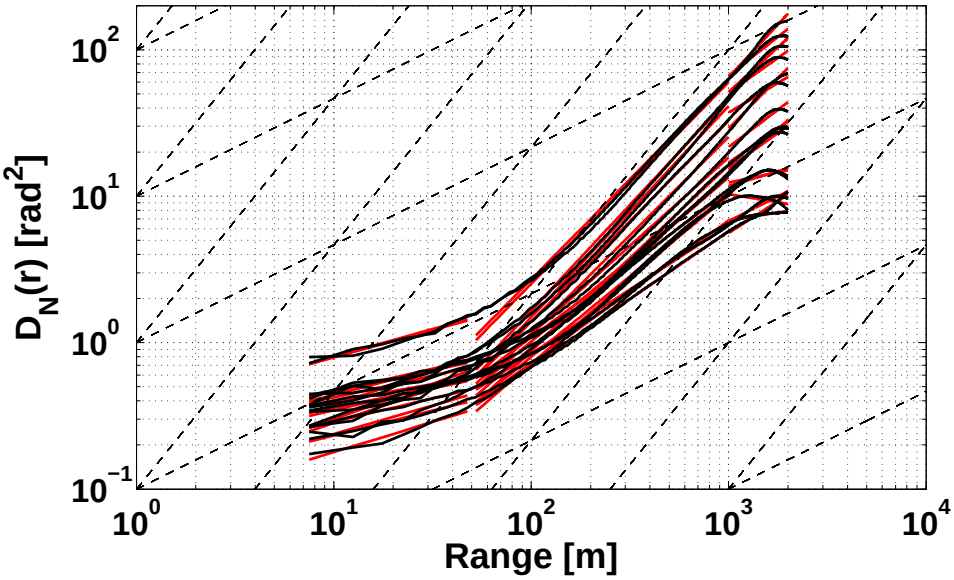

(a) Without stratified delay correction

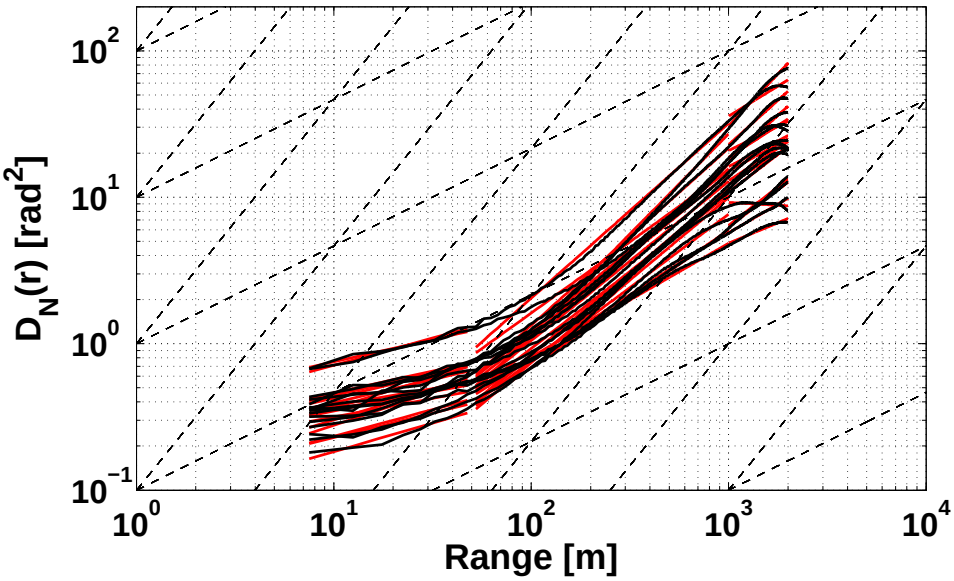

(b) After stratified delay correction

Fig. 59. Statistical analysis of atmospheric turbulence using phase screen based on unwrapped residual phases ϕ_{res}. The structure functions are derived by using unwrapped phases from an estimation interval of 5 m up to a maximum distance of 2 km. The plots are presented in log-log scale. The dotted lines represent the power-law exponents 2/3 and 5/3. The estimates at each interval are plotted with black bold lines for each interferogram and the fitting function with red bold lines. Two residual phases have been analyzed: (a) structure function derived from unwrapped residual phases without stratified delay correction; (b) structure function derived from unwrapped residual phases after stratified delay correction.

In comparison to the estimated structure function in case II, the variance of estimated structure functions in case I increases with increasing range see *Fig. 59(a)*. Nevertheless, due the improper temporal and geometric baseline distribution, a part of the stratified delay is projected into deformation and DEM error estimates (see section 3.5.1). However, residual stratified phases ($\phi_{(atmo,s),res,I}$) influence the structure function, which is related to the distance r.

The mean value and the standard deviation of fitted power-law exponents (α) for the 16 interferogram are summarized in Table 10 for each of the regimes. In general, the standard deviation of α is smaller after stratified atmospheric delay correction. α has a variation from about 0.33 to 1.20 in three regimes. The structure function follows approximately Kolmogorov's 2/3 law at large r. However, the structure function has a different behaviors than in Hanssen (2001) at small r.

Table 10. Summary of power-law exponents (α) fitted on structure function estimates in each of the three regimes. The mean value and the standard deviation of α have been calculated with 16 interferograms.

Inputs	**Regime (1) (1000, 2000] m**		**Regime (2) (50, 1000] m**		**Regime (3) [5, 50] m**	
ϕ_{res}	**Mean**	**Std. dev.**	**Mean**	**Std. dev.**	**Mean**	**Std. dev.**
case I	0.8213	0.4508	1.1968	0.1867	0.3545	0.0726
case II	0.8572	0.3381	1.0781	0.1430	0.3300	0.0672

For detailed analysis, the power-law exponent diagram as a function of distance to effective height ratio (r/h_{eff}) provided by Treuhaft and Lanyi (1987) is used as reference. Given $h_{eff} = 1$ km, the power-law exponents (α) in zenith can be derived approximately from the diagram for three regimes: regime (1), $\alpha \in [0.8, 1.0)$; regime (2), $\alpha \in [1.0, 1.5)$; regime (3), $\alpha \in [1.5, 1.6]$. Theoretically, the α in slant range is greater than in zenith up to about 25% according to the given incidence angles and different r/h_{eff} ratios.

- ◇ **Regime (1)**, at large scale the turbulence is characterized by the local isotropic turbulence. The dissipation rate is equal to the total amount of energy transfer. Ignoring the viscosity the turbulence is described by 2/3 power-law exponent (Kolmogorov, 1941; Tennekes and Lumley, 1972). Since the atmospheric signal has an evidentally larger scale than the SAR image size (5×5 km^2), it is out of the measurement capabilities. Moreover, Stromboli Island is relatively small (see section 2.4.3.2), and the number of samples for estimation decreases exponentially with increasing distance (from $r \geq 2000$ m). The estimated α is about 0.82 for case I and 0.86 for case II, which have a good agreement with the power-law exponents in zenith derived from Treuhaft and Lanyi (1987), but smaller as theoretical values in slant range. Since the Stromboli test site is about 3×3 km^2, the estimates with $r \geq 2000$ m are not reliable due to the phase noise which may induce the underestimation of the structure function.

- ◇ **Regime (2)**, when the distance r decreases to the so-called inertial subrange, the viscosity can not be ignored. The energy of turbulence is dissipated by viscous losses (Frisch., 1995). Within this diffusive length, the local invariance decreases with increasing power-law. The fitted power-law exponents α in the intermediate range has a good agreement with the expected value in Treuhaft and Lanyi (1987). The mean value of case I is larger than of case II, since the dry component of the troposphere dominated by stratified atmosphere has a much larger effective height (Treuhaft and Lanyi, 1987).

- ◇ **Regime (3)**, at the small scale the estimated α is about 1/3 for both stacks, which doesn't agree with the negative power-law exponent $-1/3$ proposed by Hanssen (2001). Based on the estimated PS coherence, the noise level can be calculated, which is about 0.75 to 0.9 rad. It is correspondent to the energy level presented in *Fig. 59*. Therefore, at very small scale the noise is dominated.

Given the estimated model parameters (α and C) and unwrapped residual phase values, the turbulence signal could be reconstructed using kriging interpolation with **power model** variogram (see Appendix G). In order to obtain reliable atmospheric signal estimates, phase unwrapping errors must be first detected and removed. Then the turbulence induced atmospheric phase can be estimated based on the power model parameters and compensated for all PSs. Finally, the final PSI estimation for all PSs is performed. Instead of the statistical method, several NWP models have included nonhydrostatic equations in order to simulate and reconstruct turbulence processes in mesoscale modelling, such as WRF and COSMOS (Skamarock et al., 2005; Rockel et al., 2008). Thanks to the high computing power available nowadays, the non-linear equation system involved in turbulence can be solved in mesoscale. However, due to rapid variation in time and the lack of on-site measurements and model inaccuracy, the simulation solution at small scale is inaccurate. Moreover, the solution is highly dependent on the initial parameter setting. Therefore, the turbulence derived from PSI estimation provides a 2-dimensional turbulence field which is very helpful for understanding its spatial distribution and can be used as a validation reference for NWP simulations.

3.5 Application of integrated stratified atmospheric delay for PSI estimation in volcanic areas

In this section, we focus on the application of integrated stratified atmospheric delay for PSI estimation in volcanic areas. It is known that the atmospheric delay has an impact in PSI estimation. As shown in *Fig. 33*, the PSI-estimated deformation is highly correlated. In order to investigate the link between the atmospheric delay and the estimation error, a simulation test is designed and performed in section 3.5.1. The PSI estimation has been carried out again after compensation of stratified atmospheric delay for the Stromboli test site. The estimation results are presented and discussed in section 3.5.2.

3.5.1 Assessment of stratified atmospheric delay impact on PSI estimation based on integrated delays

In PSI processing, it is assumed that the two nearby PSs linked by an arc are effected by same atmosphere, which is decorrelated in time (Kampes, 2006) and correlated in space. This assumption is only valid, if the atmospheric signal is governed by a turbulence-like random process. Unfortunately, the stratified atmospheric delay, which has a great impact in volcanic areas, is strongly correlated with local terrain and has a clear seasonal variation depending on T, P and e. In this section, we are concentrated on how the stratified atmospheric delay influences the PSI estimation.

The effect of the stratified atmospheric delay in PSI estimation depends on several factors: the variation of the terrain topography, the temporal baseline and the geometrical baseline distribution of the PS stack. In section 3.4.1, a strong correlation between the stratified atmospheric phase and height has been observed in a single interferogram estimated using ERA-Interim data. In order to derive the effect on PSI estimation due to the relation between the stratified delay effect and the temporal and geometrical baseline distribution, a simulation is set up based on atmospheric phases integrated using ERA-Interim data. Two test regions in the Stromboli test site have been selected, as shown in *Fig. 60(a)*. One is located on the northwest flank (NW) and the other one on the southeast flank (SE). The PS stack acquired from beam 061 is used (see Table 1). In the NW region, about 1000 PSs from the reference network have been selected, and about 700 in the SE region. In both regions, the PSs are

homogeneously distributed at different heights (see *Fig. 60(b)* and *60(c)*).

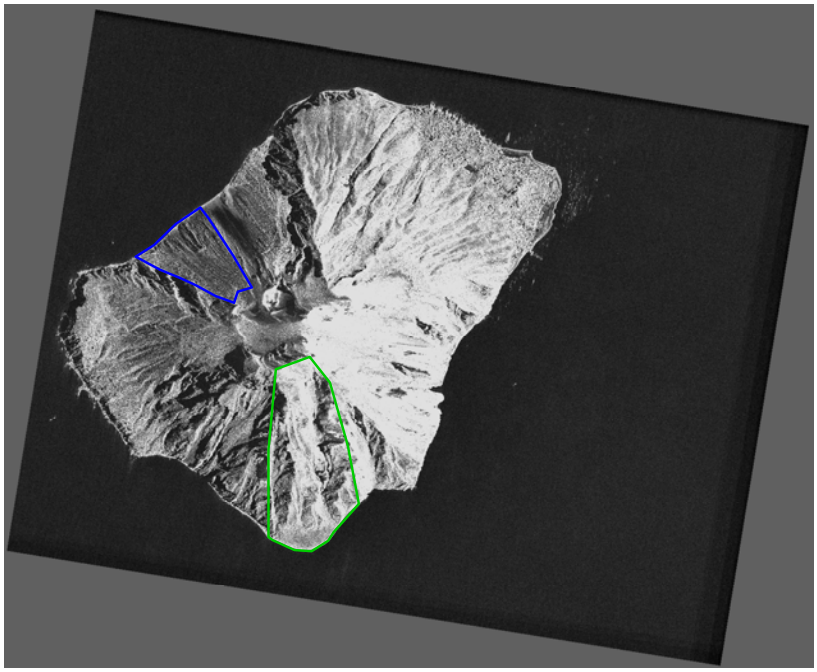

(a) Simulation regions

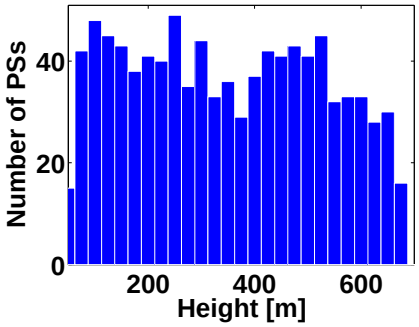

(b) Height histogram (NW)

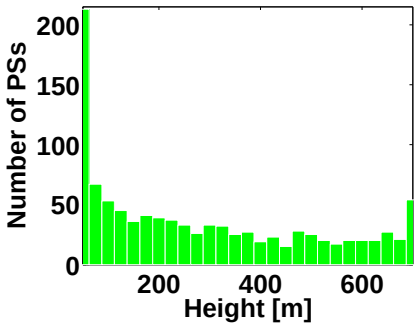

(c) Height histogram (SE)

Fig. 60. Simulation test settings: (a) two test regions in the Stromboli test site have been defined, one is located on the northwest flank (NW) and one on the southeast flank (SE); (b) the PS height histogram of the NW region; (c) the PS height histogram of the SE region.

The PS stack consists of 17 scenes (see Table 1) and the master scene was acquired on 19 June 2008 (see *Fig. 32*). Differential atmospheric phases for each region have been estimated using ERA-Interim data. The mean value of absolute differential phase has been calculated individually for each region in each interferogram and is depicted in *Fig. 61(a)*. The acquisitions span from January to October 2008, where the mean atmospheric phases present a clearly half-year period with the minimum in January and the maximum in July. As additional information, the mean h2p is plotted in *Fig. 61(b)*.

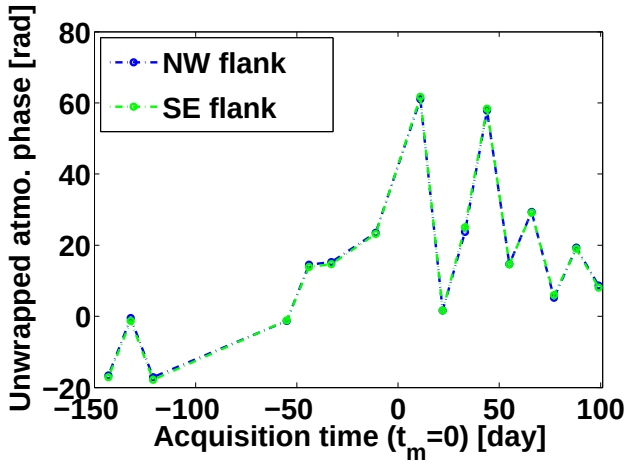

(a) Mean phase

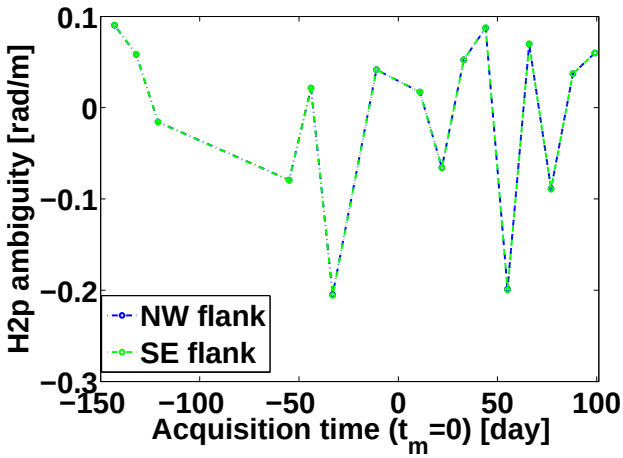

(b) Mean h2p

Fig. 61. Simulation data information. The master acquisition time is used as reference ($t_m = 0$) which is acquired on 19 June 2008. (a) Mean differential atmospheric phase for each region in each interferogram; (b) mean h2p [rad/m]. Blue color represents the NW flank and green the SE flank.

An arc network is generated according to the configuration of PSI processing; namely, the maximum arc length is set for 25 m in order to avoid abrupt topographic changes and the maximum number of arcs for one PS is 30 in order to ensure high network redundancy. Under the assumption of linear deformation, the deformation velocity and the DEM error have been estimated for each arc (Kampes, 2006). An analysis of the height-dependency of both estimates is presented in *Fig. 62* and *Fig. 63*. Both deformation and DEM error are color-coded according to the mean arc height and depicted against the arc height difference between two PSs linked by the arc.

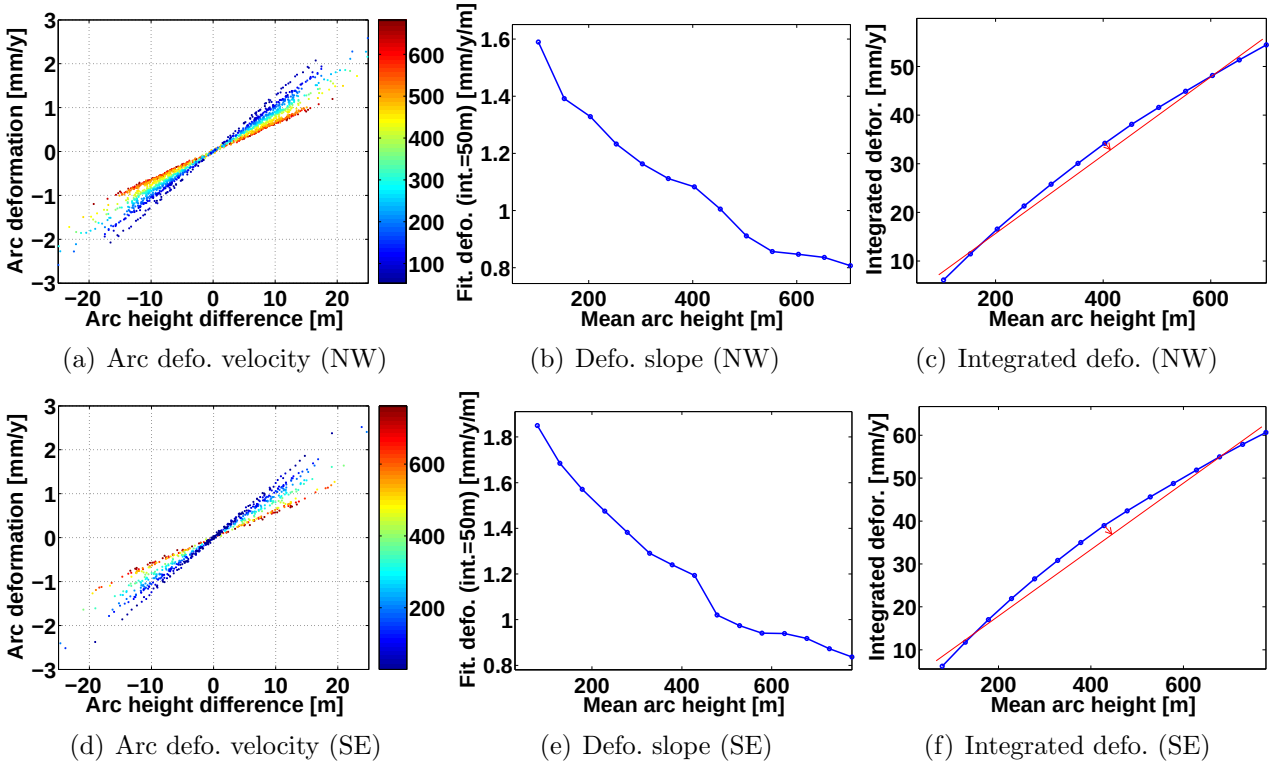

(a) Arc defo. velocity (NW) (b) Defo. slope (NW) (c) Integrated defo. (NW)

(d) Arc defo. velocity (SE) (e) Defo. slope (SE) (f) Integrated defo. (SE)

Fig. 62. Arc deformation estimates are color-coded with mean arc heights and depicted as a function of the height difference in the arc in (a) for the NW region and in (d) for the SE region. Slope estimates at defined mean height steps are presented in (b) and (e) for the NW and SE regions, respectively. Finally, the overall deformation is integrated based on the slope estimates for NW in (c) and for SE in (f).

The linear deformation can not be separated from the atmospheric delay, where the magnitude of atmospheric phases increases almost linear with increasing acquisition time(see *Fig. 61(a)*). In *Fig. 62(a)* and *(d)*, the deformation magnitude of an arc is highly correlated with the arc height difference, which increases linearly with increasing height difference. In the meantime, the arc deformation with the same arc height difference decreases with increasing height. These phenomena are induced by the variation of atmospheric delay with height, because both atmospheric delay and gradient atmospheric delay decreases with increasing height (see *Fig. 13* and *Fig. 56(c)*).

In order to estimate this deformation slope, the deformation estimates are divided into intervals. Then, the slope for each interval is estimated using linear fitting. The result is depicted in *Fig. 62(b)* and *(e)*. Due to the fact that the atmospheric pressure decreases with increasing height (see *Fig. 55*), the differential delay has a smaller impact at higher altitude than at lower altitude (see *Fig. 56*). In the NW region, the fitted deformation linear coefficient decreases from 1.6 mm/year/m at 100 m to 0.8 mm/year/m at 700 m. Equivalently, in the SE region, the slope varies from 1.8 mm/year/m at 780 m to 0.8 mm/year/m at 80 m. A simple integration of the deformation slope has been performed in order to assess the overall effect on PSI estimation. The results at each height step are illustrated in *Fig. 62(c)* and *(f)*. As expected, starting from

the lower altitude, the integrated deformation increases with increasing height. Nevertheless, this overall behavior is not linear with height. By fitting the integrated delay using a linear approximation can induce a maximum residual error of 4 mm/year.

In *Fig. 63(a)* and *Fig. 63(d)*, it is shown that DEM error estimates vary linearly with arc height difference and have an opposite sign from the deformation estimates. The projection of atmospheric delay on the topography depends on the h2p distribution of the stack (see *Fig. 61(b)*). Moreover, the variation of DEM error estimates with the mean arc height is more complicated as for the deformation estimates. The DEM error slope first decreases with increasing mean arc height up to around 330 m, then increases again (see *Fig. 63(b)* and *(e)*). The maximum absolute slope is about 0.7 m. The total integrated height error is about 18 m at the maximum mean arc height, where variation is clearly not linear.

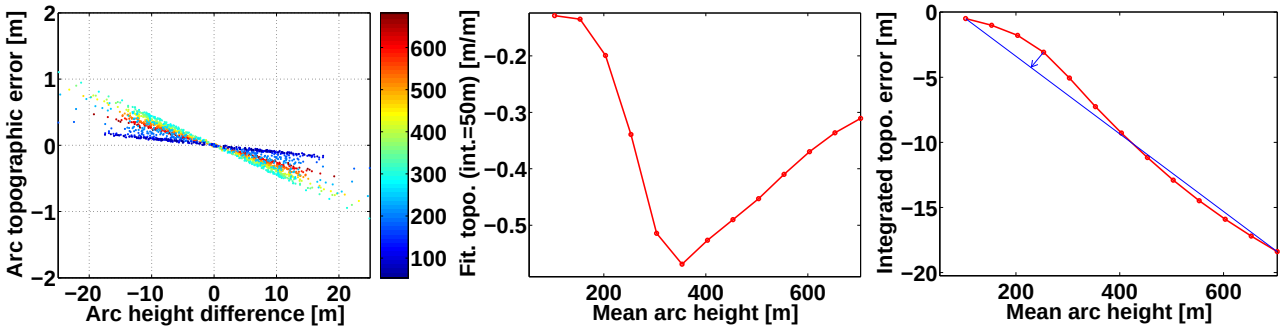

(a) DEM error (NW) (b) DEM error slope (NW) (c) Integrated DEM error (NW)

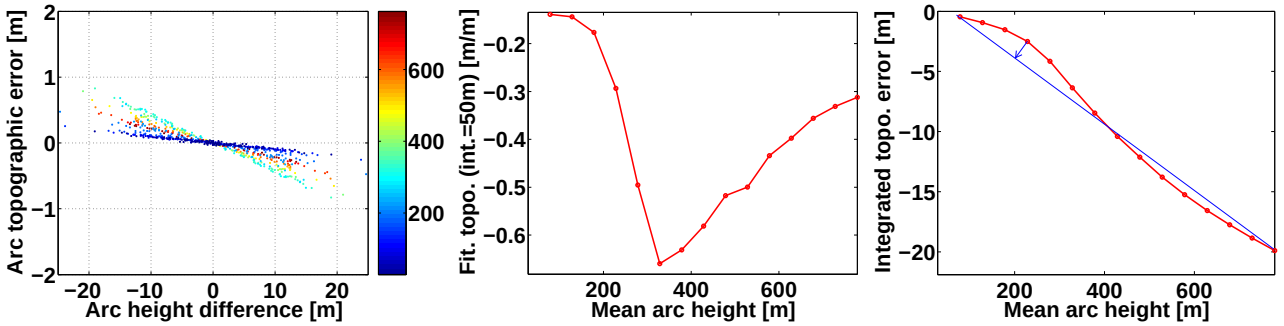

(d) DEM error (SE) (e) DEM error slope (SE) (f) Integrated DEM error (SE)

Fig. 63. Arc topography errors are color-coded with mean arc heights and depicted as a function of the height difference in the arc in (a) for the NW region and in (d) for the SE region. Slope estimates at defined mean height step is presented in (b) and (e) for the NW and SE regions, respectively. Finally, the topography error is integrated based on the slope estimates for NW in (c) and for SE in (f).

In summary, the effect of the stratified atmospheric delay in PSI estimation depends on the temporal and geometrical baseline distribution of the stack. Due to terrain topography, the atmospheric delay decreases exponentially with increasing height, which leads to a variation of estimation errors at different altitudes. Therefore, a simple linear fitting of the final PSI estimation results as a function of height is not enough in order to compensate the effect of the atmosphere (after compensation high residuals remain), as shown in *Fig. 62(c)* and *(f)* for deformation estimates and in *Fig. 63(c)* and *(f)* for topography estimates. The effect introduces errors in the arc estimation which will be afterwards integrated in the network inversion step. Moreover, the simulation test is a very useful tool in order to quantify and evaluate the estimation errors induced by the atmospheric delay in PSI processing.

3.5.2 Stratified atmospheric delay correction using ERA-Interim data on Stromboli

In order to mitigate the topography-correlated stratified atmospheric effect, the differential atmospheric phase is firstly integrated for the PSs from the reference network, then it is interpolated for all the PSs and finally it is corrected on differential phases. For each unknown SPD, an exponential function *eq. (59)* is fitted according to the SPDs from nearby PSs in the reference network (with distance < 50 m). The accuracy of the interpolated SPD is better than 0.1 mm. After this correction PSI processing is performed. The resulting PS deformation maps after atmospheric delay mitigation are presented in *Fig. 65*. In comparison to *Fig. 33*, the topography-dependent component has been effectively removed. Similar deformation patterns can be observed both in ascending and descending orbits in SdF. Some mismatches near craters are caused by the horizontal components of the deformation, which are differently projected for the ascending and descending orbits, respectively.

A close-up analysis of deformation estimates is performed in beam 061 in order to demonstrate the improvement of PSI estimates after mitigating the stratified atmospheric delay. The comparison is summarized in *Fig. 64* using deformation estimates before and after performing atmospheric delay correction. Firstly, both deformation maps are presented using the same color-scale in *Fig. 64(a)* and *Fig. 64(b)*. Obviously, spatial patterns, which are correlated with height, have been significantly reduced after the corrections with respects of scatter plots in *Fig. 64(c)* and *Fig. 64(d)*. Moreover, the deformation pattern in SdF has been preserved. Deformation difference is calculated, and then depicted in *Fig. 64(e)* with respect of the height range in NW flank (see section 3.5.1). In spite of phase noises, the maximum is about 50.0 mm/year in this range, which has a good agreement with the simulated results in *Fig. 64(f)* (see section 3.5.1).

In order to derive the stratified atmospheric delay effect, the difference is calculated based on identical PSs i by subtracting the estimates after atmospheric delay compensation from the original estimates, an example has been presented in *Fig. 64(e)*. For both deformation estimates $\Delta Defo_i = Defo_{ori,i} - Defo_{atmo,i}$ and DEM errors $\Delta Topo_i = Topo_{ori,i} - Topo_{atmo,i}$, an offset has to be corrected by means of different reference points. The maximum and the minimum value are summarized in Table 11. On the one hand, due to the temporal baseline distribution, all deformation differences have a positive correlation with height, and they are higher than 85%. On the other hand, differences of DEM errors have both positive and negative correlation with height according to different geometrical baseline distributions. Apart from beam 033, the absolute correlation is higher than 90%. Although the maximum difference is observed in beam 069 with 56.7 m, its minimum value is -5.0 m. The relative error is more than 61 m, which is larger than beam 061 with 34.9 m. Nevertheless, due to this offset in topographic estimates, external errors will be introduced by geocoding.

Table 11. Summary of statistical analysis based on the difference of two PSI results before and after performing atmospheric delay correction: maximum and minimum value of deformation difference and difference of DEM errors, and their correlation with height.

Beam	$\Delta Defo$ **[mm/year]**			$\Delta Topo$ **[m]**		
Nr.	**max**	**min**	**Height corr.[-]**	**max**	**min**	**Height corr.[-]**
033	49.2	−6.6	92.1%	5.9	−32.0	−14.5%
061	64.9	−9.7	98.2%	37.6	2.7	−92.4%
069	33.2	−5.0	87.8%	56.7	−5.0	97.4%
024	25.0	−4.5	96.3%	11.6	−2.8	94.6%

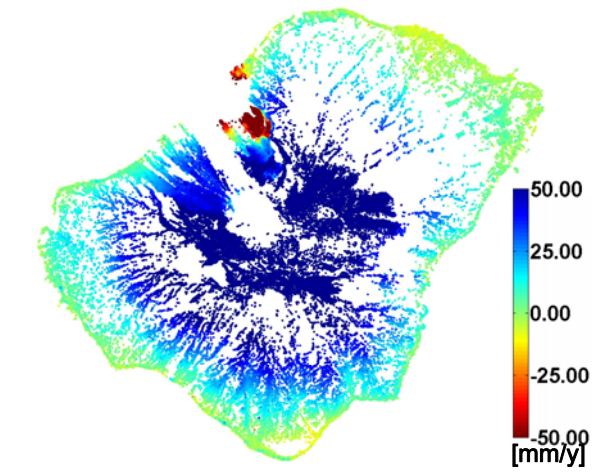

(a) Defo. without strat. atmo. correction

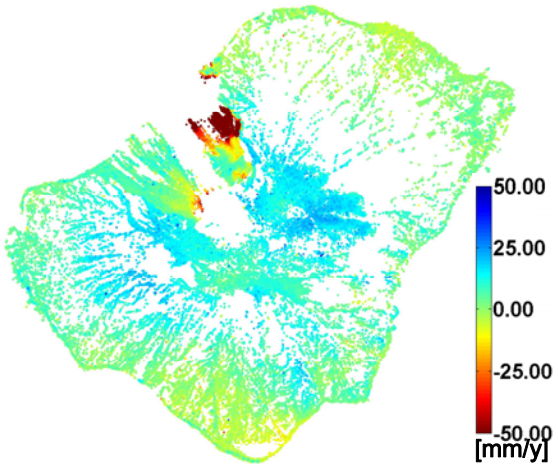

(b) Defo. with strat. atmo. correction

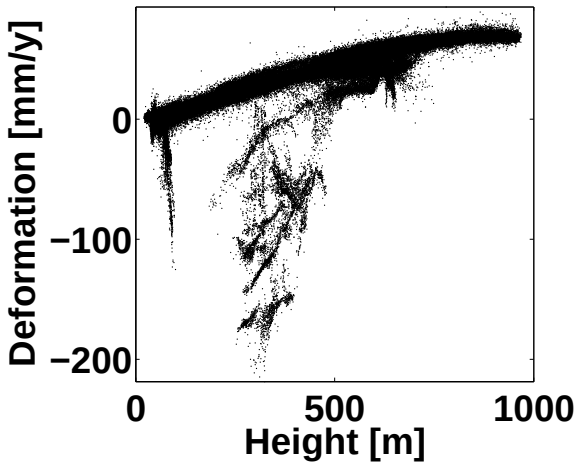

(c) Scatter plot defo. vs. height (without)

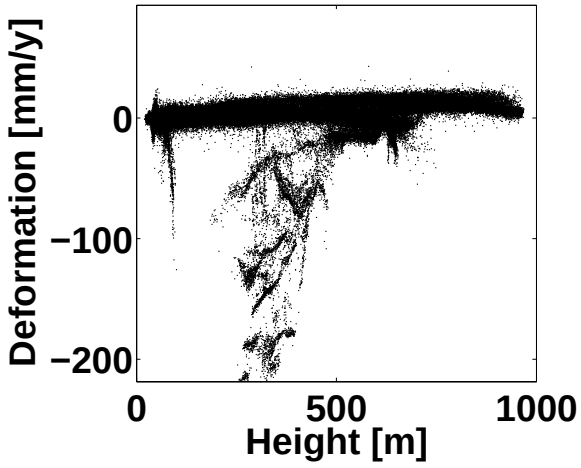

(d) Scatter plot defo. vs. height (with)

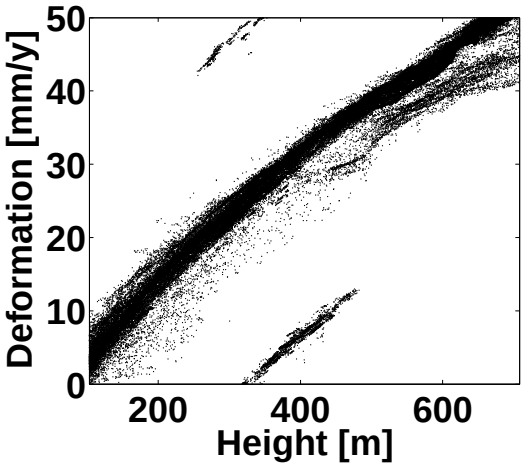

(e) (c) - (d)

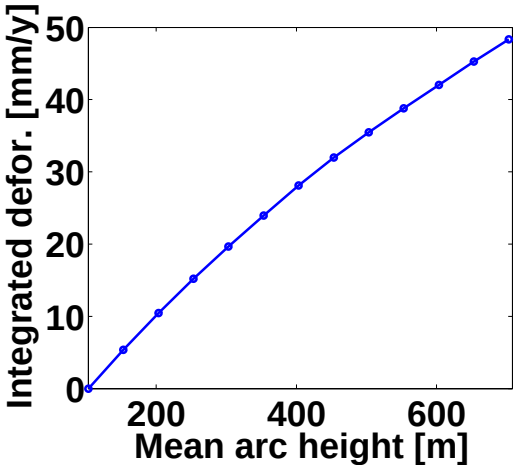

(f) Simulated results in NW flank

Fig. 64. PSI deformation estimates without and with stratified atmospheric correction: (a) deformation map without stratified atmospheric corrections; (b) deformation map with stratified atmospheric corrections; (c) and (d) are the scatter plot of deformation versus height from (a) and (b), respectively; (e) deformation difference with respect of the height range in NW flank (see section 3.5.1); (f) integrated deformation error from *Fig. 62(c)*.

.

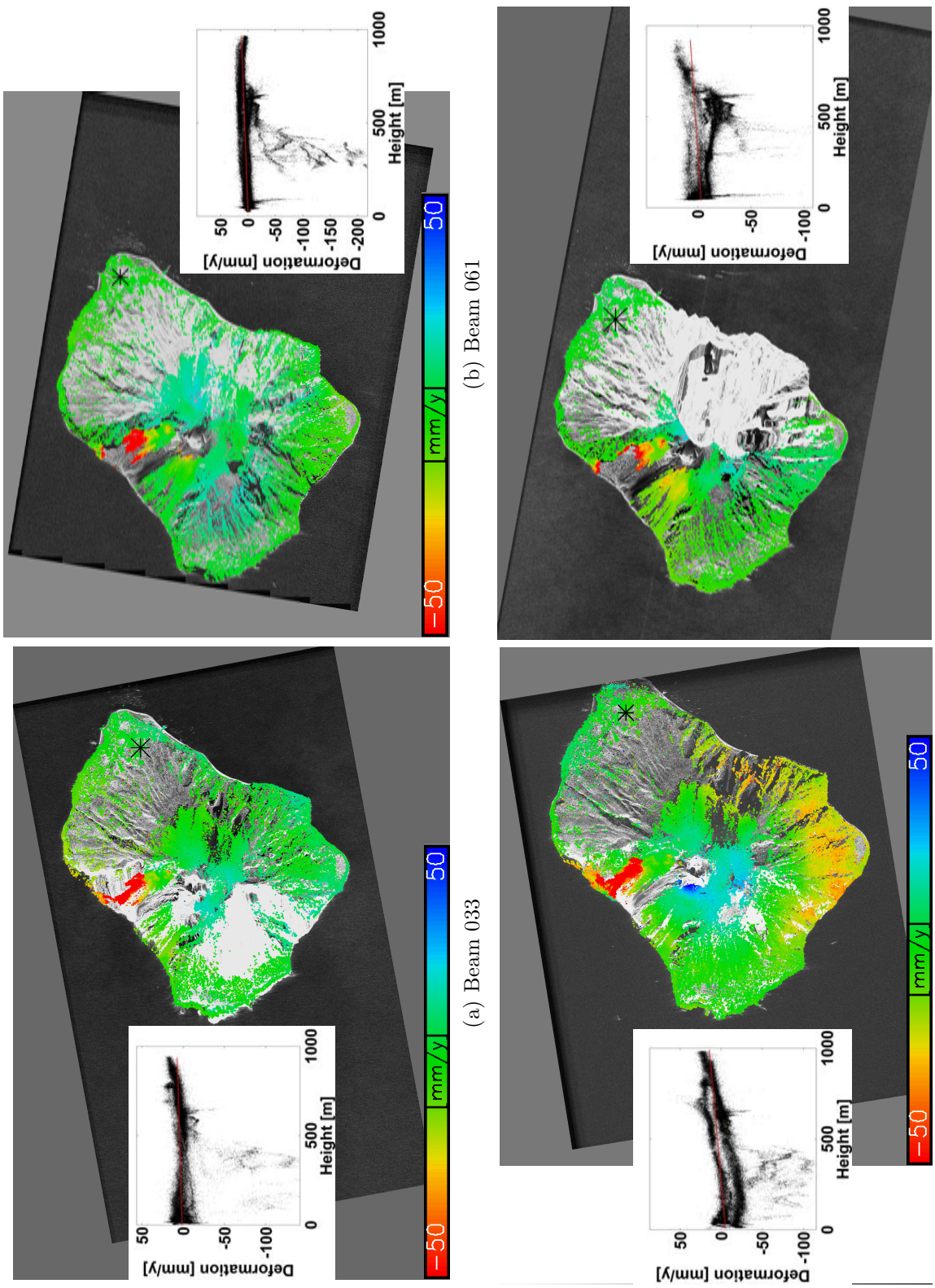

Fig. 65. PS deformation maps after mitigation of differential atmospheric phases. The geocoded average amplitude image has been used as background for four stacks, as shown in *Fig. 33*. On each deformation map, a scatter plot of deformation versus height is illustrated. A linear fit is presented in a red line on each scatter plot. The height-dependent effect is successfully removed.

3.6 Application of integrated atmospheric delay for cross-correlation

As reported in Eineder et al. (2011), 22 TerraSAR-X HRSL images from May 2008 to September 2009 have been acquired over the Venice test site in order to estimate the relative range offsets caused by geodynamic and atmospheric effects. In the study, the atmospheric delay in slant range is calculated based on a simplified exponential model suggested by Breit et al. (2010) using GPS ZPD from a nearby GPS station. In this case, the nearest GPS station is located in Rovereto, which is about 114 km away from the test site. Therefore the atmospheric conditions at the GPS station might differ considerably from those at the test site. In the paper, three corrections are compensated in the range cross-correlation measurements, namely, SET, GPS TD and ID. After corrections, the SAR slant range measurements yield a standard deviation of 3.8 cm in range. A total improvement of 8.5 cm due to the three corrections is observed. Note that the hydrostatic atmosphere (dry delay), which induces about 90% of the total delay, is smoothly distributed in space and varies slowly only at large scales. The accuracy of GPS TD depends on the defined total atmosphere height, which varies in space and in time (see section 3.3.1.2.3).

Following the proposed integration methods, the atmospheric delays along slant range for the center point of the scene have been calculated using ERA-Interim data. The standard deviation is reduced from 3.8 to 3.1 cm by using the ECMWF SPD instead of the GPS TD. Furthermore, the outliers on 27 June and 10 August 2009 are reduced from from 9.0 to 4.7 cm and from −5.5 to 0.6 cm (see *Fig. 66*). All the corrections are summarized in Table J.1 in Appendix J. A slight improvement of 0.1 cm is achieved in consideration of OTL effects. Other earth tides, such as NOTL and APL, are neglected, since the impact on the total delay is $\ll 1$ mm (see section 2.2.5.1).

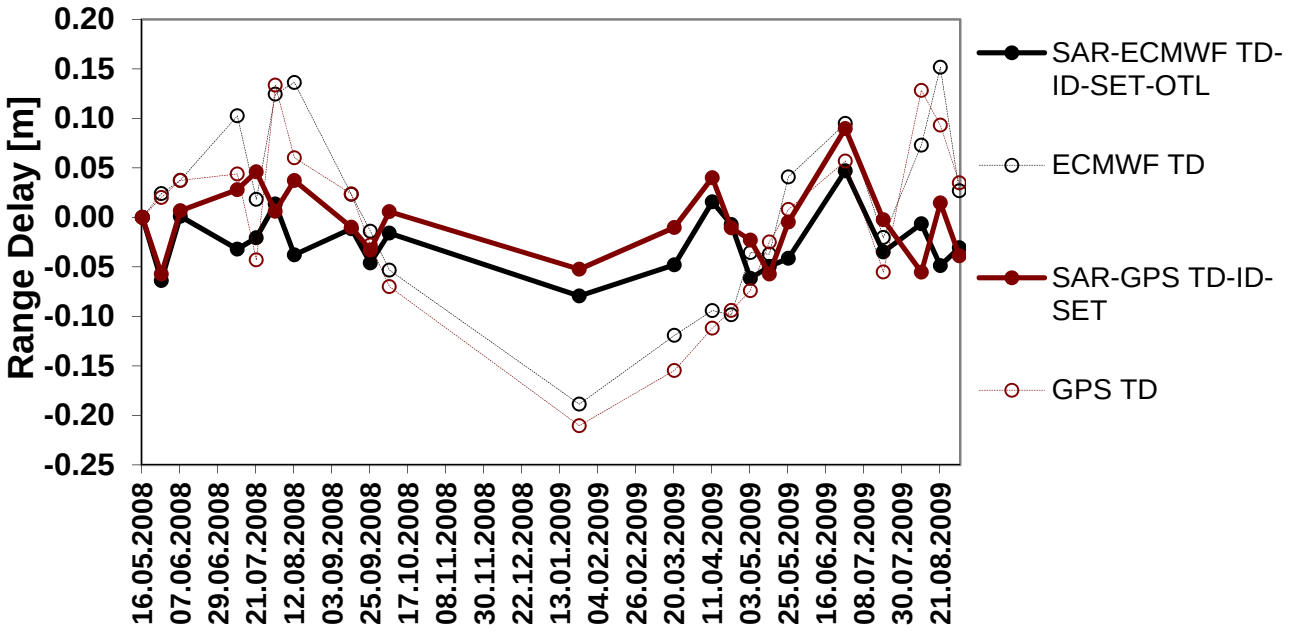

Fig. 66. Tropospheric delay correction for cross-correlation measurements. Atmospheric delays integrated using ERA-Interim data (ECMWF TD) are depicted with a dotted black line. The GPS ZPD (GPS TD) projected in slant range using the incidence angle is depicted with a dotted red line. The range delay residuals using ECMWF TD and GPS TD corrections after the correction of ionospheric delays (ID), solid earth corrections (SET) and ocean tidal correction OTL are depicted with a bold black and red line, respectively. After each correction, the mean value of the remaining time series has been compensated (centering around zero).

The correlation between the ECMWF TD and SAR TD, which is derived by correction of SET, ID and OTL on the ranging measurements, is improved from 80.6% to 83.3%, as shown in *Fig. 67(b)*. In *Fig. 67(b)*, a clear correlation is observed between the model Rng SET and SAR SET measurements from TerraSAR-X. The correlation coefficient, by the fitting of a linear model, is improved for the SET estimation from 0.76 to 0.80. Although a leverage point appears on the 24 January 2009 (winter) in *Fig. 67(a)*, the coefficient of determination R^2 with linear regression is about 91.7%. This means that only about 8% of the variation can not be explained by a linear relation dependency.

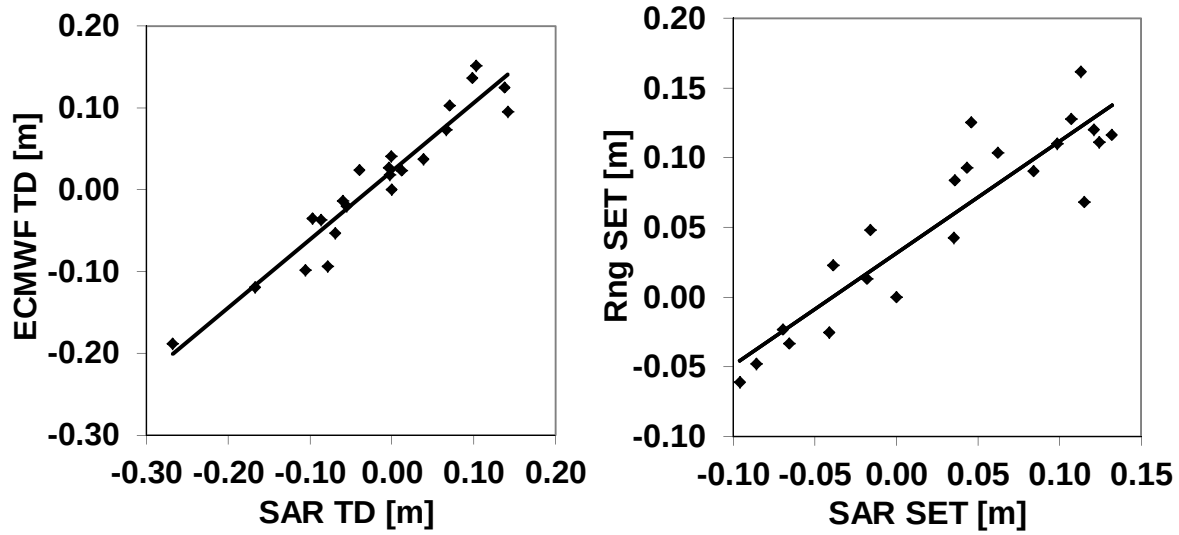

Fig. 67. Correlation analysis of cross-correlation residuals: (a) correlation between TD integrated from ECMWF data (ECMWF TD) the range residuals (SAR TD) ,which are derived from the range delay values measured after corrections of SET, ID and OTL; (b) correlation between the model-based range delays caused by SET (Rng SET) and the SET, range residuals (SAR SET), which are derived from the range delay values measured after corrections of TD, ID and OTL. A linear fitting has been carried out for each correlation plot.

4 Fusion of multi-track PSI results

In SAR imaging, the 3-dimensional backscattering object space is mapped into a 2-dimensional image space (azimuth-range plane). Thanks to the stable and accurate orbit determination of modern SAR missions, such as TerraSAR-X, the accuracy of range and azimuth measurements reaches the centimeter-range after performing sophisticated corrections (range accuracy discussed in section 2.2.6 and azimuth accuracy in Balss et al. (2013)). Nevertheless, due to the SAR imaging mapping the elevation information is lost in a single image. The coherent exploitation of stacks with techniques such as PSI allows the retrieval of the elevation of a target relative to a reference one. Moreover, the elevation accuracy, which is estimated relative to a reference point, is about 50 times worse than in range and azimuth(Zhu, 2011; Gernhardt, 2011). In order to fuse PSI results from independent PS stacks, one elevation offset per stack must be accurately estimated and compensated. In Gernhardt et al. (2012), two different methods were reported for geometrical fusion of geocoded multi-track PS results in both urban and non-urban areas. One algorithm is based on the Least Square Adjustment (LSA) using identical PS pairs from different geometries and has been proposed for urban areas. The other algorithm is based on the Iterative Closest Point (ICP) algorithm and has been proposed by Cong et al. (2010a) for non-urban areas.

In this section, the fusion algorithm for non-urban areas based on the ICP algorithm is described. Atmospheric-delay-corrected multi-track PSI estimates are used as input. Based on the experience in two test sites, namely Stromboli and Azores Island (Cong et al., 2010a,c; Cong and Eineder, 2011), there are rarely common PSs between two different acquisition geometries in non-urban areas, even between adjacent tracks. Nevertheless the PS point clouds represent a similar shape from all observation geometries. The similarity enables the ICP to find the closest point between a given "model" and a measured "data" shape or data sets instead of using correspondent points (Besl and McKay, 1992). The relative transformation has been limited to a 3-dimensional translation in this application. The translation vector can be iteratively estimated by minimization of the mean-square distance metric between model and data.

This section consist of five parts: firstly, the multi-track geometry is introduced in section 4.1; and then a short introduction of the ICP method is given in section 4.2; next, the ICP registration accuracy is discussed in section 4.3; after that, the principle of the geometrical stack fusion based on the ICP method is explained in section 4.4; finally, an example of the geometrical fusion is demonstrated using multi-track PSI results on the Stromboli test site in section 4.5.

4.1 Multi-track geometry

In multi-track geometries, the satellite illuminates the same object (P_1) from different orbits and incidence angles. For the purpose of clarity, let us assume that two observation geometries (SAR_a and SAR_b) are available (see *Fig. 68*). Prior to geocoding, range delays, such as the atmospheric delay and the SET offset, must be considered for each stack. Assuming that the range delays have been accurately compensated in $R_{1,a}$ and $R_{1,b}$, PS point clouds are geocoded to the Universal Transverse Mercator (UTM) map projection. Usually, a coarse DEM, such as SRTM DEM, is used to determine the height (phase) offset. In this case, the height error on the reference point is projected during geocoding into elevation direction and induced elevation offsets. On the other hand, the elevation accuracy is dependent on the PS Signal-to-Noise Ratio (SNR) and the stack baseline distribution (see section 4.5), even if the phase offset is perfectly determined by means of an accurately known reference point. Due to the unknown elevation offsets (l_a and l_b) along the respective elevation directions ($\vec{s}_a$ and $\vec{s}_b$), discrepancies

exist between the real position P_1 and its location in the stack a and b ($P_{1,a}$ and $P_{1,b}$). The shift vector along the elevation direction ($\vec{s}{\cdot}l$) can be projected into the UTM coordinates (x, y and z) by means of local incidence angles (θ_{loc}) and heading angles (t), and is expressed in matrix form as (Gernhardt, 2011; Gernhardt et al., 2012):

$$\vec{s}(t,\theta_{loc})\cdot l = \begin{bmatrix} \cos t\cos\theta_{loc} \\ -\sin t\cos\theta_{loc} \\ \sin\theta_{loc} \end{bmatrix} \begin{bmatrix} \Delta x \\ \Delta y \\ \Delta z \end{bmatrix}_s . \tag{67}$$

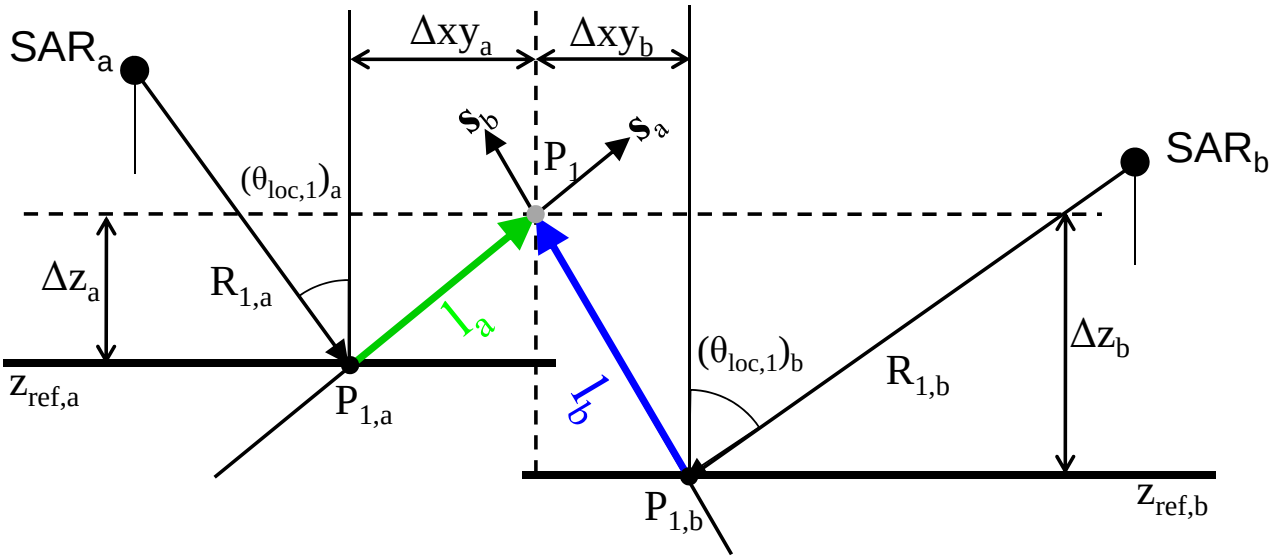

Fig. 68. Fusion geometry of multi-track PS stack in the slant range plane. The geometry of two stacks with different geometries SAR_a and SAR_b are depicted. Due to unknown elevation offsets l_a and l_b, PS P_1 is dislocated in $P_{1,a}$ and $P_{1,b}$. $R_{1,a}$ and $R_{1,b}$ are the slant ranges between the satellite SAR and the object P_1. $(\theta_{loc,1})_a$ and $(\theta_{loc,1})_b$ are the local incidence angles. $\vec{s}_a$ and $\vec{s}_b$ represent the elevation direction of $P_{1,a}$ and $P_{1,b}$. In UTM coordinate system, Δxy represents the projection of elevation offset $\vec{s}{\cdot}l$ on the horizontal plane, and Δz is the projection of $\vec{s}{\cdot}l$ on the vertical plane. $z_{ref,a}$ and $z_{ref,b}$ are unknown reference heights in different PS stacks.

A PS-DEM can be directly generated by merging the PS point clouds from different geometries after determination of the elevation offsets. On each PS in the fused point cloud, a deformation velocity is estimated from different time spans and available in different LoS directions. In order to reconstruct the 3-D deformation vector, it is assumed that different LoS deformation estimates are induced by the same deformation signal, which is homogenous in time and in space. Similar to *eq. (67)*, the LoS deformation (d_{los}) can be projected into the UTM coordinate system with the unity vector $\vec{u}$ and the 3-D deformation vector $\vec{d}_{3D}$:

$$d_{los}(t,\theta_{loc}) = \vec{u}\cdot\vec{d}_{3D} = \begin{bmatrix} \cos t\sin\theta_{loc} \\ -\sin t\sin\theta_{loc} \\ -\cos\theta_{loc} \end{bmatrix} \begin{bmatrix} d_x \\ d_y \\ d_z \end{bmatrix}_{defo} . \tag{68}$$

In order to invert the 3-D deformation vector from PSI deformation estimates, three or more independent measurements are required. *Eq. (68)* can be used as the functional equation to describe the relation between the Cartesian coordinates and the deformation measurements.

4.2 A short introduction of ICP method

ICP is a popular approach for solving the problem of registration of 3-D shapes or point sets without corresponding points (Besl and McKay, 1992; Zhang, 1994). For a given point set P with N_p points and a model shape M with N_m points, the unknown parameter is the transformation matrix $\mathbf{T}$ from P to M, which can be constructed by different operations such as rotation, translation, scale, etc. ICP estimates $\mathbf{T}$ iteratively. The initial parameters are $\mathbf{T}^{(0)}$, $P^{(0)} = P$ and iteration number $k = 0$. The k-th transformation matrix $\mathbf{T}^{(k)}$ is defined always relative to the initial data set $P^{(0)}$ in order to achieve the complete transformation at the end of the iteration. The following steps are iteratively carried out until the convergence criterion in step (3) is fulfilled:

(1) For each individual point $\vec{p}^{(k)} \in P^{(k)}$, its closest point $\vec{m}^{(k)} \in M$ is calculated (correspondent point set).

(2) Given this correspondence, the transformation matrix $\mathbf{T}^{(k)}$ between $P^{(0)}$ and M is estimated using least squares. Then the points of P are updated to $\vec{p}^{(k+1)}$.

(3) The mean square error d_k is computed with $d_k = \frac{1}{N_p} \sum_{i=1}^{N_p} \left\| \vec{m}_i^{(k)} - \vec{p}_i^{(k+1)} \right\|$.

Under assumption of accurate orbit determination, the effects of rotation, scaling, etc. are negligible in comparison with the elevation accuracy, e.g. worse than 0.5 m in the Stromboli test site (see section 4.5). Therefore, the transformation matrix $\mathbf{T}$ is limited to three degrees of freedom, a translation vector $\mathbf{t}$ in 3-D ($\mathbf{T} = \mathbf{t}$). Consequently, the step (2) is simplified as: $\vec{p}^{(k+1)} = \vec{p}^{k} + \mathbf{t}^{k}$.

4.3 ICP registration accuracy based on simulations

The registration accuracy of the ICP algorithm is highly dependent on the quality of the input data sets, the number of points and the data complexity. In order to assess the accuracy of the ICP for the problem of PS fusion, two simulation tests have been designed and performed. Firstly, the dependency of the accuracy on the SNR has been investigated. Secondly, the SRTM DEM of the Stromboli test site has been used as the simulation model in order to represent the complexity of investigating object. The dependency of the accuracy on the number of points has been evaluated. Thus a trade-off between the accuracy and the computational expense has been determined. More details on the simulated data sets are described in Appendix K.

4.3.1 Registration accuracy vs. SNR

Besl and McKay (1992) pointed out that the ICP method can handle noisy data as long as the standard deviation of a normally distributed noise is smaller than 10% of the object size. Based on the simulated object presented in *Fig. K.1*, two data sets are generated from the simulated object, one is extracted with a regular grid, and the other one with an irregular grid. Both data sets are defined as moving data sets. The simulated object is used as model data set. Independent white noise of a given SNR is added on two data sets. All points are shifted according to the translation matrix $\mathbf{t} = [20, 10, 5]$ m on the X-, Y- and Z-axes. This translation will be estimated by ICP. In order to evaluate the accuracy of the ICP, for each SNR value, 50 independent noise realizations and the corresponding ICP estimations are performed. Registration errors are derived by comparing the estimated translation matrix with the given matrix. And the standard deviation of the registration error is evaluated for each SNR and summarized in Table 12.

Table 12. The standard deviation of the registration error on X-, Y- and Z-axis, where SNR = 5, 15 and 25 dB.

Registration shape	**SNR = 5 dB**			**SNR = 15 dB**			**SNR = 25 dB**		
	δ_x[m]	δ_y[m]	Δ_z[m]	Δ_x[m]	Δ_y[m]	Δ_z[m]	Δ_x[m]	Δ_y[m]	Δ_z[m]
Regular grid	1.194	0.931	0.017	0.445	0.279	0.006	0.164	0.093	0.002
Irregular grid	1.482	1.399	0.018	0.901	0.630	0.011	0.720	0.605	0.005

The standard deviation of the registration errors increases with decreasing SNR for both moving data sets (Zhang, 1994). ICP registration of the noisy data set with the regular grid at SNR= 15 dB has a standard deviation of about 0.445 m in X-axis, 0.279 m in Y-axis and 0.006 m in Z-axis, respectively. At SNR= 5 dB, it increases to 1.194 m, 0.931 m, 0.017 m. For the irregular grid point set, the accuracy at SNR= 15 dB is about two times worse than using the regular grid point set, about 0.901 m in X-axis, 0.630 m in Y-axis and 0.011 m in Z-axis. The difference is reduced at SNR= 5 dB due to the high noise level, with the standard deviation of 1.482 m, 1.399 m and 0.018 m.

4.3.2 Registration accuracy vs. number of points

The accuracy of the ICP registration is sensitive to both, object complexity and number of points. The SRTM DEM of the Stromboli test site is used to specify the object complexity. The object can be represented discretely by a different set of points with different subsampling ratios. Therefore, the complexity is related to the number of points as well. The ICP computation time is mainly dependent on the search of nearest point, which is optimized by the K-d tree (Rusinkiewicz and Levoy, 2001). As discussed in Bentley (1990), the search time increases logarithmically with increasing number of points. In order to find a trade-off between the number of points and the computation time, an assessment has been carried out by performing ICP registration on a set of data sets with different point samples.

As described in Appendix K.2, two sets of grid lengths, which are slightly different (a constant offset of 5), are used to generate model and moving data sets from the given DEM. The data set with more points has been selected as the model data set. Random white noises with SNR $\in [5, 20]$ dB are simulated 50 times independently at each grid length and added on both data sets. Afterwards, all PSs in moving data set are shifted according to the translation matrix $\mathbf{t} = [-5.3, 16.5, 10.6]$ m. After the ICP registration, the estimated translations are compared with the true values.

The standard deviation of registration errors is depicted in *Fig. 69* for each component. The mean number of points is calculated from both data sets and used as X-axis. The minimum standard deviation is about 0.688 m in X-axis, 0.554 m in Y-axis and 0.116 m in Z-axis with more than 1.5×10^4 PS. Obviously, the standard deviation increases with decreasing number of points in three axes. The increase on two horizontal axes is more significant than for the vertical axis (Z-axis). In order to achieve an estimation accuracy of about 1 m, at least 5851 points are required (whose simulation provided standard deviation of 1.258 m, 1.246 m and 0.186 m in X-, Y- and Z-axis respectively).

Based on the simulation results, it reveals that the registration is more accurate in vertical than in horizontal. This is mainly due to the fact that the simulated object SRTM DEM presents a 2.5-D surface model, where the changes in horizontal are usually more significant than in vertical.

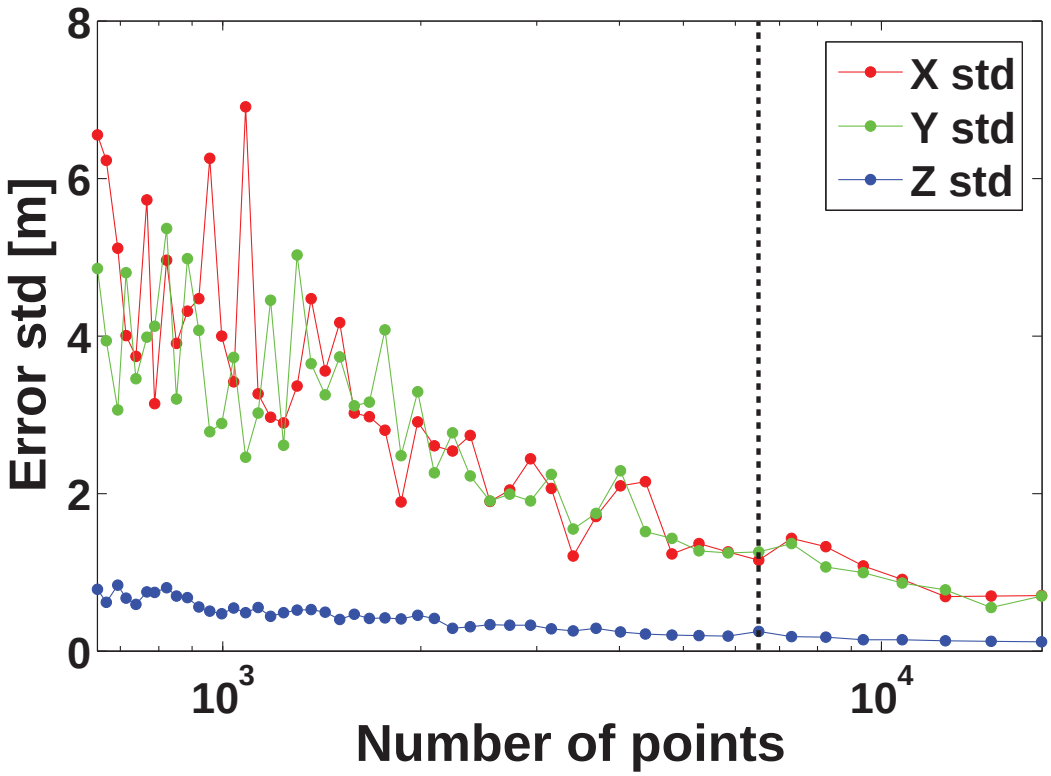

Fig. 69. The standard deviation of registration errors is depicted against the mean number of points calculated from both data sets, which is presented in logarithmic scale. The standard deviation in X-axis is plotted with red line, Y-axis with green line and Z-axis with blue line. The black dash line indicates selected threshold of 5851 points (black dashed line). Their standard deviations in X-, Y- and Z-axis are 1.258 m, 1.246 m and 0.186 m respectively.

4.4 Geometrical fusion of multi-track using ICP

Given the observation geometries of the satellite SAR_i in *Fig. 68* (SAR_a and SAR_b respectively), the main error in the estimated PS positions $\mathbf{t}_i$ is the offset l_i in the elevation direction $\vec{s}_i$:

$$\mathbf{t}_i = \vec{s}_i \cdot l_i, \tag{69}$$

where $\mathbf{t}_i$ is the translation vector, $\vec{s}_i$ is a unit vector and l_i is the magnitude of the offset. Depending on the availability of prior information, two geometrical fusion procedures are presented. In section 4.4.1, under the assumption that the offset of one stack has been precisely corrected using absolute measurements and is defined as the model stack. Then the offset of another stack is determined. In section 4.4.2, the unknown offsets of two stacks are jointly estimated when no reference information is available. The ICP algorithm is integrated into the fusion algorithm either to estimate the elevation offset directly or to obtain the distance between two stacks.

4.4.1 Multi-track fusion with absolute measurements

Let us assume that the absolute position of one stack could be fixed by means of absolute measurements, for example using corner reflector measurements with strong signals and known accurate coordinates. Then this stack is used as the model stack, denoted the model set P_1. The ICP algorithm is used to estimate the translation vector $\mathbf{t}_2$ of the unknown data set P_2 with respect to P_1. Note that the two data sets may well have different number of points

($N_1 = N_p \neq N_m = N_2$). According to *eq 69*, the elevation offset is derived from $\mathbf{t}_2$ as:

$$l_2 =< \mathbf{t}_2, \vec{s}_2 > . \tag{70}$$

4.4.2 Multi-track fusion without a priori information

In this section, the multi-track fusion approach without a priori information is introduced. Firstly, an iterative searching approach is explained for two stacks in section 4.4.2.1. In case of more than two stacks, elevation offsets are optimized based on the distance measurements of paired ICP, which is discussed in section 4.4.2.2.

4.4.2.1 Two-stack approach

Using the geometry described in section 4.1, an iterative searching approach has been developed in order to jointly estimate the offsets (l_1 and l_2) in the elevation directions ($\vec{s}_1$ and $\vec{s}_2$) of two stacks. The algorithm converges, only if the elevation vectors $\vec{s}_1$ and $\vec{s}_2$ are not parallel. In other words, two stacks from different geometries are necessary. Since both stacks are shifted along their respective elevation directions, no model stack is defined. Instead the ICP is only used to derive the distance between the two shifted stacks for given elevation offsets.

This iterative searching approach is divided into two steps:

(1) The search is performed within a coarse grid, with search offsets for each stack given by $l_i = n_i \cdot \Delta_i \in [S_{min,i}, S_{max,i}]$, such that $\Delta_i \in \mathbb{R}^+$, and $n_i \in \mathbb{Z}$, where $i = 1, 2$. For each pair of offsets $(n_1 \cdot \Delta_1, n_2 \cdot \Delta_2)$, the distance between the shifted point clouds is calculated according to $\left\|\vec{d}_s\right\|$, where

$$\vec{d}_s = ICP\Big(P_1(l_1 \cdot \vec{s}_1), P_2(l_2 \cdot \vec{s}_2)\Big). \tag{71}$$

ICP is constrained to search for an offset transformation. The pair of offsets (l_1, l_2) which minimizes this distance is selected as coarse offset estimates.

(2) A finer search range is defined around these coarse estimates with a length equal to Δ_i, namely $[l_i - \Delta_i/2,\ l_i + \Delta_i/2]$. The search approach is performed again over the new finer grid. Their results are the estimated offsets $l_1^{'}$ and $l_2^{'}$.

The search range can be iteratively refined following this principle until the total distance between two stacks changes less than a defined threshold value.

4.4.2.2 Multi-stacks approach

In the multi-stack approach, sn PS point clouds from different acquisition geometries are available, where $sn > 2$. Firstly, two-stack fusion approach is performed for $N = \frac{(sn-1)\cdot sn}{2}$ pairs. During the pairwise stack fusion as discussed in section 4.4.2.1, distances $\left\|\vec{d}_s\right\|_j$ with $j = 1, \cdots, N$ are computed for each pair, where point clouds are shifted first according to coarse grids $l_i = n_i \cdot \Delta_i$ with $i = 1, \cdots, sn$. For a given elevation offsets l_i in stack i, $sn - 1$ distance measurements are available after two-stack fusion. Instead of pairwise minimization, sn elevation offsets $(l_1, l_2, \cdots, l_{sn})$ are determined where all distances among all stacks are minimized. Similar to two-stack fusion, this approach can be carried out iteratively by refining the search grid.

4.5 Multi-track fusion results – Stromboli volcano multi-geometrical acquisitions

The Stromobli volcano (described in section 2.4.3.2) has been selected to demonstrate the proposed fusion algorithm. Four PS point clouds are available from different acquisition geometries (two descending and two ascending orbits). First of all, four stacks have been processed independently after mitigation of stratified atmospheric delay effects in phase measurements (see section 3.5.2). Afterwards, the topographic residual has been corrected on the reference height (provided from the SRTM DEM). The updated topography is used for geocoding, which transforms radar coordinates into UTM coordinate system. However, for an accurate geocoding, geodynamic and atmospheric delays in range need to be considered and compensated. A preprocessing step is thus performed in section 4.5.1. Then the elevation offsets are estimated based on the fusion method proposed in section 4.4.2. Finally, the fusion results are presented and discussed in section 4.5.2.

In order to obtain an impression of the PS localization accuracy, the theoretical accuracy is derived according to its SNR (Gernhardt, 2011), which is dependent on the coherence (Hanssen, 2001). A coherence threshold $\gamma \geq 0.7$ is used to select PSs for ICP registration. As a consequence, the minimum SNR of the selected PSs is about 5.2 dB, whereas the maximum SNR varies from 20.2 to 25.3 dB. The theoretical location accuracy has been calculated based on the pixel spacing and temporal and spatial baseline distributions. The following ranges summarize the expected accuracy for PSs in natural environments such as the Stromboli test site:

- ◇ range accuracy = 1.8 cm to 5.6 cm
- ◇ azimuth accuracy = 2.4 cm to 5.2 cm
- ◇ elevation accuracy = 51.3 cm to 131.6 cm

In summary, both range and azimuth accuracy are in the centimeter level in Stromboli. The elevation accuracy is about 25 times worse than both range and azimuth accuracy.

4.5.1 Preparation of multi-track PS point clouds

In order to ensure an accurate geocoding, range delays caused by the atmosphere and earth tides (discussed in section 2.2.1) need to be taken into account on the master geometry. Continental Drift (CD) can be neglected since the difference between four master acquisitions is within 100 days, where the tectonic deformation in Stromboli is less than 5 mm/year (Palano et al., 2012). Moreover, components with small absolute range delays ($<$ 1 cm) are ignored (see *Fig. 21*), namely, OTL and APL. In summary, three components: TD, ID and SET need to be corrected before geocoding and stack fusion.

- ◇ **Tropospheric Delay (TD)** has the largest impact on the absolute range delay, where the delay varies from 2.5 to 3.5 m depending on the incidence angle, the location and the acquisition time. For an accurate geocoding, TD at the master acquisition time has been integrated for each PS and compensated directly in range (see section 3.5.2).
- ◇ **Ionospheric Delay (ID)** has a relatively smaller impact in the centimeter-range. Since the TerraSAR-X satellite is located in the ionosphere, 75% of the total delay is compensated in range. The ionospheric delay has a value of approximately 6 cm in the ascending tracks (beam 033 and 069) and about 4 cm in descending ones. Because of the small coverage of the HRSL acquisitions, a constant delay derived from average slant ranges is corrected on master acquisition.
- ◇ **Solid Earth Tides (SET)** impact on the range delay also in the centimeter-range. Similar to ID delay, the variation of SET in the scene is neglected due to the small coverage.

Therefore, the SET is only calculated on the center coordinate of the PS point cloud. It has a total variation from −8.9 to 6.9 cm from different acquisition times. Similar to ID, this delay is treated as a constant offset and is compensated in range.

In summary, the total impact of the three delays varies from 2.758 to 3.303 m, which has been compensated for each PS. The geographic height of each PS point is updated according to the PSI topographic estimate. Finally, each of the four PS point clouds is geocoded to UTM coordinate system by means of their satellite orbits and the updated PS heights. *Fig. 70* depicts all PS point clouds overlapped directly after geocoding. Due to inaccurate elevations, the four PS point clouds are dislocated. This effect can be clearly observed along coastlines and mountain ridges.

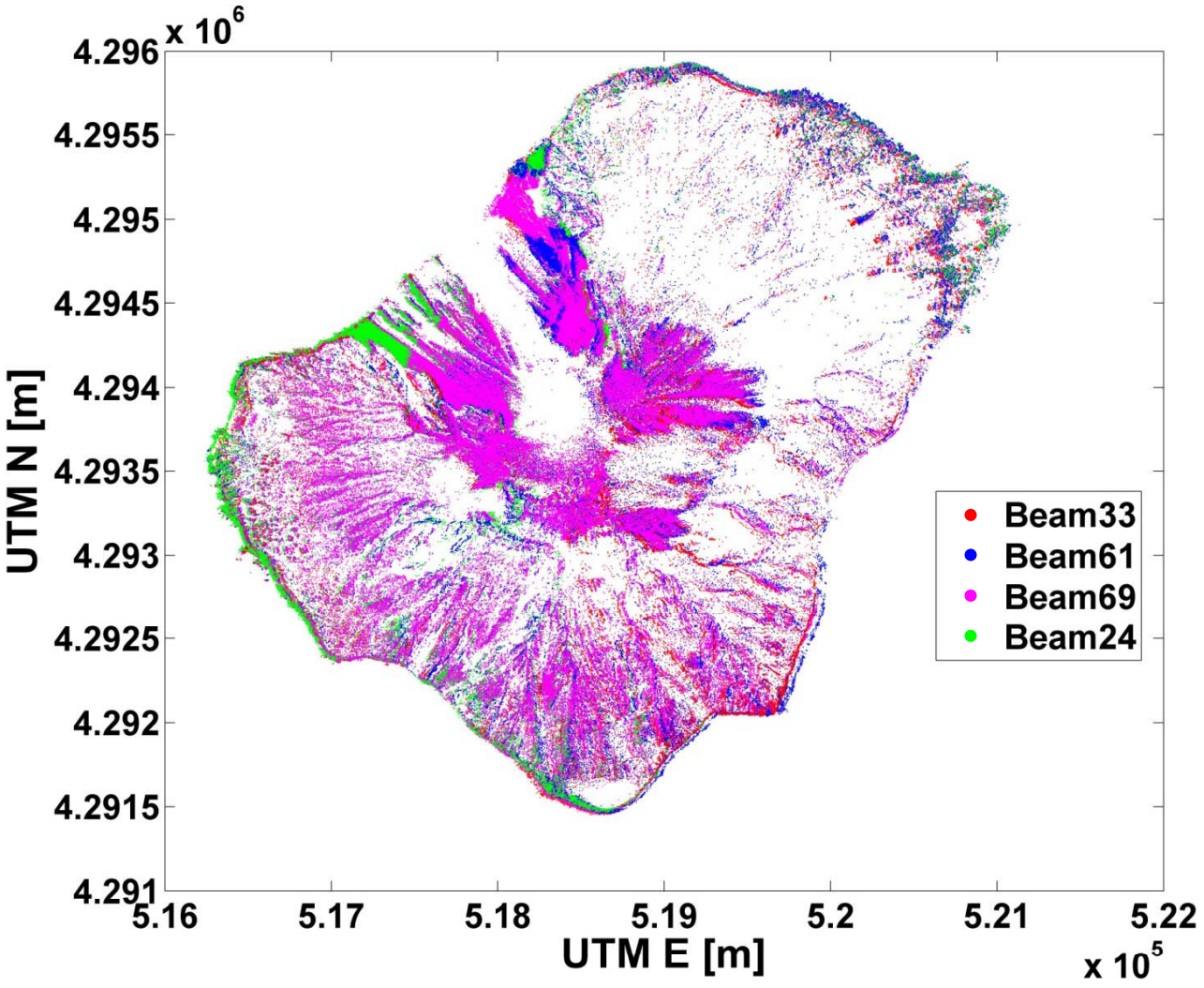

Fig. 70. Four geocoded PS point clouds in Stromboli are depicted using four different colors to indicate four TerraSAR-X HRSL beams: beam 033 (red), beam 061 (blue), beam 069 (magenta) and beam 024 (green). TD, ID and SET delays have been already corrected in range before geocoding.

4.5.2 Fusion results

In order to obtain the full coverage of the Stromboli volcano, the fusion algorithm described in section 4.4 has been applied on four geocoded PS point clouds (see section 4.5.1). The search approach has been carried out with paired adjacent tracks as well as cross-heading tracks. No master stack needs to be determined, because two stacks are moved successively along the

elevation direction within the search range to achieve the minimum distance between two point clouds using ICP.

In total, more than 4.4×10^6 PSs are available after final PS estimation. According to the analysis presented in section 4.2, a spatial subsampling of the point clouds is performed. A spatial grid is defined for each PS point cloud. The PS with the highest coherence is selected in each grid cell. For ICP fusion, six combinations of PS point cloud pairs are available, 3 adjacent pairs and 3 cross-heading pairs. For each pair a pseudo model stack is determined according to the mean coherence of selected PSs. Ignoring the noise in the PS point clouds, elevation offsets estimated from independent procedures should be identical. In practice, a mean offset is calculated for each PS point cloud.

4.5.2.1 Fused PS-DEM

In PSI processing, the SRTM DEM acquired in the year 2000 was used to partially compensate the interferometric topographic phase. In 2002-2003 and 2007, two effusive eruptions at Stromboli volcano took place. These events triggered several landslides in Sciara del Fuoco (SdF) (Bonaccorso et al., 2003; Baldi et al., 2005; Marsella et al., 2012) and thus considerable topographic changes took place. On one hand, these changes can be used to interpret geomorphological evolution (see section 5.1.1). On the other hand, an update of the reference DEM can be used for a better estimation of the deformation.

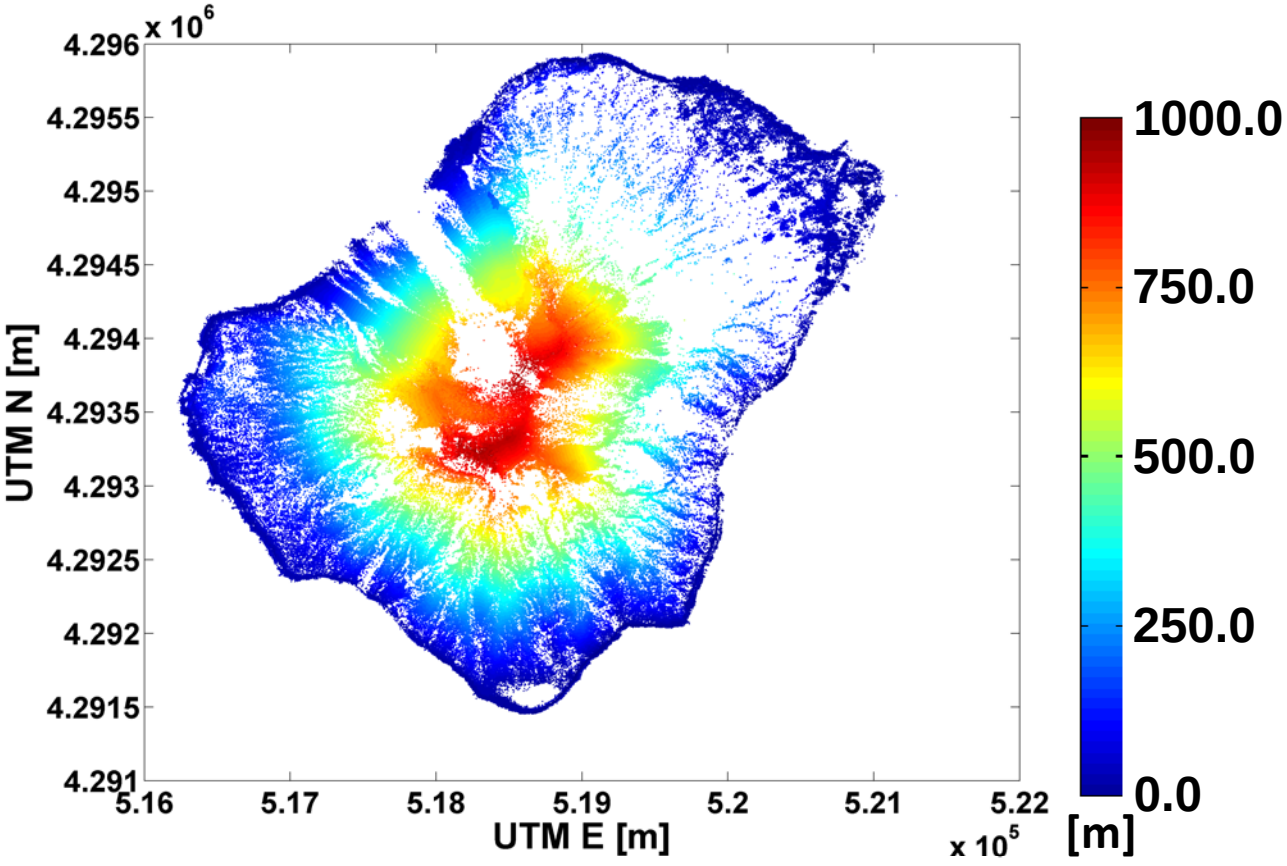

Fig. 71. Fused PS-DEM using four geocoded PS point clouds presented in *Fig. 70*. A full color cycle indicates the PS height from 0 to 1000 m.

After geometrical fusion, the discrepancies between PS point clouds caused by elevation offsets have been compensated. All PSs from different stacks are thus merged together. A updated DEM with more than 4.4×10^6 PSs is presented in *Fig. 71*. Comparing to the single geometry, the coverage is significantly improved through complementary geometries, especially in problematic

areas (shadowing and layover). Nevertheless, some regions are still uncovered, such as the SdF slope, due to rapid surface changes induced by volcanic activities and vegetation.

4.5.2.2 Deformation decomposition

The deformation velocity measured in PSI is the projection of the deformation vector along the LoS direction. For 3-D reconstruction of the deformation vector, at least three observations from different geometries are required. The functional model for inversion is constructed according to the geometrical relationship described in *eq. (68)*. As discussed in Gernhardt (2011), TerraSAR-X has a near-polar orbit which leads to weak sensibility of the northern deformation component. Therefore, the functional model is practically limited to two deformation components: the vertical component (d_z) and the east component (d_x). After restriction to (d_x, d_z), the sensitivity vector of the functional model (*eq. (68)*) must be normalized. The resulting equation is:

$$\cos t \sin \theta_{loc} \cdot d_x - \cos \theta_{loc} \cdot \mathrm{d}_z - d_{los} \cdot \sqrt{\cos^2 t \sin^2 \theta_{loc} + \cos^2 \theta_{loc}} = 0, \tag{72}$$

where d_{los} is the LoS deformation estimated by PSI and (d_x, d_z) are the unknown deformation components. In order to perform a robust model inversion, we assume that the nearby PSs are of the same origin. Practically, PSs from different geometries located in a small cube around the point of interest are selected as observations. This search is performed based on the fused PS point cloud after multi-track fusion, where the PS position has been corrected. Afterwards, a linear equation system is constructed based on *eq. (72)* applied to each PS (Gernhardt, 2011). Finally, the unknown deformation components are solved by means of LSA.

In Stromboli, a cube of 15 m $\times$ 15 m $\times$ 15 m is defined to used as homogeneous region to perform deformation inversion. Additionally, at least two geometries must be available. In total, over 17×10^4 PSs have been estimated. About 9×10^4 PSs have an accuracy better than 4 mm/year on vertical and horizontal components. Decomposed deformations are presented in *Fig. 72(a)* for the vertical component and *Fig. 72(b)* for the east component.

The deformation patterns from both components are correlated. The most active region locates on the NW flank (SdF) with a west-bound deformation of up to 200 mm/year. These deformation phenomena on the SdF slope are discussed in section 5.2. On the southern side indicated by the red ellipse in *Fig. 72*, a small vertical deformation of about -10 mm/year is observed. It might be induced by a deflation process in Stromboli (Bonaccorso et al., 2009) or by some unpredictable effects, such as volcanic eruptions caused water vapor ejection (Fiorani et al., 2011). The deformation pattern observed on the most northern part of Island might be caused by inaccurate block merging during the PSI processing.

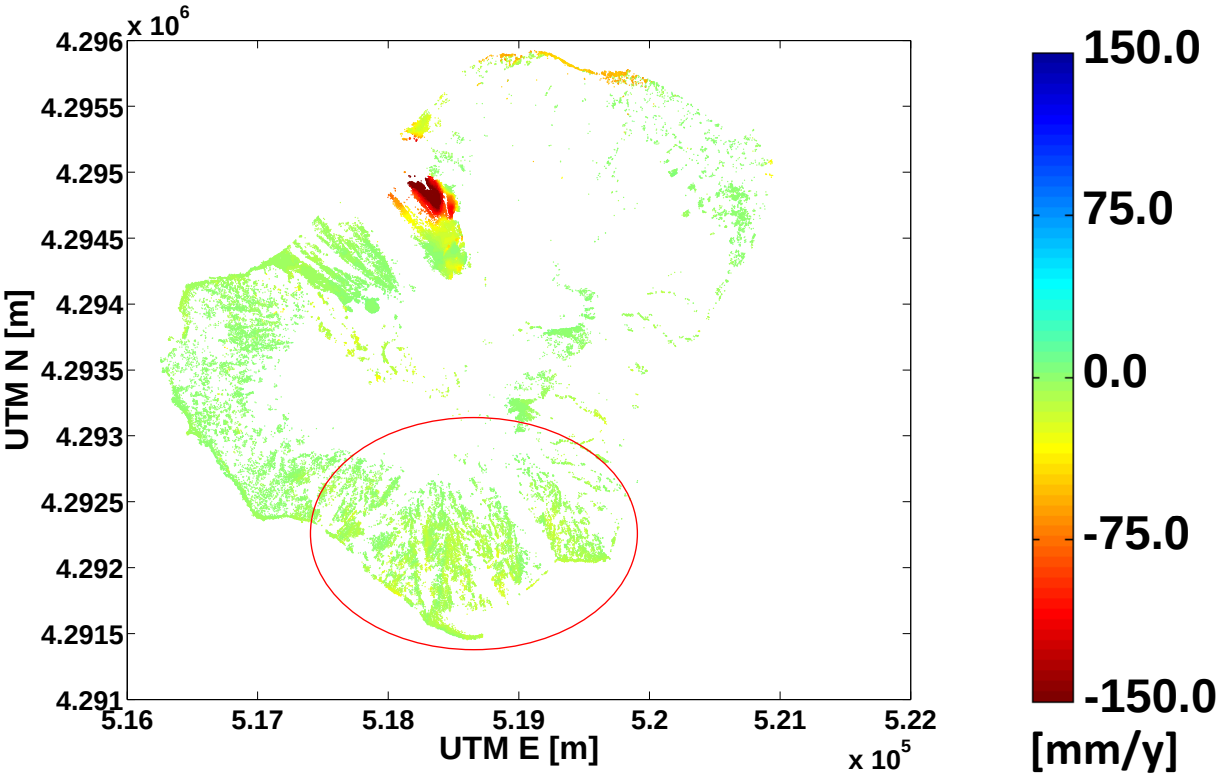

(a) Vertical deformation

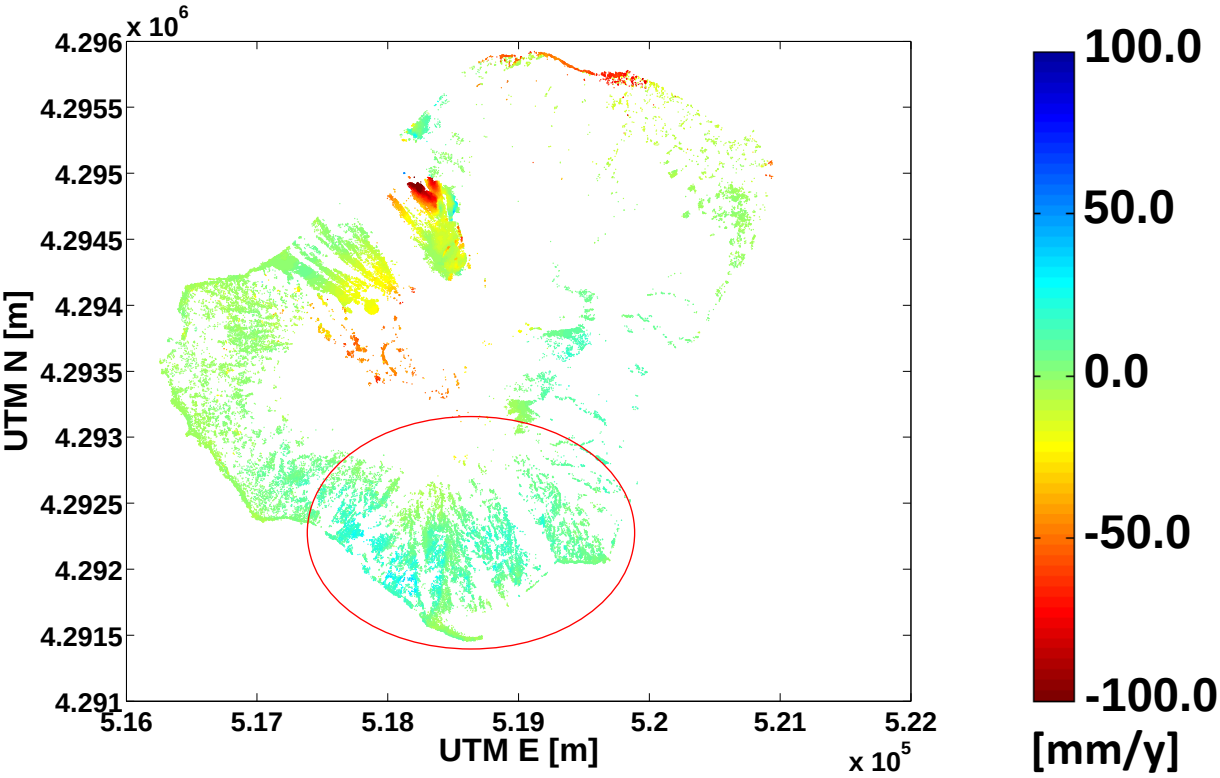

(b) East deformation

Fig. 72. Decomposed deformation estimates based on the linear deformation model: (a) in vertical and (b) in east direction. Two colorbars are from 150 to −150 mm/year in (a) and from 100 to −100 mm/year in (b). The red ellipse indicates the area with small deformation which may be induced by deflation.

5 Geological interpretations in Stromboli

The present shape of the Stromboli volcano was built up progressively by three caldera collapses and five lateral collapse events (Tibaldi, 2001). The nested horseshoe-shaped scar opening located on the North-East (NE) flank is the well-known SdF depression (see *Fig. 73*). It opens to the northwest and was formed by sector collapses from 13 ka (kiloannum = one thousand years) (Nolesini et al., 2013). This steep slope is constituted by irregular alternations of volcaniclastic layers and thin lava flows (Boldini et al., 2009). It exhibits most dynamic changes in Stromboli, due to lava flows, rock falls, landslides, lava accumulation, condensation, etc. Current volcanic activities are concentrated within the summit crater zone which is located in the upper part of the SdF and is enclosed with a thick red line in *Fig. 73* (Coppola et al., 2012). This summit crater zone has remained constantly on its current position. Nevertheless, the number and size of vents inside are varying with time due to changing magma level within the conduit (Calvari et al., 2012).

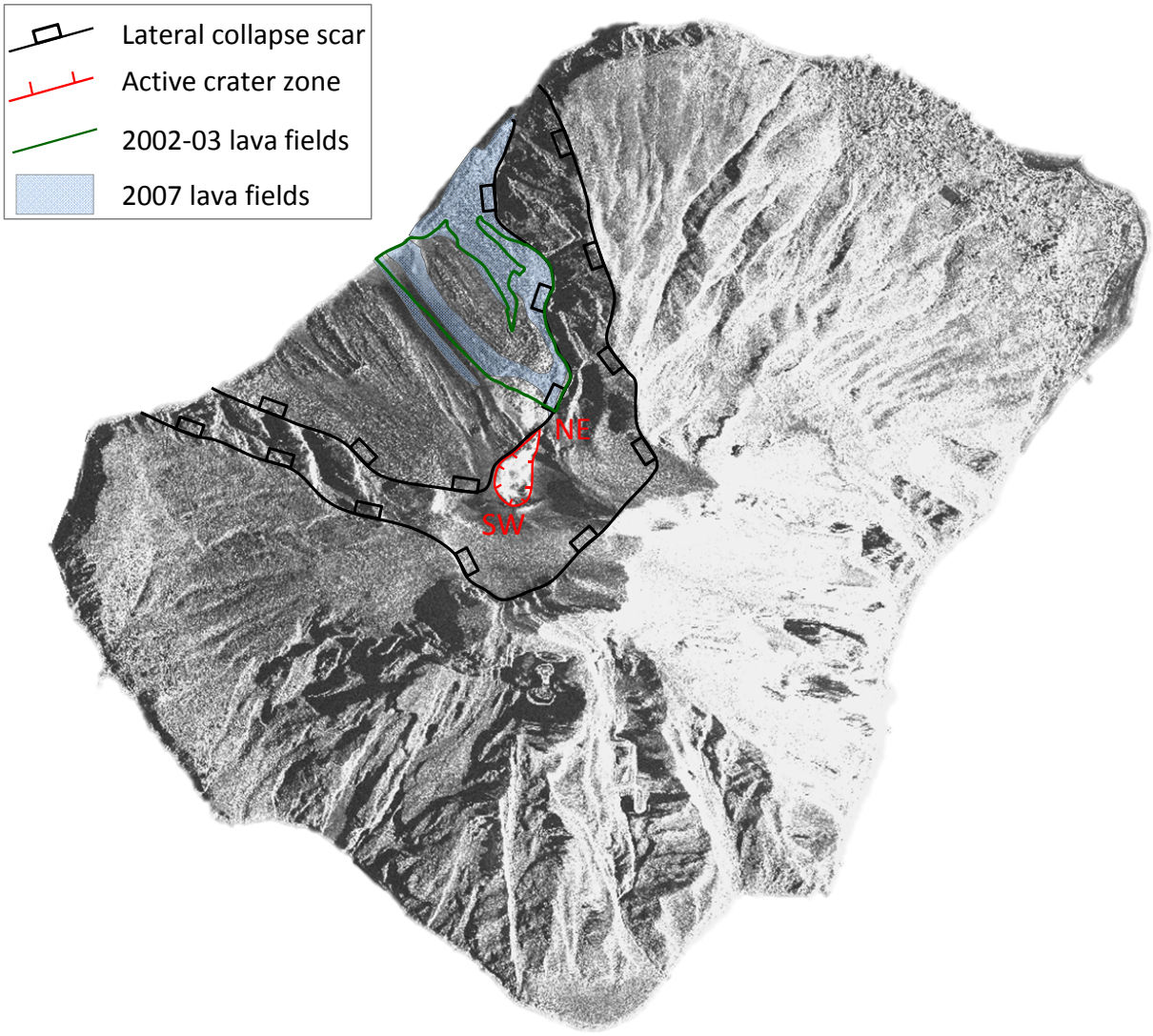

Fig. 73. Geocoded SAR mean amplitude image from beam 061 is used as the background image. The following geological structures on the SdF are depicted: lateral collapse scar on NW flanks (black line); active summit craters in the upper part of the scar (red line); lava fields from 2002-2003 (blue area) and 2007 eruptions (solid green line).

Depending on the intensity of the volcanic explosions, the activity in Stromboli is divided into two types: the normal (also known as Strombolian) activity and the major activity. The "normal" activity in Stromboli is characterized by mild explosions which take place at active craters with an interval of 10 to 20 minutes and last for a few seconds (Rosi et al., 2000; Tibaldi, 2001; Calvari et al., 2012). This activity is periodically interrupted by "major" (moderate intensity) and "paroxysms" (higher intensity) eruptions accompanied usually by more energetic explosions (Rosi et al., 2000; Nolesini et al., 2013). The two most recent major effusive eruptions, which occurred in 2002-2003 and in 2007, induced large morphological changes on the SdF. The lava fields corresponding to the multi-temporal DEM comparison reported in Marsella et al. (2012) are depicted in *Fig. 73*. In order to closely monitor volcanic risk, a new geodetic network consisting of different geodetic techniques was set up in Stromboli since 2003 (Puglisi et al., 2005). Ground deformations and volcanic activities are continuously observed and analyzed (Marchetti et al., 2009; Aiuppa et al., 2009; Casagli et al., 2009; Calvari et al., 2010, 2012).

The multi-track atmospherically mitigated PSI approach proposed in this thesis provides deformation and topographic estimates which are useful for the monitoring of surface changes. Firstly, the PS-DEM updates are used to explain large geomorphological changes on the SdF due to the 2002-2003 and 2007 effusive explosions in section 5.1.1. Moreover, this information is complemented by a visual time-analysis of SAR amplitudes over crater zone with highly complex geomorphological evolution, where thus PSI estimation cannot be performed (section 5.1.2). Secondly, the "slow" ground deformation on the SdF slope estimated using PSI processing is analyzed in section 5.2.

5.1 Topographic and morphological changes of the Sciara del Fuoco from 2000 to 2008

The SdF slope is affected by alternating constructive and destructive phases. The constructive phases are a result of lava flow emplacement from major effusive eruptions and from pyroclastic products from the continuous normal activity (Marsella et al., 2012). The destructive phases are principally related to progressive erosive processes and are occasionally contributed by mass wasting due to landslides. The topographic and geomorphological changes from 2000 to 2008 are mainly due to two effusive eruptions and sporadic volcanic activities.

5.1.1 The 2002-2003 and 2007 eruptions

The SRTM DEM acquired in 2000 has been used as reference DEM in PSI processing in order to compensate the topographic component of phase measurements (Farr et al., 2007). Due to the later flank instability related to the 30 December 2002 landslides and to the large paroxysmal eruptions in 2007, large topographic and morphological changes on the SdF are expected. These changes have been evaluated in several publications by means of multi-temporal DEMs (Baldi et al., 2005, 2008; Marsella et al., 2012).

In order to retrieve an accurate DEM update, all PSs with coherence higher than 0.7 located in a 15 m $\times$ 15 m $\times$ 15 m cube and estimated from at least two different acquisition geometries are used to calculate a local mean topographic update. The mean updates over the whole island are depicted in *Fig. 74* with a geocoded SAR mean amplitude image as background. Due to the lower spatial resolution of the reference DEM (SRTM DEM), some features over rugged terrain, such as mountain tops, valleys, or ridges, are smoothed (Rodriguez et al., 2006). Therefore, topographic changes are observed also outside of the active slope, which are mostly positive on mountain tops and ridges and are negative in valleys. Moreover, large DEM height errors can be detected over very steep terrain in Stromboli (discussed in section 2.1). Nevertheless, the

terrain changes on the SdF slope are relatively smooth and interferometric phase measurements are coherent due to the arid surface. Therefore, the SRTM DEM is used as reference in order to identify the morphological changes occurred on the SdF between the SRTM acquisition time (2000) and the acquisition time of the PSI stacks (2008). Over 5.0×10^4 average PSs topographic updates have been estimated on the slope and are depicted against height in *Fig. 74(b)*.

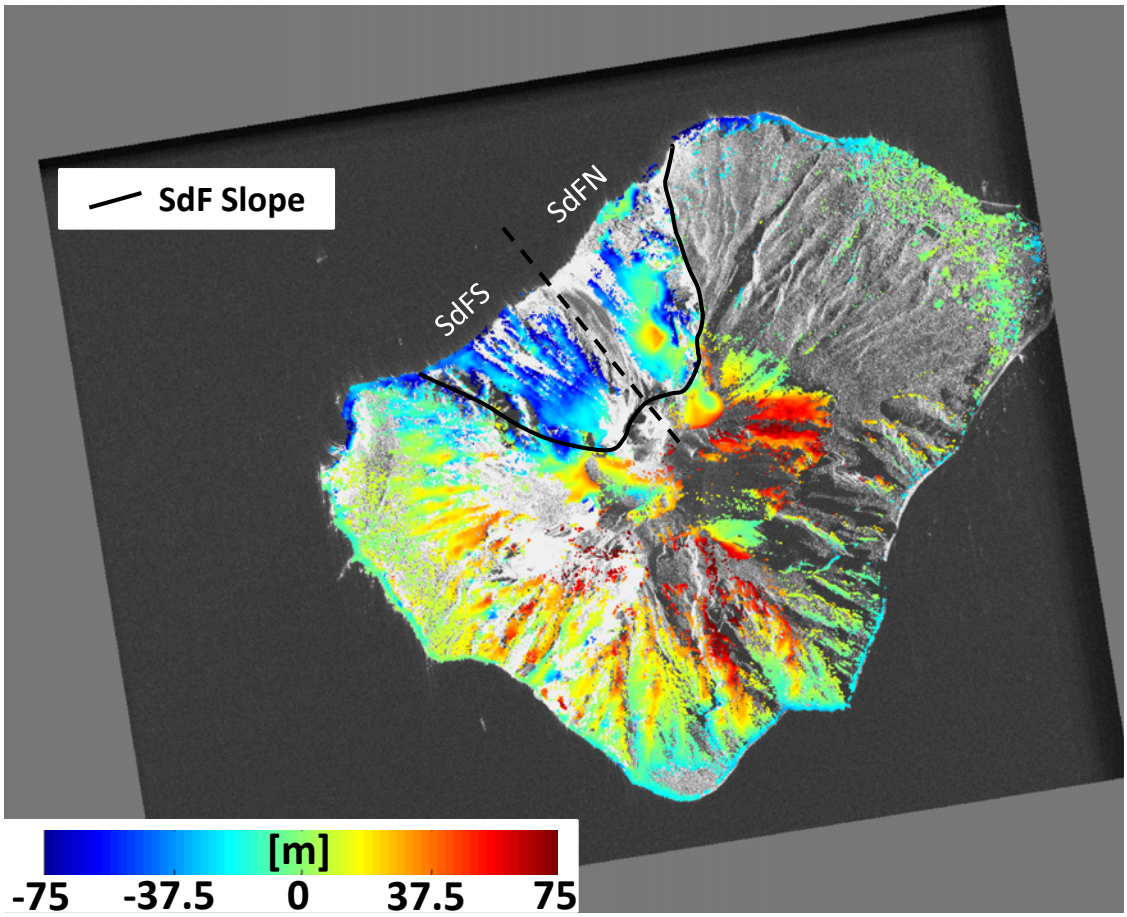

(a) Mean topographic updates (2000-2008)

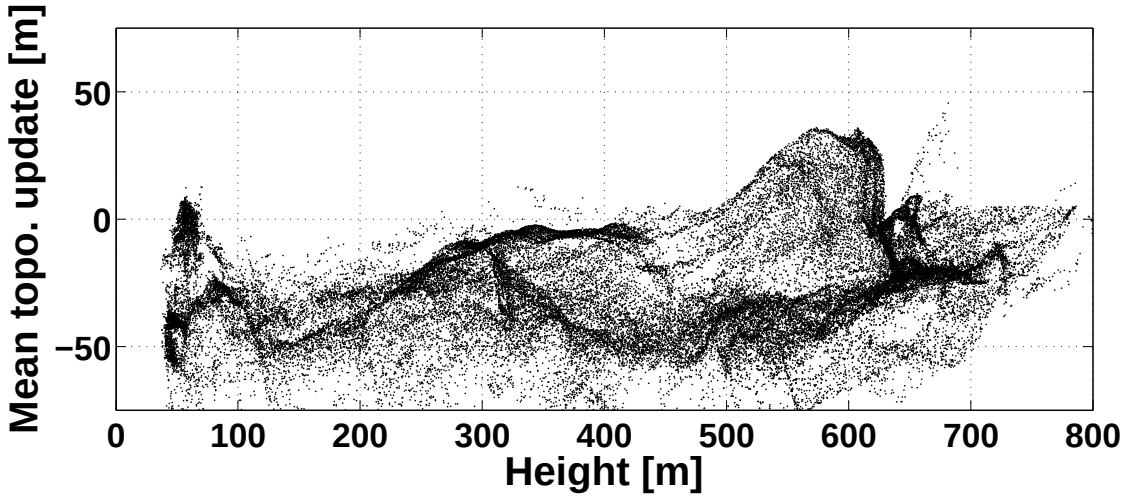

(b) Scatter plot of mean topographic updates against height on the SdF slope

Fig. 74. Average PS topographic updates: (a) Topographic changes are depicted with geocoded SAR mean amplitude image from beam 069 as background. The SdF slope depicted with black line is divided into the northern part (SdFN) and the southern part (SdFS). A full color cycle indicates the topographic difference from −75 to 75 m. (b) Mean topographic updates on the SdF is depicted against PS height.

.

The topographic changes depicted in *Fig. 74* represent the total accumulated changes from 2000 to 2008. Active areas, such as the summit crater zone and lava terraces, are decorrelated due to rapid surface changes and thus no measurements are available. On the SdF, more than 85% of PSs are measured with a negative topographic update. These mass changes are mainly caused by superimposed landslides and flank failures induced by the 2002-2003 and 2007 effusive eruptions and also partly by erosive processes and magma intrusions (Marsella et al., 2012). The slope is naturally separated into two parts by the north-west orientated lava terraces and thus is divided into the northern part (SdFN) and the southern part (SdFS), as depicted in *Fig. 74(a)*.

Due to the superimposed lava flows from different main eruption periods and the slope instability induced landslides, complicated morphological changes are observed on the SdFN (Baldi et al., 2005, 2008; Marsella et al., 2012). Two accumulation areas can be observed on the SdFN, where lava flows emitted from two major eruptions in the period from 2000 to 2008 are accumulated (see *Fig. 74(a)*). A cycle-shaped accumulated area is located directly below the summit crater zone, at an altitude of 630 m and spreading until the altitude of about 510 m. The maximum topographic increase is about 36.0 m and the average is about 17.6 m (Baldi et al., 2005; Marsella et al., 2012). A fan-shaped lava field was constructed along the coast. Unfortunately, most of the lower region of the SdF is decorrelated due to fast surface changes. Nevertheless, a small region with an average change of about 3.2 m can be measured. The largest negative changes are over -75 m, which are observed on the NW fissure along the northern SdF. These are affected by effusive activities starting on 27 February 2007 (Casagli et al., 2009; Calvari et al., 2010).

On the other hand, the morphological changes observed on the SdFS are mainly caused by progressive erosion processes. The changes are more homogeneous with an average value of about -14.7 m, since the recent lava emplacement has mainly taken place on the SdFN.

In summary, the topographic changes on the SdF estimated by PSI have a good agreement with the multi-temporal analysis reported in Baldi et al. (2005, 2008); Marsella et al. (2012). Moreover, accumulated topographic changes from 2000 to 2008 on the SdF have been analyzed based on over 5.0×10^4 PSs topographic updates. Even in the merged PSI estimates, the topographic changes over lava terraces and highly active areas (the summit cater zone and lava fields) can not be estimated due to rapid surface changes occurred during the TerraSAR-X stacks acquisition period. Furthermore, the average topographic changes have been corrected on the reference DEM, which is used for deformation analysis in section 5.2.

5.1.2 The 7 September 2008 explosive event - the morphological changes at the summit vents

During the paroxysmal eruptions in 2007, several collapses occurred within the summit crater zone and caused significant morphological changes (Marsella et al., 2012). According to the explosive activity reported in Calvari et al. (2012), three trends were observed: firstly a constant low explosive rate from January until mid March 2008; then a new trend started with increasing explosive events until mid August; finally a trend of decrease of explosive activity.

The morphological development of the crater area can be observed through the intensity changes in multi-temporal SAR images. A sequence of SAR intensity images of the summit crater zone acquired from 29 January to 27 September 2008 is presented in *Fig. 75*. During the period of increasing explosive events, the size of the vents inside the summit crater zone changed gradually on both the northern and the southern part of the crater zone. A new vent was opened on 22 June 2008 on the northern part, which caused an intensity change and can be observed in SAR images after 20 June 2008 in *Fig. 75*. During a major ash explosion on 7 September 2008, visible morphological changes at the summit vents took place. These changes

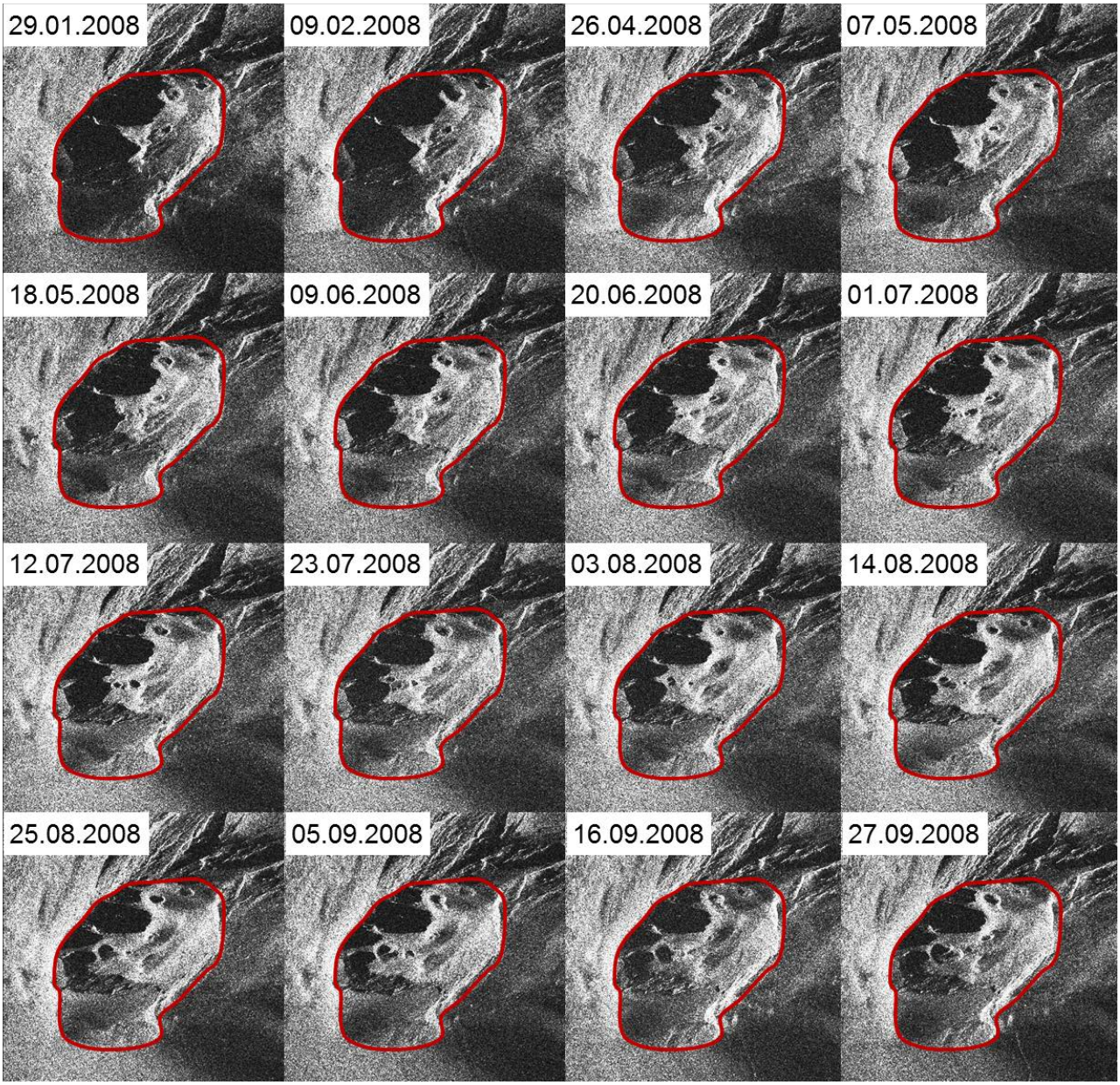

Fig. 75. A sequence of SAR intensity images around the summit crater zone acquired from 29 January to 27 September 2008 from beam 069 (ascending orbit).

can be observed by comparison of the intensity images acquired on 5 and 16 September 2008. This visual interpretation is very useful to identify the morphological changes induced even by normal activity with lower energy.

5.2 Long-term ground deformations during 2008 on the SdF slope

The long-term ground deformation on the SdF estimated by PSI is discussed in following two sections. Due to the different deformation behaviors and location, the discussion is given separately for SdFN (section 5.2.1) and for SdFS (section 5.2.2).

5.2.1 Ground deformation on the SdFN

The most active region locates on the SdFN direct by below the summit crater zone (see *Fig. 73*), where maximum deformation velocity of about −240 mm/year is observed in vertical component (see *Fig. 72(a)*) and −114 mm/year in east component (see *Fig. 72(b)*) based on the fused PS deformation maps. On the SdFN, the steep slope and loosely-compacted deposits might induce a landslide-like mass gravity movement. Therefore, the correlation between the slope angle and the deformation ratio has been evaluated based on the PSs which have a vertical deformation smaller than −5 mm/year. On each PS, the east-west gradient ($\delta x/\delta z$) derived from the updated SRTM DEM and the deformation ratio (d_e/d_v) between the east (d_e) and the vertical component (d_v) are depicted in *Fig .76*. The deformation pattern Blow the cycle-shaped accumulated area discussed in section 5.1.1 (elevation < 530 m), the deformation ratio shows a good agreement with the east-west gradient, with a the correlation of about 51.4%. The overall correlation is about 37.5%.

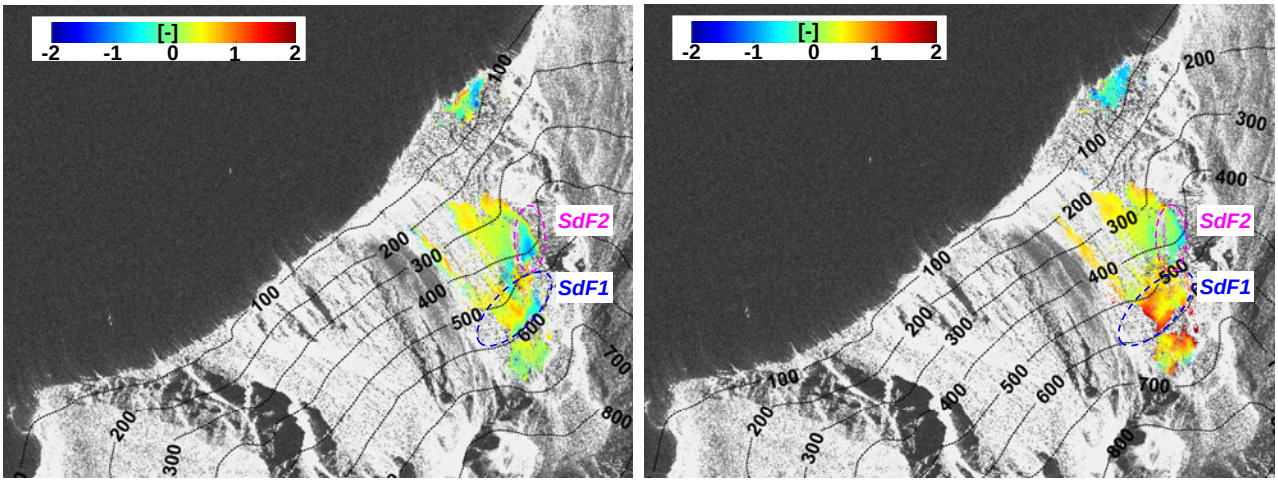

(a) East-west gradient component ($\delta d_x/\delta d_z$) (b) Deformation ratio (d_e/d_v)

Fig. 76. Analyzing the relationship between the slope angle and the deformation ratio on the SdFN: (a) the east-west gradient ($\delta x/\delta z$) derived from the updated SRTM DEM; (b) the deformation ratio (d_e/d_v) between the east (d_e) and the vertical component (d_v). Two small regions SdF1 and SdF2 are marked with blue and magenta ellipses. The average amplitude image from beam 069 is used as background image and overlaid with the isolines generated from the updated SRTM DEM.

.

For a more detailed analysis, two small regions, SdF1 and SdF2, are defined on the SdFN according to their different deformation characteristics (see *Fig. 76*). The average deformation velocity from the elevation above 500 m until the border of the summit crater zone (defined as SdF1) is about −10.3 mm/year, where the minimum deformation located on the top of the accumulation area is with an amplitude of approximately 56.0 mm/year in vertical and 67.5 mm/year to the east (see section 5.1.1). A small deformation pattern (defined as SdF2) presents a faster displacement rate in vertical of about −108.0 mm/year, which is situated on the northern side outside the landslide region defined by Boldini et al. (2009); Intrieri et al. (2013) with the elevation between 300 and 500 m. Compared to SdF1, the horizontal deformation has an inverse direction with the maximum deformation of about 41.8 mm/year (to the west). Both vertical and horizontal deformation velocities reach their minima inside the landslide region at the altitude of about 300 m and 224 m, respectively. Both deformation patterns observed on SdF1 and SdF2 have a good agreement with the displacement rate derived from the Ground Based InSAR (GB-InSAR) system installed on the NW flank of SdF (Puglisi et al., 2005; Casagli et al., 2009; Nolesini et al., 2013; Intrieri et al., 2013). This "slow" deformation velocity observed both by GB-InSAR and PSI is excluded from earth flow and small debris avalanches. This superficial movements can be interpreted as slope instability phenomena,

where the gravitational component produces a constant creep (Intrieri et al., 2013). The SdF1 region is continuously affected simultaneously by erosion and accumulation processes due to lava accumulation during normal activities. The large deformation rates in SdF2 indicates a high loss of material, which is related to the thick lava layers accumulated from recent eruptions and move like a slide (see *Fig .76*).

In summary, the large deformation on the lower part of the SdFN is mainly induced by landslide-like mass gravity movements, whereas the deformation on the upper part of the SdFN is related to lava erosion and accumulation processes.

5.2.2 Ground deformation on the SdFS

On the southern part of SdF slope, the amplitude of both vertical and horizontal deformations is less than on the northern part. However, on the upper part (altitude $\geq$ 800 m), a maximum horizontal deformation to the east is observed with an amplitude of about 68.5 mm/year. On the lower parts, the amplitude of deformation velocity (to the east) decreases from approximately 35.6 mm/year to zero linearly from 650 to 200 m. According to the field geological data published in Casagli et al. (2009), three main fissures, located on the upper part, propagated towards to the active summit crater zone (north-east). An accumulated dilation of about 1 m has been measured during last 7 years (from 2000 to 2007). These deformation processes are linked with left-lateral strike-slip plane and indicate a downthrow of the seaward block, which are unlikely to be related to contemporaneous main magma intrusions (Casagli et al., 2009).

6 Conclusion and outlook

6.1 Conclusion

In the introduction of this thesis, the challenges as well as the limitations of applying SAR interferometry to volcanic areas have been formulated and described. The aim of this thesis is to:

"develop advanced techniques in order to retrieve reliable surface deformation signal from active volcanoes using high resolution SAR images."

The Stromboli Volcano has been selected as the main test site in order to analyze the described limitations and to evaluate and validate the proposed methods.

The content of this thesis has been structured as follows. Firstly an analysis and evaluation of the potentials of high resolution SAR interferometry for reliable deformation estimation in volcanic areas has been performed. Secondly, the mitigation of the stratified atmospheric delay in both SAR ranging and differential interferometry techniques has been studied. A mitigation technique based on Numerical Weather Prediction (NWP) data has been proposed and validated for both applications. Thirdly, a technique for the geometrical fusion of PSI point of clouds in non-urban area has been proposed and demonstrated in the Stromboli test site. Finally, the resulting topography and deformation estimates have been interpreted from a geological perspective.

The following are the main research contributions of this thesis.

- The potential of applying **high resolution SAR interferometry** in volcanic areas have been studied. The Persistent Scatterer Interferometry (PSI) technique has been successfully applied in **rocky volcanoes** using TerraSAR-X High Resolution Spotlight (HRSL) images with spatial resolution of about 1 m. At this high spatial resolution, stable rocks remain coherent in the interferograms even with a large temporal baseline. Therefore, natural scatterers behave as Persistent Scatterer (PS) and can be used for PSI processing. In the Stromboli test site, the *PS density* is about 1.0×10^4 PS/km^2, which is more than 100 times higher than the PS density for a middle resolution sensor.

- The **stratified atmospheric delay** in volcanic areas has a great impact on both interferometric and absolute ranging measurements. An effective method to mitigate this delay based on the **4-dimensional NWP products** has been developed: the *direct integration method*. This method has been successfully applied to mitigate the stratified atmospheric delay for both interferometric and ranging measurements.

  Two NWP products, *ERA-Interim* and *ECMWF OP data*, based on a hydrostatic model (ECMWF) are used for integration of the stratified atmospheric delay. These products are provided four times per day (at 0, 6, 12 and 18 h respectively). The accuracy of the integrated delay derived from these products is in the ***centimeter-range*** in the zenith and in the slant range directions.

  The accuracy of the integrated delay is mainly correlated with the total water vapor content and its variation, which are themselves dependent on factors such as location, season or time. In the zenith direction, the estimation accuracy evaluated against GNSS Zenith Path Delay (ZPD) collected from seven EUREF GPS stations is in the millimeter- to centimeter-range (from about 6.0 mm to 13.0 mm). The statistical analysis of the ZPD estimation residuals at each NWP product analysis time shows that the maximal standard deviation is observed at midnight (0 h), whereas the minimum standard deviation is often in early morning (6 h). Results from the monthly analyses reveal that the integrated delay is more accurate during

the winter months than during the summer months. This seasonal effect is smaller in tropical regions, where the temperature shows no significant seasonal variation. In the slant range direction, the delay accuracy decreases to 17.5 mm due to the time difference between the SAR acquisitions and the analysis time of the available NWP products.

The *variation of atmospheric delay* has been analyzed based on the integrated ZPD on the WTZR station. Both diurnal and seasonal variations are observed in the hourly and monthly statistical analyses. The daily maximum delay is observed at 0 h and the minimum at 6 h. The seasonal variation is highly correlated with water vapor content: the minimum of ZPD is observed in the winter months and the maximum in the summer months.

The effect of the *stratified atmospheric delay* in PSI estimation depends on the temporal and geometrical baseline distribution of the stack. A simple mitigation by linear fitting of the final PSI estimation results as a function of height and its compensation is insufficient, since the atmospheric delay decreases exponentially with increasing height. The proposed direct integration method has been successfully applied in order to correct the stratified phase component of the interferometric phase on each interferogram prior to PSI estimation. As a result, the effect of the stratified delay on PSI estimation in the Stromboli test site has been effectively mitigated.

The structure function is applied in order to describe the energy of *turbulent mixing* using unwrapped residual interferometric phases. The fitted power-law exponents in intermediate and large scales have a good agreement with the expected values.

- ◇ **Geometrical fusion of multi-track PS point clouds** based on ICP has been proposed for non-urban areas due to the absence of correspondent PSs. For accurate geocoding, three delay components, TD, ID and SET, are compensated before geocoding and stack fusion. The impact of these delays varies from 2.758 m up to 3.303 m. Different geometrical fusion approaches have been introduced depending on the a priori information and on the number of geometries available. After multi-track fusion, a north and east deformation decomposition relative to a common reference in time and space can be performed. The deformation patterns observed on the Sciara del Fuoco (SdF) are interpreted as slope instability phenomena, where the gravitational component produces a constant creep. Furthermore, the fused PSI estimates of the topographic updates with respect to the reference SRTM DEM exhibit a good agreement with the literature on the two major eruptions in the Stromboli volcano in the period from 2000 to 2008.

- ◇ **Alternative methods** based on absolute ranging techniques have been introduced, namely *imaging geodesy* and *cross-correlation* methods. A detailed description of the involved range components is given as background. The range corrections due to geodetic effects, continental drifts and atmospheric delays are discussed. The applicability of the proposed stratified delay direct integration method for these methods has been demonstrated.

6.2 Outlook

In this thesis, methods for reliable deformation estimation from coherent SAR interferometric measurements in rocky volcanoes have been developed. In this section, some recommendations for further research in order to improve the proposed techniques and methods are outlined. Furthermore, potential applications based on the findings of this thesis are also proposed.

- ◇ One of main interest for obtaining atmosphere-free interferograms is to determine the **best available method** to estimate and compensate the atmospheric delay for different kinds of applications, which have different requirements on accuracy, computational efficiency and coverage. In order to achieve this goal, studies on the accuracy limitation, the availability

and the coverage of available techniques are necessary. The following research topics are thus recommended.

In the context of this thesis, the direct integration method using global NWP products has been validated with centimeter-range accuracy. The meteorological parameters are derived from both ERA-Interim and ECMWF OP data, which have limited temporal and spatial resolution. Nevertheless, the atmospheric delay has been significantly mitigated in high resolution SAR and InSAR measurements. This is due to the fact that the atmosphere is highly correlated in space. Thus an analysis of the spatial correlation of both hydrostatic and wet atmospheric delays should be performed on a global scale. Moreover, the atmospheric dynamics have a great impact on the accuracy of the direct integration method. In the CR experiment, two large outliers are observed due to strong local convection phenomena which are not accurately compensated, since the NWP products are only available four times per day. Therefore, it is important to analyze the decorrelation time of atmospheric delays.

Atmospheric delay measurements from external observations, such as GPS, satellite water vapor sensors, radiosondes and water vapor radiometers, can be used on the one hand directly for correction, on the other hand as reference data for validation. The main limitation is due to the sparse availability both in time and in space of these measurements. Another challenge is to integrate these external measurements in numerical weather assimilation in order to improve the prediction accuracy.

Another possibility is to simulate the weather condition using mesoscale weather models. In the last decades, a large number of studies have been performed in order to improve the weather prediction based on non-hydrostatic mesoscale weather models. However, the accuracy of these simulations is influenced by various factors, such as input data errors or initial model settings. Therefore, further investigations on the accuracy of mesoscale simulation in different weather conditions are required.

- ◇ The concept of *imaging geodesy* provides an independent source of atmospheric delay based on SAR range measurements, which can be used as reference data for the validation of different atmospheric delay estimation methods and for the quality control of numerical weather simulations.

- ◇ The direct integration method is efficient. Global atmospheric delay maps could be provided in near-real time. For SAR missions with high geometrical accuracy, such as TerraSAR-X mission, the accuracy of geocoding can be further improved by considering the integrated atmospheric delay. Moreover, this information is also useful for the interpretation of the effect of atmospheric delay in the interferometric phase and in absolute ranging measurements. For general purposes, several products, such as hourly and monthly global atmospheric delay variation maps, mean atmospheric delay map, can be generated by means of the integrated delay. Such products are useful for planning acquisitions and determining master image in PSI processing.

- ◇ In PSI processing, atmospheric phase screens are generated, where the atmospheric water vapor flux can be observed with a spatial resolution in the meter-range. This measurement is helpful for the understanding and modeling of small scale turbulence exchanges. In volcanic areas, this observation can be further used to detect and measure the amount of water vapor emission during volcanic eruptions.

- ◇ Other multi-image InSAR techniques, such as SBAS and SqueeSAR, can be applied after compensation of the stratified atmospheric delay to perform non-linear deformation estimation and to improve the spatial density and coverage of deformation estimates by including the Distributed Scatterer (DS).

A The effect of the Earth curvature on the incidence angle

Under the assumption that the ionosphere is a thin shell above the Earth surface, the ionospheric delay of a given slant direction can be projected using the incidence angle. The intersection angle θ'_{inc} between the radar ray and the ionosphere is different from the incidence angle θ_{inc} on the ground due to the curvature of the Earth, as depicted in *Fig. A.1(a)*. Assuming Earth is a sphere a sphere of radius R_0, the two angles are related by the law of sines:

$$\frac{R_0 + H_{iono}}{sin\theta_{inc}} = \frac{R_0}{sin\theta'_{inc}} \rightarrow \theta'_{inc} = sin^{-1}\left(\frac{R_0 sin\theta_{inc}}{R_0 + H_{iono}}\right), \tag{A.1}$$

where H_{iono} is the ionospheric height. The difference between θ_{inc} and θ'_{inc} increases with the ionosphere height and the incidence angle. As shown in *Fig. A.1(b)*, with an ionosphere height of 100 km and incidence angle of 20 °, the angle changes only on 0.3 °; with ionosphere height of 350 km and incidence angle of 50 °, the incidence angle change increases up to 3.9 °. The calculates of the correct incidence angle at a certain height is important for the both vertical ionospheric refractivity in the slant direction and the determination of the exact satellite location in three-dimensional weather model data.

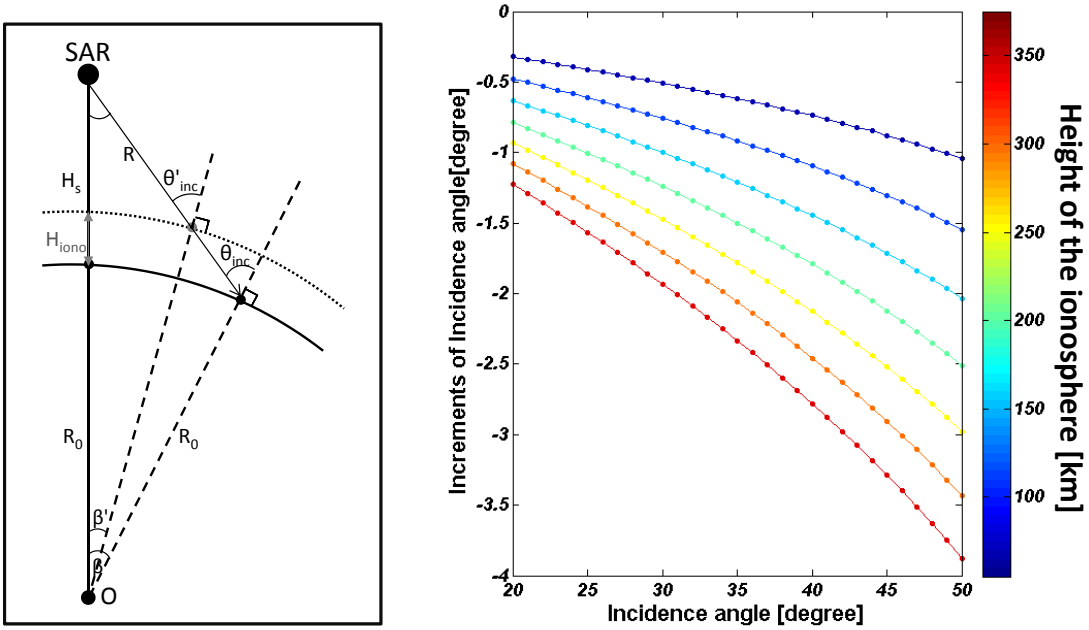

(a) (b)

Fig. A.1. Incidence angle variation due to the Earth curvature. (a) Satellite geometry and variables; (b) on the incidence angle θ_{inc} for different values of ionospheric height H_{iono}: 100, 150, 200, 250, 300 and 350 km. Each height is color-coded according to the colorbar.

B Table of absolute localization residuals - WTZR CR experiments

Table B.1. Absolute localization residuals in range of the Corner Reflector in Wettzell, Bad Kötzting, Germany. Radar measured delay differences between the expected and the measured position of the corner reflector, the Continental Drift (CD), the Solid Earth Tides (SET), the Ocean Tide Loading (OTL), the Atmospheric Pressure Loading (APL), the Tropospheric Delay (TD) and the Ionospheric Delay (ID) in range are shown in the table. The SAR acquisition time was 16:51 h UTC.

Acq. Date	**SAR Rng [m]**	**TD [m]**	**ID [m]**	**SET [m]**	**OTL [m]**	**APL [m]**	**CD [m]**	**Residual [m]**
2011-07-12	2.5356	2.7365	0.0656	0.1104	0.0030	-0.0025	0.0000	-0.3774
2011-08-14	2.5562	2.8019	0.0593	0.0758	0.0055	-0.0039	0.0011	-0.3834
2011-08-25	2.5915	2.7869	0.0571	0.1146	0.0014	-0.0003	0.0015	-0.3696
2011-09-05	2.5460	2.7588	0.0733	0.0969	-0.0008	0.0004	0.0018	-0.3843
2011-09-16	2.5221	2.7142	0.0810	0.0878	0.0028	-0.0005	0.0022	-0.3654
2011-10-30	2.5542	2.7541	0.0725	0.1138	0.0015	0.0028	0.0037	-0.3941
2011-11-10	2.4750	2.6814	0.0683	0.1096	0.0021	0.0044	0.0041	-0.3949
2011-11-21	2.4258	2.6970	0.0648	0.0495	-0.0029	0.0021	0.0045	-0.3891
2011-12-24	2.4878	2.6863	0.0293	0.1391	0.0021	0.0027	0.0054	-0.3771
2012-01-15	2.2598	2.6314	0.0259	-0.0438	-0.0026	0.0039	0.0063	-0.3612
2012-01-26	2.3728	2.6285	0.0426	0.0636	0.0023	0.0069	0.0066	-0.3778
2012-02-06	2.4651	2.6466	0.0424	0.1337	0.0014	0.0105	0.0070	-0.3766
2012-03-10	2.4740	2.7164	0.0629	0.0412	0.0048	0.0066	0.0081	-0.3661
2012-04-01	2.3796	2.6381	0.1032	-0.0003	-0.0029	-0.0065	0.0088	-0.3607
2012-04-23	2.4156	2.6375	0.1146	0.0197	0.0049	-0.0048	0.0096	-0.3658
2012-05-04	2.5317	2.6581	0.0957	0.1458	0.0039	-0.0063	0.0099	-0.3754
2012-05-26	2.3467	2.6950	0.0728	-0.0593	0.0008	0.0013	0.0107	-0.3746
2012-06-06	2.4457	2.7614	0.0762	-0.0218	0.0058	-0.0032	0.0109	-0.3836
2012-06-17	2.5800	2.8021	0.0473	0.0915	0.0040	0.0000	0.0113	-0.3763
2012-06-28	2.5314	2.7577	0.0740	0.0713	-0.0015	-0.0031	0.0118	-0.3787
2012-07-20	2.5220	2.7897	0.0635	0.0442	0.0058	-0.0016	0.0125	-0.3919
2012-08-22	2.5878	2.8075	0.0683	0.0694	0.0015	-0.0009	0.0136	-0.3717
2012-09-13	2.5357	2.7043	0.0785	0.1203	0.0023	-0.0020	0.0144	-0.3820
2012-10-05	2.5686	2.7697	0.0800	0.0867	0.0013	-0.0004	0.0151	-0.3836
2012-10-16	2.4894	2.6492	0.0664	0.1473	0.0047	-0.0011	0.0154	-0.3925
2012-10-27	2.4322	2.6428	0.0641	0.1016	0.0013	-0.0076	0.0158	-0.3857
2012-11-07	2.4825	2.7356	0.0474	0.0532	-0.0021	0.0018	0.0162	-0.3695
Mean	2.4857	2.7144	0.0665	0.0727	0.0019	-0.0001	0.0084	-0.3781
ST	0.0810	0.0596	0.0200	0.0557	0.0027	0.0043	0.0050	0.0098

C Vertical discretization of NWP products from model level to pressure level

In the hybrid model, the pressure P values correspond to the model half-levels in vertical. 8 different hybrid-models are defined in ECMWF (ECMWF, 2013). Half-level pressure can be expressed using surface pressure P_S as:

$$P_{k+\frac{1}{2}} = A_{k+\frac{1}{2}} + B_{k+\frac{1}{2}} P_S, \tag{C.1}$$

where the parameters $A_{k+\frac{1}{2}}$ and $B_{k+\frac{1}{2}}$ $(k = 1, \ldots, NL)$ for 60 model level are presented in Appendix D.

Full-level pressure P_k is expressed as:

$$P_k = \Big(P_{k-\frac{1}{2}} + P_{k+\frac{1}{2}}\Big)\Big/2. \tag{C.2}$$

Surface level of geopotential is defined as:

$$\mathbf{\Phi}_{NL+\frac{1}{2}} = \mathbf{\Phi}_S, \tag{C.3}$$

where $\mathbf{\Phi}_S$ is the surface geopotential. The geopotential on model half-levels starts from the Surface Level (SL), and can be formulated following as (Trenberth et al., 1993):

$$\mathbf{\Phi}_{k-\frac{1}{2}} = \mathbf{\Phi}_{k+\frac{1}{2}} + R_d T_{vk} \ln\Big(P_{k+\frac{1}{2}}/P_{k-\frac{1}{2}}\Big), \tag{C.4}$$

where T_{vk} is the virtual temperature at level k (see *eq. (11)*). By means of some simplifications, T_{vk} is expressed with specific humidity q and temperature T (Bechtold, 2010):

$$T_{vk} \simeq T\Big(1 + 0.608q\Big). \tag{C.5}$$

Full-level values of the geopotential are derived according to: (Bechtold and Park, 2010):

$$\mathbf{\Phi}_k = \mathbf{\Phi}_{k+\frac{1}{2}} + a_k R_d T_{vk}, \tag{C.6}$$

where $a_1 = \ln 2$ and, for $k > 1$:

$$a_k = 1 - \frac{P_{k-\frac{1}{2}}}{P_{k+\frac{1}{2}} - P_{k-\frac{1}{2}}} \ln\left(\frac{P_{k+\frac{1}{2}}}{P_{k-\frac{1}{2}}}\right). \tag{C.7}$$

D 60 Model level definitions

The 60 hybrid model is defined by ECMWF (2013). The conversion between the model level to the pressure is described in section C. In the table, the list of parameters $A_{k+\frac{1}{2}}$ and $B_{k+\frac{1}{2}}$ are presented. Pf and Ph are the full level and half level pressure corresponding to the surface pressure of 1013.250 hPa. At the last level, the half level pressure $P_{60+\frac{1}{2}} = P_S$.

Table D.1. The values of $A_{k+\frac{1}{2}}$ and $B_{k+\frac{1}{2}}$ for $NL = 60$ levels for the ECMWF model. $A_{k+\frac{1}{2}}$ is in hPa. The half and full pressure levels are presented based on the surface pressure of 1013.250 hPa.

N	A	B	Ph [hPa]	Pf [hPa]	N	A	B	Ph [hPa]	Pf [hPa]
0	0.000000	0.00000000	0.000	–	31	19027.695313	0.05169041	242.652	228.839
1	20.000000	0.00000000	0.200	0.100	32	19755.109375	0.07353383	272.059	257.356
2	38.425343	0.00000000	0.384	0.292	33	20222.205078	0.09967469	303.217	287.638
3	63.647804	0.00000000	0.636	0.510	34	20429.863281	0.13002251	336.044	319.631
4	95.636963	0.00000000	0.956	0.796	35	20384.480469	0.16438432	370.407	353.226
5	134.483307	0.00000000	1.345	1.151	36	20097.402344	0.20247594	406.133	388.270
6	180.584351	0.00000000	1.806	1.575	37	19584.330078	0.24393314	443.009	424.571
7	234.779053	0.00000000	2.348	2.077	38	18864.750000	0.28832296	480.791	461.900
8	298.495789	0.00000000	2.985	2.666	39	17961.357422	0.33515489	519.209	500.000
9	373.971924	0.00000000	3.740	3.362	40	16899.468750	0.38389215	557.973	538.591
10	464.618134	0.00000000	4.646	4.193	41	15706.447266	0.43396294	596.777	577.375
11	575.651001	0.00000000	5.757	5.201	42	14411.124023	0.48477158	635.306	616.042
12	713.218079	0.00000000	7.132	6.444	43	13043.218750	0.53570992	673.240	654.273
13	883.660522	0.00000000	8.837	7.984	44	11632.758789	0.58616841	710.263	691.752
14	1094.834717	0.00000000	10.948	9.892	45	10209.500977	0.63554746	746.064	728.163
15	1356.474609	0.00000000	13.565	12.257	46	8802.356445	0.68326861	780.346	763.205
16	1680.640259	0.00000000	16.806	15.186	47	7438.803223	0.72878581	812.830	796.588
17	2082.273926	0.00000000	20.823	18.815	48	6144.314941	0.77159661	843.263	828.047
18	2579.888672	0.00000000	25.799	23.311	49	4941.778320	0.81125343	871.420	857.342
19	3196.421631	0.00000000	31.964	28.882	50	3850.913330	0.84737492	897.112	884.266
20	3960.291504	0.00000000	39.603	35.784	51	2887.696533	0.87965691	920.189	908.651
21	4906.708496	0.00000000	49.067	44.335	52	2063.779785	0.90788388	940.551	930.370
22	6018.019531	0.00000000	60.180	54.624	53	1385.912598	0.93194032	958.148	949.349
23	7306.631348	0.00000000	73.066	66.623	54	855.361755	0.95182151	972.987	965.567
24	8765.053711	0.00007582	87.727	80.397	55	467.333588	0.96764523	985.140	979.063
25	10376.126953	0.00046139	104.229	95.978	56	210.393890	0.97966272	994.747	989.944
26	12077.446289	0.00181516	122.614	113.421	57	65.889244	0.98827010	1002.024	998.385
27	13775.325195	0.00508112	142.902	132.758	58	7.367743	0.99401945	1007.264	1004.644
28	15379.805664	0.01114291	165.089	153.995	59	0.000000	0.99763012	1010.849	1009.056
29	16819.474609	0.02067788	189.147	177.118	60	0.000000	1.00000000	1013.250	1012.049
30	18045.183594	0.03412116	215.025	202.086					

E Surface temperature and mean sea level temperature

In the hybrid model, surface temperature is usually not direct given as a parameter. Nevertheless, it can be derived according to the surface pressure and the temperature lapse rate which can be retrieved from pressure level data (Trenberth et al., 1993). In this thesis, the surface temperature T_S is computed using the temperature and pressure from the last level of full-level data, namely T_{NL} and P_{NL}. Under the assumption of a dry hydrostatic subterranean, a uniform lapse rate of $6.5 \times 10^{-3} km^{-1}$ is predefined if the surface elevation is less than 2000 m:

$$T_S = T_{NL} + \alpha T_{NL}\left(\frac{P_S}{P_{NL}} - 1\right), \qquad \text{with} \qquad \alpha = 0.0065\frac{R_d}{g_{NL}} \tag{E.1}$$

where g_{NL} is the net acceleration due to gravity at the level NL (see Appendix F).

In extreme weather conditions, such as very high or low temperature, the temperature lapse rate α is modified based on a reference temperature T_0 which is defined as $T_0 = T_S + 0.0065\mathbf{\Phi}_S/g_{NL}$:

$$\alpha = \frac{R_d}{\mathbf{\Phi}_S}\Big(290.5 - T_S\Big) \qquad \text{if} \qquad T_S \leq 290.5 \text{ K} \quad \text{and} \quad T_0 > 290.5 \text{ K} \tag{E.2a}$$

$$\alpha = 0 \quad \text{and} \quad T_S \Rightarrow \frac{1}{2}\Big(290.5 + T_S\Big) \qquad \text{if} \qquad T_S > 290.5 \text{ K} \quad \text{and} \quad T_0 > 290.5 \text{ K} \tag{E.2b}$$

$$\alpha = 0 \quad \text{and} \quad T_S \Rightarrow \frac{1}{2}\Big(255 + T_S\Big) \qquad \text{if} \qquad T_S < 255 \text{ K}. \tag{E.2c}$$

Mean sea level temperature T_{MSL} is defined as a virtual parameter. It is helpful for extrapolating temperature below the model orography Trenberth et al. (1993). The mean sea level pressure P_{MSL} is needed for extrapolation (see section 3.1.1.2). For surface orography $\mathbf{\Phi}_S/g_{NL} < 2000$ m, T_{MSL} is written as:

$$T_{MSL} = T_S + \left(1 + \alpha \ln\frac{P_{MSL}}{P_S} + \frac{1}{2}\Big(\alpha \ln\frac{P_{MSL}}{P_S}\Big)^2 + \frac{1}{6}\Big(\alpha \ln\frac{P_{MSL}}{P_S}\Big)^3\right), \quad \text{with} \quad \alpha = 0.0065\frac{R_d}{g_{NL}}. \tag{E.3}$$

For higher surface orography (≥ 2000 m), the temperature lapse rate α is reformulated as:

$$\alpha = R_d\Big(T_0^{'} - T_S\Big)/\mathbf{\Phi}_S. \tag{E.4}$$

The reference temperature $T_0^{'}$ at different heights is defined as:

$$T_0^{'} = T_{pl} \qquad \text{for} \qquad \mathbf{\Phi}_S/g_{NL} > 2500 \text{ m} \tag{E.5a}$$

$$T_0^{'} = 0.002\Big[(2500 - \frac{\mathbf{\Phi}_S}{g_{NL}})T_0 + (\frac{\mathbf{\Phi}_S}{g_{NL}} - 2000)T_{pl}\Big] \qquad \text{for} \qquad 2000 \leq \mathbf{\Phi}_S/g_{NL} \leq 2500 \text{ m}, \tag{E.5b}$$

where T_{pl} is the minimum value between T_0 and 298 K.

F Geopotential height, geometric height and its gravity variation

In this section, we concentrate on three aspects: firstly, the definition of the geopotential and the geopotential height in ECMWF system in section F.1; secondly, the conversion between the geopotenital height and the geometric height in section F.2; lastly, the conversion between the geometric height and the conventional ellipsoidal height in section F.3.

F.1 Geopotential and geopotential height in ECMWF system

For the ERA-Interim data, the geopotential $\mathbf{\Phi}$ is defined on half levels (see Appendix C) and on the Surface Level (SL) (known as orography, see section 3.1.1.2). In general, the geopotential at height z is given by Wallace and Hobbs (2006):

$$\mathbf{\Phi}(z) = \int_0^z g(z,\lambda)\mathrm{d}z, \tag{F.1}$$

where $g(z,\lambda)$ is the net acceleration due to gravity depending on its position z (geometric height) and λ (latitiude).

According the *eq. (10)* and *eq. (11)*, the geopotential difference between two pressures P_1 and P_2 yields (Vedel, 2000):

$$\mathbf{\Phi}_2 - \mathbf{\Phi}_1 = -\int_{P_1}^{P_2} RT\frac{\mathrm{d}P}{P} = -\int_{P_1}^{P_2} R_d T_v \frac{\mathrm{d}P}{P}. \tag{F.2}$$

Based on the surface geopotential $\mathbf{\Phi}_S$ (orography), the geopotential in the vertical coordinate is defined as an integration from the pressure P at height z to the surface pressure P_S:

$$\mathbf{\Phi}(z) = \mathbf{\Phi}_S + \int_P^{P_S} RT\frac{\mathrm{d}P}{P}, \tag{F.3}$$

The geopotential height Z for ECMWF products is defined as the geopotential $\mathbf{\Phi}(z)$ divided by the World Meteorological Organization (WMO) defined gravity constant $g_0 = 9.80665\ \mathrm{m/s^2}$, which is constant for all latitudes and all heights:

$$Z(z) = \frac{\mathbf{\Phi}(z)}{g_0} = Z_S + \int_{z_S}^{z} \frac{g(z,\lambda)}{g_0}\mathrm{d}z = Z_S + \frac{1}{g_0}\int_P^{P_S} RT\frac{\mathrm{d}P}{P} \quad \text{with} \quad Z_S = \frac{\mathbf{\Phi}_S}{g_0}, \tag{F.4}$$

where Z_S is the geopotential surface height in the ECMWF model.

F.2 Geopotential height and geometric height

Unlike the constant gravity g_0 defined by WMO, the gravitational acceleration g varies with its latitude λ and height z. It can be calculated separately for each position in two steps. Firstly,

the gravitational acceleration g_S at location with latitude λ on the surface of an ellipsoid can be derived based on the Somigliana's Equation (Heiskanen and Moritz, 1967):

$$g_S(\lambda) = g_e\Big(\frac{1 + k_{somig}\sin^2\lambda}{\sqrt{1 - e^2\sin^2\lambda}}\Big), \tag{F.5}$$

where $g_e = 9.7803253359$ m/s^2 is the equatorial gravity; $k_{somig} = 1.931853 \times 10^{-3}$ is the Somigliana's constant and the eccentricity $e = 0.081819$.

Then the gravitational acceleration $g(z, \lambda)$ at height z from the defined surface is derived using the inverse square law for gravity:

$$g(z, \lambda) \approx g_S(\lambda)\Big(\frac{R_s}{R_s + z}\Big)^2, \tag{F.6}$$

where R_s is the effective radius of Earth at latitude λ. Using a reference ellipsoid, e.g. World Geodetic System 1984 (WGS84), it can be written as (Mahoney, 2005):

$$R_s(\lambda) = \frac{a_{Earth}}{1 + f + g_r - 2f\sin^2\lambda}, \tag{F.7}$$

where a_{Earth}, f and g_r are the semi-major axis, the flattening and the gravitation ratio of a reference ellipsoid. For WGS84, they are $a_{Earth} = 6378137.0$ m, $f = 0.003352811$ and $g_r = 0.003449787$, respectively.

The conversion between geopotential height and geometric height can be done by writing the geopotential height in differential form based on *eq. (F.4)*:

$$g_0 \mathrm{d}Z = g(z, \lambda)\mathrm{d}z. \tag{F.8}$$

Substituting *eq. (F.8)* into *eq. (F.4)* and integrating from the reference surface 0 to z yields:

$$Z(z, \lambda) = \frac{g(z, \lambda)}{g_0} \cdot \frac{R_s(\lambda)z}{R_s(\lambda) + z}. \tag{F.9}$$

The geometric height at geopotential Z and latitude λ is solved by inverting *eq. (F.9)*:

$$z(Z, \lambda) = \frac{R_s(\lambda)Z}{\frac{g(z,\lambda)}{g_0}R_s(\lambda) - Z}. \tag{F.10}$$

F.3 Geometric height and conventional ellipsoidal height

In ECMWF products, the model orography is defined as a mean elevation above the MSL which is derived from a data set with a resolution of about 1 km. Therefore, the zero of elevation ($z = 0$ m) defined on MSL can be replaced approximately by an equipotential surface for the Earth's gravity field, so-called *geoid* (see *Fig. 8*) (Persson and Grazzini, 2007). In order to convert the geometric height $z(Z, \lambda)$ calculated from ECMWF data to the conventional ellipsoidal height h used by GPS, the geoid-undulation $N_g(Z, \lambda)$ between the reference ellipsoid WGS84 and the geoid is required (Nafisi et al., 2012):

$$h = z(Z, \lambda) + N_g(Z, \lambda). \tag{F.11}$$

In practice, $N_g(Z, \lambda)$ can be directly derived from Earth Gravitational Model (EGM). In this thesis, the latest model released in 2008 (EGM2008) with respect to WGS84 is used for conversion between the two height systems (Pavlis et al., 2008). A visualization of the EGM2008 geoid undulation is presented in *Fig. F.1* using 1500 harmonic coefficients which represent 3 arc minutes (about 5.2 km) (Bezděk and Sebera, 2013).

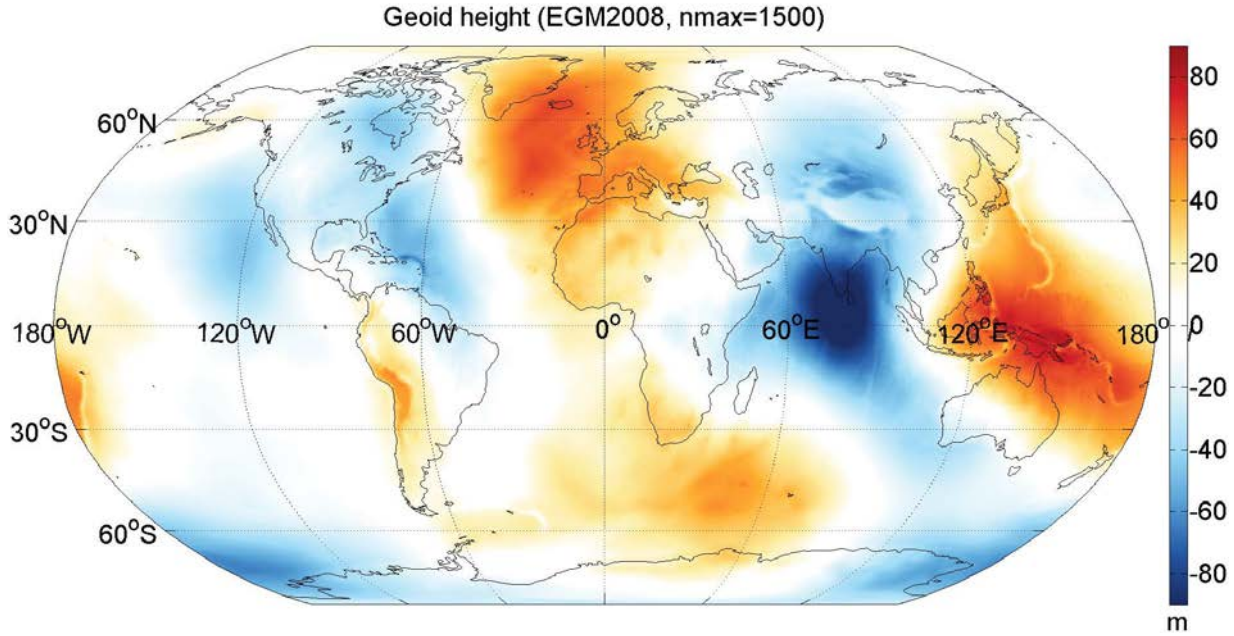

Fig. F.1. The EGM2008 geoid undulation map is calculated using 1500 harmonic coefficients which represent 3 arc minutes (about 5.2 km) (Bezděk and Sebera, 2013).

G Horizontal interpolation of weather data parameters using kriging interpolation methods

The preprocessing step of numerical weather data has been described in section 3.1.2.1. ECMWF weather data parameters are provided into two different numerical representations(Persson and Grazzini, 2007): firstly, the spectral method based on a spherical harmonic expansion (truncated at a particular wave number); secondly, the reduced Gaussian grid, which is a *Gaussian* grid, regular in longitude and nearly regular in latitude (Hortal and Simmons, 1991). For preparation, these representations are transformed into a regular grid, which is regular both in longitude and in latitude. The correspondence between the spectral truncation representation, the reduced Gaussian grid and the regular geographical grid is presented in Table 3 in section 3.2. The ERA-Interim data have a horizontal resolution of about 79 km. This coarse grid needs to be interpolated to a proper spatial resolution (e.g. SRTM DEM resolution) for refractivity integration (see section 3.3).

In this section, firstly a short introduction of interpolation method based on simple kriging is given in section G.1. Different kinds of variogram models are then introduced in section G.2. The definitions and the formula summarized in section G.1 and G.2 are referred to Deutsch and Journel (1997); Wackernagel (2003). Finally, kriging results for weather data parameters using different variogram models are analyzed in section G.3.

G.1 Kriging interpolation - a short introduction

In this section the basic notation and definitions of simple kriging and ordinary kriging are introduced. Kriging is defined as "a collection of generalized linear regression techniques", which minimizes "the estimation variance defined from a prior model for a covariance" (Deutsch and Journel, 1997). The simplest form of the kriging method (Simple Kriging (SK)) can be written as a multiple regression model:

$$Z^*_{SK}(\mathbf{x}_0) = m(\mathbf{x}_0) + \sum_{\alpha=1}^{n} \omega_\alpha \Big(Z(\mathbf{x}_\alpha) - m(\mathbf{x}_\alpha) \Big), \tag{G.1}$$

where $Z(\mathbf{x})$ is a random function defined at a location $\mathbf{x}$ of the spatial domain $\mathcal{D}$; $Z(\mathbf{x}_\alpha)$ is the random variable at n locations of $\mathbf{x}_\alpha$; $Z(\mathbf{x}_0)$ is the random variable at an additional location of $\mathbf{x}_0$; $Z^*_{SK}(\mathbf{x}_0)$ is its estimate applying the SK method; $m(\mathbf{x}) = E[Z(\mathbf{x})]$ is the location-dependent expected value of $Z(\mathbf{x})$; and ω_α are weights correspondent to the residuals $Z(\mathbf{x}_\alpha) - m(\mathbf{x}_\alpha)$.

If the expected value $E[Z(\mathbf{x})] = m$ is constant at any point $\mathbf{x}$ over the whole domain $\mathcal{D}$, the random function $Z(\mathbf{x})$ is called stationary. Then, the SK is used to estimate the residual from a known mean value m. Under this assumption equation *(G.1)* can be thus expressed as:

$$Z^*_{SK}(\mathbf{x}_0) = m + \sum_{\alpha=1}^{n} \omega_\alpha \Big(Z(\mathbf{x}_\alpha) - m \Big), \tag{G.2}$$

The variance of SK estimation error is expressed as $\sigma^2_{SK} = var(Z^*_{SK}(\mathbf{x}_0) - Z(\mathbf{x}_0))$, and can be expanded as:

$$\sigma^2_{SK} = E\Big[(Z^*_{SK}(\mathbf{x}_0) - Z(\mathbf{x}_0))^2\Big] \tag{G.3a}$$

$$= E\Big[(Z^*_{SK}(\mathbf{x}_0))^2 + (Z(\mathbf{x}_0))^2 - 2Z^*_{SK}(\mathbf{x}_0)Z(\mathbf{x}_0)\Big] \tag{G.3b}$$

$$= \sum_{\alpha=1}^{n}\sum_{\beta=1}^{n}\omega_\alpha\omega_\beta C(\mathbf{x}_\alpha - \mathbf{x}_\beta) + C(\mathbf{x}_0 - \mathbf{x}_0) - 2\sum_{\alpha=1}^{n}\omega_\alpha C(\mathbf{x}_\alpha - \mathbf{x}_0), \tag{G.3c}$$

where the covariance function under assumption of second-order stationary is written as:

$$cov[Z(\mathbf{x}_\alpha), Z(\mathbf{x}_\beta)] = C(\mathbf{x}_\alpha - \mathbf{x}_\beta). \tag{G.4}$$

In order to minimize the estimation variance, the first derivative $\frac{\partial\sigma^2_E}{\partial\omega_\alpha}$ with respect to all weights should be zero. The equation system dependent on the weights ω_β is thus expressed as:

$$\sum_{\beta=1}^{n}\omega_\beta C(\mathbf{x}_\alpha - \mathbf{x}_\beta) = C(\mathbf{x}_\alpha - \mathbf{x}_0) \quad \text{for} \quad \alpha = 1, \ldots, n. \tag{G.5}$$

Taking *eq. (G.5)* into *eq. (G.3)*, the variance of SK estimation is:

$$\sigma^2_{SK} = C(\mathbf{0}) - \sum_{\alpha=1}^{n}\omega_\alpha C(\mathbf{x}_\alpha - \mathbf{x}_0). \tag{G.6}$$

The weights ω_α have to be determined by solving the equation system (G.5) in order to minimize the variance.

Ordinary Kriging (OK) is the most commonly used kriging method. Unlike the SK, OK requires no a priori information of mean value m, where the sum of the weights $\sum_{\alpha=1}^{n}\omega_\alpha$ is constrained to one. Thus the mean value m in *eq. (G.2)* is canceled out. The OK is written as:

$$Z^*_{OK}(\mathbf{x}_0) = \sum_{\alpha=1}^{n}\omega_\alpha Z(\mathbf{x}_\alpha), \tag{G.7}$$

The stationary OK system can be written as:

$$\begin{cases} \sum_{\beta=1}^{n}\omega_\beta^{OK}\gamma(\mathbf{x}_\alpha - \mathbf{x}_\beta) + \mu_{OK} = \gamma(\mathbf{x}_\alpha - \mathbf{x}_0) \quad \text{for} \quad \alpha = 1, \ldots, n. \\ \sum_{\beta=1}^{n}\omega_\beta^{OK} = 1, \end{cases} \tag{G.8}$$

where ω_β^{OK} are the OK weights and μ_{OK} is the Lagrange parameter. The OK method is used to interpolate the numerical weather data on the basis of a predefined covariance function.

G.2 Variogram and covariance function specification

The variogram is defined as the variance of the increment $Z(\mathbf{x}+\mathbf{h}) - Z(\mathbf{x})$ at a pair of points $\mathbf{x}$ and $\mathbf{x}+\mathbf{h}$. For a intrinsic stationary of order-two random function, the variogram can be written as:

$$\gamma(\mathbf{h}) = \frac{1}{2} var\Big[Z(\mathbf{x}+\mathbf{h}) - Z(\mathbf{x})\Big] = \frac{1}{2} E\Big[(Z(\mathbf{x}+\mathbf{h}) - Z(\mathbf{x}))^2\Big]. \tag{G.9}$$

The definition of a covariance function $C(\mathbf{h})$ on the basis of a hypothesis of stationarity of the first two moments is given by:

$$C(\mathbf{h}) = \begin{cases} E[Z(\mathbf{x})] = m & \text{for all } \mathbf{x} \in \mathcal{D} \\ E[Z(\mathbf{x}+\mathbf{h})Z(\mathbf{x})] - m^2 = C(\mathbf{h}) & \text{for all } \mathbf{x}, \mathbf{x}+\mathbf{h} \in \mathcal{D}. \end{cases} \tag{G.10}$$

Therefore, a variogram function can be derived from a covariance function by the formula:

$$\gamma(\mathbf{h}) = C(\mathbf{0}) - C(\mathbf{h}). \tag{G.11}$$

The variogram function should be predefined for kriging interpolation. The following covariance functions will be evaluated in this appendix:

(1) **Nugget-effect model** is a covariance function $C(\mathbf{h})$ that models a discontinuity at the origin $|\mathbf{h}| = 0$. The *nugget-effect model* can be expressed with a positive value b as :

$$C_{nug}(\mathbf{h}) = \begin{cases} b \text{ for } |\mathbf{h}| = 0 \\ 0 \text{ for } |\mathbf{h}| > 0. \end{cases} \tag{G.12}$$

(2) **Exponential covariance function** decreases exponentially with increasing distance a.

$$C_{exp}(\mathbf{h}) = b \exp^{(-\frac{|\mathbf{h}|}{a})} \quad \text{with} \quad a, b > 0. \tag{G.13}$$

This model is continuous but not differentiable at the origin. It falls off asymptotically towards zero from $|\mathbf{h}| \mapsto \infty$.

(3) **Spherical model** is a commonly used covariance function.

$$C_{sph}(\mathbf{h}) = \begin{cases} b\Big(1 - \frac{3}{2}\frac{|\mathbf{h}|}{a} + \frac{1}{2}\frac{|\mathbf{h}|^3}{a^3}\Big) & \text{for } 0 \le |\mathbf{h}| \le a \\ 0 & \text{for } |\mathbf{h}| > a. \end{cases} \tag{G.14}$$

where a indicates the range of the spherical covariance (in other words, the covariance vanishes when the range is reached); the parameter b represents the maximal value of the

covariance which steadily decreases, from the maximum b at the origin, until it vanishes when the range of the spherical covariance is reached.

(4) **Gaussian model** Gaussian model is defined by an effective range a and positive variance contribution value b.

$$C_{gau}(\mathbf{h}) = b\left[1 - \exp\left(-\frac{(3\mathbf{h})^2}{a^2}\right)\right]. \tag{G.15}$$

(5) **Power model** Power model is defined by two parameters: a power ω $(0 < \omega < 2)$ and a positive slope c.

$$C_{pow}(\mathbf{h}) = c \cdot h^{\omega}. \tag{G.16}$$

G.3 Comparison of results from different kriging models

In practice, the Ordinary Kriging (OK) interpolation has been applied using a geostatistical Matlab toolbox *mGstat* from Pebesma and Wesseling (1997). In order to evaluate the interpolation accuracy, the weather data of the Hierro test site from ERA-Interim and ECMWF operational data (OP) have been used. The Interim data (T255) has been interpolated to the OP resolution (T1279) using: (1) bilinear interpolation (see section G.3.2); (2) different covariance functions (see section G.3.3). The interpolation results haven been compared with the OP data. Due to the difference of the horizontal resolutions, a significant difference exists between the weather surface data, such as surface pressure and surface temperature. A mask generated based on the model orography in order to determine the valid areas for statistical analysis (see section G.3.1).

G.3.1 Orography mask

Due to different horizontal resolutions, there are some discrepancies between the model orographies (surface geopotential) of the ERA-Interim and the OP data. Their orographies are presented in *Fig. G.1(a)* and *Fig. G.1(b)* respectively. The orography of OP data spans 6 ° in latitude from north (30 °) to south (25 °) and 8 ° in longitude from east (340 °) to west (347 °) (see *Fig. G.1(a)*). In order to ensure the correct kriging interpolation, a larger area is defined for ERA-Interim data. Its orography is shown in *Fig. G.1(b)* which covers about 21 ° in latitude north (38 °) to south (18.2 °) and about 20 ° in longitude from east (334.4 °) to west (353.7 °). A rectangle in *Fig. G.1(b)* indicates the coverage of OP data.

The range of selected ERA-Interim orography (inside the rectangle) is from about −93.6 to 4211.4 m^2s^{-2}, whereas the range of the orography from OP data is from about −723.2 to 12447.0 m^2s^{-2}. Therefore, a mask has been generated in order to eliminate those points with the geopotential larger than 100 m^2s^{-2} and smaller than 20 m^2s^{-2}. The corresponding masked points are displayed in dark blue in *Fig. G.1(c)*.

G.3.2 Bilinear Interpolation

Two MSL pressure data sets extracted from ERA-Interim and OP data on 4 December 2011 at 6 a.m. have been selected for evaluation of different spatial interpolation methods. Both data sets are presented in *Fig. G.2* with the same coverage of model orography. The mean value of the MSL pressure from ERA-Interim in the rectangle is about 1.02187×10^5 Pa, and the

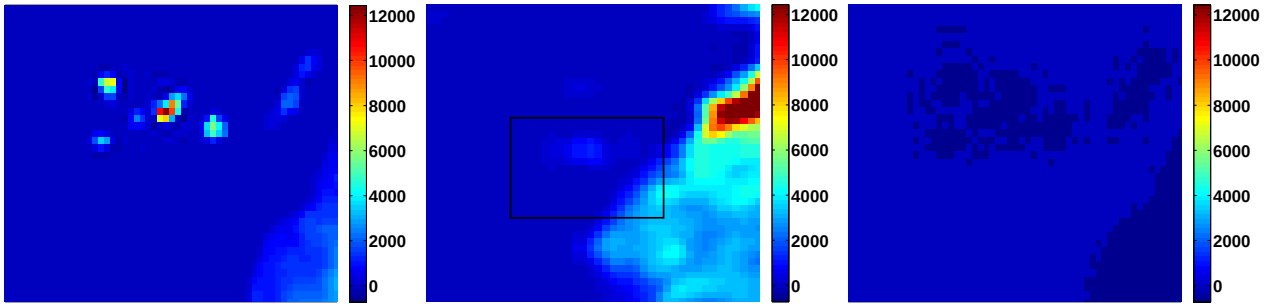

(a) OP orography (b) ERA-Interim orography (c) Orography mask

Fig. G.1. Model orography from OP data and ERA-Interim: (a) OP orography, with maximum value of 12447.0 m^2s^{-2} and minimum value of -723.2 m^2s^{-2}; (b) ERA-Interim orography, with maximum value of 4211.4 m^2s^{-2} and minimum value of -93.6 m^2s^{-2}; (c) the mask generated based on OP orography by eliminating those with surface geopotential larger than 100 m^2s^{-2} and smaller than 20 m^2s^{-2} (the invalid values are depicted in dark blue). For visual comparison, the same color-scale defined by the minimum and the maximum value of (a) has been used.

maximum and the minimum values are 1.02480×10^5 and 1.01945×10^5 Pa respectively. Due to the orography differences, the mean value from OP is about 1.02200×10^5 Pa, which is about 13 Pa larger than the one that from ERA-Interim, whereas the maximum is about 45.1 Pa larger and the minimum value is about 6.8 Pa larger.

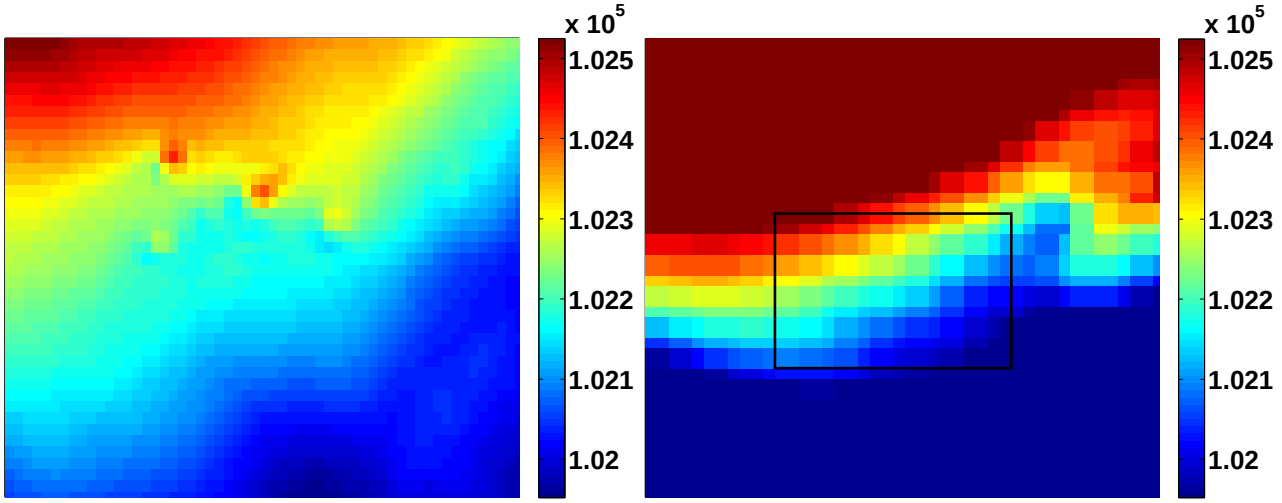

(a) OP MSL pressure (b) ERA-Interim MSL pressure

Fig. G.2. The MSL pressure data sets from OP data and ERA-Interim on 4 December 2011 at 6 a.m.: (a) MSL pressure from OP, the maximum and the minimum pressure are 1.02480×10^5 Pa and 1.01945×10^5 Pa; (b) MSL pressure from ERA-Interim, the maximum and the minimum are 1.02576×10^5 Pa and 1.01880×10^5 Pa.

The MSL pressure from ERA-Interim has been interpolated into the OP resolution using *linear*, *cubic* and *spline* interpolator. Then the interpolated results have been compared with the MSL pressure data set from OP data. The difference maps are displayed in *Fig. G.3*, where the orography mask has been applied to avoid the large difference caused by the different orographies. Furthermore, a constant colorbar is defined for all difference maps with the minimum value -210 Pa in blue and the maximum value 210 Pa in red. No significant differences between the three interpolations are observed. Statistically, the mean values of the difference from the three interpolation methods are -7.0, -7.2 and -7.5 Pa, respectively. The standard deviations are also similar, with values of 37.8, 39.3, 40.9 Pa. In summary, the linear interpolation performs better in this MSL pressure interpolation.

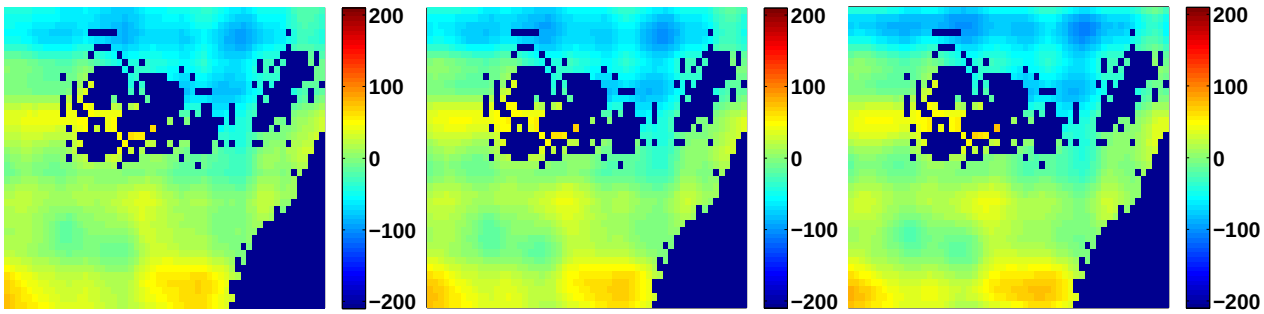

(a) linear (b) cubic (c) spline

Fig. G.3. MSL pressure difference maps between the interpolated ERA-Interim data based on three interpolation methods and the OP data as the reference: (a) linear interpolation, the mean value is about −7.0 Pa and the standard deviation is 37.8 Pa; (b) cubic interpolation, the mean value is about −7.2 Pa and the standard deviation is 39.3 Pa;(c) spline interpolation, the mean value is about −7.5 Pa and the standard deviation is 40.9 Pa. A constant colorbar (from −210 to 210 Pa) has been used for the three difference maps.

G.3.3 Kriging interpolation

Influence of the covariance function. Ordinary kriging interpolation has been applied on the MSL pressure data from ERA-Interim (described in section G.3.2) by using the exponential and spherical covariance functions with a maximum range of 7 and the Gaussian function with a maximum range of 1. The difference maps have been calculated by subtracting the MSL pressure from the OP data set. Visually, interpolation results using the three covariance functions delivers similar results. Comparing to the results using bilinear interpolation, the discrepancies around the boundary decrease. The standard deviation using spherical model is about 36.5 Pa, which is slight worse than using exponential model of about 0.1 Pa and better than using Gaussian model of 1.5 Pa. The mean values are −5.3, −5.2 and −5.5 Pa for exponential, spherical and Gaussian model. Since kriging interpolations using spherical and exponential model have similar performances at the same range, the spherical model has been selected in this thesis.

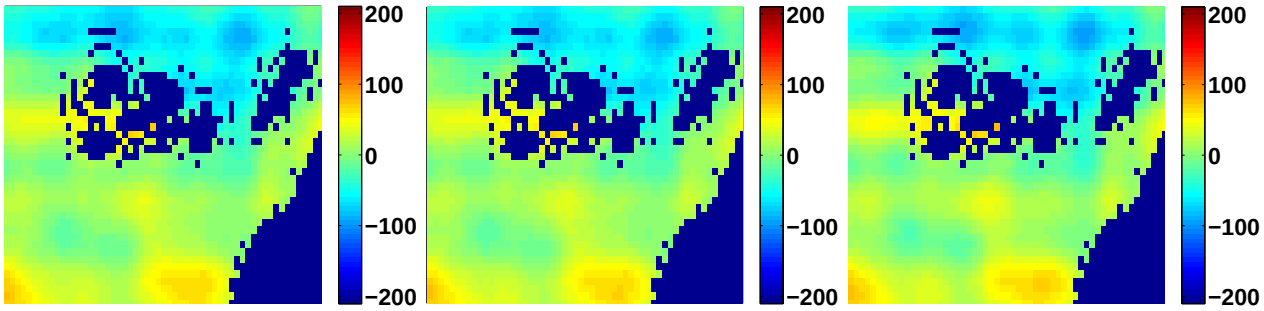

(a) Exponential model (b) Spherical model (c) Gaussian model

Fig. G.4. MSL pressure difference maps using kriging interpolation based on: (a) exponential model with range 7; (b) spherical model with range 7; (c) Gaussian model with range 1. The OP data set in *Fig. G.2(a)* is used as the reference. The mean values are −5.3, −5.2 and −5.5 Pa, and the standard deviations are 36.4, 36.5 and 38.0 Pa. The colorbar spans from −210 to 210 Pa.

Influence of the range parameter. The range parameter effect of the kriging interpolation is discussed in this paragraph. For this test, the spherical function is used. The maximum range has been determined based on the longest side of the data set: 20. The interpolation is performed with a range from 1 to 20. For each interpolated results, a difference map with respect to the reference data from OP has been calculated. Furthermore, its standard deviation and its mean value have been evaluated for each range value and depicted in *Fig. G.5*. The

standard deviation decreases dramatically from about 68.4 to 36.6 Pa with increase of the range parameter from 1 to 4 (see *Fig. G.5(a)*). Then, the standard deviation stabilizes around the range 7 (see *Fig. G.5(b)*). The minimum standard deviation 35.9 Pa is achieved with range 12.

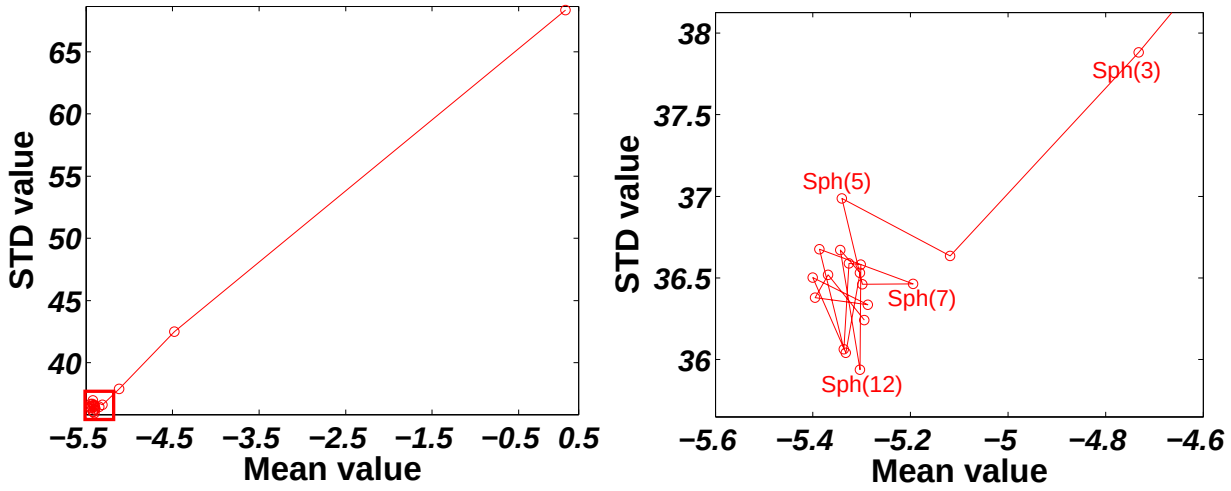

(a) (b)

Fig. G.5. In (a), the mean values and the standard deviation values of the difference maps are depicted, which are calculated by subtracting the OP MSL pressure from the interpolated Interim MSL pressure using spherical function with a range parameter with values from 1 to 20. (b) is a selected zoom of (a) from range 3 to 20.

Summarizing the analysis according to the covariance function and the range parameter, the spherical model with a constant range length 7 has been selected for horizontal interpolation in preprocessing step (see section 3.1.2.1).

H GPS Validation (2-years time series)

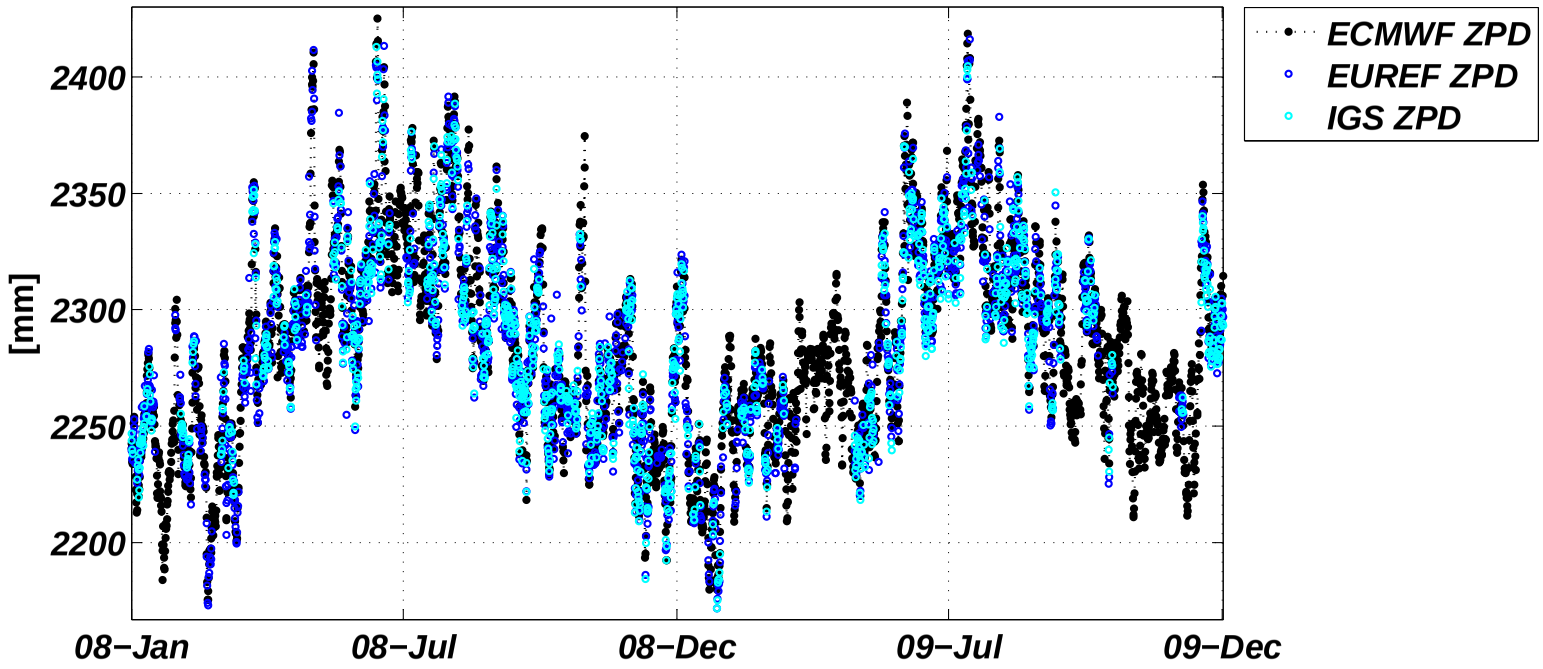

(a) ECMWF ZPD, EUREF ZPD and IGS ZPD

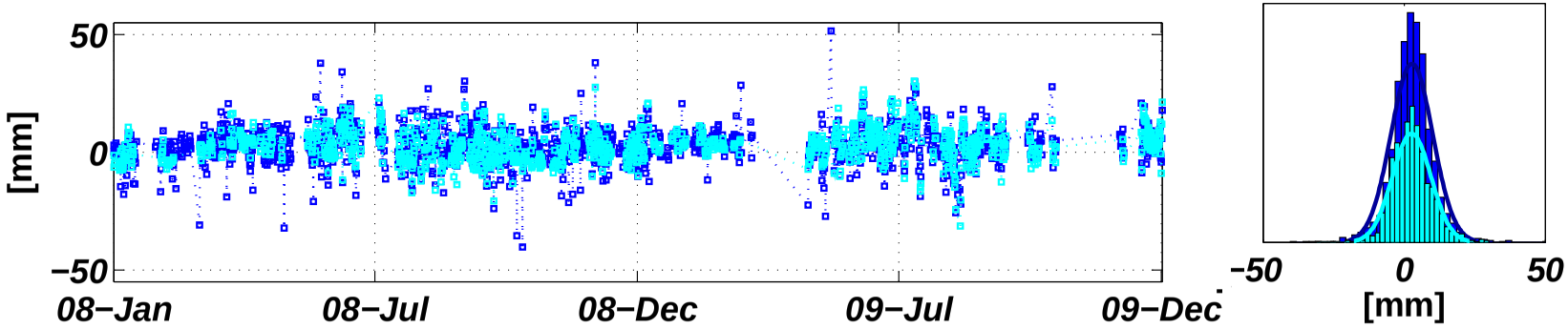

(b) ZPD differences

(c) Histogram

Fig. H.1. Validation of ECMWF ZPD with GPS ZPD derived from EUREF and IGS services on the KELY station. In total, 2924 ECMWF entries from 1 January 2008 to 31 December 2009 are used for validation. In (a), three time series are depicted: ZPD_{ECMWF} integrations illustrated with black circles and connected with black dashed lines; ZPD_{GPS} time series derived from EUREF (ZPD_{EUREF}) depicted with blue circles; ZPD_{GPS} time series from IGS (ZPD_{IGS}) plotted with cyan circles. The differences between ZPD_{ECMWF} and ZPD_{EUREF}, ZPD_{ECMWF} and ZPD_{IGS} are presented in (b). Their histograms are generated accordingly in (c).

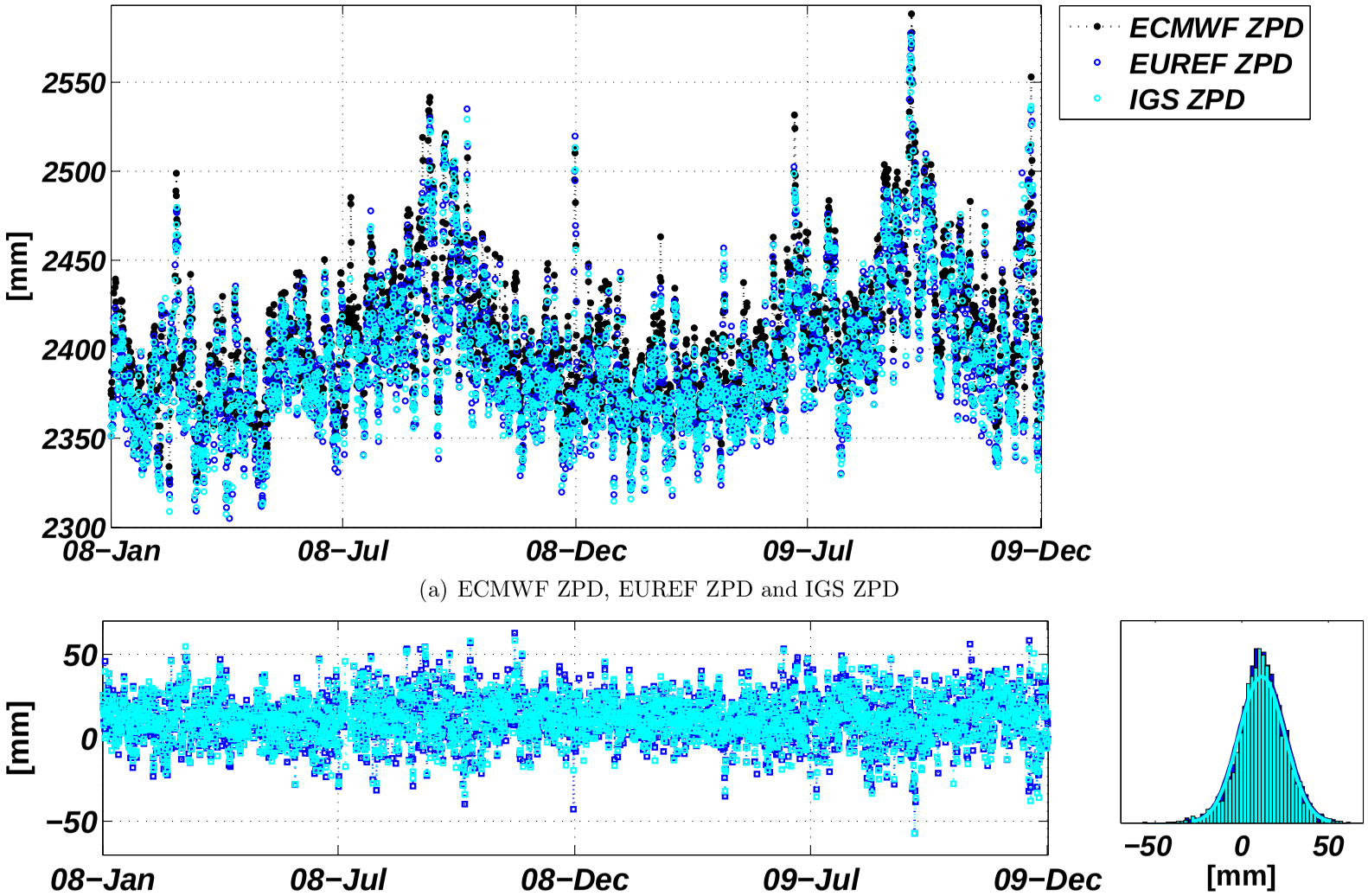

(a) ECMWF ZPD, EUREF ZPD and IGS ZPD

(b) ZPD differences

(c) Histogram

Fig. H.2. Validation of ECMWF ZPD with GPS ZPD derived from EUREF and IGS services on the MAS1 station. In total, 2924 ECMWF entries from 1 January 2008 to 31 December 2009 are used for validation. In (a), three time series are depicted: ZPD_{ECMWF} integrations illustrated with black circles and connected with black dashed lines; ZPD_{GPS} time series derived from EUREF (ZPD_{EUREF}) depicted with blue circles; ZPD_{GPS} time series from IGS (ZPD_{IGS}) plotted with cyan circles. The differences between ZPD_{ECMWF} and ZPD_{EUREF}, ZPD_{ECMWF} and ZPD_{IGS} are presented in (b). Their histograms are generated accordingly in (c).

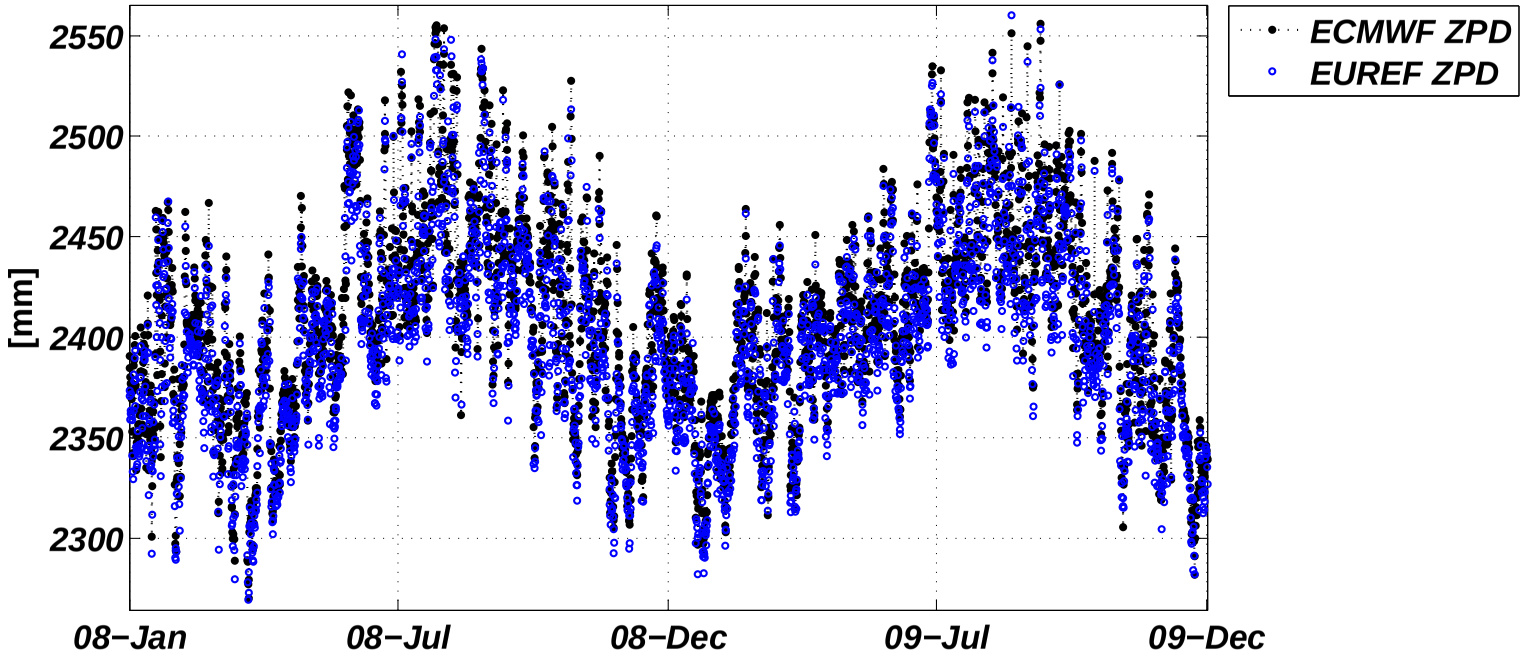

(a) ECMWF ZPD and EUREF ZPD

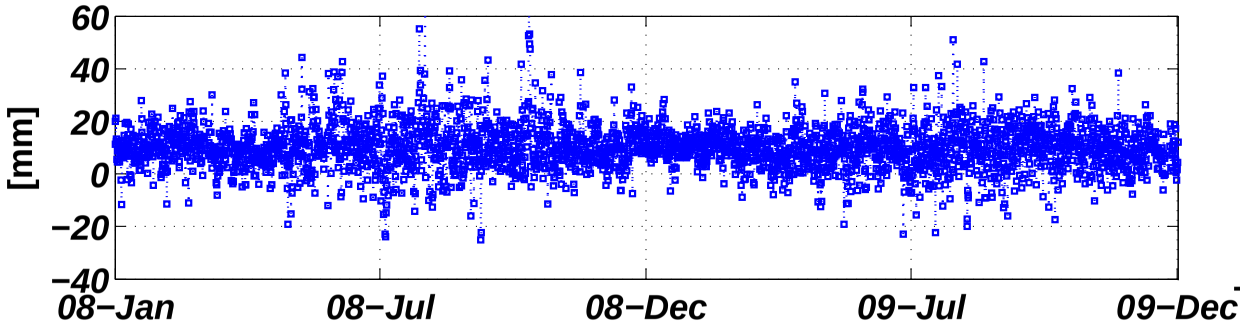

(b) ZPD differences

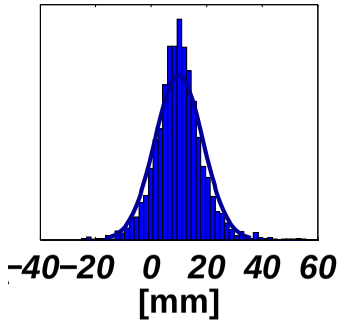

(c) Histogram

Fig. H.3. Validation of ECMWF ZPD with GPS ZPD derived from EUREF on the BORJ station. In total, 2924 ECMWF entries from 1 January 2008 to 31 December 2009 are used for validation. In (a), three time series are depicted: ZPD_{ECMWF} integrations illustrated with black circles and connected with black dashed lines; ZPD_{GPS} time series derived from EUREF (ZPD_{EUREF}) depicted with blue circles. The difference between ZPD_{ECMWF} and ZPD_{EUREF} is presented in (b). The histogram is generated accordingly in (c).

I Table of absolute localization residuals using ERA-Interim - WTZR CR experiments

Table I.1. Absolute localization residuals in range of the Corner Reflector in Wettzell, Bad Kötzting, Germany. Radar measured delay differences between the expected and the measured position of the corner reflector, the Continental Drift (CD), the Solid Earth Tides (SET), the Ocean Tide Loading (OTL), the Atmospheric Pressure Loading (APL), the ECMWF SPD and the Ionospheric Delay (ID) in range are shown in the table. The SAR acquisition time was 16:51 h UTC.

Acq. Date	**SAR Rng [m]**	**SPD [m]**	**ID [m]**	**SET [m]**	**OTL [m]**	**APL [m]**	**CD [m]**	**Residual [m]**
2011-07-12	2.5356	2.7613	0.0656	0.1104	0.0030	-0.0025	0.0000	-0.4022
2011-08-14	2.5562	2.7975	0.0593	0.0758	0.0055	-0.0039	0.0011	-0.3790
2011-08-25	2.5915	2.7958	0.0571	0.1146	0.0014	-0.0003	0.0015	-0.3785
2011-09-05	2.5460	2.7440	0.0733	0.0969	-0.0008	0.0004	0.0018	-0.3696
2011-09-16	2.5221	2.7146	0.0810	0.0878	0.0028	-0.0005	0.0022	-0.3658
2011-10-30	2.5542	2.7703	0.0725	0.1138	0.0015	0.0028	0.0037	-0.4103
2011-11-10	2.4750	2.6807	0.0683	0.1096	0.0021	0.0044	0.0041	-0.3942
2011-11-21	2.4258	2.7023	0.0648	0.0495	-0.0029	0.0021	0.0045	-0.3944
2011-12-24	2.4878	2.6908	0.0293	0.1391	0.0021	0.0027	0.0054	-0.3816
2012-01-15	2.2598	2.6426	0.0259	-0.0438	-0.0026	0.0039	0.0063	-0.3724
2012-01-26	2.3728	2.6385	0.0426	0.0636	0.0023	0.0069	0.0066	-0.3877
2012-02-06	2.4651	2.6515	0.0424	0.1337	0.0014	0.0105	0.0070	-0.3815
2012-03-10	2.4740	2.7254	0.0629	0.0412	0.0048	0.0066	0.0081	-0.3750
2012-04-01	2.3796	2.6422	0.1032	-0.0003	-0.0029	-0.0065	0.0088	-0.3648
2012-04-23	2.4156	2.6390	0.1146	0.0197	0.0049	-0.0048	0.0096	-0.3674
2012-05-04	2.5317	2.6685	0.0957	0.1458	0.0039	-0.0063	0.0099	-0.3858
2012-05-26	2.3467	2.7206	0.0728	-0.0593	0.0008	0.0013	0.0107	-0.4002
2012-06-06	2.4457	2.7571	0.0762	-0.0218	0.0058	-0.0032	0.0109	-0.3793
2012-06-17	2.5800	2.8194	0.0473	0.0915	0.0040	0.0000	0.0113	-0.3936
2012-06-28	2.5314	2.7633	0.0740	0.0713	-0.0015	-0.0031	0.0118	-0.3843
2012-07-20	2.5220	2.7740	0.0635	0.0442	0.0058	-0.0016	0.0125	-0.3763
2012-08-22	2.5878	2.7687	0.0683	0.0694	0.0015	-0.0009	0.0136	-0.3328
2012-09-13	2.5357	2.6971	0.0785	0.1203	0.0023	-0.0020	0.0144	-0.3749
2012-10-05	2.5686	2.7547	0.0800	0.0867	0.0013	-0.0004	0.0151	-0.3686
2012-10-16	2.4894	2.6798	0.0664	0.1473	0.0047	-0.0011	0.0154	-0.4230
2012-10-27	2.4322	2.6401	0.0641	0.1016	0.0013	-0.0076	0.0158	-0.3829
2012-11-07	2.4825	2.7267	0.0474	0.0532	-0.0021	0.0018	0.0162	-0.3607
Mean	2.4857	2.7173	0.0665	0.0727	0.0019	-0.0001	0.0084	-0.3810
ST	0.0810	0.0554	0.0200	0.0557	0.0027	0.0043	0.0050	0.0175

J Table of residuals using ERA-Interim - cross-correlation experiment in Venice

Table J.1. The residuals derived from cross-correlation measurements in range in test site Venice, Italy. Range offsets are relative to the master acquisition at 16 May 2008. The Solid Earth Tides (SET), the Ocean Tide Loading (OTL), the ECMWF Tropospheric Delay (TD) and the Ionospheric Delay (ID) in range are shown in the table. The SAR acquisition time was 05:18 h UTC.

Acq. Date	**Rel. SAR Rng [m]**	**Rel.TD [m]**	**Rel.SET [m]**	**Rel. ID [m]**	**OTL [m]**	**Residual [m]**
2008-05-16	0.0000	0.0000	0.0000	0.0000	0.0000	0.0000
2008-05-27	0.0086	0.0240	0.0479	0.0028	-0.0023	-0.0639
2008-06-07	0.1550	0.0374	0.1201	0.0056	-0.0092	0.0011
2008-07-10	0.0355	0.1026	-0.0334	0.0013	-0.0029	-0.0321
2008-07-21	0.1256	0.0181	0.1277	0.0056	-0.0052	-0.0206
2008-08-01	0.2380	0.1244	0.1110	0.0018	-0.0126	0.0134
2008-08-12	0.0393	0.1363	-0.0479	-0.0009	-0.0103	-0.0380
2008-09-14	0.1067	0.0233	0.1101	0.0021	-0.0172	-0.0115
2008-09-25	-0.1050	-0.0141	-0.0233	-0.0009	-0.0206	-0.0461
2008-10-06	-0.1055	-0.0533	-0.0253	0.0050	-0.0160	-0.0159
2009-01-24	-0.1644	-0.1886	0.1254	0.0051	-0.0269	-0.0793
2009-03-20	-0.1041	-0.1192	0.0837	0.0022	-0.0229	-0.0480
2009-04-11	0.0313	-0.0941	0.1164	0.0066	-0.0132	0.0156
2009-04-22	-0.0539	-0.0984	0.0426	0.0011	0.0080	-0.0072
2009-05-03	-0.0873	-0.0355	0.0228	0.0002	-0.0132	-0.0616
2009-05-14	0.0188	-0.0371	0.0929	0.0046	0.0080	-0.0496
2009-05-25	0.1085	0.0408	0.1035	0.0038	0.0017	-0.0414
2009-06-27	0.2063	0.0948	0.0683	0.0049	-0.0086	0.0469
2009-07-19	-0.1272	-0.0203	-0.0610	-0.0024	-0.0086	-0.0349
2009-08-10	0.1496	0.0730	0.0905	0.0064	-0.0138	-0.0064
2009-08-21	0.2523	0.1516	0.1617	0.0048	-0.0172	-0.0487
2009-09-01	-0.0082	0.0269	0.0130	-0.0003	-0.0172	-0.0307
Mean	0.0327	0.0087	0.0567	0.0027	-0.0100	-0.0254
ST	0.1226	0.0872	0.0663	0.0027	0.0093	0.0302

K Multi-track fusion: simulated data sets

Two objects have been simulated for simulation tests in section 4.2: in section K.1, a membrane object has been generated and then two point data sets are extracted from this object; in section K.2, different point data sets by means of different downsampling rates are generated based on the DEM in Stromboli.

K.1 Membrane object

The original membrane object is presented in *Fig. K.1*. The maximum magnitude in Z is about 2.5, which represents the height ratio. The x axis spans from 0 to 108, and the y axis from 0 to 144. Two point sets are generated based on the original object. One is extracted with a regular grid (1369 points) and the other one is extracted with an irregular grid (1728 points). Furthermore, independent random white noises are added on all three components of two data sets for the simulation, where the SNR varies from 5 to 20 dB.

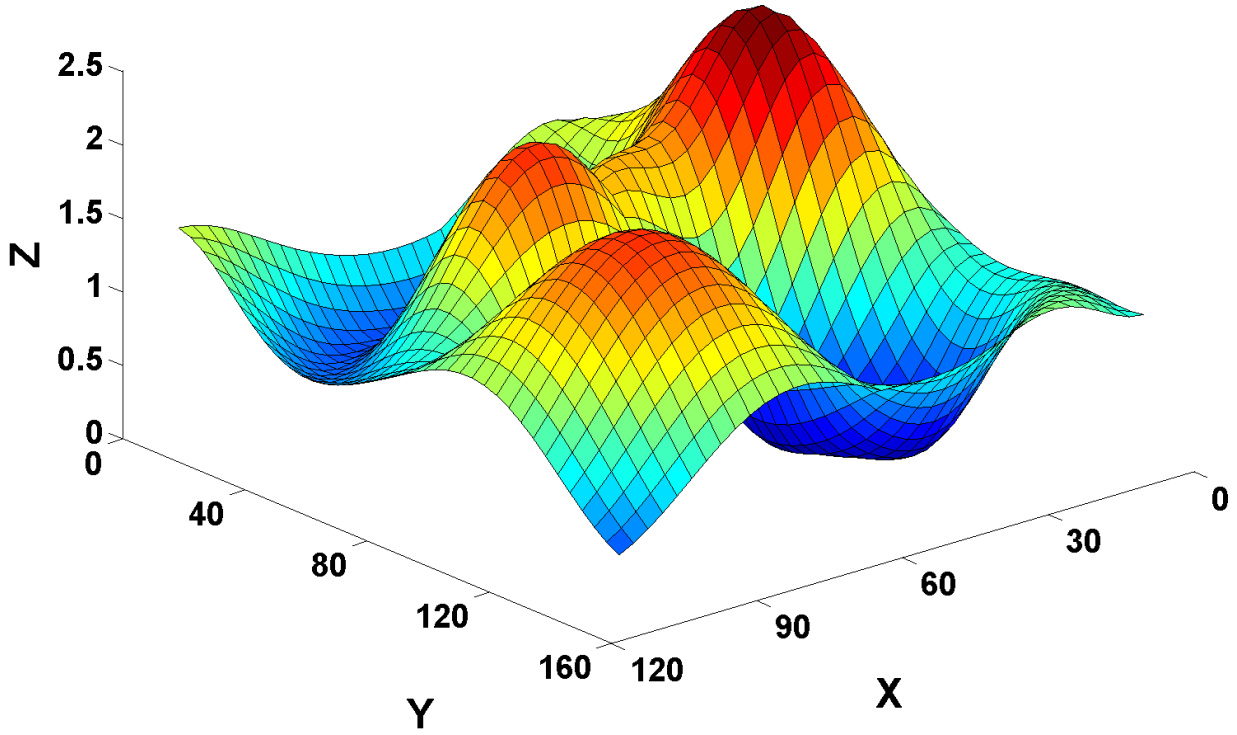

Fig. K.1. Simulated membrane object with the maximum magnitude in Z of about 2.5. The x axis spans from 0 to 108, and the y axis from 0 to 144.

K.2 Digital elevation model: Stromboli volcano

In order to retrieve the effective number of PSs for ICP, a smoothed DEM from Stromboli is used as input. As shown in *Fig. K.2*, more than 85×10^3 pseudo PSs are extracted with a regular grid. For ICP simulation, two sets of grid lengths are used to sparsify the original data to generate static and moving data sets. In order to obtain different PS samples, two grid lengths are slightly different with a constant offset of 5. Within a defined grid, one pseudo PS is randomly selected. The minimum grid length for the static data set is 25 and the maximum

length is 145, where the maximum number of PSs in static data sets is 20629 and the minimum is 669. Moreover, the maximum number of PSs in moving data sets is 14379 and the minimum is 624. For each grid length, ICP is then applied on the sparsified static and moving data sets, where the static data set is defined as model data set.

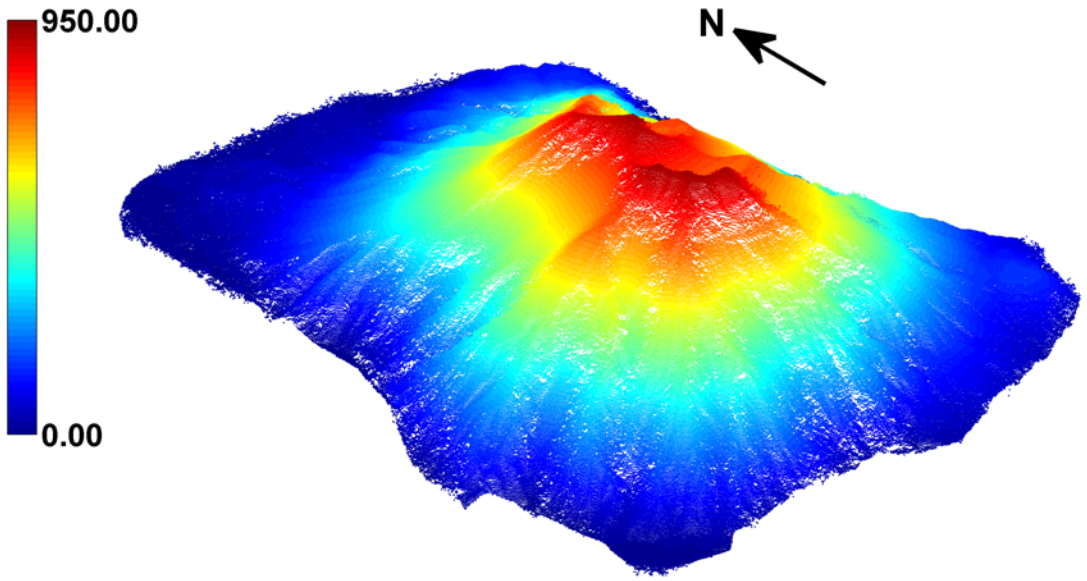

Fig. K.2. More than 85×10^3 pseudo PSs selected according to a regular grid from a smoothed DEM of Stromboli. All PSs are color-coded with their heights, which vary from 0 (blue) to 950 m(red).

References

Adam, N., Rodriguez Gonzalez, F., Parizzi, A., Liebhart, W., 2011. Wide area persistent scatterer interferometry: algorithms and examples. In: Fringe Workshop 2011. pp. 1–4.

Adams, R. J., Perger, W. F., Rose, W. I., Kostinski, A., 1996. Measurements of the complex dielectric constant of volcanic ash from 4 to 19 GHz. Journal of Geophysical Research 101 (B4), 8175–8185.

Agnew, D. C., 1997. NLOADF: a program for computing ocean-tide loading. Journal of Geophysical Research 102, 5109–5110.

Agnew, D. C., 2005. SPOTL: some programs for ocean-tide loading.

Aiuppa, A., Federico, C., Giudice, G., Giuffrida, G., Guida, R., Gurrieri, S., Liuzzo, M., Moretti, R., Papale, P., 2009. The 2007 eruption of Stromboli Volcano: Insights from real-time measurement of the volcanic gas plume CO2/SO2 ratio. Journal of Volcanology and Geothermal Research 182 (3-4), 221–230.

Altamimi, Z., Métivier, L., Collilieux, X., 2012. ITRF2008 plate motion model. Journal of Geophysical Research 117 (B7), 1–14.

Amelung, F., Jónsson, S., 2000. Widespread uplift and trapdoor faulting on Galapagos volcanoes observed with radar interferometry. Nature 407, 993–996.

Askne, J., Nordius, H., 1987. Estimation of tropospheric delay for microwaves from surface weather data. Radio Science 22 (3), 379–386.

Baldi, P., Coltelli, M., Fabris, M., Marsella, M., Tommasi, P., 2008. High precision photogrammetry for monitoring the evolution of the NW flank of Stromboli volcano during and after the 2002-2003 eruption. Bulletin of Volcanology 70 (6), 703–715.

Baldi, P., Fabris, M., Marsella, M., Monticelli, R., 2005. Monitoring the morphological evolution of the Sciara del Fuoco during the 2002–2003 Stromboli eruption using multi-temporal photogrammetry. ISPRS Journal of Photogrammetry and Remote Sensing 59 (4), 199–211.

Balss, U., Cong, X., Brcic, R., Rexer, M., Minet, C., Breit, H., 2012. High precision measurement on the absolute localization accuracy of TerraSAR-X. In: IGARSS 2012. pp. 1625–1628.

Balss, U., Eineder, M., Fritz, T., Breit, H., Minet, C., 2011. Techniques for high accuracy relative and absolute localization of TerraSAR-X/TanDEM-X data. In: IGARSS 2011. pp. 2464–2467.

Balss, U., Gisinger, C., Cong, X., Brcic, R., Steigenberger, P., Eineder, M., Pail, R., U., H., 2013. High resolution geodetic earth observation with TerraSAR-X: correction schemes and validation. In: IGARSS 2013. pp. 4499 – 4502.

Bamler, R., Eineder, M., 2004. Split bandinterferometry versus absolute ranging with wideband SAR systems. In: IGARSS 2004. pp. 980–984.

Bamler, R., Eineder, M., 2005. Accuracy of differential shift estimation by correlation and split-bandwidth interferometry for wideband and delta-k SAR systems. IEEE Geoscience and Remote Sensing Letters 2 (2), 151–155.

Bamler, R., Hartl, P., 1998. Synthetic aperture radar interferometry. Inverse Problems 14 (4), R1–R54.

Bawden, G. W., Thatcher, W., Stein, R. S., Hudnut, K. W., Peltzer, G., 2001. Tectonic contraction across Los Angeles after removal of groundwater pumping effects. Nature 412 (6849), 812–5.

Bechtold, P., 2010. Atmospheric thermodynamics. Tech. Rep. June 2009, ECMWF.

Bechtold, P., Park, S., 2010. Atmospheric moist convection. Tech. Rep. March 2009, ECMWF.

Bentley, J. L., 1990. K-d trees for semidynamic point sets. In: Proceedings of the Sixth Annual Symposium on Computational Geometry. ACM, pp. 187–197.

Berardino, P., Casu, F., Fornaro, G., Lanari, R., Manunta, M., Manzo, M., Pepe, A., Pepe, S., Sansosti, E., Serafino, F., Solaro, G., Tizzani, P., Zeni, G., 2007. Surface deformation analysis of the Campi Flegrei caldera, Italy, by exploiting the ENVISAT ASAR data with the SBAS-DInSAR technique. In: IGARSS 2007. pp. 1159–1162.

Berardino, P., Fornaro, G., Lanari, R., Sansosti, E., 2002. A new algorithm for surface deformation monitoring based on small baseline differential SAR interferograms. IEEE Transactions on Geoscience and Remote Sensing 40 (11), 2375–2383.

Besl, P. J., McKay, N. D., 1992. Method for registration of 3-D shapes. In: Robotics-DL tentative. International Society for Optics and Photonics, pp. 586–606.

Beutler, G., 2005. Methods of celestial mechanics - volume II: application to planetary system, geodynamics and satellite geodesy. Vol. II. Springer.

Bevis, M., Businger, S., Chiswell, S., Herring, T. A., Anthes, R. A., Rocken, C., Ware, R. H., 1994. GPS meterology: mapping zenith wet delays onto precipitable water. Journal of Applied Meteorology 33 (3), 379–386.

Bevis, M., Businger, S., Herring, T. A., Rocken, C., Anthes, R. A., Ware, R. H., 1992. GPS meteorology: remote sensing of atmospheric water vapor using the global positioning system. Journal of Geophysical Research 97 (92), 787–801.

Bezděk, A., Sebera, J., 2013. Matlab script for 3D visualizing geodata on a rotating globe. Computers & Geosciences 56, 127–130.

Bock, O., Keil, C., Richard, E., Flamant, C., Bouin, M.-N., 2005. Validation of precipitable water from ECMWF model analyses with GPS and radiosonde data during the MAP SOP. Quarterly Journal of the Royal Meteorological Society 131 (612), 3013–3036.

Boehm, J., Heinkelmann, R., Mendes Cerveira, P. J., Pany, A., Schuh, H., 2009. Atmospheric loading corrections at the observation level in VLBI analysis. Journal of Geodesy 83 (11), 1107–1113.

Böhm, J., 2004. Troposphärische Laufzeitverzögerungen in der VLBI. Ph.D. thesis, Vienna University of Technology.

Boldini, D., Wang, F., Sassa, K., Tommasi, P., 2009. Application of large-scale ring shear tests to the analysis of tsunamigenic landslides at the Stromboli Volcano, Italy. Landslides 6 (3), 231–240.

Bonaccorso, A., Bonforte, A., Gambino, S., Mattia, M., Guglielmino, F., Puglisi, G., Boschi, E., 2009. Insight on recent Stromboli eruption inferred from terrestrial and satellite ground deformation measurements. Journal of Volcanology and Geothermal Research 182 (3), 172–181.

Bonaccorso, A., Calvari, S., Garfì, G., Lodato, L., Patanè, D., 2003. Dynamics of the December 2002 flank failure and tsunami at Stromboli Volcano inferred by volcanological and geophysical observations. Geophysical Research Letters 30 (18), 1941.

Bos, M. S., Baker, T. F., 2005. An estimate of the errors in gravity ocean tide loading computations. Journal of Geodesy 79 (1-3), 50–63.

Brcic, R., Parizzi, A., Eineder, M., Bamler, R., Meyer, F., 2011. Ionospheric effects in SAR interferometry: An analysis and comparison of methods for their estimation. In: IGARSS 2011. pp. 1497 – 1500.

Breit, H., Fritz, T., Balss, U., Lachaise, M., Niedermeier, a., Vonavka, M., 2010. TerraSAR-X SAR processing and products. IEEE Transactions on Geoscience and Remote Sensing 48 (2), 727–740.

Brunner, F. K., Gu, M., 1991. An improved model for the dual frequency ionospheric correction of GPS observations. Manuscripta geodaetica 16 (3), 205–214.

Bruyninx, C., 2004. The EUREF Permanent Network: a multi-disciplinary network serving surveyors as well as scientists. GeoInformatics 7, 32–35.

Calvari, S., Büttner, R., Cristaldi, A., Dellino, P., Giudicepietro, F., Orazi, M., Peluso, R., Spampinato, L., Zimanowski, B., Boschi, E., 2012. The 7 September 2008 Vulcanian explosion at Stromboli Volcano: multiparametric characterization of the event and quantification of the ejecta. Journal of Geophysical Research 117 (B5), B05201.

Calvari, S., Lodato, L., Steffke, A., Cristaldi, A., Harris, A., Spampinato, L., Boschi, E., 2010. The 2007 Stromboli eruption: event chronology and effusion rates using thermal infrared data. Journal of Geophysical Research: Solid Earth (1978–2012) 115 (B4).

Casagli, N., Tibaldi, A., Merri, A., Del Ventisette, C., Apuani, T., Guerri, L., Fortuny-Guasch, J., Tarchi, D., 2009. Deformation of Stromboli Volcano (Italy) during the 2007 eruption revealed by radar interferometry, numerical modelling and structural geological field data. Journal of Volcanology and Geothermal Research 182 (3), 182–200.

Casu, F., Manconi, A., Pepe, A., Lanari, R., 2011. Deformation Time-Series Generation in Areas Characterized by Large Displacement Dynamics: The SAR Amplitude Pixel-Offset SBAS Technique. IEEE Transactions on Geoscience and Remote Sensing 49 (7), 2752–2763.

Catalão, J., Nico, G., Hanssen, R. F., Catita, C., 2011. Merging GPS and atmospherically corrected InSAR data to map 3-D terrain displacement velocity. IEEE Transactions on Geoscience and Remote Sensing 49 (6), 2354–2360.

Cimini, D., Pierdicca, N., Pichelli, E., Ferretti, R., Mattioli, V., Bonafoni, S., Montopoli, M., Perissin, D., 2012. On the accuracy of integrated water vapor observations and the potential for mitigating electromagnetic path delay error in InSAR. Atmospheric Measurement Techniques Discussions 5 (1), 839–880.

CODE, 2012. CODE research on the homepage of the astronomic institut at University Bern. URL `aiuws.unibe.ch/ionosphere/`

Colesanti, C., Ferretti, A., Prati, C., Rocca, F., 2003. Monitoring landslides and tectonic motions with the permanent scatterers technique. Engineering Geology 68, 3–14.

Cong, X., Balss, U., Eineder, M., Fritz, T., 2012a. Imaging geodesy-centimeter-level ranging accuracy with TerraSAR-X: an update. IEEE Geoscience and Remote Sensing Letters 9 (5), 948–952.

Cong, X., Eineder, M., 2011. Detection of the deformation and generation of high density PS-DEM in volcanic area using multi-stack high resolution TerraSAR-X images. In: Proceedings of 4th TerraSAR-X Science Team Meeting. pp. 1–2.

Cong, X., Eineder, M., 2012. Volcano deformation measurement using persistent scatterer interferometry with atmospheric delay corrections. In: EUSAR 2012. pp. 681–684.

Cong, X., Eineder, M., Brcic, R., Adam, N., Minet, C., 2011. Validation of centimeter-Level SAR geolocation accuracy after correction for atmospheric delay using ECMWF weather data. In: Fringe Workshop 2011. pp. 1–4.

Cong, X., Eineder, M., Fritz, T., 2012b. Volcanic deformation monitoring using TanDEM-X acquisitions-study case: el Hierro (2011-2012). In: IGARSS 2012. pp. 3887–3890.

Cong, X., Eineder, M., Gernhardt, S., Minet, C., 2010a. Diverse methods to monitoring volcanic deformation. In: IGARSS 2010. pp. 661–664.

Cong, X., Eineder, M., Minet, C., 2010b. Monitoring volcanic area with radar interferometry - case study Fogo Volcano within Exupéry project. In: EUSAR 2010. pp. 1134–1137.

Cong, X., Hinz, S., Eineder, M., Parizzi, A., 2008. Ground deformation measurement with radar interferometry in Exupéry. In: Second Workshop on USEReST 2008. pp. 1–4.

Cong, X., Minet, C., Eineder, M., 2010c. Deformation monitoring using SAR interferometry on the Azores within Exupéry project. In: Fringe Workshop 2009. pp. 1–4.

Coppola, D., Piscopo, D., Laiolo, M., Cigolini, C., Delle Donne, D., Ripepe, M., 2012. Radiative heat power at Stromboli volcano during 2000–2011: Twelve years of MODIS observations. Journal of Volcanology and Geothermal Research 215, 48–60.

Costantini, M., 1998. A Novel Phase Unwrapping Method Based on Network Programming. IEEE Transactions on Geoscience and Remote Sensing 36 (3), 813–821.

Dai, A., Trenberth, K. E., Karl, T. R., 1999. Effects of clouds, soil moisture, precipitation, and water vapor on diurnal temperature range. Journal of Climate 12 (8), 2451–2473.

Dai, A., Wang, J., Ware, R. H., Van Hove, T., 2002. Diurnal variation in water vapor over North America and its implications for sampling errors in radiosonde humidity. Journal of Geophysical Research: Atmospheres (1984–2012) 107 (D10), ACL–11.

Dam, T. M., 2005. Current status of publicly available atmospheric mass loading products. In: IERS Workshop on Combination. pp. 1–5.

Dam, T. M., Blewitt, G., Heflin, M. B., 1994. Atmospheric pressure loading effects on global

positioning system coordinate determinations. Journal of Geophysical Research 99 (B12), 23939–23950.

Dam, T. M., Collilieux, X., Wuite, J., Altamimi, Z., Ray, J., 2012. Nontidal ocean loading: amplitudes and potential effects in GPS height time series. Journal of Geodesy.

Dam, T. M., Herring, T. a., 1994. Detection of atmospheric pressure loading using very long baseline interferometry measurements. Journal of Geophysical Research 99 (B3), 4505–4517.

Danklmayer, A., Döring, B. J., Schwerdt, M., Chandra, M., 2009. Assessment of atmospheric propagation effects in SAR images. IEEE Transactions on Geoscience and Remote Sensing 47 (10), 3507–3518.

Davis, J. L., Herring, T. A., Shapiro, I. I., Rogers, A. E. E., Elgered, G., 1985. Geodesy by radio interferometry: effects of atmospheric modeling errors on estimates of baseline length. Radio Science 20 (6), 1593–1607.

Dee, D. P., Uppala, S. M., 2009. Variational bias correction of satellite radiance data in the ERA-Interim reanalysis. Quarterly Journal of the Royal Meteorological Society 1841 (October), 1830–1841.

Dee, D. P., Uppala, S. M., Simmons, A. J., Berrisford, P., Poli, P., Kobayashi, S., Andrae, U., Balmaseda, M. A., Balsamo, G., Bauer, P., Bechtold, P., Beljaars, A., van de Berg, L., Bidlot, J., Bormann, N., Delsol, C., Dragani, R., Fuentes, M., Geer, A. J., Haimberger, L., Healy, S. B., Hersbach, H., Hólm, E. V., Isaksen, L., Kå llberg, P., Köhler, M., Matricardi, M., McNally, A. P., Monge-Sanz, B. M., Morcrette, J.-J., Park, B.-K., Peubey, C., de Rosnay, P., Tavolato, C., Thépaut, J.-N., Vitart, F., 2011. The ERA-Interim reanalysis: configuration and performance of the data assimilation system. Quarterly Journal of the Royal Meteorological Society 137 (656), 553–597.

Delacourt, C., Briole, P., Achache, J., 1998a. Tropospheric corrections of SAR interferograms with strong topography. Application to Etna. Geophysical Research Letters 25 (15), 2849.

Delacourt, C., Briole, P., Achache, J., 1998b. Tropospheric corrections of SAR interferograms with strong topography. Application to Etna. Geophysical Research Letters 25 (15), 2849–2852.

Deutsch, C. V., Journel, A. G., 1997. GSLIB: geostatistical software library and user's guide. Oxford University Press.

DiCaprio, C. J., Simons, M., 2008. Importance of ocean tidal load corrections for differential InSAR. Geophysical Research Letters 35 (22), 1–5.

Doerry, A. W., Brock, B. C., 2009. Radar cross section of triangular trihedral reflector with extended bottom plate. Tech. Rep. May, Sandia National Laboratories.

Doin, M.-P., Lasserre, C., Peltzer, G., Cavalié, O., Doubre, C., 2009. Corrections of stratified tropospheric delays in SAR interferometry: validation with global atmospheric models. Journal of Applied Geophysics 69 (1), 35–50.

Dong, D., Fang, P., Bock, Y., Cheng, M. K., Miyazaki, S., 2002. Anatomy of apparent seasonal variations from GPS-derived site position time series. Journal of Geophysical Research 107 (April), 9.

Doornbos, E., Scharroo, R., Klinkrad, H., Zandbergen, R., Fritsche, B., 2002. Improved modelling of surface forces in the orbit determination of ERS and ENVISAT. Canadian Journal of Remote Sensing 28 (4), 535–543.

Dow, J. M., Neilan, R. E., Rizos, C., 2009. The international GNSS Service in a changing landscape of global navigation satellite systems. Journal of Geodesy 83 (3-4), 191–198.

Duan, J., Devis, M., Fang, P., Dock, Y., Chiswell, S., Businger, S., Rocken, C., Solheim, F., Hove, T. v., Ware, R., McClusky, S., Herring, T. A., King, R. W., 1995. GPS meteorology direct estimation of the absolute value of precipitable water. Journal of Applied Meteorology 35, 830–838.

ECMWF, 2013. Model level definitions.
URL `www.ecmwf.int/products/data/technical/model_levels/index.html`

Eineder, M., 2003. Problems and solutions for InSAR digital elevation model generation of

mountainous terrain. In: Fringe Workshop 2003. pp. 1–9.
Eineder, M., Minet, C., Steigenberger, P., Cong, X., Fritz, T., 2011. Imaging geodesy-toward centimeter-level ranging accuracy with TerraSAR-X. IEEE Transactions on Geoscience and Remote Sensing 49 (2), 661–671.
Farr, T. G., Rosen, P. A., Caro, E., Crippen, R., Duren, R., Hensley, S., Kobrick, M., Paller, M., Rodriguez, E., Roth, L., et al., 2007. The shuttle radar topography mission. Reviews of Geophysics 45 (2).
Ferretti, A., Bianchi, M., Novali, F., Tamburini, A., 2008. Volcanic deformation mapping using PSInSAR TM : Piton de la Fournaise , Stromboli and Vulcano test sites for the Globvolcano project. In: USEReST 2008. pp. 1–4.
Ferretti, A., Fumagalli, A., Novali, F., Prati, C., Rocca, F., Rucci, A., 2011. A new algorithm for processing interferometric data-stacks: SqueeSAR. IEEE Transactions on Geoscience and Remote Sensing 49 (9), 3460–3470.
Ferretti, a., Prati, C., Rocca, F., 2000. Nonlinear subsidence rate estimation using permanent scatterers in differential SAR interferometry. IEEE Transactions on Geoscience and Remote Sensing 38 (5), 2202–2212.
Ferretti, A., Prati, C., Rocca, F., 2001. Permanent scatterers in SAR interferometry. IEEE Transactions on Geoscience and Remote Sensing 39 (1), 8–20.
Fiorani, L., Colao, F., Palucci, A., Poreh, D., Aiuppa, A., Giudice, G., 2011. First-time lidar measurement of water vapor flux in a volcanic plume. Optics Communications 284 (5), 1295–1298.
Flentje, H., Dörnbrack, a., Fix, a., Ehret, G., Hólm, E., 2007. Evaluation of ECMWF water vapour fields by airborne differential absorption lidar measurements: a case study between Brazil and Europe. Atmospheric Chemistry and Physics 7 (19), 5033–5042.
Fornaro, G., Franceschetti, G., Lanari, R., Migliaccio, M., Moreira, J. R., Papathanassiou, K. P., Puglisi, G., Riccio, D., Schwabisch, M., 1996. On the survey of volcanic sites: the SIR-C/X-SAR interferometry. In: IGARSS 1996. pp. 350–352.
Frisch., U., 1995. Turbulence: the legacy of A. N. Kolmogorov. Cambridge University Press.
Fritz, T., Breit, H., Eineder, M., 2008. TerraSAR-X products tips and tricks. In: Proceedings of 3rd TerraSAR-X Science Team Meeting.
Gabriel, A. K., Goldstein, R. M., 1988. Crossed orbit interferometry: theory and experimental results from SIR-B. International Journal of Remote Sensing 9 (5), 857–872.
Gernhardt, S., Cong, X., Eineder, M., Hinz, S., Bamler, R., 2012. Geometrical fusion of multitrack PS point clouds. IEEE Geoscience and Remote Sensing Letters 9 (1), 38–42.
Gernhardt, S. M., 2011. High rrecision 3D localization and motion analysis of persistent scatterers using meter-resolution radar satellite data. Ph.D. thesis, Technische Universität München.
Gisinger, C., 2012. Atmospheric corrections for TerraSAR-X derived from GNSS observations. Master's thesis, Technische Universitaet Muenchen.
Goldstein, R. M., 1995. Atmospheric limitations to repeat-track radar interferometry. Geophysical Research Letters 22 (18), 2517–2520.
Goldstein, R. M., Zebker, H. A., Werner, C. L., 1988. Satellite radar interferometry: two-dimensional phase unwrapping. Radio Science 23 (4), 713–720.
Gong, W., Meyer, F., Webley, P. W., Morton, D., Liu, S., 2010. Performance analysis of atmospheric correction in InSAR data based on the Weather Research and Forecasting Model (WRF). In: IGARSS 2010. pp. 2900–2903.
Hanssen, R. F., 1999. High-resolution water vapor mapping from interferometric radar measurements. Science 283 (5406), 1297–1299.
Hanssen, R. F., 2001. Radar interferometry: data interpretation and error analysis. Vol. 2. Springer.
Hanssen, R. F., Zebker, H. A., Klees, R., Barlag, S., 1998. On the use of meteorological observations in SAR interferometry. In: IGARSS 1998. Vol. 2782562. pp. 1644–1646.

Healy, S. B., 2011. Refractivity coefficients used in the assimilation of GPS radio occultation measurements. Journal of Geophysical Research 116 (D1), 1–10.

Heiskanen, W., Moritz, H., 1967. Physical geodesy. Bulletin Géodésique (1946-1975) 86 (1), 491–492.

Hobiger, T., 2006. VLBI as a tool to probe the ionosphere. Ph.D. thesis, Vienna University of Technology.

Hobiger, T., Ichikawa, R., Koyama, Y., Kondo, T., 2008. Fast and accurate ray-tracing algorithms for real-time space geodetic applications using numerical weather models. Journal of Geophysical Research 113 (20), 1–14.

Hobiger, T., Kinoshita, Y., Shimizu, S., Ichikawa, R., Furuya, M., Kondo, T., Koyama, Y., 2010. On the importance of accurately ray-traced troposphere corrections for interferometric SAR data. Journal of Geodesy 84 (9), 537–546.

Hooper, A., 2008. A multi-temporal InSAR method incorporating both persistent scatterer and small baseline approaches. Geophysical Research Letters 35 (16), 5.

Hooper, A., Segall, P., Zebker, H. A., 2007. Persistent scatterer interferometric synthetic aperture radar for crustal deformation analysis, with application to Volcán Alcedo, Galápagos. Journal of Geophysical Research 112 (B7), 1–21.

Hort, M., 2009. Exupéry-a mobile fast response system for managing a volcanic crisis. In: AGU Fall Meeting Abstracts. Vol. 1. p. 2050.

Hortal, M., Simmons, A. J., 1991. Use of reduced gaussian grids in spectral models. Monthly Weather Review 119, 1057–1074.

Intrieri, E., Di Traglia, F., Del Ventisette, C., Gigli, G., Mugnai, F., Luzi, G., Casagli, N., 2013. Flank instability of Stromboli volcano (Aeolian Islands, Southern Italy): integration of GB-InSAR and geomorphological observations. Geomorphology 201, 60–69.

Jehle, M., Perler, D., Small, D., Schubert, A., Meier, E., 2008. Estimation of atmospheric path delays in TerraSAR-X data using models vs. measurements. Sensors 8 (12), 8479–8491.

Jung, H.-S., Lu, Z., Won, J. S., Poland, M. P., Miklius, A., 2011. Mapping three-dimensional surface deformation by combining multiple-aperture interferometry and conventional interferometry: application to the June 2007 eruption of Kilauea Volcano, Hawaii. IEEE Geoscience and Remote Sensing Letters 8 (1), 34–38.

Jung, H.-S., Won, J. S., Kim, S.-W., 2009. An improvement of the performance of multiple-aperture SAR interferometry (MAI). IEEE Transactions on Geoscience and Remote Sensing 47 (8), 2859–2869.

Kampes, B. M., 2006. Radar interferometry: persistent scatterer technique. Vol. 12. Springer.

King, M. A., 2005. Validation of ocean tide models around Antarctica using onshore GPS and gravity data. Journal of Geophysical Research 110 (B08401).

King, M. A., Altamimi, Z., Boehm, J., Bos, M., Dach, R., Elosegui, P., Fund, F., Hernández-Pajares, M., Lavallee, D., Mendes Cerveira, P. J., Penna, N., Riva, R. E. M., Steigenberger, P., Dam, T. M., Vittuari, L., Williams, S., Willis, P., 2010. Improved constraints on models of glacial isostatic adjustment: A review of the contribution of ground-based geodetic observations. Surveys in Geophysics 31 (5), 465–507.

Kolmogorov, A. N., 1941. The local structure of turbulence in incompressible viscous fluid for very large Reynolds numbers. Dokl. Akad. Nauk SSSR 30 (4), 299–303.

Kruczyk, M., 2008. Tropospheric delay EPN products and meteorological ZTD and IPW data sources - conformity study. Tech. rep., EUREF Publication.

Lanari, R., Lundgren, P., Sansosti, E., 1998. Dynamic deformation of Etna Volcano observed by satellite radar interferometry. Geophysical Research Letters 25 (10), 1541.

Lanari, R., Mora, O., Manunta, M., Mallorqui, J. J., Berardino, P., Sansosti, E., 2004. A small-baseline approach for investigating deformations on full-resolution differential SAR interferograms. IEEE Transactions on Geoscience and Remote Sensing 42 (7), 1377–1386.

Li, Z., Fielding, E. J., Cross, P., 2009. Integration of InSAR time-series analysis and water-vapor correction for mapping postseismic motion after the 2003 Bam (Iran) earthquake. IEEE

Transactions on Geoscience and Remote Sensing 47 (9), 3220–3230.
Li, Z., Muller, J. P., Cross, P., Albert, P., Fischer, J., Bennartz, R., 2007. Assessment of the potential of MERIS near Infrared water vapour products to correct ASAR interferometric measurements. International Journal of Remote Sensing 27 (2), 349–365.
Li, Z., Pasquali, P., Cantone, A., Singleton, A., Funning, G., Forrest, D., 2012. MERIS atmospheric water vapor correction model for wide swath interferometric synthetic aperture radar. IEEE Geoscience and Remote Sensing Letters 9 (2), 257–261.
Liebhart, W., Adam, N., Parizzi, A., 2010. Least squares estimation of PSI networks for large scenes with multithreaded singular value decomposition. In: EUSAR 2010. p. 4.
Liebhart, W., Adam, N., Rodriguez Gonzalez, F., Parizzi, A., Cong, X., 2012. Four level least squares adjustment in persistent scatterer interferometry for the wide area product. In: IGARSS 2011. pp. 3859–3862.
Lindenbergh, R., Keshin, M., Marel, H. v. d., Hanssen, R. F., 2008. High resolution spatiotemporal water vapour mapping using GPS and MERIS observations. International Journal of Remote Sensing 29 (8), 2393–2409.
Mackenzie, J. S., Ringrose, P. S., 1986. Use of SEASAT SAR imagery for geological mapping in a volcanic terrain: Askja Caldera, Iceland. International Journal of Remote Sensing 7 (2), 181–194.
Mahoney, M., 2005. A discussion of various measures of altitude.
URL `mtp.mjmahoney.net/www/notes/altitude/altitude.html`
Marchetti, E., Genco, R., Ripepe, M., 2009. Ground deformation and seismicity related to the propagation and drainage of the dyke feeding system during the 2007 effusive eruption at Stromboli Volcano (Italy). Journal of Volcanology and Geothermal Research 182 (3), 155–161.
Marsella, M., Baldi, P., Coltelli, M., Fabris, M., 2012. The morphological evolution of the Sciara del Fuoco since 1868: reconstructing the effusive activity at Stromboli Volcano. Bulletin of volcanology 74 (1), 231–248.
Massonnet, D., 1993. Radar interferometry: limits and potential. Geoscience and Remote Sensing, IEEE Transactions on 31 (2), 455 – 464.
Massonnet, D., Briole, P., Arnaud, A., 1995. Deflation of Mount Etna monitored by spaceborne radar interferometry. Nature 375, 567–570.
Massonnet, D., Feigl, K. L., 1998. Radar interferometry and its application to changes in the earth's surface. Reviews of Geophysics 36 (4), 441–500.
Massonnet, D., Feigl, K. L., Rossi, M., Adragna, F., 1994. Radar interferometric mapping of deformation in the year after the Landers earthquake. Nature 369, 227–230.
Massonnet, D., Rossi, M., Carmona, C., Adragna, F., Peltzer, G., Feigl, K. L., Rabaute, T., 1993. The displacement field of the Landers earthquake mapped by radar interferometry. Nature 364, 138–142.
Massonnet, D., Thatcher, W., Vadon, H., 1996. Detection of postseismic fault-zone collapse following the Landers earthquake. Nature 382, 612–616.
Matsumoto, K., Sato, T., Takanezawa, T., Ooe, M., 2001. GOTIC2: a program for computation of oceanic tidal loading effect. Journal of the Geodetic Society of Japan 47 (1), 243–248.
Mccarthy, D. D., 1996. IERS Conventions. Tech. Rep. July, IERS.
Mccarthy, D. D., 2003. IERS conventions. Tech. rep., International Earth Rotation and Reference Systems Service (IERS).
Meade, C., Sandwell, D., 1996. Synthetic aperture radar for geodesy. Science 27 (August), 1181–1182.
Meyer, F., 2011. Performance requirements for ionospheric correction of low-frequency SAR data. IEEE Transactions on Geoscience and Remote Sensing 49 (10), 3694–3702.
Meyer, F., Bamler, R., Jakowski, N., Fritz, T., 2006. The potential of low-frequency SAR systems for mapping ionospheric TEC distributions. IEEE Geoscience and Remote Sensing Letters 3 (4), 560–564.
Milbert, D., 2012. Solid earth tide.

URL http://home.comcast.net/~dmilbert/softs/solid.htm

Mohr, J. J., Madsen, S. N., 2001. Geometric calibration of ERS satellite SAR images. IEEE Transactions on Geoscience and Remote Sensing 39 (4), 842–850.

Mooney, P. a., Mulligan, F. J., Fealy, R., 2011. Comparison of ERA-40, ERA-Interim and NCEP/NCAR reanalysis data with observed surface air temperatures over Ireland. International Journal of Climatology 31 (4), 545–557.

Moreira, J., Schwabisch, M., Fomaro, G., Lanari, R., Bamler, R., Just, D., Steinbrecher, U., Breit, H., Eineder, M., Franceschetti, G., Geudtner, D., Rinkel, H., 1995. X-interferometry: first results. IEEE Transactions on Geoscience and Remote Sensing 33 (4), 950 – 956.

Nafisi, V., Urquhart, L., Santos, M. C., Nievinski, F. G., Böhm, J., Wijaya, D. D., Schuh, H., Ardalan, A. A., Hobiger, T., Ichikawa, R., Zus, F., Wickert, J., Gegout, P., 2012. Comparison of ray-tracing packages for troposphere delays. IEEE Transactions on Geoscience and Remote Sensing 50 (2), 469–481.

Nico, G., Tomé, R., Catalão, J., Miranda, P. M. A., 2011. On the use of the WRF Model to mitigate tropospheric phase delay effects in SAR interferograms. IEEE Transactions on Geoscience and Remote Sensing 49 (12), 4970–4976.

Niell, A. E., 2000. Improved atmospheric mapping functions for VLBI and GPS. Earth and Planetary Science Letters 52, 699–702.

Nolesini, T., Di Traglia, F., Del Ventisette, C., Moretti, S., Casagli, N., 2013. Deformations and slope instability on Stromboli volcano: Integration of GBInSAR data and analog modeling. Geomorphology 180, 242–254.

Owens, J. C., 1967. Optical refractive index of air : dependence on pressure, temperature and composition. Applied Optics 6 (1), 51–58.

Pacione, R., Sciarretta, C., Vespe, F., Faccani, C., Ferretti, R., Fionda, E., Ferraro, C., Nardi, a., 2001. GPS meteorology: validation and comparisons with ground-based microwave radiometer and mesoscale model for the Italian GPS permanent stations. Physics and Chemistry of the Earth, Part A: Solid Earth and Geodesy 26 (3), 139–145.

Palano, M., Ferranti, L., Monaco, C., Mattia, M., Aloisi, M., Bruno, V., Cannavò, F., Siligato, G., 2012. GPS velocity and strain fields in Sicily and southern Calabria, Italy: Updated geodetic constraints on tectonic block interaction in the central Mediterranean. Journal of Geophysical Research: Solid Earth (1978–2012) 117 (B7).

Parizzi, A., Cong, X., Eineder, M., 2010. First Results from Multifrequency Interferometry. A comparison of different decorrelation time constants at L, C, and X Band. In: Fringe Workshop 2009. pp. 1–5.

Pavlis, N. K., Holmes, S. A., Kenyon, S. C., Factor, J. K., 2008. An earth gravitational model to degree 2160: EGM2008. EGU General Assembly, 13–18.

Pebesma, E. J., Wesseling, C. G., 1997. Gstat, a program for geostatistical modelling, prediction and simulation.

Peltzer, G., Crampé, F., King, G., 1999. Evidence of nonlinear elasticity of the crust from the Mw7.6 Manyi (Tibet) earthquake. Science 286 (5438), 272–276.

Peltzer, G., Rosen, P. A., 1995. Surface displacement of the 17 May 1993 Eureka Valley, California, earthquake observed by SAR interferometry. Science 268 (5215), 1333–6.

Persson, A., Grazzini, F., 2007. User guide to ECMWF forecast products. Tech. Rep. March, ECMWF.

Petit, G., Luzum, B., 2010. IERS Conventions 2010. Tech. rep., IERS.

Petrov, L., 2004. Study of the atmospheric pressure loading signal in very long baseline interferometry observations. Journal of Geophysical Research 109 (B3), 1–14.

Povic, J., 2006. ETA Model in Weather Forecast. Ph.D. thesis, Royal Institute of Technology.

Pritchard, M. E., Simons, M., 2002. A satellite geodetic survey of large-scale deformation of volcanic centres in the central Andes. Nature 418 (6894), 167–71.

Puglisi, G., Bonaccorso, A., Mattia, M., Aloisi, M., Bonforte, A., Campisi, O., Cantarero, M., Falzone, G., Puglisi, B., Rossi, M., 2005. New integrated geodetic monitoring system at

Stromboli Volcano (Italy). Engineering Geology 79 (1), 13–31.
Remy, D., Bonvalot, S., Briole, P., Murakami, M., 2003. Accurate measurements of tropospheric effects in volcanic areas from SAR interferometry data: application to Sakurajima volcano (Japan). Earth and Planetary Science Letters 213 (3-4), 299–310.
Rockel, B., Will, A., Hense, A., 2008. The regional climate model COSMO-CLM (CCLM). Meteorologische Zeitschrift 17 (4), 347–348.
Rodriguez, E., Morris, C. S., Belz, J. E., 2006. A global assessment of the SRTM performance. Photogrammetric Gngineering and Remote Sensing 72 (3), 249–260.
Rodriguez Gonzalez, F., Bhutani, A., Adam, N., 2011. L1 network inversion for robust outlier rejection in persistent scatterer interferometry. In: IGARSS 2011. pp. 75–78.
Romm, J., 1994. A new forerunner for continental drift. Nature 367, 407 – 408.
Rosen, P. A., Hensley, S., Joughin, I. R., Li, F. K., Madsen, S. N., Rodríguez, E., Goldstein, R. M., 2000. Synthetic aperture radar interferometry. Processings of the IEEE 88 (3), 333–382.
Rosen, P. A., Hensley, S., Zebker, H. A., Webb, F. H., Fielding, E. J., 1996. Surface deformation and coherence measurements of Kilauea Volcano, Hawaii, from SIR-C radar interferometry. Journal of Geophysical Research 101, 23109–23125.
Rosi, M., Bertagnini, A., Landi, P., 2000. Onset of the persistent activity at Stromboli Volcano (Italy). Bulletin of Volcanology 62 (4-5), 294–300.
Rüeger, J. M., 2002. Refractive Index Formulae for Radio Waves Refractive Index Formulae for Radio Waves. In: IFG XXII International Congress. pp. 1–13.
Rusinkiewicz, S., Levoy, M., 2001. Efficient variants of the ICP algorithm. In: Proceedings Third International Conference on 3-D Digital Imaging and Modeling. IEEE Comput. Soc, pp. 145–152.
Saastamoinen, J., 1972. Atmospheric correction for the troposphere and stratosphere in radio ranging satellites. Geophysical Monograph Series 15, 247–251.
Sahoo, S., Reising, S. C., Padmanabhan, S., Vivekanandan, J., Iturbide-sanchez, F., 2011. Three-dimensional humidity retrieval using a network of compact microwave radiometers to correct for variations in wet tropospheric path delay in spaceborne interferometric SAR imagery. IEEE Transactions on Geoscience and Remote Sensing 49 (9), 3281–3290.
Scarth, A., 1994. Volcanoes: An introduction, the louise Edition. UCL Press, London.
Schäfler, A., Dörnbrack, A., Kiemle, C., Rahm, S., Wirth, M., 2010. Tropospheric water vapor transport as determined from airborne Lidar measurements. Journal of Atmospheric and Oceanic Technology 27 (12), 2017–2030.
Schäfler, A., Dörnbrack, A., Wernli, H., Kiemle, C., Pfahl, S., 2011. Airborne lidar observations in the inflow region of a warm conveyor belt. Quarterly Journal of the Royal Meteorological Society 137 (658), 1257–1272.
Scharroo, R., Visser, P., 1998. Precise orbit determination and gravity field improvement for the ERS satellites error source. Journal of Geophysical Research 103 (C4), 8113–8127.
Scherneck, H.-G., 1991. A parametrized solid earth tide model and ocean tide loading effects for global geodetic baseline measurements. Geophysical Journal International 106 (3), 677–694.
Schubert, A., Jehle, M., Small, D., Meier, E., 2012. Mitigation of atmospheric perturbations and solid Earth movements in a TerraSAR-X time-series. Journal of Geodesy 86 (4), 257–270.
Schulzweida, U., Kornblue, L., Quast, R., 2009. Cdo user's guide.
URL `www.mpimet.mpg.de/fileadmin/software/cdo/cdo.pdf`
Schwerdt, M., Bräutigam, B., Bachmann, M., Döring, B., Schrank, D., Gonzalez, J. H., 2010. Final TerraSAR-X calibration results based on novel efficient methods. IEEE Transactions on Geoscience and Remote Sensing 48 (2), 677–689.
Shimada, M., Isoguchi, O., Tadono, T., Isono, K., 2009. PALSAR radiometric and geometric calibration. IEEE Transactions on Geoscience and Remote Sensing 47 (12), 3915–3932.
Sigmundsson, F., Hreinsdóttir, S., Hooper, A., Arnadóttir, T., Pedersen, R., Roberts, M. J., Oskarsson, N., Auriac, A., Decriem, J., Einarsson, P., Geirsson, H., Hensch, M., Ofeigsson,

B. G., Sturkell, E., Sveinbjörnsson, H., Feigl, K. L., 2010. Intrusion triggering of the 2010 Eyjafjallajökull explosive eruption. Nature 468 (7322), 426–30.

Silva, R., Havskov, J., Bean, C., Wallenstein, N., 2012. Seismic swarms, fault plane solutions, and stress tensors for São Miguel Island central region (Azores). Journal of Seismology 16 (3), 389–407.

Skamarock, W. C., Klemp, J. B., Dudhia, J., Gill, D. O., Barker, D. M., Wang, W., Powers, J. G., 2005. A description of the advanced research wrf version 2. Tech. rep., DTIC Document.

Smith, E. K., Weintraubt, S., 1953. The Constants in the Equation for Atmospheric Refractive Index at Radio Frequencies. In: Proceedings of the I.R.E. pp. 1035–1037.

Solheim, F. S., Vivekanandan, J., Ware, R. H., Rocken, C., 1999. Propagation delays induced in GPS signals by dry air, water vapor, hydrometeors, and other particulates. Journal of Geophysical Research 104 (D8), 9663–9670.

Steigenberger, P., Tesmer, V., Krügel, M., Thaller, D., Schmid, R., Vey, S., Rothacher, M., 2007. Comparisons of homogeneously reprocessed GPS and VLBI long time-series of troposphere zenith delays and gradients. Journal of Geodesy 81 (6-8), 503–514.

SWACI, 2012. Space weather application center ionosphere.
URL `swaciweb.dlr.de`

Tarayre, H., Massonnet, D., 1996. Atmospheric Propagation heterogeneities revealed by ERS-1 interferometry. Geophysical Research Letters 23 (9), 989–992.

Tennekes, H., Lumley, J. L., 1972. A first course in turbulence. The MIT press.

Thayer, G. D., 1974. An improved equation for the radio refractive index of air. Radio Science 9 (10), 803–807.

Tibaldi, A., 2001. Multiple sector collapses at Stromboli volcano, Italy: how they work. Bulletin of Volcanology 63 (2-3), 112–125.

Tregoning, P., Boers, R., O'Brien, D., 1998. Accuracy of absolute precipitable water vapor estimates from GPS observations. Journal of Geophysical Research 103 (D22), 28701–28710.

Trenberth, K. E., Berry, J. C., Buja, L. E., 1993. Vertical interpolation and truncation of model-coordinate data. Tech. rep., National Center for Atmospheric Research Boulder, Colorado.

Treuhaft, R. N., Lanyi, G. E., 1987. The effect of the dynamic wet troposphere on radio interferometric measurements. Radio Science 22 (2), 251–265.

Tuttas, S., 2011. Joint gravimetric and geometric survey of geophysical signals - Feasibility study for the TERENO alpine and prealpine Ammer observatory. Ph.D. thesis, Technische Universitaet Muenchen.

Uppala, S. M., Kallberg, P. W., Simmons, A. J., Andrae, U., Bechtold, V. D. C., Fiorino, M., Gibson, J. K., Haseler, J., Hernandez, A., Kelly, G. A., Li, X., Onogi, K., Saarinen, S., Sokka, N., Allan, R. P., Andersson, E., Arpe, K., Balmaseda, M. A., Beljaars, A., Berg, L. V. D., Bidlot, J., Bormann, N., Caires, S., Chevallier, F., Dethof, A., Dragosavac, M., Fisher, M., Fuentes, M., Hagemann, S., Hólm, E., Hoskins, B. J., Isaksen, L., Janssen, P. A. E. M., Jenne, R., Mcnally, a. P., Mahfouf, J.-F., Morcrette, J.-J., Rayner, N. A., Saunders, R. W., Simon, P., Sterl, A., Trenberth, K. E., Untch, A., Vasiljevic, D., Viterbo, P., Woollen, J., 2005. The ERA-40 re-analysis. Quarterly Journal of the Royal Meteorological Society 131 (612), 2961–3012.

Vedel, H., 2000. Conversion of WGS84 geometric heights to NWP model HIRLAM geopotential heights. Danish Meteorological Institute.

Wackernagel, H., 2003. Multivariate Geostatistics. Springer.

Wallace, J. M., Hobbs, P. V., 2006. Atmospheric Science: An Introductory Survey, 2nd Edition. Elsevier Inc.

Wicks, C. W., Thatcher, W., Dzurisin, D., Svarc, J., 2006. Uplift, thermal unrest and magma intrusion at Yellowstone caldera. Nature 440 (7080), 72–5.

Wikipedia, 2013a. Canary islands. [Online; accessed 20-May-2013].
URL `en.wikipedia.org/w/index.php?title=Canary_Islands&oldid=555578677`

Wikipedia, 2013b. Kangerlussuaq. [Online; accessed 20-May-2013].
URL en.wikipedia.org/w/index.php?title=Kangerlussuaq&oldid=553681822

Wikipedia, 2013c. Norderney. [Online; Stand 20. Mai 2013].
URL de.wikipedia.org/w/index.php?title=Norderney&oldid=117946797

William, G. C., 1983. Vertical interpolation of heights and temperatures for model input/output. Tech. Rep. December, U.S. Department of Commerce.

Williams, C. A., Wadge, G., 1998. The effects of topography on magma chamber deformation models: Application to Mt. Etna and radar interferometry. Geophysical research letters 25 (10), 1549–1552.

Williams, S., Bock, Y., Fang, P., 1998. Integrated satellite interferometry: tropospheric noise, GPS estimates and implications for interferometric synthetic aperture radar products. Journal of Geophysical Research: Solid Earth (1978–2012) 103 (B11), 27051–27067.

Williams, S. D. P., Penna, N. T., 2011. Non-tidal ocean loading effects on geodetic GPS heights. Geophysical Research Letters 38 (9), 3–7.

Yague-Martinez, N., Eineder, M., Cong, X., Minet, C., 2012. Ground displacement measurement by TerraSAR-X image correlation: the 2011 Tohoku-Oki aarthquake. IEEE Geoscience and Remote Sensing Letters 9 (4), 539–543.

Yoon, Y. T., Eineder, M., Yague-Martinez, N., Montenbruck, O., 2009. TerraSAR-X precise trajectory estimation and quality assessment. IEEE Transactions on Geoscience and Remote Sensing 47 (6), 1859–1868.

Zebker, H. A., Cervelli, P., Segall, P., Garbeil, H., Mouginis-mark, P., Rowland, S., 1999. A shallow-dipping dike fed the 1995 flank eruption at Fernandina Volcano, Galapagos, observed by satellite radar interferometry. Geophysical Research Letters 26 (8), 1077–1080.

Zebker, H. A., Rosen, P. A., 1994. On the derivation of coseismic displacement fields using differential radar interferometry: the Landers earthquake. In: IGARSS 1994. pp. 286–288.

Zebker, H. A., Villasenor, J., 1992. Decorrelation in interferometric radar echoes. IEEE Transactions on Geoscience and Remote Sensing 30 (5), 950–959.

Zhang, H., Cong, X., Eineder, M., Bletzinger, K.-U., 2010. An integrated approach to determine parameters of a 3D volcano model by using InSAR data with metamodel technique. In: IGARSS 2010. pp. 1648–1651.

Zhang, Z., 1994. Iterative point matching for registration of free-form curves and surfaces. International Journal of Computer Vision 13 (2), 119–152.

Zhu, X., 2011. Very high resolution tomographic SAR inversion for urban infrastructure monitoring: a sparse and nonlinear tour. Ph.D. thesis, Technische Universität München.

Zschau, J., 1989. Earth tides. In: Mueller, I., Zerbini, S. (Eds.), The Interdisciplinary Role of Space Geodesy. Vol. 22 of Lecture Notes in Earth Sciences. Springer Berlin Heidelberg, pp. 31–36.

List of Figures

List of Tables